

From First-Principles to Machine Learning:
Advancing Bandgap Predictions in
Strain-Engineered III-V Semiconductors

Dissertation

zur

Erlangung des Doktorgrades
der Naturwissenschaften
(Dr. rer. nat.)

dem

Fachbereich Physik
der Philipps-Universität Marburg

vorgelegt von

Badal Mondal

aus

Habra, Indien

Marburg, 2023

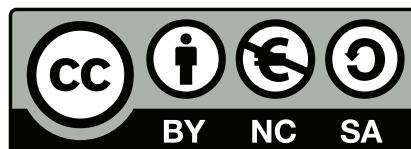
Die vorliegende Dissertation wurde von Juni 2018 bis September 2019 am Fachbereich Physik der Philipps-Universität Marburg unter Leitung von Prof. Dr. Bruno Eckhardt[†] und von September 2019 bis Juli 2023 an der Fakultät für Chemie und Mineralogie der Universität Leipzig unter Leitung von Prof. Dr. Ralf Tonner-Zech angefertigt.

Vom Fachbereich Physik der Philipps-Universität Marburg
als Dissertation angenommen am : 12.10.2023

Erstgutachter : Prof. Dr. Ralf Tonner-Zech
Zweitgutachterin : Prof. Dr. Kerstin Volz

Tag der mündlichen Prüfung : 19.10.2023
Hochschulkenziffer : 1180

The original document is available on the publication server of the
Philipps-Universität Marburg
<http://archiv.ub.uni-marburg.de>



This work is licensed under the
Creative Common
Attribution
NonCommercial
ShareAlike
4.0 International License.

To view a copy of this license, visit
<http://creativecommons.org/licenses/by-nc-sa/4.0>

Abstract

Semiconductor compounds composed of elements from groups 13 and 15 (main groups III and V) of the periodic table, commonly referred to as III-V semiconductors, are integral to modern (opto-)electronics. They play a critical role in applications such as solar cells, light-emitting diodes, optical telecommunication, laser technology, photodetectors, and high-speed electronics. The performance and characteristics of these devices heavily rely on the bandgap value and its direct or indirect character. Consequently, tailoring bandgaps to specific applications is a major goal in semiconductor research field. This holds immense importance in advancing the capabilities and efficiency of semiconductor-based technologies.

This thesis focuses on two primary approaches for tuning bandgaps in III-V semiconductors: varying composition and applying strain to the materials. To identify tailored materials for specific applications, it is crucial to assess the dependence of bandgaps on composition and strain across a broad range of materials. However, experimental methods face limitations in exploring the vast chemical space of combinations of III- and V-elements with variations in composition and strain due to challenges in synthesizing new materials.

In this thesis, a density functional theory (DFT)-based first-principles approach is established to accurately predict bandgaps in strained III-V compound semiconductor materials. A robust scheme is developed within the DFT framework to accurately model the application of various types of strain on a material. The study reveals that not only do the bandgap values change under strain but also the nature of the bandgap can transition from direct to indirect or vice versa. The established DFT protocol enables a comprehensive mapping of bandgap properties with composition and strain in multinary III-V semiconductors, facilitating efficient screening of promising materials for device designs. The investigated materials span binary III-V systems such as GaAs, GaP, GaSb, InP, InAs, InSb, and Si, as well as various ternary materials including GaAsP, GaAsN, GaPSb, GaAsSb, GaPBi, and GaAsBi.

Furthermore, as the composition-strain space expands, standalone DFT approaches become computationally demanding for higher-order systems, such as quaternary and pentanary III-V semiconductor materials. The number of DFT calculations required increases significantly in those systems (\sim millions). To address this, a hybrid approach is developed by integrating a support vector machine-based supervised machine learning (ML) model with DFT. This hybrid DFT-ML approach reduces the number of DFT calculations required by a factor of 1000 while maintaining high prediction accuracy. The effectiveness of this approach is demonstrated through the mapping of bandgaps in the III-V quaternary compound GaAsPSb across its entire composition range and a wide range of strain values, which would otherwise be impractical with standalone DFT method. This hybrid approach enables computationally efficient bandgap predictions across a diverse range of materials and strains, offering a rapid virtual screening capability for the discovery of novel semiconductor materials in (opto-)electronic applications.

Acknowledgements

I am grateful to have dedicated the past five years to my comprehensive doctoral studies, conducted jointly at the Physics Department of Philipps-University Marburg and the Faculty for Chemistry and Mineralogy of Leipzig University. The completion of my research and this thesis would not have been possible without the generous assistance and support of numerous individuals. I express my heartfelt appreciation to all those who aided me throughout my research journey, providing valuable scientific discussions as well as personal encouragement and guidance.

First and foremost, I express my sincere gratitude to my former supervisor, Prof. Dr. Bruno Eckhardt[†], for his outstanding mentorship and for imparting his profound knowledge of physics during my initial two years at the Physics Department of Philipps-University Marburg. It was an immense honor to have been his Ph.D. student, and I am grateful for the privilege of conducting research under his guidance.

I am deeply indebted to my supervisor, Prof. Dr. Ralf Tonner-Zech, for his unwavering support and guidance throughout the final three years of my doctoral studies. I sincerely thank him for his continuous encouragement, valuable insights, and invaluable suggestions during the course of this study.

My deepest appreciation to Prof. Dr. Kertin Volz for the highly stimulating collaboration and consistent support throughout my studies. I am also grateful to Prof. Dr. Julia Westermayer for our excellent collaboration.

I extend my sincere gratitude to all my former colleagues at Philipps-University Marburg and my current colleagues at Leipzig University for providing an environment of vibrant exchange and thoughtful discussions. Special thanks to Dr. Moritz Linkmann and Huchen Li, who made me feel at home in Germany and generously shared their experiences.

Furthermore, I sincerely thank all my current colleagues at Leipzig University. Their comprehensive discussions, fruitful interactions, and valuable feedback in group seminars and conferences have greatly contributed to my research and intellectual growth. I am truly thankful for their support and collaborative spirit.

I express special thanks to Dr. Fabian Pieck, Dr. Andreas Beyer, Dr. Marcel Kröner, Dr. Oliver Maßmeyer, and Dr. Thilo Hepp for the engaging discussions and enjoyable times we had at the RTG conferences.

I am grateful for the opportunity to be a part of the interdisciplinary research training group, Functionalization of Semiconductors, supported by the Deutsche Forschungsgemeinschaft (DFG). My participation in the graduate school (GRK 1782) was truly enriching.

I acknowledge with gratitude the Philipps-University Marburg international office, Beatrix Payer, Renate Schmid, Isabelle Kimmel, Marieka Sycha, and Sandy Ehlers for their incredible support and patience in handling my numerous requests. I sincerely appreciate your assistance in facilitating my pursuit of doctoral studies.

I am grateful to several High-Performance Computing Centers, including HRZ Marburg, GOETHE-CSC Frankfurt, ZIH TU Dresden, and HLR Stuttgart, for providing the essential computational resources that were instrumental in carrying out the computational work presented in this thesis.

Finally, I express my deepest appreciation to my family for their never-ending support and belief in me throughout this journey.

List of Publications

The following section presents a complete list of publications and conference contributions, in chronological order, since acceptance into the doctoral program at Philipps-University Marburg.

Publications in Peer-reviewed Journals

1. B. Mondal, and R. Tonner-Zech, “Systematic strain-induced bandgap tuning in binary III-V semiconductors from density functional theory”, *Phys. Scr.* **2023**, *98*, 065924.
arXiv: 2208.10596.
2. B. Mondal, M. Kröner, T. Hepp, K. Volz, and R. Tonner-Zech, “Accurate first principles band gap predictions in strain engineered ternary III-V semiconductors”, *Phys. Rev. B* **2023**, *108*, 035202.
arXiv: 2302.14547.
3. B. Mondal, J. Westermayr, and R. Tonner-Zech, “Machine learning for accelerated bandgap prediction in strain-engineered quaternary III-V semiconductors”, *J. Chem. Phys.* **2023**, *159*, 104702.
arXiv: 2305.03666.

Other Accepted Reports and Publications

1. A. Feige, L. Bradaczek, M. Michak, D. Günther, M. Grauer, B. Mondal, C. Giacobbe, E. L. Bright, C. Benndorf, R. Tonner-Zech, and O. Oeckler, “The crystal chemistry of binary beryllium dipnictides – new binary structure types between Zintl polyanions and Grimm Sommerfeld compounds”, *Acta Cryst.* **2022**, *A78*, e270-e271.
2. B. Mondal, R. U. Khan, F. Kreuter, P. Maue, S. Pan, F. Pieck, H. Weiske, and R. Tonner-Zech, “Organic functionalization on solid sur-

faces”, in High Performance Computing in Science and Engineering ’22, in press.

3. F. Pieck, J.-N. Luy, F. Kreuter, B. Mondal, and R. Tonner-Zech, “Reactivity of organic molecules on semiconductor surfaces revealed by density functional theory”, in High Performance Computing in Science and Engineering ’21, (Eds.: W. E. Nagel, D. H. Kröner, and M. M. Resch), Springer International Publishing, Cham, **2023**, pp. 113–131.

Oral Presentations

- Badal Mondal, Andreas Beyer, Kerstin Volz, and Bruno Eckhardt, “Morphological stability analysis of (pseudo-)ternary epitaxial surface”, *RTG 1782 Functionalization of Semiconductors* (Schwäbisch Gmünd, Germany) **2019**, Contributed talk.
- Badal Mondal and Ralf Tonner, “Substrate, temperature and pressure effect (strain) on electronic properties of III-V semiconductors from ab-initio approach”, *RTG 1782 Functionalization of Semiconductors* (Höchst, Germany) **2020**, Contributed talk.
- Badal Mondal and Ralf Tonner, “Strain induced direct-indirect transition in ternary III-V semiconductor from ab-initio approach”, *RTG 1782 Functionalization of Semiconductors* (Herborn, Germany) **2021**, Contributed talk.
- Badal Mondal and Ralf Tonner-Zech, “Strain induced bandgap transition in III-V semiconductors”, *20th International Conference on Metalorganic Vapor Phase Epitaxy* (Stuttgart, Germany) **2022**, Contributed talk.
- Badal Mondal and Ralf Tonner-Zech, “Strain-induced bandgap transition in III-V semiconductors”, *German Physical Society* (Regensburg, Germany) **2022**, Contributed talk.
- Badal Mondal and Ralf Tonner-Zech, “Predicting bandgap in strain-engineered multinary III-V semiconductors”, *German Physical Society* (Dresden, Germany) **2023**, Contributed talk.

Poster Presentations

- Badal Mondal and Ralf Tonner, “Strain induced direct-indirect transition in III-V semiconductor materials from ab-initio approach”, *Symposium on Theoretical Chemistry* (Würzburg, Germany) **2021**.
- Badal Mondal and Ralf Tonner-Zech, “Strain-induced bandgap transition in III-V semiconductors”, *Psi-k conference* (Lausanne, Switzerland) **2022**.
- Badal Mondal and Ralf Tonner-Zech, “Strain-induced bandgap transition in III-V semiconductors”, *Symposium on Theoretical Chemistry* (Heidelberg, Germany) **2022**.
- Badal Mondal, Raza Ullah Khan, Florian Kreuter, Patrick Maue, Sudip Pan, Fabian Pieck, Hendrik Weiske, and Ralf Tonner-Zech, “Organic functionalization on solid surfaces”, *High-Performance Computing in Science & Engineering – 25th Results and Review Workshop of the HLRs* (Stuttgart, Germany) **2022**.

Contents

| | |
|--|------------|
| Abstract | i |
| Acknowledgements | iii |
| List of Publications | v |
| 1 Introduction | 1 |
| 1.1 Semiconductors in Technologies | 1 |
| 1.2 Semiconductor Electronic Properties | 2 |
| 1.3 Material Selection | 4 |
| 1.4 Bandgap Engineering | 5 |
| 1.5 Theoretical Approaches | 8 |
| 1.5.1 First-Principles Approach | 9 |
| 1.5.2 Machine Learning Approach | 10 |
| 1.6 Scope and Organization of the Thesis | 11 |
| 2 Theoretical Background | 12 |
| 2.1 Schrödinger Equation | 12 |
| 2.2 Born-Oppenheimer Approximation | 14 |
| 2.3 Density Functional Theory | 15 |
| 2.3.1 Hohenberg-Kohn Theorem | 16 |
| 2.3.2 Kohn-Sham Theory | 18 |
| 2.4 Quantum Mechanics for Solid | 21 |
| 2.4.1 Periodicity and Reciprocal Space | 21 |
| 2.4.2 Bloch's Theorem | 24 |
| 2.5 Density Functional Theory for Solid | 24 |
| 2.5.1 Periodic Electron Density | 24 |
| 2.5.2 Kohn-Sham Equation for Solid | 25 |
| 2.5.3 Plane-Wave Basis Expansion | 26 |
| 2.5.4 Periodic Kohn-Sham in Plane-Wave Basis | 28 |
| 2.5.5 Projector Augmented-Wave Method | 29 |
| 2.6 Electronic Properties | 31 |
| 2.6.1 Bandstructure | 31 |

| | | |
|----------|---|------------|
| 2.6.2 | Bandgap | 32 |
| 2.6.3 | Electron Spin and Spin-Orbit Coupling | 33 |
| 2.6.4 | Bandgap Determination Problem | 33 |
| 2.6.5 | Bandstructures in Non-Crystalline Solid | 34 |
| 2.7 | Density Functional Approximations | 34 |
| 2.7.1 | Approximate Exchange-Correlation Functional | 34 |
| 2.7.2 | Dispersion Correction | 37 |
| 2.8 | Modeling III-V Compounds | 39 |
| 2.8.1 | Special Quasi-Random Structure | 39 |
| 2.8.2 | Bandstructure folding | 41 |
| 2.8.3 | Bloch Spectral Weights | 42 |
| 2.8.4 | Effective Bandstructure | 43 |
| 2.8.5 | Bandgap Nature Determination Protocol | 44 |
| 2.9 | Machine learning | 47 |
| 2.9.1 | Support Vector Machine | 47 |
| 2.9.2 | Kernel Method | 51 |
| 2.9.3 | SVM Classifier Algorithms | 52 |
| 2.9.4 | Support Vector Regression | 53 |
| 2.9.5 | Model Performance Evaluation | 54 |
| 3 | Methods | 56 |
| 3.1 | Density Functional Theory Setup | 56 |
| 3.1.1 | Materials Modeling | 56 |
| 3.1.2 | Strain Modeling | 57 |
| 3.1.3 | Computational Setup | 58 |
| 3.2 | Machine Learning Setup | 59 |
| 3.2.1 | Model Description | 59 |
| 3.2.2 | Feature Representation | 59 |
| 3.2.3 | Performance Evaluation Metrics | 61 |
| 3.2.4 | Hyperparameter Optimization | 61 |
| 3.2.5 | Model Training | 61 |
| 4 | Results | 62 |
| 5 | Summary | 72 |
| | Zusammenfassung | 76 |
| | Bibliography | 98 |
| | Scientific Contributions | 99 |
| | Abbreviations and Acronyms | 183 |

Chapter 1

Introduction

1.1 Semiconductors in Technologies

Semiconductor compounds have emerged as pivotal materials in modern technologies. They serve as the backbone for a wide range of devices that have become integral to our everyday life. These versatile materials form the foundation for electronic circuits, photovoltaic cells, light-emitting diodes (LEDs), and lasers, powering essential technologies such as computers, electric vehicles, smartphones, and modern communication networks [1, 2].

One key characteristic that makes semiconductors unique is their ability to transition between electrically insulating and conducting states through suitable manipulation. This property plays a crucial role in the functioning of transistors, which are the fundamental building blocks of integrated circuits [3]. Transistors enable complex computational operations by rapidly switching their electrical resistance in response to an applied voltage, facilitating the processing and storage of vast amounts of information.

Another significant application of semiconductors lies in the field of photovoltaics. Photovoltaic devices harness the power of sunlight by converting solar energy into electricity through the photoelectric effect [4]. This effect involves the excitation of electrons within the semiconductor, leading to the generation of mobile charge carriers that can be extracted for electrical use. Photovoltaic systems have gained tremendous attention due to their potential to provide clean, renewable energy, thereby reducing dependence on fossil fuels and mitigating the environmental impact of energy production.

Semiconductors also play a crucial role in optoelectronics, where they exhibit the ability to convert electrical energy into light. This property finds practical applications in various devices such as LEDs, which have become the most prevalent light source worldwide, illuminating our homes, offices,

and public spaces [5]. Lasers, another significant application of semiconductors, have revolutionized modern optical telecommunication and information technology. They enable high-speed data transmission over long distances, facilitating the global connectivity that drives our modern world [6, 7].

To comprehend the underlying principles behind the exceptional performance of semiconductors, it is essential to understand their bandstructure. The bandstructure of semiconductors provides insight into the energy levels available to electrons and the allowed transitions within the material, thereby governing their electronic properties and behavior. This understanding is crucial for optimizing the design and performance of semiconductor devices, enabling the development of more efficient and advanced technologies.

1.2 Semiconductor Bandstructure and Electronic Properties

Semiconductors exhibit fascinating electronic properties that stem from their distinctive bandstructure. Similar to how atoms have infinitely many energy levels, solids possess an infinite number of allowed bands. However, for practical purposes, most bands with high energies are disregarded. Likewise, low-energy bands associated with core orbitals (e.g., 1s electrons) are usually inert and ignored as they remain filled with electrons at all times.

The electronic bands of utmost importance for electronics and optoelectronics are those near the Fermi level. In semiconductors, the Fermi level is surrounded by a “bandgap”, an energy range where no electronic states exist. The closest band above the bandgap is called the conduction band (CB), and the closest band beneath the bandgap is called the valence band (VB). Figure 1.1 depicts a schematic of the semiconductor bandstructure.

Based on the wavevectors (\mathbf{k}) of the states surrounding the bandgap, it is classified as either a “direct bandgap” or an “indirect bandgap”. The bandgap is called a direct bandgap if the lowest-energy state in the CB, known as the conduction band minimum (CBM), has the same \mathbf{k} as the highest-energy state of the VB, referred to as the valence band maximum (VBM). If they are different, it is called an indirect bandgap.

The bandgap value in a semiconductor plays a crucial role in determining its properties, such as conductivity and optical characteristics. It signifies the energy required to excite an electron from the VB to the CB. When the VB is completely filled with electrons and the CB is entirely empty, no available states exist for electron movement, resulting in a lack of net charge carrier mobility. Consequently, there is no flow of electric current.

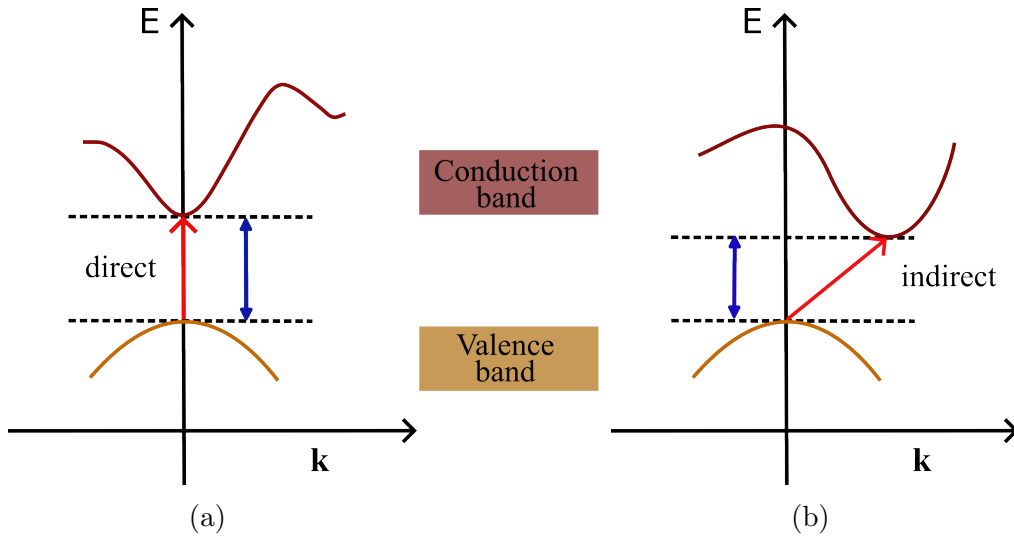


Figure 1.1: Schematic representation of semiconductor bandstructure. The red arrows indicate the electronic excitation in a) direct bandgap and b) indirect bandgap semiconductors. The corresponding bandgap values are represented by blue arrows.

However, when some electrons are excited from the VB to the CB, such as through light absorption or the application of an external electric field, the semiconductor becomes conductive. The excited CB electron (along with the hole in the VB) can freely move within the crystal lattice, serving as charge carriers for conducting electric current. Thus, by manipulating this excitation process, the generation and flow of current can be controlled.

Alternatively, the excited electron in the CB can undergo radiative recombination with a hole in the VB, resulting in the emission of light. This process forms the foundation of optoelectronics.

For materials with a direct bandgap, valence electrons can be directly excited into the CB by photons with energies exceeding the bandgap. This direct transition allows efficient radiative recombination, leading to strong light emission. Consequently, direct bandgap materials find extensive use in optoelectronic applications such as LEDs and semiconductor lasers.

On the other hand, indirect bandgap materials require momentum transfer, often through interactions with phonons, to satisfy conservation laws during electronic transitions. These indirect “forbidden” transitions have lower probabilities and weaker intensities, making indirect bandgap materials less suitable for optoelectronic applications. However, they are still crucial for electronic applications, such as in solar cells, where the advantage of reduced radiative recombination probabilities can be effectively utilized.

Clearly, the behavior and capabilities of semiconductor devices are significantly influenced by both the value and nature of the bandgap, whether it is direct or indirect. Hence, the bandgap plays a critical role in shaping the performance and properties of these devices. By manipulating the bandgap, it is possible to design materials with desired electrical and optical properties, thereby creating devices with diverse capabilities. Consequently, tailoring the bandgap of materials to specific applications is a major goal in the field of (opto-)electronics.

1.3 Material Selection

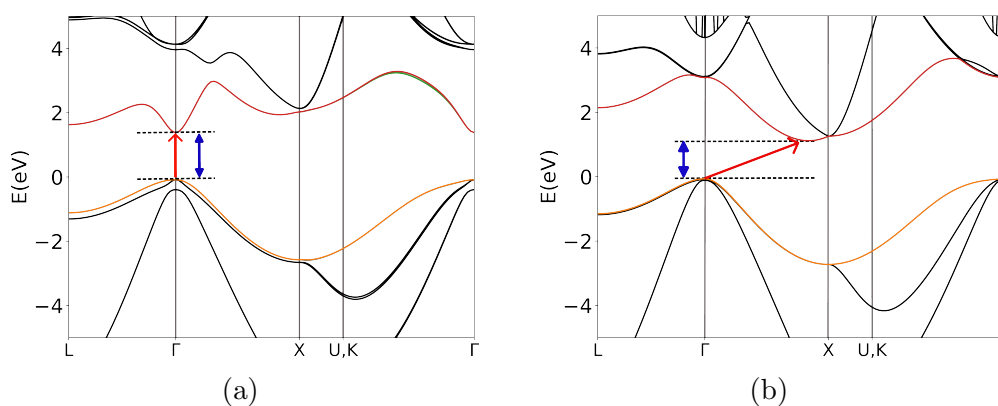


Figure 1.2: Bandstructure of a) direct bandgap GaAs and b) indirect bandgap Si. The red arrows indicate the electronic excitations. The bandgap values are shown by blue arrows.

While silicon is widely known and utilized in electronics and photovoltaics, its indirect bandgap (Figure 1.2b) limits its suitability for optoelectronic applications. One particular material class, the III-V compound semiconductors, composed of elements from groups 13 and 15 of the periodic table (commonly referred to as main groups III and V), offer great potential in the field of optoelectronics [7, 8]. Isoelectronic with Si, these materials can exhibit direct bandgap (Figure 1.2a), making them ideal for optoelectronics.

In this thesis, the focus is specifically on III-V materials of the type $A_{\text{III}}B_{\text{V}}$ with $A = \text{Ga, In}$ and $B = \text{N, P, As, Sb, Bi}$. Among the binary III-V materials, the investigation consists of GaAs, GaP, GaSb, InP, InAs, and InSb. Additionally, Si is included for the purpose of specific comparisons. These materials are not only of great interest for fundamental research but also find applications in various fields such as microelectronics, solar cells, laser technology, and LEDs [1, 2, 9].

In the category of ternary materials, GaAsP is explored, an experimentally well-studied and promising candidate for LEDs, detectors, and Si-based multi-junction solar cells [10–17]. Additionally, GaAsN, a promising laser-active material [18–21]; GaPSb, a candidate for vertical cavity emitting surface lasers [22–26]; GaAsSb, which has potential as a material for tandem solar cells [27, 28]; GaPBi, a promising material for near-infrared photonic device application on Si [29, 30]; and GaAsBi, another material being explored for near- and mid-infrared photonic devices [31–33] are investigated.

In the quaternary material class, the analysis on GaAsPSb is presented. Although this specific quaternary compound has not been extensively studied, its binary and ternary subsystems (GaAs, GaP, GaSb, GaAsP, GaAsSb, and GaPSb), as mentioned earlier, have been successfully synthesized and applied in various research fields. Moreover, the theoretical analysis provided in this thesis offer valuable insights for future experimental exploration of this material system.

1.4 Bandgap Engineering

This thesis explores two key strategies that have emerged to enhance the performance and versatility of III-V semiconductor materials: compositional bandgap engineering and strain engineering.

Compositional bandgap engineering involves modifying the chemical composition of semiconductors to tailor their bandgap values. By combining elementary (binary) III-V materials, compound III-V semiconductors can be designed with desired bandgap properties [34–41]. The extensive chemical space of III-V semiconductors enables fine-tuning of the bandgap, offering diverse opportunities for various device applications within this material class. Figure 1.3 illustrates the concept of modifying bandgap properties through compositional engineering. The lines connecting the binary compounds in this figure depict the changes in bandgap (value and nature) when they are combined to create compound semiconductors.

On the other hand, strain engineering involves the deliberate application of strain to semiconductors to modulate their bandgap properties. This can be achieved through mechanical strain [42–48] or substrate-induced strain [5, 40, 49–51]. Mechanical strain refers to the application of external pressure or stress on the semiconductor material, leading to a change in its bandgap. An example of mechanical strain-induced alteration of photoresponse in Si-nanomembrane (NM) photodetector is shown in Figure 1.4. Here, the photocurrent increases with an increase in the applied external pressure, indicating a change in the optical bandgap value of Si under strain [45].

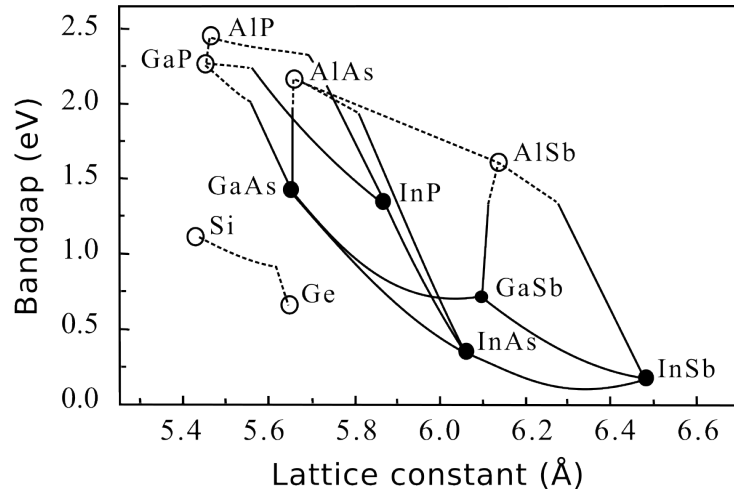


Figure 1.3: Illustration demonstrating the variation of bandgap with composition in compound semiconductors, depicted in terms of lattice constant. Solid and empty circles represent direct and indirect bandgaps, respectively. Likewise, solid and dotted lines indicate direct and indirect bandgaps, respectively. Bandgaps are calculated from Vegard's law with bandgap bowing. Figure adapted with permission from Reference [34].

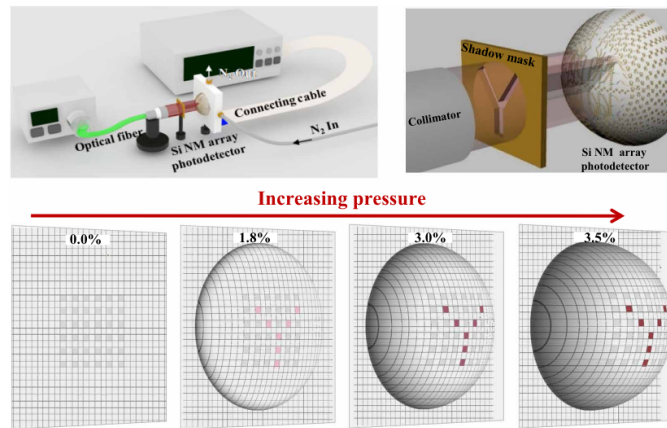


Figure 1.4: The effect of strain on the bandgap nature of a Si-nanomembrane photodetector. The first row presents a schematic of the experimental setup. The second row displays photocurrent mapping images of a representative letter 'Y' under increasing applied external pressure. With applied pressure, strain induces a left-to-right increase in photocurrent in Si-NM pixels due to changing Si optical bandgap under strain. Beyond a threshold strain, the Si optical bandgap aligns with the incident 1310 nm light. Figure adapted from Reference [45].

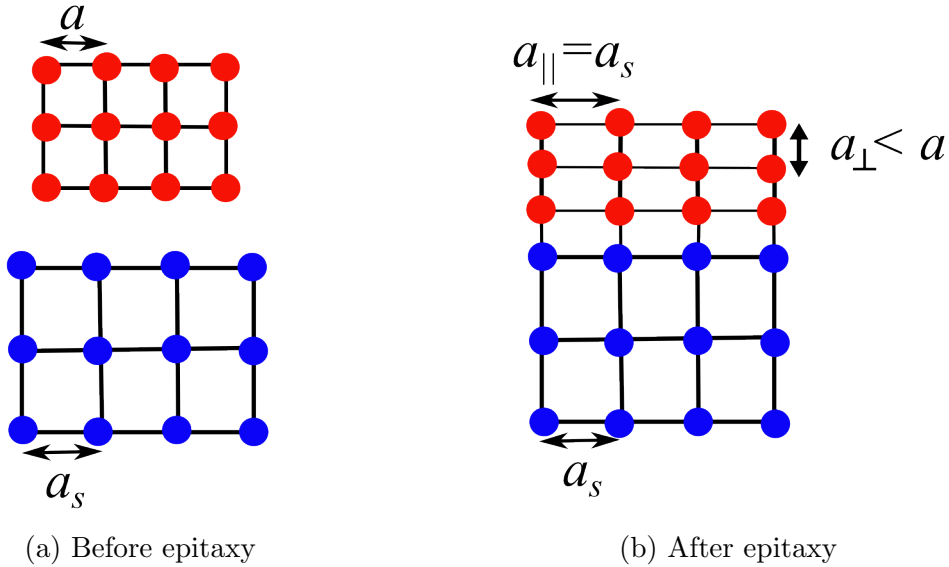


Figure 1.5: Schematic representation of lattice parameter relaxation in epitaxy. The substrate and layer are shown in blue and red, respectively. The layer lattice parameter (a) relaxes after epitaxy. The in-plane lattice parameters of the layer (a_{\parallel}) adapt to the substrate lattice parameters (a_s). In response, the out-of-plane lattice parameter (a_{\perp}) relaxes to a smaller value. Only the case where $a < a_s$ is shown. In the case when $a > a_s$, a_{\perp} would relax to a larger value, i.e., $a_{\perp} > a$. Figure adapted from Reference [57].

Substrate-induced strain occurs when a semiconductor material is grown on a substrate with a different lattice parameter. Epitaxial growth [51–56], commonly used for fabricating III-V semiconductor materials, is an example of substrate-induced strain. In epitaxy, when two layers of crystals with slightly different lattice parameters are deposited as a heterostructure, they can exhibit a common in-plane lattice parameter parallel to the interface. Notably, in epitaxial deposition, the substrate thickness is significantly larger than the deposited layer, resulting in lattice relaxation of the epitaxial layer.

Figure 1.5 illustrates a schematic of epitaxial lattice relaxation. Here, the lattice parameter of the layer is adjusted to match that of the substrate, leading to built-up strain in the layer. Achieving perfect lattice matching between the substrate and epitaxial layer in processes like epitaxy is rarely feasible due to limited substrate options. Additionally, direct epitaxy of III-V layers on Si substrate is particularly desirable, as it can leverage the already existing and mature complementary metal-oxide semiconductor (CMOS) technology for cost-effective production [5, 40, 49–51]. In such cases, the presence of the substrate-induced strain becomes inevitable.

In these scenarios, the bandgap of the optically active layer is significantly influenced not only by the composition but also by the strain induced by the substrate [58, 59]. Epitaxial growth of the same material on different substrates or on the same substrate with varying degrees of lattice relaxation, such as in multiple quantum well (MQW) structures, can alter the bandgap properties significantly [26, 60, 61].

Another close analog of substrate-induced strain is the core-shell lattice mismatch strain in coated nanowires [62–66] and nanoparticles [67–73]. In these systems, the bandgaps of the core nanowires or quantum dots are tuned by inducing strain through the shell layer with different lattice parameters than the core material [62–73].

Therefore, the combined approaches of compositional and strain engineering in III-V semiconductors provide pathways for optimizing the material properties for various technological applications. Thus, a comprehensive understanding of the material-specific dependence of the bandgap on composition and strain is crucial for selecting suitable materials for specific applications. Experimentally, growing new materials is often challenging because of thermodynamic or kinetic limitations, such as phase separation or inter-surface instabilities, in addition to the need for optimizing growth conditions and precursors [36, 39–41, 50, 53]. Hence, the experimental exploration of the extensive composition-strain space in these materials is currently limited to only a few combinations of materials and strain values. This results in the undersampling of regions in the composition-strain space. Therefore, standalone experimental approaches potentially can miss optimal materials. Thus, theoretical methods that are accurate and computationally efficient are crucial for effectively screening and guiding the materials' design.

1.5 Theoretical Approaches

There are two primary categories of theoretical methods that are commonly used to analyze electronic properties in semiconductor materials: empirical/semi-empirical methods and first-principles methods.

Empirical/semi-empirical methods, such as the tight-binding method [74–76] and k·p method [9, 76] are computationally efficient and relatively easy to apply. However, they rely on empirical fitting parameters, which limit their predictive capability for new materials, a key objective in computational materials design. In contrast, first-principles methods, such as density functional theory (DFT) [77–80] and quasiparticle methods (e.g., GW) [81–84], do not require empirical fitting parameters and are thus considered predictive. Therefore, in this thesis, first-principles method is employed.

1.5.1 First-Principles Approach

One of the most widely used first-principles approaches in material science is DFT. For analyzing electronic properties, such as the bandgap of semiconductor materials, DFT with hybrid functionals, like HSE06 [85, 86], has shown excellent accuracy [87]. However, this thesis utilizes the modified Becke-Johnson (m-BJ) functional, also known as the TB09 functional [88], to predict the bandgap of III-V materials. Specifically designed for predicting bandgap properties in semiconductors, the m-BJ functional offers the advantage of being relatively computationally cheap while maintaining accuracy comparable to computationally expensive GW methods or DFT with hybrid functionals [88, 89]. It can be reliably applied to very large systems in an efficient way, enabling studies involving numerous (\sim thousands) large systems, as targeted in this thesis.

The m-BJ functional has previously been successfully applied to calculate bandgap properties across a diverse set of semiconductor compounds. From small bandgap (~ 1 eV) binary semiconductors to large bandgap (~ 22 eV) rare-gas solids, this functional has been applied to group IV semiconductors (e.g., Si, Ge), III-V semiconductors (e.g., GaAs, GaN, AlP), II-VI semiconductors (e.g., ZnS, CdS), transition metal oxides (e.g., MnO, FeO, NiO), and rare-gas solids from Ne to Xe [88, 90–94]. Subsequently, it has been demonstrated in accurately predicting the bandgap in compound semiconductors, including III-V (e.g., GaAsBi, GaAsP, GaAsN) and II-VI (e.g., HgCdTe) materials [18, 95, 96]. Notably, Rosenow et al. successfully calculated the bandgaps of a large number of GaAsN compositions (up to 12% N) with this functional, in systems containing up to 432 atoms [18].

While, previous studies utilizing the m-BJ functional have focused on unstrained systems [18, 88, 90–94, 97], this work extends the application of the functional to accurately predict bandgaps in III-V semiconductors under a wide range of strains. This expands the scope of applicability and potential of the m-BJ functional in the semiconductor field.

Importantly, DFT has also proven to be successful in predicting structural properties. Crystal structures, lattice parameters, elastic constants, and phase stabilities in various alloy materials, such as Cd-, Mg-, Cu-, Al-, Zn-, Zr-, Ti-, and Ni-alloys, have been extensively studied using DFT methods [93, 98–104]. In the III-V semiconductor field, for instance, in multinary III-V materials like GaSb, InSb, AlGaAs, GaAsP, GaAsSb, InGaP, and InGaAs, such structural properties have been analyzed by DFT methods [18, 50, 95, 96, 105–110]. With its ability to predict both the structural and electronic properties entirely from first-principles, DFT represents a powerful tool for predictive material screening.

1.5.2 Machine Learning Approach

While the DFT approach has been successful in predicting bandgaps for multinary III-V materials, its application to higher-order systems beyond ternary poses limitations. The composition-strain space becomes exponentially large when moving to quaternary and pentanary systems. This leads to computational bottleneck, as a comprehensive mapping of bandgaps in those systems requires a substantial number of DFT calculations¹ (\sim millions) per element combination.

In order to address this computational limitation, a machine learning (ML) approach is adopted in this thesis. ML techniques leverage data-driven models to predict materials' properties. These models can learn complex relationships between the material properties and enable the predictions of properties with significantly reduced computational cost [111–113].

In the field of bandgap prediction for semiconductor materials, several ML methods have been developed over the decades. For instance, ML methods based on kernel ridge regression (KRR), alternating conditional expectations (ACE), decision trees, and support vector machines (SVM) models have been successfully employed to predict bandgaps in perovskites [114, 115]. Setyawan et al. estimated the bandgap of inorganic scintillator materials using ordinary least squares regression (OLSR) ML models [116]. The bandgap of a large number of chalcopyrite solar materials has been predicted by ML methods based on OLSR and least absolute shrinkage and selection operator (LASSO) models [117]. Similar ML models, including Gaussian process regression (GPR), were used to predict bandgaps of functionalized MXene compounds [118]. Weston and Stampfl combined DFT with various ML models to predict the bandgap of quaternary kesterite semiconductors [119]. ML methods based on neural networks and SVM models also have been successfully applied to predict bandgaps of different binary II-VI, III-V, and IV-IV semiconductors, as well as ternary I-III-VI₂, II-IV-V₂, III-VI-VII, and IV-V-VII compounds [120–123].

In this thesis, a SVM-based ML model is developed that is capable of predicting bandgap properties for multinary III-V semiconductors. Previous studies on ML-based semiconductor bandgap prediction have consistently demonstrated the superior performance of the SVM-based models [119–125]. However, while previous ML-based approaches have mainly focused on unstrained compounds, the newly devised model accurately predicts bandgaps in strained systems.

¹Within 0 – 100% composition and –5 to +5% strain range, for a resolution of 0.1% in both composition and strain, the number of DFT calculations require for a quaternary compound of type AB_xC_yD_{100-x-y} = 50,651,601.

1.6 Scope and Organization of the Thesis

The research presented in this thesis establishes the methodology and addresses the challenges for predictive computational modeling of bandgap properties in strain-engineered III-V semiconductors. The integrated first-principles calculations and ML techniques provide a comprehensive and powerful approach to exploring bandgap properties across the vast range of strained semiconductor materials. It sets the stage for future computational materials design approaches in strain engineering, both for established materials and for the discovery of new ones. The ultimate goal of this work is to provide comprehensive guidelines for studying bandgap properties in strained materials, facilitating the development of novel semiconductor materials with tailored bandgap characteristics.

The thesis is organized as follows:

- Chapter 2 provides a comprehensive theoretical background on the DFT and ML methods, which form the foundation of this thesis. It covers the principles, mathematical formalism, and key concepts of DFT, as well as the fundamentals of the ML methods employed.
- Chapter 3 presents a detailed overview of the computational methods used in this study, emphasizing the steps taken to ensure accurate and reliable results. It discusses the computational procedures, software tools, and techniques employed to obtain robust predictions.
- Chapter 4 outlines the main findings of the study. The chapter begins with an examination of binary III-V semiconductor systems in Section 4.1. Section 4.2 then expands the scope to ternary systems. Finally, Section 4.3 showcases the integration of ML approach in quaternary III-V systems.
- Chapter 5 summarizes the objectives and major achievements of the thesis. It provides a comprehensive conclusion that highlights the significance of the developed theoretical approach in bandgap engineering for strained III-V semiconductors. The implications and potential future directions of the research are discussed.
- Additional details of the individual projects, a data availability statement, and the reprints of the scientific contributions that are part of this thesis are attached at the end.

Chapter 2

Theoretical Background

This chapter provides a comprehensive overview of the theoretical foundation underlying the methods employed in this thesis. While detailed derivations of the methods will be omitted, the main objective here is to provide a clear understanding of their principles. For more in-depth information on the methods beyond what is covered here, refer to these quantum chemistry [126–129], solid-state physics [9, 75, 130], and machine learning [111–113] textbooks.

2.1 Schrödinger Equation

Central to the field of quantum mechanics is the understanding that the behavior of physical systems at the microscopic scale fundamentally differs from that at the macroscopic level, which can be suitably described by classical physics. The fundamental equation governing quantum mechanics is the Schrödinger equation. It represents an eigenvalue problem in which a system’s Hamiltonian operator, \hat{H} , acts upon a wavefunction representing the system. In the most general bra-ket notation, the time-independent, non-relativistic Schrödinger equation for N electrons and K nuclei reads

$$\hat{H}|\Psi_n\rangle = E_n|\Psi_n\rangle \quad (2.1)$$

where $|\Psi_n\rangle$ represents the n -th eigenstate with its corresponding energy E_n . The wavefunction, $|\Psi_n\rangle$, provides a complete description of a quantum system in the state n . It depends on the spatial and spin coordinates of all the particles within the system and allows the calculation of observables such as energy, momentum, and position. In most general form, the wavefunction can be defined as:

$$\Psi_n(\mathbf{r}, \boldsymbol{\sigma}, \mathbf{R}, \underline{S}) = \langle \mathbf{r}, \boldsymbol{\sigma}, \mathbf{R}, \underline{S} | \Psi_n \rangle \quad (2.2)$$

2.1. SCHRÖDINGER EQUATION

with

| | |
|--|---|
| $\mathbf{r}_i = (x_i, y_i, z_i)$ | Coordinate vector of electron i |
| $\underline{\mathbf{r}} = (\mathbf{r}_1, \mathbf{r}_2, \dots, \mathbf{r}_N)$ | Set of all electron coordinates |
| $\mathbf{R}_A = (x_A, y_A, z_A)$ | Coordinate vector of atomic nuclei A |
| $\underline{\mathbf{R}} = (\mathbf{R}_1, \mathbf{R}_2, \dots, \mathbf{R}_K)$ | Set of all atomic nuclei coordinates |
| σ_i | Spin coordinate of electron i |
| $\underline{\sigma} = (\sigma_1, \sigma_2, \dots, \sigma_N)$ | Set of spin coordinates of all electrons |
| S_A | Spin coordinate of spin of atomic nucleus A |
| $\underline{S} = (S_1, S_2, \dots, S_K)$ | Set of spin coordinates of all atomic nuclei |

The non-relativistic Hamilton operator, $\hat{H}(\underline{\mathbf{r}}, \underline{\mathbf{R}})$, is composed of one- and two-particle terms that describe the kinetic energy and interaction between all constituents of the system.

$$\hat{H}(\underline{\mathbf{r}}, \underline{\mathbf{R}}) = \hat{T}_N(\underline{\mathbf{R}}) + \hat{T}_e(\underline{\mathbf{r}}) + \hat{V}_{ee}(\underline{\mathbf{r}}) + \hat{V}_{Ne}(\underline{\mathbf{r}}, \underline{\mathbf{R}}) + \hat{V}_{NN}(\underline{\mathbf{R}}) \quad (2.3)$$

Hamiltonian (2.3) does not include the relativistic effects, e.g., relativistic kinetic energy correction and interactions of magnetic moments such as spin-orbit coupling. In atomic units¹, different energy operators can be expressed as follows:

$$\text{Kinetic energy of nuclei} \quad \hat{T}_N(\underline{\mathbf{R}}) = -\frac{1}{2} \sum_A \frac{1}{M_A} \nabla_{\mathbf{R}_A}^2 \quad (2.4)$$

$$\text{Kinetic energy of electrons} \quad \hat{T}_e(\underline{\mathbf{r}}) = -\frac{1}{2} \sum_i \nabla_{\mathbf{r}_i}^2 \quad (2.5)$$

$$\text{Electron-electron interaction} \quad \hat{V}_{ee}(\underline{\mathbf{r}}) = + \sum_i \sum_{j>i} \frac{1}{|\mathbf{r}_i - \mathbf{r}_j|} \quad (2.6)$$

$$\text{Nucleus-electron interaction} \quad \hat{V}_{Ne}(\underline{\mathbf{r}}, \underline{\mathbf{R}}) = - \sum_A \sum_i \frac{Z_A}{|\mathbf{r}_i - \mathbf{R}_A|} \quad (2.7)$$

$$\text{Nucleus-nucleus interaction} \quad \hat{V}_{NN}(\underline{\mathbf{R}}) = + \sum_A \sum_{B>A} \frac{Z_A Z_B}{|\mathbf{R}_A - \mathbf{R}_B|} \quad (2.8)$$

Z_A and M_A are the atomic number and mass of nucleus A .

Solving the Schrödinger equation 2.1 allows us to determine the allowable energy states and associated wavefunctions of a quantum system. This equation serves as the foundation for understanding the electronic structure and properties of atoms, molecules, and solids.

¹In atomic unit, fundamental constants such as the electron mass (m_e), electron charge (e), and reduced Planck's constant (\hbar) are set to unity.

For simplicity, in the following, the spin contributions are disregarded and will be addressed in a separate section. Moreover, in this thesis, the focus is only on the lowest energy state of Equation 2.1. At the ground state (assuming non-degenerate), the Schrödinger equation 2.1 simplifies to:

$$\hat{H}(\underline{\mathbf{r}}, \underline{\mathbf{R}})\Psi(\underline{\mathbf{r}}, \underline{\mathbf{R}}) = E\Psi(\underline{\mathbf{r}}, \underline{\mathbf{R}}) \quad (2.9)$$

where Ψ denotes the ground-state wavefunction with ground-state energy E ,

$$E = \min_n E_n \quad (2.10)$$

2.2 Born-Oppenheimer Approximation

In comparison to nuclei, electrons possess significantly lighter masses. Thus the electrons can rapidly respond and adjust to changes in the system's geometry. This characteristic permits the simplification of electronic-nuclear interactions. This is known as Born-Oppenheimer approximation (BOA) [126]. According to the BOA, nuclear motion is considered slow and adiabatic, while electronic motion is regarded as rapid and highly responsive to changes in nuclear positions. This significant difference in kinetic response between electrons and nuclei allows the separation of their respective wavefunctions. By decoupling the total wavefunction $\Psi(\underline{\mathbf{r}}, \underline{\mathbf{R}})$ into nuclear, Ψ_N , and electronic contributions, Ψ_e , we obtain:

$$\Psi(\underline{\mathbf{r}}, \underline{\mathbf{R}}) = \Psi_N(\underline{\mathbf{R}}) \Psi_{e,\underline{\mathbf{R}}}(\underline{\mathbf{r}}) \quad (2.11)$$

where the electronic wavefunction $\Psi_{e,\underline{\mathbf{R}}}(\underline{\mathbf{r}})$ depends parametrically on the atomic positions $\underline{\mathbf{R}}$. Within the BOA, Equation 2.9 simplifies to:

$$\left[\hat{H}_{e,\underline{\mathbf{R}}}(\underline{\mathbf{r}}) + V_{NN,\underline{\mathbf{R}}} \right] \Psi_{e,\underline{\mathbf{R}}}(\underline{\mathbf{r}}) = U_{e,\underline{\mathbf{R}}} \Psi_{e,\underline{\mathbf{R}}}(\underline{\mathbf{r}}) \quad (2.12)$$

where $\hat{H}_{e,\underline{\mathbf{R}}}$ represents the electronic Hamiltonian operator:

$$\hat{H}_{e,\underline{\mathbf{R}}}(\underline{\mathbf{r}}) = \hat{T}_e(\underline{\mathbf{r}}) + \hat{V}_{ee}(\underline{\mathbf{r}}) + \hat{V}_{Ne,\underline{\mathbf{R}}}(\underline{\mathbf{r}}) \quad (2.13)$$

The different terms in Equation 2.13 follow from Equations 2.4–2.8. However, the term $\hat{V}_{Ne,\underline{\mathbf{R}}}(\underline{\mathbf{r}})$ depends on the nuclear positions $\underline{\mathbf{R}}$ parametrically. The term $V_{NN,\underline{\mathbf{R}}}$ in Equation 2.12 is a constant and dependent solely on nuclear positions $\underline{\mathbf{R}}$. Omitting $V_{NN,\underline{\mathbf{R}}}$ from Equation 2.12, we obtain:

$$\hat{H}_{e,\underline{\mathbf{R}}}(\underline{\mathbf{r}})\Psi_{e,\underline{\mathbf{R}}}(\underline{\mathbf{r}}) = E_{e,\underline{\mathbf{R}}}\Psi_{e,\underline{\mathbf{R}}}(\underline{\mathbf{r}}) \quad (2.14)$$

with $E_{e,\underline{\mathbf{R}}}$ represents the ‘pure’ electronic energy.

Given the particular configuration of nuclei (\mathbf{R}), Equation 2.14 is solved to search for the electronic ground-state wavefunction $\Psi_{e,\mathbf{R}}(\mathbf{r})$ and ground-state energy $E_{e,\mathbf{R}}$. The total electronic energy, including nuclear repulsion ($U_{e,\mathbf{R}}$), is then obtained by adding the constant nuclear repulsion term $V_{\text{NN},\mathbf{R}}$:

$$U_{e,\mathbf{R}} = E_{e,\mathbf{R}} + V_{\text{NN},\mathbf{R}} \quad (2.15)$$

In this thesis, we work within BOA. For convenience, in the following, the indices from Equation 2.14 are dropped:

$$\hat{H}(\mathbf{r})\Psi(\mathbf{r}) = E\Psi(\mathbf{r}) \quad (2.16)$$

2.3 Density Functional Theory

Obtaining analytical solutions for Equation 2.16 in systems with more than one electron is not feasible. The standard numerical approach of discretizing space into grids to solve the problem described by Equation 2.16 leads to exponential growth in computational resources (time and storage) [131]. Consequently, employing such brute-force methods to solve many-electron problems is impractical in (modern) classical computers. In this context, DFT has emerged as one of the most widely used methods for addressing many-electron problems by reformulating Equation 2.16 into a numerically tractable form [127, 128].

Central to DFT is the electron density, which represents the probability distribution of electrons within a system. The corresponding electron density operator $\hat{\rho}$ is defined as:

$$\hat{\rho}(\mathbf{r}) = \sum_{i=1}^N \delta(\mathbf{r} - \mathbf{r}_i) \quad (2.17)$$

where \mathbf{r}_i is the coordinate of electron i . The electron density $\rho(\mathbf{r})$ of the system in a state with an electronic wavefunction Ψ can then be obtained by taking the expectation value of the electron density operator,

$$\begin{aligned} \rho(\mathbf{r}) &= \langle \Psi | \hat{\rho}(\mathbf{r}) | \Psi \rangle \\ &= \int d^3\mathbf{r}_1 d^3\mathbf{r}_2 \dots d^3\mathbf{r}_N \Psi^*(\mathbf{r}_1, \mathbf{r}_2, \dots, \mathbf{r}_N) \hat{\rho}(\mathbf{r}) \Psi(\mathbf{r}_1, \mathbf{r}_2, \dots, \mathbf{r}_N) \\ &= N \int d^3\mathbf{r}_2 d^3\mathbf{r}_3 \dots d^3\mathbf{r}_N |\Psi(\mathbf{r}, \mathbf{r}_2, \mathbf{r}_3, \dots, \mathbf{r}_N)|^2 \end{aligned} \quad (2.18)$$

This definition of electron density follows the space integral over the electron density gives the total number of electrons, and is non-negative everywhere,

i.e.,

$$\int d^3\mathbf{r} \rho(\mathbf{r}) = N \quad \text{with} \quad \rho(\mathbf{r}) \geq 0 \quad (2.19)$$

When the wavefunction corresponds to the ground state (Ψ_0), the resulting electron density ($\rho_0(\mathbf{r})$) is referred to as the ground-state electron density.

According to DFT, we can find the ground-state energy E by optimizing the electron density $\rho(\mathbf{r})$ to minimize the total energy. The electron density thus offers a plausible alternative to the wavefunction.

The key advantage of DFT lies in the fact that the electron density $\rho(\mathbf{r})$ depends only on a single variable \mathbf{r} , unlike the N variables (N is the number of particles/electrons in the system) in the wavefunction. This simplicity enables to construct relatively simple numerical schemes to obtain the ground-state energy E .

2.3.1 Hohenberg-Kohn Theorem

In 1964, Pierre Hohenberg and Walter Kohn developed two theorems that lay the foundation for modern DFT [77, 132]. Both theorems can be proved through a proof by contradiction (*reductio ad absurdum*) [77].

The theorems assume that the many-electron Hamiltonian has the form (see Equation 2.13)

$$\hat{H}(\underline{\mathbf{r}}) = \hat{T}(\underline{\mathbf{r}}) + \hat{V}_{\text{ee}}(\underline{\mathbf{r}}) + \hat{V}_{\text{ext}}(\underline{\mathbf{r}}) \quad (2.20)$$

with the external potential operator $\hat{V}_{\text{ext}}(\underline{\mathbf{r}})$

$$\hat{V}_{\text{ext}}(\underline{\mathbf{r}}) = \int d^3\mathbf{r} \hat{\rho}(\mathbf{r}) v_{\text{ext}}(\mathbf{r}) \quad (2.21)$$

In addition to the Coulomb potential of ion cores ($-\sum_A \frac{Z_A}{|\mathbf{r}-\mathbf{R}_A|}$), the external potential $v_{\text{ext}}(\mathbf{r})$ can also include other influences, such as external fields.

2.3.1.1 First Hohenberg-Kohn Theorem

The first Hohenberg-Kohn theorem states that the ground-state electron density $\rho_0(\mathbf{r})$ uniquely determines the external potential $v_{\text{ext}}(\mathbf{r})$ (to within a constant). Since $v_{\text{ext}}(\mathbf{r})$ fixes the Hamiltonian \hat{H} (Equation 2.20) and the Hamiltonian determines the many-particle states, the ground state of a many-particle system is a unique functional of the ground-state electron density $\rho_0(\mathbf{r})$.

$$\rho_0 \Rightarrow v_{\text{ext}} \Rightarrow \hat{H} \Rightarrow \Psi_0, E_0 \quad (2.22)$$

2.3. DENSITY FUNCTIONAL THEORY

The reverse statement of the above is also true: the external potential, together with the number of electrons N , uniquely determines the ground-state electron density $\rho_0(\mathbf{r})$, assuming a non-degenerate ground state.

$$v_{\text{ext}} \Rightarrow \text{unique } \hat{H} \Rightarrow \text{unique } \Psi_0 \Rightarrow \text{unique } \rho_0 \quad (2.23)$$

Therefore, the first Hohenberg-Kohn theorem, together with the reverse statement in Equation 2.23, establishes a one-to-one correspondence between the ground-state electron density $\rho_0(\mathbf{r})$ and the external potential $v_{\text{ext}}(\mathbf{r})$ (as long as the ground state is non-degenerate).

Since the complete ground-state energy is a functional of the ground-state electron density, its individual components must also be functionals of ρ_0 . We can express the ground-state energy $E_0[\rho_0]$ as:

$$E_0[\rho_0] = \underbrace{T[\rho_0] + E_{\text{ee}}[\rho_0]}_{\text{system independent/ universal term}} + \underbrace{\int d^3\mathbf{r} \rho_0(\mathbf{r}) v_{\text{ext}}(\mathbf{r})}_{\text{system dependent}} \quad (2.24)$$

In Equation 2.24, the last term represents interactions within the external potential, such as the nuclear-electron interaction, which depends on the specific system. However, the first two terms, the kinetic energy of the electrons $T[\rho_0]$ and their interactions with each other $E_{\text{ee}}[\rho_0]$, are completely independent of the system. These terms combine to define a universally valid functional known as the Hohenberg-Kohn functional ($F_{\text{HK}}[\rho_0]$):

$$E_0[\rho_0] = F_{\text{HK}}[\rho_0] + \int d^3\mathbf{r} \rho_0(\mathbf{r}) v_{\text{ext}}(\mathbf{r}) \quad (2.25)$$

with

$$F_{\text{HK}}[\rho_0] = T[\rho_0] + E_{\text{ee}}[\rho_0] \quad (2.26)$$

Since $F_{\text{HK}}[\rho_0]$ is a universal functional, it applies equally well to the hydrogen atom as to large molecules such as proteins or to solids. Therefore, if the exact form of $F_{\text{HK}}[\rho_0]$ is known, the Schrödinger equation can be solved exactly. However, the explicit form of this functional is currently unknown. In practical applications, approximate forms of $F_{\text{HK}}[\rho_0]$ are often employed.

2.3.1.2 Second Hohenberg-Kohn Theorem

The second Hohenberg-Kohn theorem transfers the variational principle to DFT. This theorem states that the Hohenberg-Kohn functional $F_{\text{HK}}[\rho_0]$ delivers the lowest energy (ground-state energy) of the system, if and only if the input electron density corresponds to the true ground-state density ρ_0 . Any other trial densities $\tilde{\rho}$ inevitably lead to higher energy (states).

Therefore, through the variational principle, one can find the ground-state energy E_0 and ground-state density ρ_0 of a many-electron system (with an external potential v_{ext}) by minimizing the total energy functional $E[\tilde{\rho}]$ by varying the trial densities $\tilde{\rho}$,

$$E_0 = \min_{\tilde{\rho}} E[\tilde{\rho}],$$

$$E[\tilde{\rho}] = F_{\text{HK}}[\tilde{\rho}] + \int d^3\mathbf{r} \tilde{\rho}(\mathbf{r}) v_{\text{ext}}(\mathbf{r}) \quad (2.27)$$

2.3.1.3 Summary of Hohenberg-Kohn Theorems

In summary, all properties of a system defined by an external potential v_{ext} are determined by the ground-state density (first Hohenberg-Kohn theorem), which in turn can be obtained by minimizing the total energy functional, $F_{\text{HK}}[\tilde{\rho}] + \int d^3\mathbf{r} \tilde{\rho}(\mathbf{r}) v_{\text{ext}}(\mathbf{r})$ (second Hohenberg-Kohn theorem).

2.3.2 Kohn-Sham Theory

Despite being the foundation of DFT, the Hohenberg-Kohn theorems offer no practical realization. Equation 2.26 introduces the functional $F[\rho]$, containing the kinetic energy functional $T[\rho]$ and the electron-electron interaction $E_{\text{ee}}[\rho]$, but their explicit forms are unknown. However, at least the classical Coulomb interaction energy of the charge density with itself, denoted by $J[\rho]$, can be extracted from the latter term, as it is precisely known:

$$E_{\text{ee}}[\rho] = J[\rho] + E_{\text{XC}}[\rho] \quad (2.28)$$

with

$$J[\rho] = \frac{1}{2} \int \int d^3\mathbf{r} d^3\mathbf{r}' \frac{\rho(\mathbf{r}) \rho(\mathbf{r}')}{|\mathbf{r} - \mathbf{r}'|} \quad (2.29)$$

The functional $E_{\text{XC}}[\rho]$, known as the exchange-correlation functional, represents the *non-classical* contribution to the electron-electron interaction, encompassing self-interaction correction, exchange, and Coulomb correlations. Substituting Equation 2.29 into Equation 2.26 reformulates $F[\rho]$ as:

$$F[\rho] = T[\rho] + J[\rho] + E_{\text{XC}}[\rho] \quad (2.30)$$

This, in turn, represents a significant reformulation of the previous ‘unknown’ problem: in Equation 2.30, only $J[\rho]$ is known exactly, while the explicit forms of the other two contributions are completely unknown and must be approximated for practical purposes.

2.3. DENSITY FUNCTIONAL THEORY

The significant breakthrough in approximating the kinetic energy functional ($T[\rho]$) was accomplished by Walter Kohn and Lu Jeu Sham in their pioneering work on the Kohn-Sham theory [78]. The fundamental idea underlying this theory is to map the interacting multi-electron system onto a system of non-interacting electrons that yields the same electron density as the actual system.

For this purpose, a set of auxiliary orbitals $\{\psi_i\}$, known as the Kohn-Sham orbitals, is constructed; such that:

$$\rho(\mathbf{r}) = \sum_{i=1}^N |\psi_i(\mathbf{r})|^2 = \rho_0(\mathbf{r}) \quad \text{with } \langle \psi_i | \psi_j \rangle = \delta_{i,j} \quad (2.31)$$

The kinetic energy of such non-interacting electrons (T_{KS}) with the same density as the real interacting one can be calculated exactly from the Kohn-Sham orbitals:

$$T_{\text{KS}} = -\frac{1}{2} \sum_{i=1}^N \langle \psi_i | \nabla^2 | \psi_i \rangle \quad (2.32)$$

Of course, the non-interacting kinetic energy does not equal the true kinetic energy of the interacting system, despite both systems sharing the same density. The correction to the kinetic energy is further accounted for by introducing a separation to the functional $F[\rho]$ (see Equation 2.30):

$$F[\rho] = T_{\text{KS}}[\rho] + J[\rho] + (E_{\text{XC}}[\rho] + T[\rho] - T_{\text{KS}}[\rho]) \quad (2.33)$$

$$= T_{\text{KS}}[\rho] + J[\rho] + E_{\text{XC}}^{\text{KS}}[\rho] \quad (2.34)$$

with redefining the exchange-correlation functional within Kohn-Sham DFT ($E_{\text{XC}}^{\text{KS}}[\rho]$) as:

$$E_{\text{XC}}^{\text{KS}}[\rho] := E_{\text{XC}} + T[\rho] - T_{\text{KS}}[\rho] \quad (2.35)$$

Notice, in Equation 2.35, in spite of its name, $E_{\text{XC}}^{\text{KS}}$ contains not only the non-classical effects of self-interaction correction, exchange, and correlation, which are contributions to the potential energy of the system but also accounts for the kinetic energy correction.

By substituting the energy terms from Equations 2.34, the total energy E in Kohn-Sham DFT (see Equation 2.25) can be expressed as:

$$E = T_{\text{KS}}[\psi_1, \psi_2, \dots, \psi_N] + J[\rho] + E_{\text{XC}}^{\text{KS}}[\rho] + \int d^3\mathbf{r} \rho(\mathbf{r}) v_{\text{ext}}(\mathbf{r}) \quad (2.36)$$

Applying the minimization principle then leads to the following ground-state energy (E_0) expression:

$$E_0 = \min_{\substack{\text{orthonormal} \\ \psi_1, \psi_2, \dots, \psi_N}} \left[T_{\text{KS}}[\psi_1, \psi_2, \dots, \psi_N] + J[\rho] + E_{\text{XC}}^{\text{KS}}[\rho] + \int d^3\mathbf{r} \rho(\mathbf{r}) v_{\text{ext}}(\mathbf{r}) \right] \quad (2.37)$$

The constrained minimization problem in Equation 2.37 can be solved using the Lagrangian multiplier formalism with the following Lagrange function L :

$$L = T_{\text{KS}}[\psi_1, \psi_2, \dots, \psi_N] + J[\rho] + E_{\text{XC}}^{\text{KS}}[\rho] + \int d^3\mathbf{r} \rho(\mathbf{r}) v_{\text{ext}}(\mathbf{r}) - \sum_{i=1}^N \sum_{j=1}^N \lambda_{i,j} (\langle \psi_i | \psi_j \rangle - \delta_{ij}) \quad (2.38)$$

Minimizing L with respect $\psi_1, \psi_2, \dots, \psi_N$ and employing the definitions of T_{KS} and $J[\rho]$ from Equations 2.32 and 2.29 lead to the Kohn-Sham equation:

$$\left[-\frac{1}{2} \nabla^2 + v_{\text{H}}(\mathbf{r}) + v_{\text{XC}}(\mathbf{r}) + v_{\text{ext}}(\mathbf{r}) \right] \psi_i(\mathbf{r}) = \epsilon_i \psi_i(\mathbf{r}) \quad (2.39)$$

with

- the electron density $\rho(\mathbf{r})$ generated from the Kohn-Sham orbitals:

$$\rho(\mathbf{r}) = \sum_{i=1}^N |\psi_i(\mathbf{r})|^2 \quad (2.40)$$

- the correlation-free interelectronic interaction potential, also called the Hartree potential $v_{\text{H}}(\mathbf{r})$:

$$v_{\text{H}}(\mathbf{r}) = \int d^3\mathbf{r}' \frac{\rho(\mathbf{r}')}{|\mathbf{r} - \mathbf{r}'|} \quad (2.41)$$

- the exchange-correlation potential $v_{\text{XC}}(\mathbf{r})$ as such is generally not known and thus is determined from the corresponding exchange-correlation energy functional $E_{\text{XC}}[\rho]$:

$$v_{\text{XC}}(\mathbf{r}) = \frac{\delta E_{\text{XC}}[\rho]}{\delta \rho(\mathbf{r})} \quad (2.42)$$

- the external potential v_{ext} consists of the Coulomb potential of the ion cores:

$$v_{\text{ext}} = - \sum_A \frac{Z_A}{|\mathbf{r} - \mathbf{R}_A|} \quad (2.43)$$

Additionally, it can also include other influences, such as external fields.

- $\epsilon_i = \lambda_{ii}$ are the Kohn-Sham eigenvalues and are re-definitions of the Lagrange multipliers in Equation 2.38.

The potential expressions in Equation 2.39 can be conveniently combined to define an effective potential $v_{\text{eff}}(\mathbf{r})$. Consequently, the Kohn-Sham equation takes the form of one-particle equations for a non-interacting reference system with an effective potential:

$$\left[-\frac{1}{2}\nabla^2 + v_{\text{eff}}(\mathbf{r}) \right] \psi_i(\mathbf{r}) = \epsilon_i \psi_i(\mathbf{r}) \quad (2.44)$$

where

$$v_{\text{eff}}(\mathbf{r}) \equiv v_{\text{H}}(\mathbf{r}) + v_{\text{XC}}(\mathbf{r}) + v_{\text{ext}}(\mathbf{r}) \quad (2.45)$$

The Kohn-Sham equations in Equation 2.44 need to be solved self-consistently since the Hartree potential and the exchange-correlation potential depend on the Kohn-Sham orbitals $\psi_i(\mathbf{r})$ through the density $\rho(\mathbf{r})$. It is important to note that the Kohn-Sham theory is, *in principle, exact*. The approximation only enters when an explicit form of the unknown exchange-correlation energy functional E_{XC} and the corresponding potential v_{XC} is used. The central goal of modern DFT is to find increasingly accurate approximations for these quantities.

2.4 Quantum Mechanics for Solid

2.4.1 Periodicity and Reciprocal Space

In the context of solids, solving the many-electron Schrödinger equation (Equation 2.16) becomes computationally prohibitive due to the large system size. However, crystalline substances, which are the focus of this work, possess translational symmetry. This allows us to simplify the problem by approximating large systems as an infinite repetition of a small volume known as a unit cell connected by the Born-von Karman periodic boundary condition (PBC).

Mathematically, a crystal is described by a three-dimensional point lattice, where lattice points are decorated with atoms forming the basis. The lattice is spanned by three linearly independent basis vectors, denoted as \mathbf{a}_1 , \mathbf{a}_2 , and \mathbf{a}_3 . The periodic structure is then obtained by all possible translations \mathbf{t} within the crystal structure:

$$\mathbf{t} = m_1\mathbf{a}_1 + m_2\mathbf{a}_2 + m_3\mathbf{a}_3 \quad m_1, m_2, m_3 \in \mathbb{Z} \quad (2.46)$$

There are 14 Bravais lattices that belong to 7 crystal classes, each representing a unique arrangement of lattice points in three-dimensional space. These lattices define the fundamental repeating pattern in a crystal.

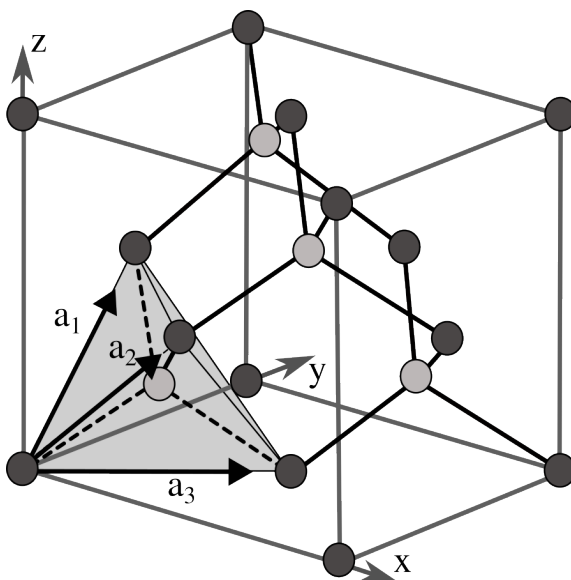


Figure 2.1: Schematic of zincblende structure unit cell. The primitive cell is shown in gray shading. The primitive basis vectors \mathbf{a}_1 , \mathbf{a}_2 , and \mathbf{a}_3 are shown by arrows. Figure adapted from Reference [133].

While the unit cell is not uniquely defined, commonly used definitions include the crystallographic or conventional unit cell, which maintains full lattice symmetry but may contain multiple lattice points. Another choice is the primitive unit cell (or primitive cell), which contains only one lattice point but exhibits full lattice symmetry only for primitive Bravais lattices. A notable concept related to the unit cell is the Wigner-Seitz cell. This cell encloses the region of space that is closer to a chosen lattice point than to any other lattice point. It provides a unique representation of the crystal structure around a specific lattice point.

Depending on the choice of basis vectors, different crystal structures can be formed and named after prototype structures. Figure 2.1 illustrates the conventional and primitive unit cells of a zincblende structure. It consists of two interpenetrating face-centered cubic lattices. All the materials studied in this thesis possess zincblende structure.

Similar to the unit cell in real space, the reciprocal space is constructed using three reciprocal basis vectors denoted as \mathbf{b}_1 , \mathbf{b}_2 and \mathbf{b}_3 :

$$\mathbf{b}_1 = 2\pi \frac{\mathbf{a}_2 \times \mathbf{a}_3}{V_{\text{cell}}}, \quad \mathbf{b}_2 = 2\pi \frac{\mathbf{a}_3 \times \mathbf{a}_1}{V_{\text{cell}}}, \quad \mathbf{b}_3 = 2\pi \frac{\mathbf{a}_1 \times \mathbf{a}_2}{V_{\text{cell}}} \quad (2.47)$$

where $V_{\text{cell}} = |\mathbf{a}_1 \cdot (\mathbf{a}_2 \times \mathbf{a}_3)|$ represents the volume of the unit cell.

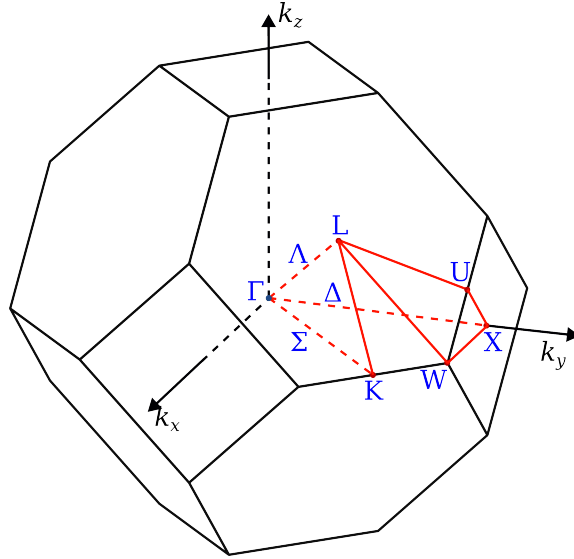


Figure 2.2: Schematic representation of the first Brillouin zone of a face-centered cubic lattice. High symmetry paths are indicated in red. The symmetry points are marked in blue. Figure adapted from Reference [134].

The translation vectors \mathbf{g} in reciprocal space can be expressed as:

$$\mathbf{g} = m_1 \mathbf{b}_1 + m_2 \mathbf{b}_2 + m_3 \mathbf{b}_3 \quad m_1, m_2, m_3 \in \mathbb{Z} \quad (2.48)$$

The basis vectors of the real and reciprocal space are orthogonal to each other, i.e.

$$\mathbf{a}_i \cdot \mathbf{b}_j = 2\pi \delta_{ij} \quad (2.49)$$

From Equation 2.46–2.49, clearly, an important property of the reciprocal lattice is that the scalar product of translation vectors of the lattice and the reciprocal lattice are multiples of 2π :

$$\mathbf{t} \cdot \mathbf{g} = 2\pi m \quad (m \in \mathbb{Z}) \quad \Rightarrow \quad e^{i\mathbf{g} \cdot \mathbf{t}} = 1 \quad (2.50)$$

Analogous to the elementary cell in real space, similar constructs can be defined in reciprocal space. One such construct that is of particular importance for describing the electronic properties of our interest is the Brillouin zone. It is the Wigner-Seitz cell in reciprocal space. Figure 2.2 depicts the Brillouin zone of a face-centered cubic lattice. Although the Brillouin zone shown is three-dimensional, our analysis in this thesis focuses solely on the high symmetry paths within the Brillouin zone (highlighted in red), which suffice for studying electronic properties such as the bandgap. This will be elaborated further in Section 2.6.

By leveraging translational symmetry, the entire crystal structure can be described solely by considering the (primitive) unit cell and its repeated patterns. The following section aims to clarify how the electronic structure of a crystal can be described.

2.4.2 Bloch's Theorem

Consider the Schrödinger equation

$$\left[-\frac{1}{2}\nabla^2 + v(\mathbf{r}) \right] \Psi(\mathbf{r}) = E \Psi(\mathbf{r}) \quad (2.51)$$

with some *periodic potential* $v(\mathbf{r})$ that satisfies:

$$v(\mathbf{r} + \mathbf{L}) = v(\mathbf{r}) \quad (2.52)$$

where \mathbf{L} is the periodicity.

Bloch's theorem states that solutions to the Schrödinger equation 2.51 in such a periodic potential take the form of a plane wave modulated by a periodic function. In other words, the eigenfunction $\Psi(\mathbf{r})$ of equation 2.51 can be expressed in the form:

$$\Psi_{\mathbf{k}}(\mathbf{r}) = u_{\mathbf{k}}(\mathbf{r}) e^{i\mathbf{k}\cdot\mathbf{r}} \quad (2.53)$$

where \mathbf{r} represents position, the wavevector \mathbf{k} is the crystal momentum vector, and $u_{\mathbf{k}}$ is a periodic function with the same periodicity as \mathbf{L} , i.e.

$$u_{\mathbf{k}}(\mathbf{r} + \mathbf{L}) = u_{\mathbf{k}}(\mathbf{r}) \quad (2.54)$$

The function Ψ of the form (2.53) is known as the “Bloch function” or “Bloch state”. It is important to note that while the functions u are periodic with periodicity \mathbf{L} , the Bloch functions Ψ do not possess the same periodicity in general, i.e., $\Psi(\mathbf{r} + \mathbf{L}) \neq \Psi(\mathbf{r})$ (except for the case when $\mathbf{k} = 0$). Nevertheless, the eigenstates of Hamiltonian with a periodic potential fulfill the constraint described by Equation 2.53.

2.5 Density Functional Theory for Solid

2.5.1 Periodic Electron Density

As discussed in Section 2.4.1, solids can be represented by the periodic repetition of a unit cell with lattice periodicity \mathbf{t} (Equation 2.46). This follows that the electron density $\rho(\mathbf{r})$, also exhibits lattice periodicity, i.e.:

$$\rho(\mathbf{r} + \mathbf{t}) = \rho(\mathbf{r}) \quad (2.55)$$

2.5.2 Kohn-Sham Equation for Solid

Since the electron density $\rho(\mathbf{r})$ is lattice-periodic, following Equations 2.41 and 2.42, so also the Hartree potential (v_{H}) and exchange-correlation potential (v_{XC}). The external potential (v_{ext}) is also lattice-periodic as the atoms are lattice-periodic. Therefore, the sum of these potentials, $v_{\text{eff}}(\mathbf{r}) = v_{\text{H}}(\mathbf{r}) + v_{\text{XC}}(\mathbf{r}) + v_{\text{ext}}(\mathbf{r})$, in Equation 2.45, is lattice-periodic. Hence, we can apply the Bloch theorem 2.53 to the Kohn-Sham orbitals ($\psi_j(\mathbf{r})$ ¹) in Equation 2.44:

$$\psi_{n\mathbf{k}}(\mathbf{r}) = u_{n\mathbf{k}}(\mathbf{r}) e^{i\mathbf{k}\cdot\mathbf{r}} \quad (2.56)$$

Here, n represents integer indices ($j \mapsto (n, \mathbf{k})$), also called the “band indices”, and $\psi_{n\mathbf{k}}$ are referred to as the Kohn-Sham Bloch functions. The functions $u_{n\mathbf{k}}(\mathbf{r})$ are now lattice-periodic and they satisfy:

$$u_{n\mathbf{k}}(\mathbf{r} + \mathbf{t}) = u_{n\mathbf{k}}(\mathbf{r}) \quad (2.57)$$

The normalized Kohn-Sham Bloch functions satisfy

$$\int_{\text{unit cell}} d^3\mathbf{r} |\psi_{n\mathbf{k}}(\mathbf{r})|^2 = 1 \quad (2.58)$$

The electron density can then be calculated from the occupied Kohn-Sham Bloch states as follows:

$$\rho(\mathbf{r}) = \frac{1}{\Omega_{\text{BZ}}} \sum_{n=1}^{\text{occ}} \int_{\text{BZ}} d^3\mathbf{k} |\psi_{n\mathbf{k}}(\mathbf{r})|^2 \quad (2.59)$$

where $\Omega_{\text{BZ}} = |\mathbf{b}_1 \cdot (\mathbf{b}_2 \times \mathbf{b}_3)|$ is the volume of the Brillouin zone (BZ), and \int_{BZ} refers to the volume integral over the Brillouin zone.

By substituting the Kohn-Sham Bloch functions (Equation 2.56) into Equation 2.44, we arrive at the Kohn-Sham equation for solid:

$$\left[-\frac{1}{2}\nabla^2 + v_{\text{eff}}(\mathbf{r}) \right] \psi_{n\mathbf{k}}(\mathbf{r}) = \epsilon_{n\mathbf{k}} \psi_{n\mathbf{k}}(\mathbf{r})$$

with $v_{\text{eff}}(\mathbf{r}) = v_{\text{H}}(\mathbf{r}) + v_{\text{XC}}(\mathbf{r}) + v_{\text{ext}}(\mathbf{r})$ (2.60)

Equation 2.60 establishes the foundation of the Kohn-Sham DFT for solid, also referred to as “periodic Kohn-Sham DFT”. This formulation allows us to investigate the electronic structure of solids, as detailed in the subsequent discussion.

¹We now denote the indices by j to avoid confusion with imaginary number i in the Bloch functions.

2.5.3 Plane-Wave Basis Expansion

As pointed out in Section 2.3.2, the Kohn-Sham equations are solved self-consistently. This requires initializing the Kohn-Sham Bloch functions in Equation 2.60, which in turn requires appropriately selecting the form of the periodic function $u(\mathbf{r})$ (Equation 2.57).

In periodic Kohn-Sham DFT calculations, there are primarily three different types of basis functions that satisfy the Bloch theorem: real-space basis functions (e.g., wavelets), atom-centered basis functions (e.g., Gaussian-type orbitals), and plane waves. In this thesis, the plane-wave basis expansion is utilized.

In the plane-wave basis, the lattice-periodic function $u(\mathbf{r})$ is constructed using plane waves as follows:

$$u(\mathbf{r}) = \frac{1}{\sqrt{V_{\text{cell}}}} \sum_{\mathbf{g}=0}^{\infty} C_{\mathbf{g}} e^{i\mathbf{g}\cdot\mathbf{r}} \quad (2.61)$$

Here, $e^{i\mathbf{g}\cdot\mathbf{r}}$ are the plane waves with the translation vectors in reciprocal space \mathbf{g} (Equation 2.48) and $C_{\mathbf{g}}$ are the corresponding coefficients. Subsequently, the Bloch functions (Equation 2.56) under the plane-wave expansion can be expressed as:

$$\psi_{n\mathbf{k}}(\mathbf{r}) = \frac{1}{\sqrt{V_{\text{cell}}}} \sum_{\mathbf{g}=0}^{\infty} C_{n\mathbf{k},\mathbf{g}} e^{i(\mathbf{g}+\mathbf{k})\cdot\mathbf{r}} \quad (2.62)$$

It is important to note that since the plane waves are inherently lattice-periodic, the resulting Bloch functions $\psi_{n\mathbf{k}}(\mathbf{r})$ automatically fulfill the Bloch theorem.

2.5.3.1 Plane-Wave Cutoff

The exact description of Bloch functions in Equation 2.62 needs an infinite number of plane waves. However, for practical purposes, only those plane waves are included whose \mathbf{g} -vector has a length smaller than a cutoff value g_{cut} , $|\mathbf{g}| < g_{\text{cut}}$. Furthermore, it has been observed that if the volume of the cell is changed (e.g., volume optimization), this criterion (i.e., same basis set for each \mathbf{k} -point) leads to a very rough energy-volume curve and, generally, slower energy convergence. To address this, a modified criterion, $|\mathbf{g} + \mathbf{k}| < g_{\text{cut}}$, is often employed. With this modified criterion, the number of plane waves included in the basis set varies for each \mathbf{k} -point, resulting in improved behavior for energy-volume calculations. As the volume changes, the total number of plane waves changes smoothly [135].

Moreover, in practice, instead of the g_{cut} value, the cutoff criteria are determined based on the plane wave kinetic energy, $E_{\text{cut}} = \frac{1}{2} g_{\text{cut}}^2$. All plane waves with kinetic energy lower than E_{cut} are included in the basis set. This can be expressed as:

$$\frac{1}{2} |\mathbf{g} + \mathbf{k}|^2 < E_{\text{cut}} \quad (2.63)$$

With this cutoff criterion, the basis expansion of Bloch functions in Equation 2.62 becomes:

$$\psi_{n\mathbf{k}}(\mathbf{r}) = \frac{1}{\sqrt{V_{\text{cell}}}} \sum_{\mathbf{g}=0}^{N_b} C_{n\mathbf{k},\mathbf{g}} e^{i(\mathbf{g}+\mathbf{k})\cdot\mathbf{r}} \quad (2.64)$$

Here, the summation includes only those \mathbf{g} -vectors that satisfy $|\mathbf{g} + \mathbf{k}| < g_{\text{cut}}$, and N_b represents the total number of \mathbf{g} -vectors that satisfy this condition. By increasing the value of g_{cut} (or equivalently, E_{cut}), we can improve the accuracy of the basis representation of $\psi_{n\mathbf{k}}(\mathbf{r})$. Therefore, E_{cut} serves as a convergence parameter, and one gradually increases its value until convergence is achieved in the property being investigated (e.g., total energy).

2.5.3.2 Brillouin Zone Sampling

Typically, a Brillouin zone contains a large number of \mathbf{k} -points. However, in practical calculations, only a subset of \mathbf{k} -points are used. In that case, we approximate the Brillouin zone integral in Equation 2.59 by:

$$\rho(\mathbf{r}) = \frac{1}{N_k} \sum_{n=1}^{\text{occp}} \sum_{\mathbf{k} \in \mathbf{k}\text{-mesh}} |\psi_{n\mathbf{k}}(\mathbf{r})|^2 \quad (2.65)$$

where N_k represents the number of \mathbf{k} -points in the \mathbf{k} -mesh and n denotes the band index. In the discretized \mathbf{k} -mesh as in Equation 2.65, the electron density is nevertheless lattice-periodic, $\rho(\mathbf{r} + \mathbf{t}) = \rho(\mathbf{r})$.

One of the most commonly used approaches for Brillouin zone sampling is the Monkhorst-Pack regular grid [136]. For instance, the \mathbf{k} -mesh resulted from a $10 \times 10 \times 10$ Monkhorst-Pack regular grid samples the Brillouin zone of a simple-cubic lattice into 10^3 uniformly spaced \mathbf{k} -points. The \mathbf{k} -points are arranged on a cubic grid with spacing $(\mathbf{b}_1/10, \mathbf{b}_2/10, \mathbf{b}_3/10)$.

How well the set of chosen \mathbf{k} -points samples the Brillouin zone is again another convergence parameter. One gradually increases the density of \mathbf{k} -points in the Brillouin zone until convergence is achieved in the investigated property (e.g., total energy).

2.5.4 Periodic Kohn-Sham in Plane-Wave Basis

We now insert the basis expansion from Equation 2.64 into the periodic Kohn-Sham equation (Equation 2.60). This yields the following expression [137, 138]:

$$\sum_{\mathbf{g}'=0}^{N_b} \left[\frac{1}{2} |\mathbf{g}' + \mathbf{k}_\nu|^2 \delta_{\mathbf{g}\mathbf{g}'} + v_{\nu,\text{eff}}(\mathbf{g} - \mathbf{g}') \right] C_{n\mathbf{k}_\nu, \mathbf{g}'} = \epsilon_{n\mathbf{k}_\nu} C_{n\mathbf{k}_\nu, \mathbf{g}} \quad (2.66)$$

$$\text{with } v_{\text{eff}}(\mathbf{g} - \mathbf{g}') = v_{\text{H}}(\mathbf{g} - \mathbf{g}') + v_{\text{xc}}(\mathbf{g} - \mathbf{g}') + v_{\text{ext}}(\mathbf{g} - \mathbf{g}') \quad (2.67)$$

where, the index ν enumerates the \mathbf{k} -points in the \mathbf{k} -mesh ($\nu = 1, \dots, N_{\mathbf{k}}$), n represents the band index, and the summation includes the N_b number of \mathbf{g}' -vectors that satisfy $|\mathbf{g}' + \mathbf{k}_\nu| < g_{\text{cut}}$. This formulation corresponds to the momentum representation of the periodic Kohn-Sham equation. This representation offers several advantages, in particular when implementing in software, including fast Fourier transformation (FFT) and efficient energy calculations.

Furthermore, in Equation 2.66, the external and Hartree potentials are combined to compute the electrostatic potential (v_{Hext}):

$$v_{\text{Hext}}(\mathbf{g}) := v_{\text{H}}(\mathbf{g}) + v_{\text{ext}}(\mathbf{g}) = -\frac{4\pi\rho_{\text{tot}}(\mathbf{g})}{|\mathbf{g}|^2} \quad (\mathbf{g} \neq 0) \quad (2.68)$$

$$\text{with } \rho_{\text{tot}}(\mathbf{g}) = -\rho(\mathbf{g}) + \sum_{\text{unit cell}}^A Z_A e^{i\mathbf{g}\cdot\mathbf{R}_A} \quad (2.69)$$

Note that at $\mathbf{g} = 0$, the term $v_{\text{Hext}}(\mathbf{g} = 0)$ in Equation 2.68 diverges. Thus, in plane-wave Kohn-Sham DFT, the $\mathbf{g} = 0$ component of v_{Hext} is neglected. However, this does not affect the wavefunctions $\psi_{n\mathbf{k}}$ and only results in a constant shift of all the eigenvalues $\epsilon_{n\mathbf{k}}$.

Additionally, for computational efficiency, the exchange-correlation potential $v_{\text{xc}}(\mathbf{g})$ is typically computed using real-space integration due to its lower cost compared to the Fourier transforms in momentum space.

$$v_{\text{xc}}(\mathbf{g}) = \frac{1}{V_{\text{cell}}} \int_{\text{unit cell}} d^3\mathbf{r} e^{i\mathbf{g}\cdot\mathbf{r}} v_{\text{xc}}(\mathbf{r}) \quad (2.70)$$

Reformulating Equation 2.66 in matrix form gives:

$$\mathbf{H}^{\text{KS}}(\mathbf{k}) \mathbf{C}_n(\mathbf{k}) = \epsilon_n(\mathbf{k}) \mathbf{C}_n(\mathbf{k}) \quad (2.71)$$

This equation represents an eigenvalue equation. Diagonalizing the Kohn-Sham matrix \mathbf{H}^{KS} yields the eigenvalues (band energies ϵ_n) and the vector of plane-wave expansion coefficients \mathbf{C}_n .

The coefficients, \mathbf{C}_n s, are then used to calculate the Bloch wave functions using Equation 2.64, which can subsequently be employed to calculate the electron densities using Equation 2.65.

$$\mathbf{C}_n(\mathbf{k}) \rightarrow \psi_{n\mathbf{k}}(\mathbf{r}) \rightarrow \rho(\mathbf{r}) \rightarrow \rho(\mathbf{g}) = \frac{1}{V_{\text{cell}}} \int_{\text{unit cell}} d^3\mathbf{r} \rho(\mathbf{r}) e^{i\mathbf{g}\cdot\mathbf{r}} \quad (2.72)$$

Finally, in the plane-wave formalism, the total energy (E_{tot}) can be easily computed as [138]:

$$\begin{aligned} E_0 = & \frac{1}{N_k} \sum_{\nu=1}^{N_k} \sum_{n=1}^N \sum_{\mathbf{g}=0}^{N_b} \frac{1}{2} |\mathbf{k}_\nu + \mathbf{g}|^2 |C_{n\mathbf{g}}(\mathbf{k}_\nu)|^2 \\ & + \frac{1}{2} 4\pi \sum_{\mathbf{g}=1}^{N_b} \frac{|\rho_{\text{tot}}(\mathbf{g})|^2}{|\mathbf{g}|^2} + \sum_{\mathbf{g}=0}^{N_b} v_{\text{xc}}(\mathbf{g}) \rho(\mathbf{g}) \end{aligned} \quad (2.73)$$

It is important to note that the $\mathbf{g} = 0$ term in the second term of Equation 2.73 corresponds to the electrostatic interaction of the total charge density $\rho_{\text{tot}}(\mathbf{r})$ with itself. Therefore, excluding the $\mathbf{g} = 0$ term here yields the correct expression for energy [138].

2.5.5 Projector Augmented-Wave Method

The Bloch functions $\psi_{n\mathbf{k}}(\mathbf{r})$ exhibit rapid oscillations near highly-charged nuclei (Figure 2.3). Therefore, one needs a very large plane-wave cutoff g_{cut} to reach a converged result. However, including a large number of plane waves in the basis expansion increases computational cost due to the large matrix sizes, such as the Kohn-Sham matrix (Equation 2.71). To avoid a large number of plane waves, one approach is to use the projector augmented-wave (PAW) method [139–141]. In PAW, the Bloch states are expanded using the following representation:

$$\psi_{n\mathbf{k}}(\mathbf{r}) = \tilde{\psi}_{n\mathbf{k}}(\mathbf{r}) + \phi(\mathbf{r}) - \tilde{\phi}(\mathbf{r}) \quad (2.74)$$

where $\tilde{\psi}_{n\mathbf{k}}(\mathbf{r})$ is a “smooth Bloch state” that is expanded in plane waves, as described in Equation 2.64. $\phi(\mathbf{r})$ and $\tilde{\phi}(\mathbf{r})$ are auxiliary functions, where $\phi(\mathbf{r})$ exhibits rapid oscillations near the nucleus, while $\tilde{\phi}(\mathbf{r})$ is smooth (refer to Figure 2.3 for an illustration).

A cutoff radius r_c is defined, ensuring that the auxiliary functions match when the distance from the nucleus exceeds r_c :

$$\phi(\mathbf{r}) - \tilde{\phi}(\mathbf{r}) = 0 \quad \text{for } |\mathbf{r}| > r_c \quad (2.75)$$

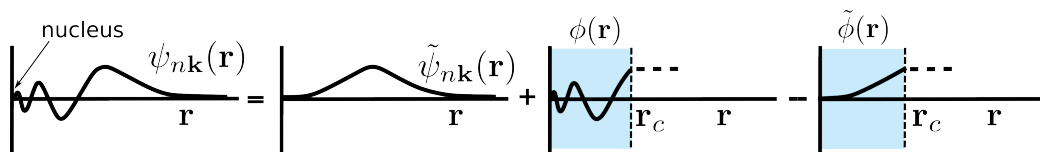


Figure 2.3: Schematic representation of the projector augmented-wave (PAW) scheme. The Bloch state is represented by $\psi_{n\mathbf{k}}(\mathbf{r})$. The decomposition to the smooth Bloch state ($\tilde{\psi}_{n\mathbf{k}}(\mathbf{r})$), hard auxiliary function ($\phi(\mathbf{r})$), and the soft auxiliary function ($\tilde{\phi}(\mathbf{r})$) are shown. Figure adapted from Reference [142].

The cutoff radii are chosen for each atom type so that the spheres around the atoms, defined by the respective cutoff radius, do not overlap. This “locality” makes the algorithm efficient.

The auxiliary functions ϕ and $\tilde{\phi}$ are obtained using predefined projector functions p_j and two predefined local basis sets φ_j and $\tilde{\varphi}_j$ on each atom:

$$\begin{aligned}\phi(\mathbf{r}) &= \sum_j \varphi_j(\mathbf{r}) \langle p_j | \tilde{\psi}_{n\mathbf{k}} \rangle \\ \tilde{\phi}(\mathbf{r}) &= \sum_j \tilde{\varphi}_j(\mathbf{r}) \langle p_j | \tilde{\psi}_{n\mathbf{k}} \rangle\end{aligned}\quad (2.76)$$

where the projection $\langle p_j | \tilde{\psi}_{n,\mathbf{K}} \rangle$ of smooth Bloch states onto the atom-centered projector function is computed through a real-space integral:

$$\langle p_j | \tilde{\psi}_{n\mathbf{k}} \rangle = \int_{\text{whole crystal}} d^3\mathbf{r} p_j(\mathbf{r} - \mathbf{R}_A) \tilde{\psi}_{n\mathbf{k}} \quad (2.77)$$

In a PAW calculation, one optimizes $\tilde{\psi}_{n\mathbf{k}}(\mathbf{r})$ to obtain the lowest energy. Since $\tilde{\psi}_{n\mathbf{k}}(\mathbf{r})$ is smooth, a low cutoff g_{cut} can be chosen in the plane-wave expansion (Equation 2.64). Once $\tilde{\psi}_{n,\mathbf{k}}(\mathbf{r})$ is obtained, the auxiliary functions $\phi(\mathbf{r})$ and $\tilde{\phi}(\mathbf{r})$ can be directly computed following Equation 2.76. The requirement in Equation 2.75 can be easily met by selecting appropriate basis functions φ_j and $\tilde{\varphi}_j$. However, it should be emphasized that using highly optimized basis sets $\{\varphi_j\}$, $\{\tilde{\varphi}_j\}$ and projector functions $\{p_j\}$ is crucial to achieving accurate total energy.

The PAW method offers a significant advantage as it provides a formal equivalence to all-electron methods (with a frozen core) while maintaining computational efficiency comparable to pseudopotential calculations [141]. However, unlike pseudopotential approaches where the core region projection is performed using a static projection kernel, PAW dynamically updates this projection kernel during the SCF cycle.

2.6 Electronic Properties

2.6.1 Bandstructure

The description of electrons in terms of Bloch functions underlies the concept of electronic bandstructures. In solid-state physics, bandstructure refers to the arrangement of allowed energy levels for electrons in a solid. It determines the electrical and optical properties of materials and plays a crucial role in understanding phenomena such as conductivity, magnetism, and semiconductors.

The eigenstates of the periodic Kohn-Sham DFT (Equation 2.60) are represented by Bloch states:

$$\psi_{n\mathbf{k}}(\mathbf{r}) = u_{n\mathbf{k}}(\mathbf{r}) e^{i\mathbf{k}\cdot\mathbf{r}} \quad (2.78)$$

where \mathbf{k} denotes the crystal momentum vector or wavevector. For each \mathbf{k} value, there are multiple solutions to the single-electron Kohn-Sham equations labeled by n , the band index representing different energy bands. Within a band (for fixed n), the energy levels continuously vary with \mathbf{k} , forming a smooth band of states. This variation is known as the dispersion relation, $\epsilon_n(\mathbf{k})$, for electrons in that band.

Furthermore, $\psi_{n\mathbf{k}}$ in Equation 2.78 is unique only up to a constant translation vector in reciprocal space (\mathbf{g}), meaning $\psi_{n\mathbf{k}} = \psi_{n(\mathbf{k}+\mathbf{g})}$. Therefore, without loss of generality, the wavevector \mathbf{k} can be restricted to the first Brillouin zone of the reciprocal lattice. Wavevectors that differ by \mathbf{g} are equivalent (outside the first Brillouin zone) since they represent the same set of Bloch states.

Visualizing the shape of a band as a function of wavevector in four-dimensional space (ϵ vs. k_x, k_y, k_z) is challenging. Instead, it is customary to plot band dispersions, which show the values of $\epsilon_n(\mathbf{k})$ along special high-symmetry points or lines in the first Brillouin zone. These points or lines are assigned labels such as Γ , X, L, U, W, K, etc., and are connected by straight lines often denoted as Δ , Λ , Σ , or $[100]$, $[111]$, and $[110]$ respectively. This graphical representation is commonly known as the “bandstructure”. Figure 2.4 illustrates the bandstructure of the solid material GaAs.

The bandstructure of materials exhibits differences depending on their dimensionality, whether they are one-, two-, or three-dimensional. However, in this thesis, the focus is solely on analyzing the bandstructure of three-dimensional solids.

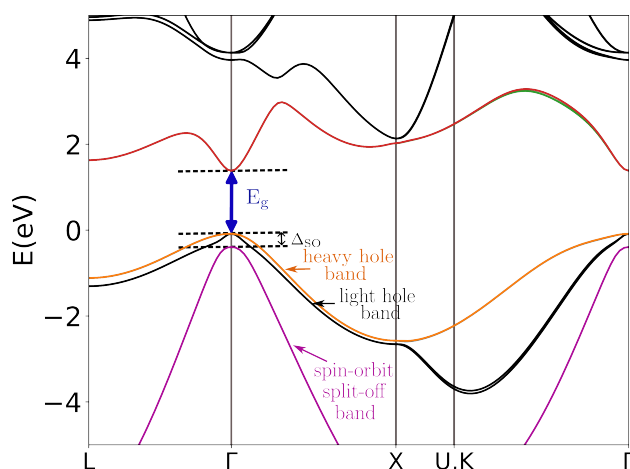


Figure 2.4: The calculated bandstructure of GaAs using DFT. The bandgap value (E_g) and spin-orbit split-off energy (Δ_{SO}) are shown. The heavy hole band, light hole band, and spin-orbit split-off bands are highlighted.

2.6.2 Bandgap

In semiconductors, there are two important bands: the valence band (VB) and the conduction band (CB). The VB is the highest occupied band at 0 K, while the CB is the lowest unoccupied band. These bands play a critical role in electronic and optoelectronic applications. The smallest energy gap between the highest occupied states in the VB, the valence band maximum (VBM), and the lowest unoccupied states in the CB, the conduction band minimum (CBM), is referred to as the “bandgap”. Within this region, no electronic states exist.

In semimetals, the bands are typically referred to as the “conduction band” or “valence band” depending on whether the charge transport is more electron-like or hole-like, similar to semiconductors. In metals, however, the bands are neither electron-like nor hole-like and are commonly referred to as the “valence band” as they are composed of valence orbitals.

The classification of bandgaps in semiconductors is based on the wavevectors of the states surrounding the bandgap. If the CBM has the same wavevector (\mathbf{k}) as VBM, the bandgap is categorized as a “direct bandgap”. On the other hand, if the wavevectors are different, it is referred to as an “indirect bandgap”. For example, GaAs has the VBM and CBM located at the same position in the \mathbf{k} -vector, at the Γ -point, making it a direct bandgap semiconductor (Figure 2.4). The calculated bandgap energy of GaAs is 1.47 eV at 0 K. In contrast, Si is an example of an indirect bandgap semiconductor with a bandgap energy of 1.19 eV at 0 K.

2.6.3 Electron Spin and Spin-Orbit Coupling

Up until now, another intrinsic property of electrons, their spin, has been neglected. However, in the relativistic formulation of quantum mechanics, the spin and orbital angular momentum couple to form a total angular momentum known as spin-orbit coupling (SOC). This coupling becomes more pronounced for heavier elements due to relativistic effects. In the context of this study, spin-orbit coupling is particularly relevant as it leads to a splitting of p-states into $p_{3/2}$ - and $p_{1/2}$ -states, resulting in a splitting of the valence bands in the investigated semiconductors.

For instance, in GaAs, the inclusion of SOC leads to the splitting of the VB degeneracy at the Γ -point (Figure 2.4). This splitting gives rise to the heavy hole and light hole bands, denoted as such based on the curvature of the bands, which are inversely proportional to the carrier effective masses [143]. These bands are separated from the spin-orbit split-off band by an amount denoted as Δ_{SO} . This splitting is formed due to the spin-orbit interaction between the (p- and s-) orbitals that constitute the VB.

It is important to note that the influence of SOC on the bandgap of III-V semiconductors can depend on various factors, including the elements in the material and the specific composition.

2.6.4 Bandgap Determination Problem

In the Kohn-Sham DFT, the bandgap refers to the energy difference between the highest occupied and lowest unoccupied Kohn-Sham orbitals. However, it is important to note that the Kohn-Sham bandgap does not necessarily correspond to the exact fundamental gap of the system.

This discrepancy arises because the Kohn-Sham DFT describes a fictitious non-interacting system. The Kohn-Sham energies do not represent the true quasiparticle electronic structure of the system. The fundamental gap, on the other hand, represents the true energy difference between the highest occupied and lowest unoccupied electronic states in the real interacting-electron system.

Even with the exact exchange-correlation functional, the Kohn-Sham bandstructure does not provide the true fundamental bandgap as it does not include the finite and positive derivative discontinuity [144, 145]. Moreover, there is currently no known exact exchange-correlation functional, and approximations must be employed. These approximations additionally contribute to the discrepancy between the Kohn-Sham bandgap and the fundamental gap. Factors such as the accuracy of the self-consistency cycle used in solving the Kohn-Sham equations also contribute to this difference.

Despite these limitations, Kohn-Sham DFT calculations often exhibit good agreement with experimental measurements of bandgaps [146]. However, in order to obtain a more accurate description of bandgaps, alternative approaches can be employed. One such approach is the use of time-dependent DFT, which can be employed to calculate the true bandstructure. Another approach is the use of hybrid functionals, which incorporate a portion of Hartree-Fock exact exchange. Hybrid functionals have shown improvements in predicting bandgaps, particularly in semiconductors. Alternatively, the GW approximations or many-body perturbation theory-based methods can provide improved descriptions of the bandgap in a variety of materials [88]. It is worth noting that these methods are often challenging in practice due to high computational costs, particularly when applied to large systems such as those used in this thesis.

2.6.5 Bandstructures in Non-Crystalline Solid

While electronic bandstructures are commonly associated with crystalline materials, it is important to note that quasi-crystalline and amorphous solids also exhibit bandgaps. However, investigating the bandstructures of these materials theoretically presents additional challenges due to their lack of crystal symmetry, making it difficult to establish precise dispersion relations. In the upcoming section (Section 2.8.4), we will explore an alternative approach for constructing the “effective bandstructure” of non-crystalline solids. This method provides a means to understand and analyze the electronic properties of these materials, despite their complex structural characteristics.

2.7 Density Functional Approximations

While the Kohn-Sham theory (Section 2.3.2) is exact in principle, one crucial component of this theory, namely the exchange-correlation functional, remains unknown. Therefore, practical applications of density functional theory rely on approximations for this functional.

2.7.1 Approximate Exchange-Correlation Functional

The first approximation introduced for the exchange-correlation functional was by Walter Kohn and Lu Jeu Sham in 1965, known as the local density approximation (LDA) [78]. In LDA, the energy of a small-volume element corresponds to that of a free electron gas with the same density, making the exchange-correlation energy (E_{XC}) dependent solely on the local electron

density. The exchange part of LDA is based on Slater’s formalism, and various implementations exist for the correlation part, which generally yields similar results.

Moving beyond LDA, the generalized gradient approximation (GGA) represents the next level of approximation. GGA incorporates an additional dependence on the local gradient of the electron density. There are many different GGA functionals available. In general, GGA functionals provide improved accuracy compared to LDA functionals for various material properties, particularly in relation to the structural properties [101, 103, 104]. Nevertheless, LDA and GGA functionals tend to exhibit significant errors when predicting the bandgaps of materials [18, 147, 148]. This limitation restricts their effectiveness in accurately determining bandgaps.

The next class of “pure” density functionals is the meta-GGA. These functionals include a term that depends on the second derivative of the electron density, also referred to as the kinetic energy density. In this thesis, the m-BJ functional (also known as TB09) [88] is utilized, which is a specific meta-GGA functional optimized for calculating electronic properties, especially semiconductor bandgaps. This functional is of particular importance for this work, and therefore, a more detailed description of this functional is provided in the following.

The exchange potential in the m-BJ functional is based on the work of Becke and Johnson (BJ). In short, the BJ potential ($v_{X,\sigma}^{BJ}(\mathbf{r})$) approximates the optimized effective potential (OEP), which, in turn, approximates the electronic exchange term. This is a multiplicative potential and can be expressed as [149]:

$$v_{X,\sigma}^{BJ}(\mathbf{r}) = v_{X,\sigma}^{BR}(\mathbf{r}) + \frac{1}{\pi} \sqrt{\frac{5}{6}} \sqrt{\frac{t_\sigma(\mathbf{r})}{\rho_\sigma(\mathbf{r})}} \quad (2.79)$$

where

$$\rho_\sigma = \sum_{j=1}^{N_\sigma} |\psi_{j,\sigma}|^2 \quad \text{is the electron density,}$$

$$t_\sigma = (1/2) \sum_{j=1}^{N_\sigma} \nabla \psi_{j,\sigma}^* \cdot \nabla \psi_{j,\sigma} \quad \text{is the kinetic energy density}$$

and

$$v_{X,\sigma}^{BR}(\mathbf{r}) = -\frac{1}{b_\sigma(\mathbf{r})} \left[1 - e^{-x_\sigma(\mathbf{r})} - \frac{1}{2} x_\sigma(\mathbf{r}) e^{-x_\sigma(\mathbf{r})} \right] \quad (2.80)$$

is the Becke-Roussel (BR) potential [150], which models the Coulomb potential created by the exchange hole.

x_σ in equation 2.80 is determined from a nonlinear equation involving ρ_σ , $\nabla\rho_\sigma$, $\nabla^2\rho_\sigma$, and t_σ . b_σ is then calculated as follows:

$$b_\sigma = \left[\frac{x_\sigma^3 e^{-x_\sigma}}{8\pi \rho_\sigma} \right]^{1/3}$$

The term $\sqrt{t/\rho}$ in equation 2.79 reproduces the step-like structure of the OEP in atoms and can be regarded as a screening term.

The BJ potential has been shown to improve the description of bandgaps compared to LDA and PBE, although the improvement is modest. Fabien Tran and Peter Blaha further improved this approach with the *modified* Becke-Johnson (m-BJ) approximation, introducing a parameter c to adjust the relative weights of the two terms in the BJ potential:

$$v_{X,\sigma}^{mBJ}(\mathbf{r}) = cv_{X,\sigma}^{BR}(\mathbf{r}) + (3c - 2) \frac{1}{\pi} \sqrt{\frac{5}{6}} \sqrt{\frac{t_\sigma(\mathbf{r})}{\rho_\sigma(\mathbf{r})}} \quad (2.81)$$

The c value in Equation 2.81 is calculated for every studied system and is chosen to depend linearly on the square root of the average of $|\nabla\rho|/\rho$:

$$c = \alpha + \beta \left(\frac{1}{V_{\text{cell}}} \int_{\text{cell}} \frac{|\nabla\rho(\mathbf{r}')|}{\rho(\mathbf{r}')} d^3\mathbf{r}' \right)^{1/2} \quad (2.82)$$

where V_{cell} is volume of the unit cell, and α and β are two free parameters. The linear combination in Equation 2.81 ensures that the LDA exchange potential is recovered for any value of c when considering a constant electron density. For $c = 1$, the original BJ potential is recovered.

In certain cases, the c parameter itself is varied instead of the free parameters α and β . It has been observed that, in general, the bandgap values exhibit a monotonic increase with c . By optimizing the c values, a better agreement with experimental results can be achieved [148].

It is important to note that m-BJ is an orbital-independent exchange-correlation potential that solely depends on semilocal quantities. It represents the first semilocal potential that achieves accuracy comparable to more computationally expensive hybrid and GW methods while maintaining the computational efficiency of LDA or GGA [88]. Consequently, this functional can be efficiently applied to very large systems, as in the case of this thesis, where the use of hybrid or GW methods would be impractical.

It should be noted that the m-BJ functional is a potential-only functional, meaning it lacks a corresponding m-BJ exchange-correlation energy term. It combines a meta-GGA exchange term with LDA correlation. Therefore, m-BJ calculations can not be self-consistent with respect to the total energy, and thus certain calculations, such as Hellmann-Feynman forces and ionic relaxations, can not be performed within the scope of m-BJ calculations.

2.7.2 Dispersion Correction

One major limitation of approximate DFT is its inadequate description of dispersion interactions, which are long-range electron correlation effects. Due to the absence of mechanisms addressing electron density fluctuations or molecular orbital fluctuations, these forces are not accounted for or are only insufficiently considered within approximate DFT. Dispersion forces are crucial in various molecular and condensed-phase systems, particularly in absorption studies and systems characterized by dispersion-bound interactions.

Several correction schemes exist to incorporate dispersion interactions into the DFT framework. The existing schemes can be categorized into two main types [151]. The highly parametrized meta-hybrid M0XX family of functionals is excluded from the discussion of this thesis.

The first type involves augmenting the semi-local or hybrid functional ($E_{xc}^{SL/hybrid}$) with a correlation dispersion term ($E_{c,disp}$), resulting in what is known as van der Waals functionals:

$$E_{xc} = E_{xc}^{SL/hybrid} + E_{c,disp} \quad (2.83)$$

In this approach, the dispersion is included self-consistently in density functionals, e.g., via response functions and/or non-local dispersion kernels. Prominent methods under this category include the vdW-DF methods [152, 153] and the rVV10 method [154, 155]. These types of corrections are, in general, of the following type:

$$E_{c,disp} = \frac{1}{2} \int \int \rho(\mathbf{r}) \Phi(\mathbf{r}, \mathbf{r}') \rho(\mathbf{r}') d^3\mathbf{r} d^3\mathbf{r}' \quad (2.84)$$

The kernel Φ depends on the electron density ρ , its derivative $\nabla\rho$, and the distance $|\mathbf{r} - \mathbf{r}'|$ between points. These schemes require a double spatial integration and are generally computationally expensive.

The other class of correction schemes is the post-SCF-type corrections which model dispersion based on atomic polarizabilities. This category can be further divided into two subcategories: corrections that explicitly consider the electron density and semi-classical approaches that are electron-density independent.

Notable methods in the first subcategory include the exchange-hole dipole moment approach of Becke and Johnson (XDM) [156, 157], the Tkatchenko-Scheffler (TS) model [158], and its many-body dispersion (MBD) successor [159]. These methods employ a Hirshfeld-type atomic partitioning of the electron density. In the second subcategory, one of the most cost-effective dispersion correction schemes is the semi-classical DFT-D methods by Grimme et al. [160].

In this thesis, the third-generation DFT-D scheme with Becke-Johnson type damping (DFT-D3(BJ)) [160, 161] is utilized. This scheme simply adds a dispersion energy (E_{disp}) to the Kohn-Sham DFT energy ($E_{\text{KS-DFT}}$):

$$E_{\text{DFT}}^{\text{D3(BJ)}} = E_{\text{KS-DFT}} + E_{\text{disp}} \quad (2.85)$$

The dispersion energy is obtained as the sum of atom-pairwise contributions:

$$E_{\text{disp}} = - \sum_{A < B} \sum_{j=6,8} f_j^{\text{damp}}(R_{AB}) \frac{C_j^{AB}}{R_{AB}^j} \quad (2.86)$$

where C_j^{AB} s are the dispersion coefficients and R_{AB} is the distance between atoms pairs A - B . The Becke-Johnson damping function f_j^{damp} is calculated as follows:

$$f_j(R_{AB}) = \frac{s_j R_{AB}^j}{R_{AB}^j + (a_1 R_{0,AB} + a_2)^j} \quad (2.87)$$

The sixth-order coefficients in Equation 2.86 are derived from averaged dipole polarizabilities α using the Casimir-Polder equation. Notably, instead of deriving the dipole polarizabilities from isolated atoms, they are determined from simple hydrides associated with each element. This approach allows for the incorporation of coordination number dependence into the dispersion coefficients. The expression for C_6^{AB} considering coordination number dependence is given as follows:

$$C_6^{AB} = \frac{3}{\pi} \int_0^\infty \frac{1}{m} \left[\alpha^{A_m H_n}(i\omega) - \frac{n}{2} \alpha^{H_2}(i\omega) \right] \times \frac{1}{k} \left[\alpha^{B_k H_l}(i\omega) - \frac{n}{2} \alpha^{H_2}(i\omega) \right] d\omega \quad (2.88)$$

where $\alpha^{H_2}(i\omega)$ represents the corresponding dipole polarizability for the dihydrogen molecule, while m, n, k, l are stoichiometric factors. The terms $\alpha^{A_m H_n}(i\omega)$ and $\alpha^{B_k H_l}(i\omega)$ correspond to the averaged dipole polarizabilities of the reference molecules $A_m H_n$ and $B_k H_l$, respectively.

The eighth-order coefficients then follow the recursion relation:

$$C_8^{AB} = 3C_6^{AB} \sqrt{Q^A Q^B} \quad \text{with} \quad Q^A = s_{42} \sqrt{Z^A} \frac{\langle r^4 \rangle^A}{\langle r^2 \rangle^A} \quad (2.89)$$

where the $\langle r^2 \rangle$ and $\langle r^4 \rangle$ are the multipole-type expected values derived from atomic densities.

The parameters $s_6, s_8, a_1,$ and a_2 in equation 2.87 are fit parameters that depend on the functionals used, with $s_6 = 1$ apply to GGA and hybrid functionals. The cut-off distance in the damping term is calculated using the C -coefficients:

$$R_{0,AB} = \sqrt{\frac{C_8^{AB}}{C_6^{AB}}} \quad (2.90)$$

It is important to note that, in this thesis, the dispersion correction is employed during the structure optimization only. When conducting bandgap calculations with m-BJ functional, only single-point calculations are performed. In this step, the inclusion of dispersion correction has no impact since the post-SCF DFT-D3(BJ) method only improves the total energy of the system.

2.8 Modeling III-V Compounds

2.8.1 Special Quasi-Random Structure

While the supercell approach with random distribution of constituents can be used to model mixed compounds, such as crystals with defects or alloys, it still provides only an approximate description of the system within periodic cells. Despite using large supercells and random occupation, the structures generated within a *finite supercell* can deviate from the “perfect” randomness. In particular, there is a significant likelihood that the local correlations between the chemical species occupying nearby lattice sites will not perfectly match the desired randomness.

To improve the description of such configurationally disordered alloys, Zunger et al. developed the special quasi-random structures (SQS) approach [162]. An SQS represents the best periodic supercell approximation to the true disordered state for a given number of atoms per supercell. The quality of an SQS is measured in terms of the number of correlations of the fully disordered state it is able to match exactly. Typically, one attempts to preferably match shorter-range correlations while gradually enlarging the supercell to extend the range of matching correlations until convergence of the properties of interest. Initially, the focus was on matching pair correlations, although for better performance, multibody correlations should also be considered.

The original approach involved exhaustively checking all possible site occupations in cells of a given size until the correlation function of the perfectly disordered state was reproduced to the best extent possible. However, this exhaustive enumeration algorithm becomes computationally infeasible for relatively large supercells exceeding 1000 atoms. To overcome this challenge, a more efficient stochastic approach for SQS generation was developed by van de Walle et al. [163], allowing the use of large cell sizes.

In this thesis, the stochastic SQS approach, as implemented in the alloy theoretical automated toolkit (ATAT) [163], is utilized. This approach follows a cluster design method capable of handling multicomponent and multisublattices. The algorithm aims to find SQS that precisely matches the maximum number of correlation functions, unlike the previous implementation that focused on minimizing the distance between SQS correlations and disordered state correlations. To achieve this, the objective function traditionally used for stochastic SQS searches was generalized to include a term that ‘rewards’ a perfect correlation match within a specified distance range. The objective function is then minimized to obtain the best SQS with the minimum value of the objective function.

The algorithm proceeds as follows: A cluster α is defined as a list of sites that are considered in the calculation of a particular correlation with σ_j specifying the occupation of lattice site j . The correlation ρ_α associated to a cluster α in an SQS σ is defined as the average of the cluster functions over all symmetrically equivalent clusters α' :

$$\rho_\alpha(\sigma) = \langle \Gamma_{\alpha'}(\sigma) \rangle_\alpha \quad (2.91)$$

where σ represents the vector of all the σ_j variables. The cluster-function Γ_α is calculated using the following expression:

$$\Gamma_\alpha = \prod_j \gamma_{\alpha_j, M_j}(\sigma_j) \quad (2.92)$$

M_j in Equation 2.92 indicates distinct chemical species that can occupy site j . $\gamma_{\alpha_j, M_j}(\sigma_j)$ satisfies $\gamma_{0, M_j}(\sigma_j) = 1$ ($\alpha_j = 0$ when site j does not belong to cluster α) and follows the orthogonality condition:

$$\frac{1}{M} \sum_{\sigma_j=0}^{M_j-1} \gamma_{\alpha_j, M_j}(\sigma_j) \gamma_{\beta_j, M_j}(\sigma_j) = \begin{cases} 1 & \text{if } \alpha_j = \beta_j \\ 0 & \text{otherwise} \end{cases} \quad (2.93)$$

The objective function (to be minimized) is then defined as:

$$O = -\omega L + \sum_{\alpha \in A} |\Delta \rho_\alpha(\sigma)| \quad (2.94)$$

where $\Delta \rho_\alpha(\sigma)$ denote the deviation of correlations of a SQS σ from its ideal disordered state. It is calculated as $\Delta \rho_\alpha(\sigma) = \rho_\alpha(\sigma) - \rho_\alpha(\sigma^{\text{rnd}})$, where $\rho_\alpha(\sigma^{\text{rnd}})$ denotes the correlations of the fully disordered state at some given composition.

To calculate $\rho_\alpha(\sigma^{\text{rnd}})$, one can exploit the fact that in the ideal disordered state, the site occupations are independent. Therefore, this quantity can be easily calculated as:

$$\rho_\alpha(\sigma^{\text{rnd}}) = \left\langle \prod_j \gamma_{\alpha_j, M_j}(\sigma_j) \right\rangle_\alpha = \prod_j \langle \gamma_{\alpha_j, M_j}(\sigma_j) \rangle_\alpha \quad (2.95)$$

The set A in Equation 2.94 specifies a user-specified collection of clusters. The parameter L represents the largest distance between pairs within a cluster such that for all clusters of this type $\Delta\rho_\alpha(\sigma) = 0$. The weighting factor ω is a user-specified parameter that assigns importance to the range of perfect correlation matching in the objective function (with a default value of 1).

In order to minimize equation 2.94, all supercells are first enumerated with the user-specified number N of atoms per cell. The lattice sites of each cell are randomly occupied according to the specified composition on each sublattice. The best supercell with the minimum objective function is determined from the generated cells.

A simulated annealing is then performed by attempting jumps into other supercells and permutations of atoms within the same sublattice. These jumps and permutations are accepted or rejected based on a Metropolis algorithm. A newly visited supercell and configuration are accepted if they yield a lower objective function value than the best SQS obtained so far.

The implementation in the ATAT requires input parameters such as the supercell size N , the primitive cell serving as the basis for possible supercells, the composition, and the size of the clusters to be formed. The cluster sizes are specified by the maximum distance for pairs, triplets, and larger clusters.

While the algorithm allows for optimization of the shape and size of the supercell, this thesis focuses on systems that solely exhibit the zincblende crystal structure. Hence, the cell shape is not optimized. Furthermore, to avoid spurious image cell interactions, also known as periodicity errors, large supercell are required [18]. Therefore, smaller SQS supercells that may be allowed for the given composition are not searched.

2.8.2 Bandstructure folding

In the supercell bandstructure, the bands undergo folding [164, 165]. As the unit cell dimension increases with respect to the primitive cell, the Brillouin zone shrinks proportionally, resulting in the folding of primitive bands within the supercell. This is illustrated schematically in Figure 2.5, where the bandstructure of a one-dimensional polymer folds as the unit cell dimension is increased [165].

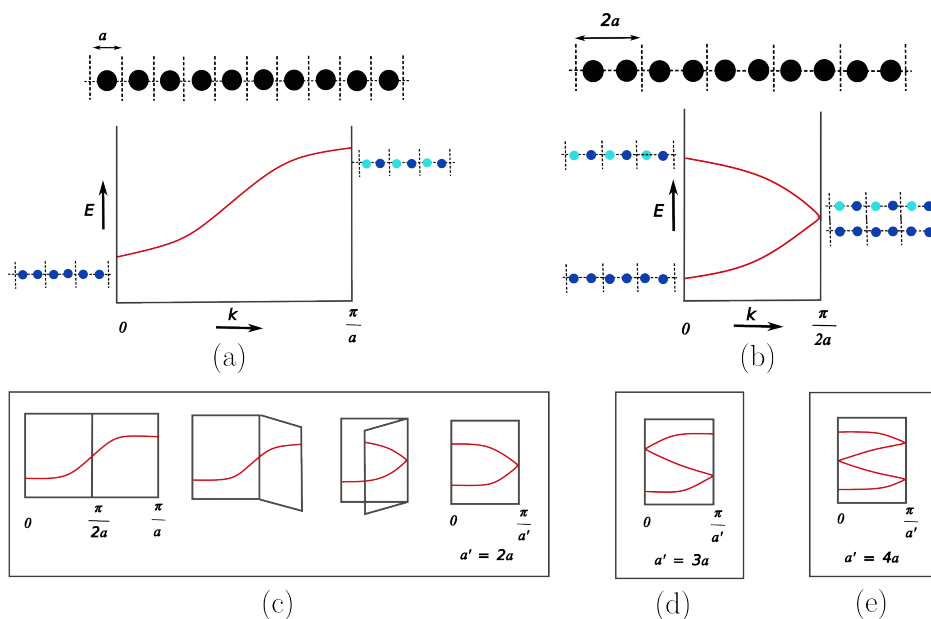


Figure 2.5: Band folding in a one-dimensional polymer. a) Bandstructure of a polymer with one atom per unit cell. b) Bandstructure of a polymer with two atoms per unit cell. The Brillouin zone is halved as the unit cell is doubled. c) Folding of the bandstructure from (a) to (b). d) – e) Multiple foldings of bands occur when the unit cell is tripled or quadrupled. Figure adapted from Reference [165].

Despite the folding, the value of the bandgap can still be determined as the energy difference between the highest occupied and the lowest unoccupied band in the folded band structure. However, in folded bands, the primitive Bloch character of the bands becomes mixed up. Consequently, straightforward determination of the Bloch character of the CBM and VBM in those bands is not possible, and thus the nature of the bandgaps.

2.8.3 Bloch Spectral Weights

The most successful approach that connects the supercell bandstructure with the primitive basis representation is based on Bloch spectral weight (BSW) [166, 167]. This is obtained by mapping the Brillouin zone of a supercell onto the underlying reference primitive cell, a process known as band unfolding.

The BSWs ($\omega_{m,\mathbf{K}}(\mathbf{k}_\nu)$) are obtained by projecting the supercell Bloch states ($|\mathbf{K}m\rangle$) onto the reference primitive cell Bloch states ($|\mathbf{k}n\rangle$):

$$\omega_{m,\mathbf{K}}(\mathbf{k}) = \sum_n |\langle \mathbf{K}m | \mathbf{k}n \rangle|^2 \quad (2.96)$$

The BSW $\omega_{m,\mathbf{K}}(\mathbf{k})$ amounts to Bloch character \mathbf{k} that is present in $|\mathbf{K}m\rangle$ at the m -th energy eigenstates ϵ_m and satisfies the normalization condition $\sum \omega_{m,\mathbf{K}}(\mathbf{k}) = 1$. A supercell wavevector \mathbf{K} can *unfold* into a primitive wavevector \mathbf{k} if:

$$\mathbf{k} = \mathbf{K} + \mathbf{G} \quad (2.97)$$

where \mathbf{G} corresponds to the translation vector of the supercell reciprocal space (Equation 2.48).

In general, the folding of states of different wavevectors in the supercell depends on both the geometry and symmetry of the supercell and the underlying primitive cell. However, in the case of plane-wave basis sets, like those used in this thesis, the BSWs can be easily constructed solely from the plane-wave coefficients $C_{m,\mathbf{K}}$, that form the supercell eigenstates [166–169]. In the plane-wave formalism, Equation 2.96 simplifies to:

$$\omega_{m,\mathbf{K}}(\mathbf{k}) = \sum_{\mathbf{g}} |C_{m,\mathbf{K}}(\mathbf{g} + \mathbf{k} - \mathbf{K})|^2 \quad (2.98)$$

where \mathbf{g} represents the translation vector in the reciprocal space of primitive cell. The advantage of this expression is that the states of the primitive cell do not have to be known in order to do the unfolding.

2.8.4 Effective Bandstructure

As pointed out earlier in Section 2.6.1, a wavevector and the electronic bandstructure in a solid are only defined if translational symmetry is present. Disordered systems such as supercell SQS, described above, lack translational symmetry both on the atomic and mesoscopic scales. Therefore, in such systems, the concepts of bandstructure are lost. Nevertheless, in many cases, the identity of the translationally invariant states of pure crystal turns out to be preserved in the alloys. Hence, it is useful to retain the formalism of a bandstructure for these as well. This is known as effective bandstructure (EBS) [168–170]. The EBSs are useful for a phenomenological description of trends in properties under investigation with alloy composition.

The EBS is constructed using the BSWs described in the previous section. This process involves first calculation of the spectral function $A(\mathbf{k}; \epsilon)$. The spectral functions can be calculated using the BSWs as follows:

$$A(\mathbf{k}; \epsilon) \equiv \sum_m \omega_{m,\mathbf{K}}(\mathbf{k}) \delta(\epsilon - \epsilon_m(\mathbf{K})) \quad (2.99)$$

The EBS is then constructed from the spectral functions. To achieve this, the $(\mathbf{k}; \epsilon)$ -space is mapped onto $(\mathbf{k}_\nu; \epsilon_\mu)$ grid with energy intervals of size $\delta\epsilon$.

Each point on the grid is assigned a weight $\delta N(\mathbf{k}_\nu; \epsilon_\mu)$, which represents the number of primitive cell bands crossing the point $(\mathbf{k}_\nu; \epsilon_\mu)$ and can be understood as the Bloch character. The quantity $\delta N(\mathbf{k}_\nu; \epsilon_\mu)$ is calculated as follows:

$$\begin{aligned} \delta N(\mathbf{k}_\nu; \epsilon_\mu) &\equiv \int_{\epsilon_\mu - \delta\epsilon/2}^{\epsilon_\mu + \delta\epsilon/2} A(\mathbf{k}_\nu; \epsilon) d\epsilon \\ &= \sum_m \omega_{m,\mathbf{K}}(\mathbf{k}_\nu) \int_{\epsilon_\mu - \delta\epsilon/2}^{\epsilon_\mu + \delta\epsilon/2} \delta(\epsilon - \epsilon_m(\mathbf{K})) d\epsilon \end{aligned} \quad (2.100)$$

Finally, δN is averaged over the wavevectors \mathbf{k}_ν that are related by symmetry operations of the primitive cell Brillouin zone.

For spinor wave functions, such as those considering spin-orbit coupling, the two spin components can be treated independently.

2.8.5 Bandgap Nature Determination Protocol from Supercell Calculations

Analysis of the EBSs in strained III-V systems shows that the VBM remains located at the Γ -point, regardless of the applied strain. Only the CBM changes position in reciprocal space when subject to strain. Moreover, the CBM occurs exclusively at the Γ -, L-, and (near) X-points under strain. This is shown in the (selected) EBSs of strained GaAsP and GaAsN in Figures 2.6 and 2.7. The EBSs for other strained systems can be found in Supplementary Information in References [146] and [171]. These observations suggest that tracing the CBM only at these specific \mathbf{k} -points is sufficient to determine the bandgap nature. It is important to note that due to the effective nature of the bandstructures, distinguishing between the near X-point and the X-point itself is challenging. Therefore, in the following, only the BSWs at the Γ -, L-, and X-point are considered.

Furthermore, for zincblende structures and the chosen supercell size of $6 \times 6 \times 6$ in this thesis (see Section 3.1.3), the Γ -, L-, and X-points of the primitive bandstructure fold to the Γ -point in the supercell. Thus, by exclusively considering the BSWs of the CB at the Γ -point within the supercell effectively allow to determine the nature of the bandgap.

These two findings combined have significantly simplified the determination of the bandgap nature from supercell calculations. By performing supercell DFT calculations that solely sample the reciprocal space at the Γ -point¹, and unfolding only the CB, allows to efficiently determine the bandgap nature while reducing the computational expense associated with DFT calculations.

¹This enables the use of the computationally efficient Γ -only version of VASP.

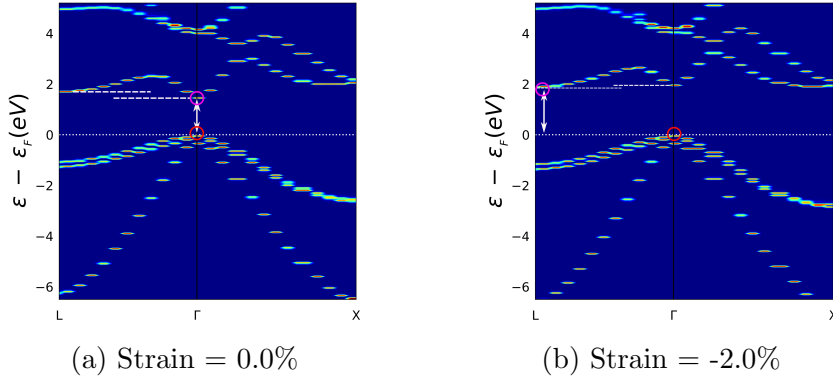


Figure 2.6: Snapshots of the $\text{GaAs}_{96.3}\text{P}_{3.7}$ bandstructure under biaxial strain, with positive and negative strain values representing tensile and compressive strains, respectively. The bandgaps are indicated by arrows. The VBM and CBM are highlighted in red and magenta circles, respectively. Figure adapted with permission from Reference [171].

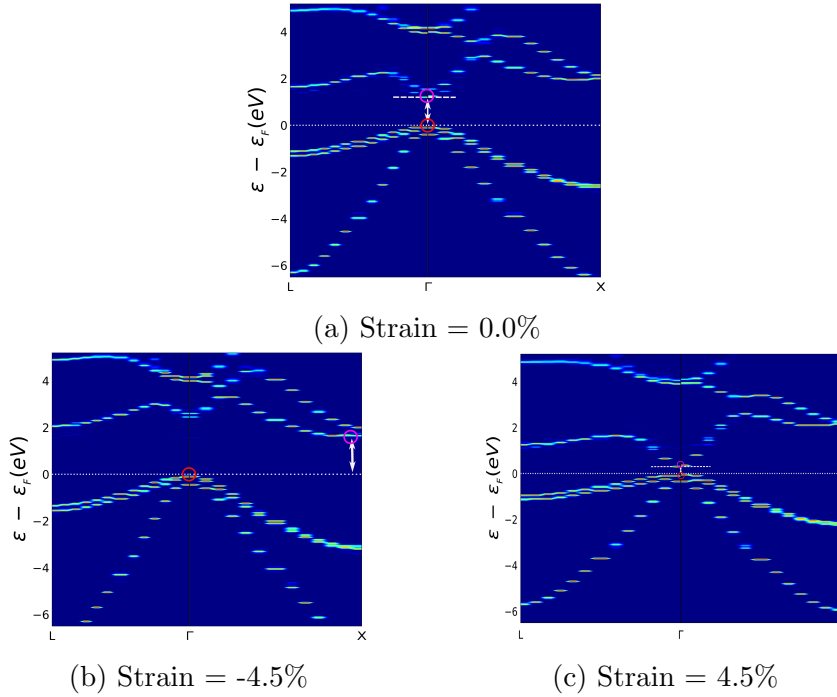


Figure 2.7: Snapshots of the $\text{GaAs}_{99.5}\text{N}_{0.5}$ bandstructure under biaxial strain, with positive and negative strain values representing tensile and compressive strains, respectively. The bandgaps are indicated by arrows. The VBM and CBM are highlighted in red and magenta circles, respectively. Figure adapted with permission from Reference [171].

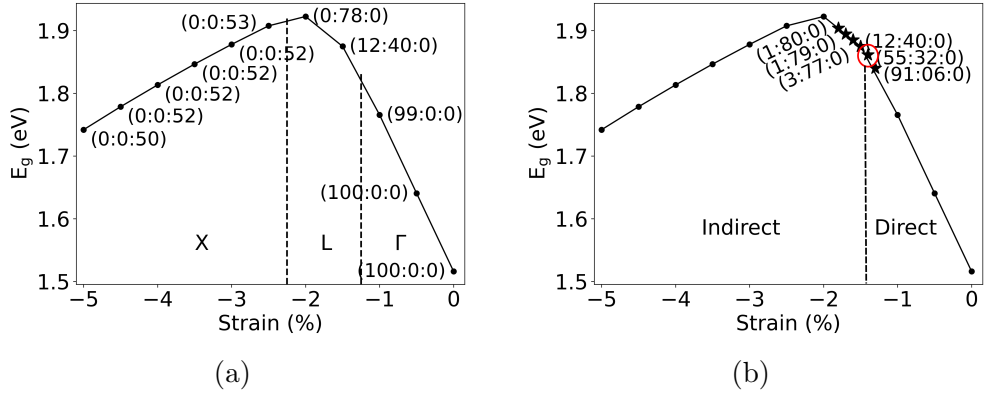


Figure 2.8: Variation of the bandgap value (E_g) for $\text{Ga}_{100}\text{As}_{96.3}\text{P}_{3.7}$ under isotropic strain. The negative signs in the strain values indicate compressive strain. The Γ -, L-, and X-BSW values of the folded supercell CB are provided in parentheses as $(\Gamma:L:X)$. The values are given in %. Vertical lines in (a) demarcate the regions where the character of the CBM changes. In (b), strain resolution is increased to determine the direct-indirect transition point more accurately. Figure adapted with permission from Reference [171].

Figure 2.8 illustrates the steps involved in determining the nature of the bandgap through supercell calculations. The figures show the bandgap variation for $\text{Ga}_{100}\text{As}_{96.3}\text{P}_{3.7}$ SQS supercell under isotropic compressive strain. The Γ -, L-, and X-BSWs of the folded CB are provided in parentheses¹.

In Figure 2.8a, it can be seen that the unstrained structure exhibits 100% Γ -BSW, indicating the position of CBM at the Γ -point and, thus, a direct bandgap. As the strain increases, the Γ -BSW decreases (first number in brackets) while the L-BSW increases (second number in brackets). Eventually, when the strain reaches a certain level (here, between -1 and -1.5% strain), the L-BSW becomes dominant, indicating the shift of the CBM to the L-point and the transition of the bandgap from direct to indirect.²

To further accurately determine the transition point from a direct to an indirect bandgap, calculations with higher strain resolution are performed, as shown in Figure 2.8b. In this specific example, the transition occurs at a strain value of -1.4% . It is important to note that the last strained structure with a direct bandgap before the transition is defined as the transition point (indicated by the red circle in Figure 2.8b).

¹Only the three BSWs are shown in the figures, while the BSWs for other unfolded k-points are not presented. Therefore, the total BSWs shown in the figure may not add up to 100%.

²Further compression leads to a transition from L-character to X-character.

2.9 Machine learning

In the field of machine learning, supervised learning models are utilized for classification and regression analysis tasks [173]. In supervised learning, a set of training examples $\mathbf{x}_1 \dots \mathbf{x}_N$ is provided (also called features), along with their corresponding labels $y_1 \dots y_N$. The objective is to predict the label y_{N+1} for a new input \mathbf{x}_{N+1} . Figure 2.9 schematically presents the working principle of supervised learning. In this example, the features represent shapes, while the labels correspond to their respective shape names. Once the model is trained, it can be used to predict the labels for new test shapes.

There are two main categories in supervised learning: classification and regression [111, 112]. Figure 2.10 illustrates the distinction between these two learning categories. Classification involves creating an appropriate separation boundary and assigning the data to specific categories. Regression, on the contrary, predicts continuous variables and analyzes the relationship between dependent and independent variables. Common classification algorithms include linear classifiers, decision trees, k-nearest neighbors, random forest, and support vector machines (SVM). Popular regression algorithms include linear regression, polynomial regression, and logistical regression.

In this thesis, the SVM model is utilized. In the following section, an overview of this model and its key characteristics are provided.

2.9.1 Support Vector Machine

The fundamental feature of SVM is that it constructs a (set of) hyperplane(s) in a high-dimensional space, which can be used for classification and regression tasks.

For the SVM classification, also known as support vector classification (SVC) model, a training dataset of N points, each consisting of a feature \mathbf{x}_i and a class label y_i is given. For binary class data, y_i can be, for example, either 1 or -1 . The goal is to find the hyperplane that separates the points with $y_i = 1$ from those with $y_i = -1$ while maximizing the distance between the hyperplane and the nearest points.

By maximizing the margin, the model aims to reduce its generalization error, which measures the performance of the trained models on unseen or new data. A low generalization error suggests that the model has successfully learned the relevant patterns and can make accurate predictions on new data. On the other hand, a high generalization error indicates that the model is overfitting the training data, meaning it has memorized the training examples too well and fails to generalize to new data.

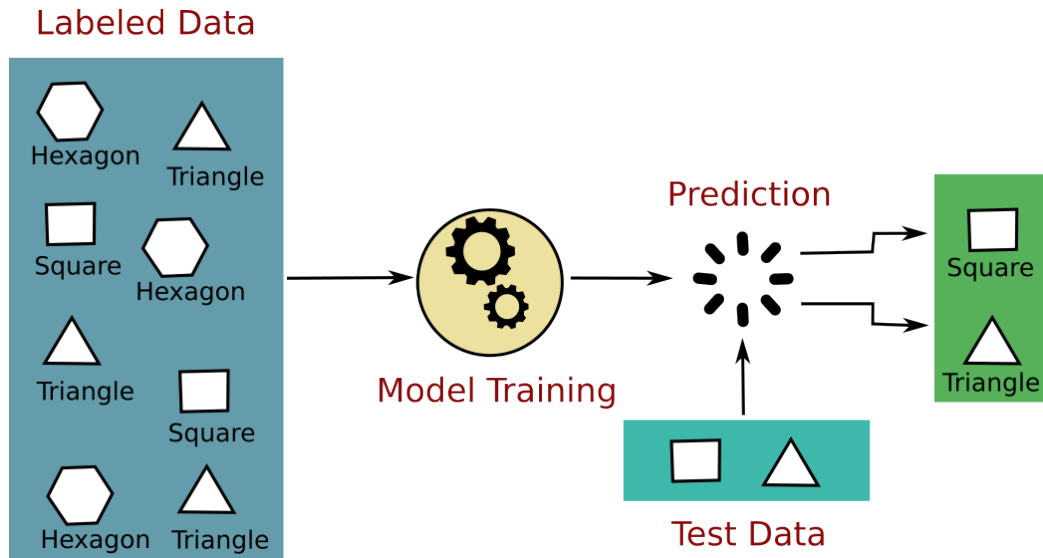


Figure 2.9: Schematic of supervised learning working principle. The model is trained using a labeled data set and subsequently employed to predict labels for unknown data. Figure adapted from Reference [172].

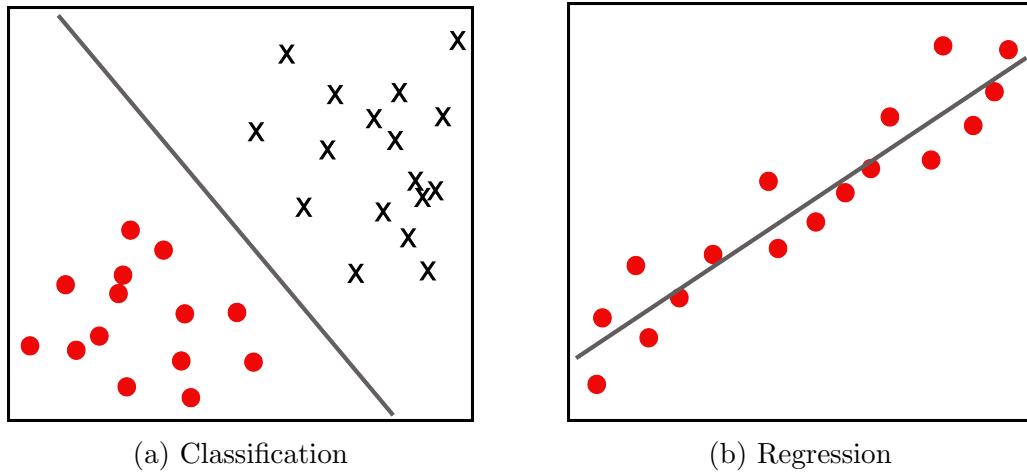


Figure 2.10: Comparison of classification and regression machine learning techniques. The scatter plot represents the original data with dots and cross symbols. The machine-learned decisions are illustrated by lines, indicating the decision boundary for classification and the fitting curve for regression.

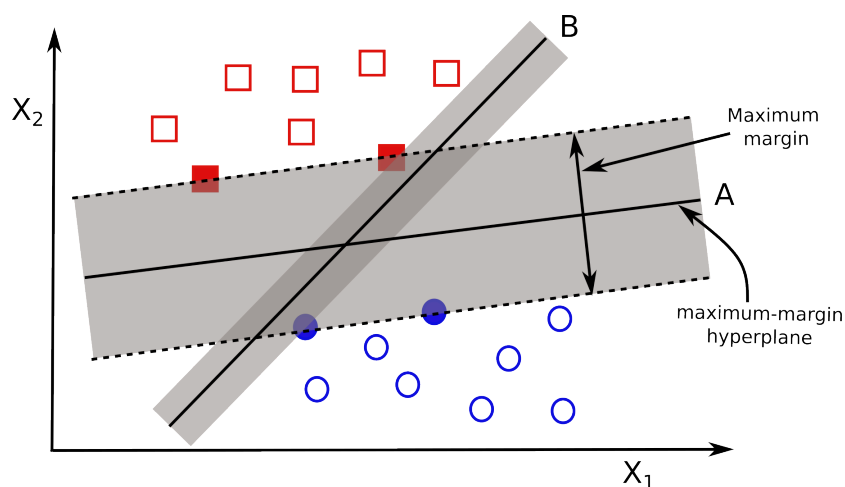


Figure 2.11: Illustration of SVM training with dataset using a two-class dataset. Two hyperplanes, A and B, are depicted, with A exhibiting a larger margin. The data points situated on the margin (filled squares and circles) are the support vectors.

Figure 2.11 visually illustrates the concept of the maximum-margin hyperplane using a linearly separable dataset. In this case, two parallel hyperplanes can be selected to effectively separate the two classes, ensuring the maximum distance between them. The bounded region between these hyperplanes is called the “margin”, with the decision hyperplane positioned equidistant from them. The objective is to optimize the positioning of the decision hyperplane to achieve the maximum margin and, consequently, the “maximum-margin hyperplane”. In the figure, ‘A’ represents the maximum-margin hyperplane, which is clearly superior to ‘B’ in terms of generalization error. Notably, the maximum-margin hyperplane is completely determined by those \mathbf{x}_i that lies nearest to it. These \mathbf{x}_i s are called support vectors (SVs).

Mathematically, SVM is formulated as follows. Any hyperplane can be written as the set of points \mathbf{x} satisfying

$$\mathbf{w}^\top \mathbf{x} - b = 0 \quad (2.101)$$

where \mathbf{w} is the normal vector to the hyperplane and $\frac{b}{\|\mathbf{w}\|}$ determines the offset of the hyperplane from the origin along the normal vector \mathbf{w} .

In the case of linearly separable data, two parallel hyperplanes can be chosen to bind the margin, satisfying the constraints

$$\begin{aligned} \mathbf{w}^\top \mathbf{x}_i - b &\geq 1, & \text{if } y_i = 1 \\ \mathbf{w}^\top \mathbf{x}_i - b &\leq -1, & \text{if } y_i = -1 \end{aligned} \quad (2.102)$$

These constraints state that each data point must lie on the correct side of the margin. This can be rewritten as:

$$y_i(\mathbf{w}^\top \mathbf{x}_i - b) \geq 1, \quad \text{for all } 1 \leq i \leq N \quad (2.103)$$

The optimization problem for SVM is then formulated as follows:

$$\underset{\mathbf{w}, b}{\text{minimize}} \quad \frac{1}{2} \mathbf{w}^\top \mathbf{w} \quad (2.104)$$

$$\text{subject to} \quad y_i(\mathbf{w}^\top \mathbf{x}_i - b) \geq 1, \quad i = 1, \dots, N \quad (2.105)$$

The \mathbf{w} and b that solve this problem determine our classifier, $\mathbf{x} \mapsto \text{sgn}(\mathbf{w}^\top \mathbf{x} - b)$ where $\text{sgn}()$ is the sign function.

However, perfect linear separation (“hard margin”) is not always possible in real-world datasets. To handle cases where data points are not perfectly separable, regularization is introduced, leading to the “soft margin” concept. The optimization problem becomes minimizing a regularized risk function ($\hat{f}(\lambda)$):

$$\hat{f}(\lambda) = \lambda \mathbf{w}^\top \mathbf{w} + \left[\frac{1}{N} \sum_{i=1}^N \max(0, 1 - y_i(\mathbf{w}^\top \mathbf{x}_i - b)) \right] \quad (2.106)$$

where the first term in equation 2.106, $\mathbf{w}^\top \mathbf{w}$ controls the margins. The minimization of $\frac{1}{2} \mathbf{w}^\top \mathbf{w}$ maximizes the margin. The second term, inside the square bracket, is the misclassification error. In this case we use the hinge loss function, $\ell(y, f(x)) := \max(0, 1 - yf(x))$. Its value is 0 for correctly classified data points. Otherwise, the data points on the wrong side get a penalty. The parameter $\lambda > 0$ thus determines the trade-off between margin maximization and penalty for misclassifications.

The optimization problem in Equation 2.106 can be rewritten as a constrained optimization problem with a differentiable objective function:

$$\underset{\mathbf{w}, b, \zeta}{\text{minimize}} \quad \frac{1}{2} \mathbf{w}^\top \mathbf{w} + C \sum_{i=1}^N \zeta_i$$

$$\text{subject to} \quad y_i(\mathbf{w}^\top \mathbf{x}_i - b) \geq 1 - \zeta_i, \quad \zeta_i \geq 0, \quad i = 1, \dots, N \quad (2.107)$$

where we introduce a slack variable ζ_i for each sample, and C is now the regularization parameter (λ is inversely related to C). The C parameter controls the trades of the misclassification vs the margin maximization. The misclassification and, thus, the accuracy of the model strongly depends on C and are tuned to optimize predictions.

2.9.2 Kernel Method

The kernel method is a powerful technique used within SVM models to create nonlinear classifiers. It achieves this by employing the kernel trick, which simplifies the learning task by mapping the original feature space of the data into a new space using a kernel function [174]. This mapping allows for linear separation or fitting of the data, even when dealing with complex, nonlinear relationships while reducing the computational cost associated with large datasets.

The SVM algorithm with the kernel method is similar in structure to the standard SVM algorithm, with the key difference being the replacement of every dot product with a nonlinear kernel function. This modification enables the algorithm to find the maximum-margin hyperplane in the transformed feature space. Although the resulting classifier is a hyperplane in this transformed space, it may be nonlinear in the original input space.

In this thesis, the radial basis function (RBF) kernel method is used. The RBF kernel (k) can be defined as:

$$k(\mathbf{x}_i, \mathbf{x}_j) = e^{-\gamma\|\mathbf{x}_i - \mathbf{x}_j\|^2} \quad (2.108)$$

The parameter $\gamma (> 0)$ determines the inverse of the area of influence of a sample \mathbf{x}_i and decays with the distance to another sample \mathbf{x}_j . A low value of γ means the influence reaches ‘far’, and a high value implies a ‘closer’ influence. The choice of γ has a significant impact on the behavior of the model and can be tuned to optimize the predictive performance.

The kernel function in Equation 2.108 satisfies the following relationship:

$$k(\mathbf{x}_i, \mathbf{x}_j) = \varphi(\mathbf{x}_i)^\top \varphi(\mathbf{x}_j) \quad (2.109)$$

This equation ensures that the kernel function captures the inner product of the transformed feature vectors, allowing for efficient computation and avoiding the need to explicitly calculate the transformed feature vectors $\varphi(\mathbf{x}_i)$. Within the kernel method, the goal is to learn a nonlinear classification rule that corresponds to a linear classification rule for the transformed data points $\varphi(\mathbf{x}_i)$.

Including the kernel trick, the primal problem corresponding to the soft-margin formulation of SVM (Equation 2.107) becomes:

$$\begin{aligned} & \underset{\mathbf{w}, b, \xi}{\text{minimize}} && \frac{1}{2} \mathbf{w}^\top \mathbf{w} + C \sum_{i=1}^N \xi_i \\ & \text{subject to} && y_i(\mathbf{w}^\top \varphi(\mathbf{x}_i) - b) \geq 1 - \xi_i, \quad \xi_i \geq 0, \quad i = 1, \dots, N \end{aligned} \quad (2.110)$$

2.9.3 SVM Classifier Algorithms

Two notable recent algorithms for finding the SVM classifier are sub-gradient descent and coordinate descent. Both techniques offer significant advantages when dealing with large datasets.

Sub-gradient descent algorithms directly work with the expression 2.106 that defines the SVM classifier. On the other hand, coordinate descent algorithms operate based on the dual problem. By solving for the Lagrangian dual of the primal problem, Equation 2.110, we obtain the simplified dual problem:

$$\begin{aligned} & \underset{\alpha}{\text{minimize}} && \frac{1}{2} \alpha^T Q \alpha - \mathbf{1}^T \alpha \\ & \text{subject to} && y^T \alpha = 0, \quad 0 \leq \alpha_i \leq C, \quad i = 1, \dots, N \end{aligned} \quad (2.111)$$

where $\mathbf{1}$ is a vector of all ones, and Q is an $N \times N$ positive semidefinite matrix defined as:

$$Q_{ij} \equiv y_i y_j k(\mathbf{x}_i, \mathbf{x}_j) \quad (2.112)$$

The terms α_i are the Lagrange multipliers also called the dual coefficients. They are upper-bounded by C . Since the dual optimization problem is a quadratic function of the α_i subject to linear constraints, it can be efficiently solved using quadratic programming algorithms. The algorithm solves for the dual coefficients α_i .

In the transformed feature space, the weight vector \mathbf{w} satisfies:

$$\mathbf{w} = \sum_{i=1}^N y_i \alpha_i \varphi(\mathbf{x}_i) \quad (2.113)$$

Once the optimization problem is solved, the offset b can be calculated as follows (using Equation 2.113 for \mathbf{w} and Equation 2.109 for kernel function k):

$$b = \mathbf{w}^T \varphi(\mathbf{x}_i) - y_i = \left[\sum_{j=1}^N y_j \alpha_j \varphi(\mathbf{x}_j)^T \varphi(\mathbf{x}_i) \right] - y_i \quad (2.114)$$

$$= \left[\sum_{j=1}^N y_j \alpha_j k(\mathbf{x}_j, \mathbf{x}_i) \right] - y_i \quad (2.115)$$

Finally, the decision function output for a new sample \mathbf{x} becomes:

$$\mathbf{w}^T \varphi(\mathbf{x}) - b = \left[\sum_{i \in SV} y_i \alpha_i k(\mathbf{x}_i, \mathbf{x}) \right] - b \quad (2.116)$$

The predicted class \hat{y} corresponds to the sign of this decision function output:

$$\hat{y} = \text{sgn}(\mathbf{w}^\top \varphi(\mathbf{x}) - b) = \text{sgn} \left(\left[\sum_{i \in SV} y_i \alpha_i k(\mathbf{x}_i, \mathbf{x}) \right] - b \right) \quad (2.117)$$

Notably, in Equation 2.116, we only need to sum over the support vectors (SVs), which are the samples lying within the margin. This is because the dual coefficients α_i are zero for the other samples. This allows for more efficient computation of the decision function and classification process.

2.9.4 Support Vector Regression

A version of SVM for regression, the support vector regression (SVR), was proposed in 1996 [175]. SVR offers a robust approach to regression problems with the ability to handle nonlinear relationships between input variables and the target variable. There are three different implementations of SVR: linear SVR, ε -SVR, and ν -SVR. In this thesis, the ε -SVR model is used to train and predict the bandgap values. Therefore, in the following, I present only the formulation of this model.

Given training vectors $\mathbf{x}_i \in \mathbb{R}^p$, $i = 1, \dots, N$, and an output vector $y \in \mathbb{R}^N$, ε -SVR solves the following primal problem:

$$\begin{aligned} & \underset{\mathbf{w}, b, \xi, \xi^*}{\text{minimize}} && \frac{1}{2} \mathbf{w}^\top \mathbf{w} + C \sum_{i=1}^N (\xi_i + \xi_i^*) \\ & \text{subject to} && y_i - (\mathbf{w}^\top \varphi(\mathbf{x}_i) - b) \leq \varepsilon + \xi_i, \\ & && (\mathbf{w}^\top \varphi(\mathbf{x}_i) - b) - y_i \leq \varepsilon + \xi_i^*, \\ & && \xi_i, \xi_i^* \geq 0, \quad i = 1, \dots, N \end{aligned} \quad (2.118)$$

Here, an additional parameter ε is introduced to define the margin size around the predicted regression function. It determines the tolerance for errors in the regression model. Data points for which predictions are within the ε -tube are considered to have acceptable errors and do not contribute to the training loss function penalty. Otherwise, a penalty is added, determined by the variables ξ_i or ξ_i^* , depending on whether their predictions lie above or below the ε -tube.

The corresponding dual problem of Equation 2.118 is:

$$\begin{aligned} & \underset{\alpha, \alpha^*}{\text{minimize}} && \frac{1}{2} (\alpha - \alpha^*)^\top Q (\alpha - \alpha^*) + \varepsilon \mathbf{1}^\top (\alpha + \alpha^*) - y^\top (\alpha - \alpha^*) \\ & \text{subject to} && \mathbf{1}^\top (\alpha - \alpha^*) = 0, \quad 0 \leq \alpha, \alpha^* \leq C, \quad i = 1, \dots, N \end{aligned} \quad (2.119)$$

Where $\mathbf{1}$ represents the vector of all ones, and Q is a positive semidefinite matrix defined as $Q_{ij} \equiv k(\mathbf{x}_i, \mathbf{x}_j)$. The prediction (\hat{y}) for a new sample \mathbf{x} is then given by:

$$\hat{y} = \left[\sum_{i \in SV} (\alpha - \alpha_i^*) k(\mathbf{x}_i, \mathbf{x}) \right] - b \quad (2.120)$$

In the prediction equation (Equation 2.120), SV represents the set of support vectors. α and α_i^* are the dual coefficients. b is the offset. The α and b values are determined through the optimization process.

2.9.5 Model Performance Evaluation

The SVM model training involves learning from a labeled dataset comprising inputs (features) and corresponding correct outputs (labels). The models adjust their parameters through a loss function to minimize errors and improve accuracy. To ensure the proper training of the ML models and the comprehensiveness of the training dataset, learning curves are constructed [176, 177].

A learning curve is a representation of the relationship between a model's performance and the amount of training data it has been exposed to. It shows how the model's performance improves or stabilizes as the training dataset size increases.

A typical learning curve is constructed by plotting the performance metric, such as error rate or loss, on the y-axis against the size of the training dataset on the x-axis. The curve is generated by repeatedly training the model on different subsets of the available training data and evaluating its performance on a separate validation or test set. The training set size is incrementally increased, and the model's performance is recorded at each step. One characteristic unique to ML algorithms is that the out-of-sample error (ε) of predicted properties follows an inverse power law (decay) with training set size N [173, 176]:

$$\varepsilon \propto \frac{1}{N^b} \quad (2.121)$$

The exponent b here determines the rate at which the error decreases.

To facilitate the analysis of learning curves, it is convenient to plot them on log-log plots. The relationship between the training set size and the model's performance becomes a straight line on the log-log scale. By examining the learning curve on a log-log plot, we can easily determine the model's performance characteristics. The linear nature of the log-log plot provides a clearer understanding of the behavior of the model as the amount of training data increases.

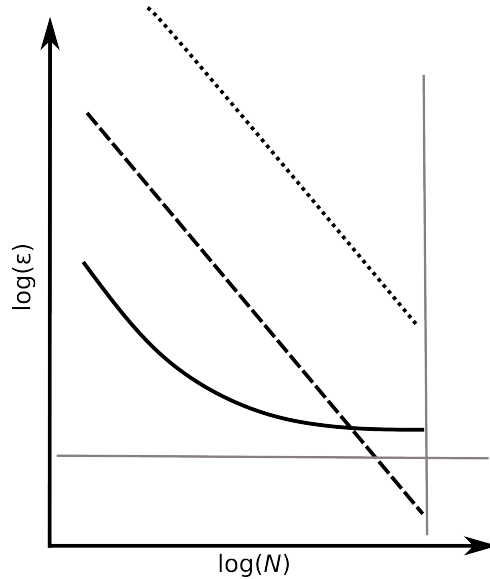


Figure 2.12: Machine learning prediction error (ε) vs training set size (N) on log–log scale. Horizontal and vertical thin lines indicate exemplary target accuracy and available training set size, respectively. The lines illustrate the performance of ML models. The solid line corresponds to a model with incomplete information, the dotted line represents a model with less physical representation, and the dashed line indicates a model with good physical representation. Figure adapted with permission from Reference [176].

Figure 2.12 illustrates a schematic of learning curves with varying model performance [176]. The dashed line represents a model that has achieved the required accuracy with the given training set size, indicating it is a good model. However, the dotted line shows a model that can still improve its performance with more data to reach the required accuracy.

The model’s performance may also saturate at a large training set size, as shown by the solid line in the figure. This decline in performance suggests that the model has already learned most of the relevant information from the data, and additional data may not significantly improve its performance.

Learning curves enable the comparison of multiple models trained on different amounts of data and help in identifying the model that performs better. They also assist us in determining the data requirements for achieving desired performance levels and optimizing resource usage.

Therefore, examining the shape and trend of the learning curves allows us to assess the models’ effectiveness, determine data requirements, make informed comparisons between different models, and provide insights into potential overfitting or underfitting issues.

Chapter 3

Methods

3.1 Density Functional Theory Setup

3.1.1 Materials Modeling

In this thesis, the binary III-V materials are modeled using primitive cells, while for ternary and quaternary materials, supercell approach is employed. Specifically, SQS supercells of size $6 \times 6 \times 6$ are used. This specific supercell size choice is based on the findings reported by Rosenow et al. [18]. Smaller SQS supercells introduce artificial interactions of the local strain fields between periodic image cells, leading to a significant underestimation of bandgap values.

Alternative methods, such as the virtual-crystal approximation (VCA) [178] and coherent-potential approximation (CPA) [178], consider only average site occupations, neglecting atomic distribution. However, studies have shown that microscopic atomic arrangements significantly affect bandgap values in such disordered alloys [18, 162, 179].

The SQS methodology, on the other hand, appropriately captures the inherent randomness in disordered materials. Moreover, the relaxation of atomic positions within the supercell effectively incorporates the influence of the local environment on the electronic properties, thereby providing a realistic representation of these materials. This approach has successfully been applied to obtain electronic and thermodynamic properties of disordered materials [18, 162, 180–184].

The SQS cells are generated using ATAT software [102, 163, 185]. For all materials, except GaAsN systems, one SQS cell is employed per composition. In the case of GaAsN, the bandgap strongly depends on specific arrangements of nitrogen atoms within the supercell, even within the SQS approach [18]. Thus, in this case, 10 SQS cells are used for each composition.

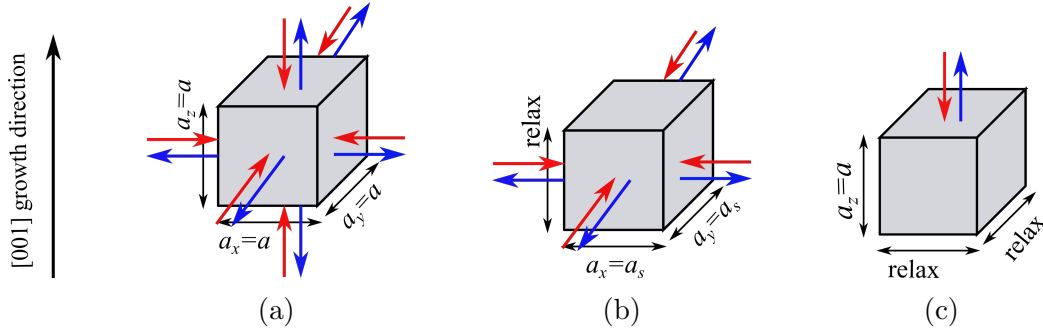


Figure 3.1: Strain models for a) isotropic strain, b) biaxial strain, and c) uniaxial strain. The blue and red arrows represent tensile and compressive strain, respectively. In the case of biaxial strain, a_s corresponds to the lattice parameter of the (epitaxial) substrate. The z -direction is defined as the epitaxial growth direction. Figures adapted from Reference [146].

3.1.2 Strain Modeling

In this thesis, uniaxial, biaxial, and isotropic strains are modeled as schematically depicted in Figure 3.1. This figure illustrates the corresponding lattice parameters that remain fixed or are allowed to relax in the modeling of different strains.

The isotropic strain is modeled by uniformly increasing or decreasing all lattice parameters (Figure 3.1a). In this case, the atomic positions of the strained structure are optimized while keeping the volume fixed. For biaxial strain, the in-plane lattice parameters are fixed to the lattice parameter of an (imaginary) substrate a_s while allowing relaxation in the growth direction (Figure 3.1b). Finally, uniaxial strain is modeled by varying the lattice parameter in the z -direction while allowing relaxation in the in-plane lattice parameters (Figure 3.1c).

These modeling approaches align well with experimental methods used to apply strain to III-V semiconductor materials. For isotropic strain, the diamond anvil cell is commonly used to simulate isotropic pressure [186–188], which corresponds to the above isotropic strain model. Biaxial strain is typically achieved through epitaxial growth [26, 35, 189, 190]. In epitaxy, the lattice parameter of the deposited layer is adjusted to match that of the substrate, resulting in a common in-plane lattice parameter parallel to the interface (Figure 1.5). The described biaxial strain model accurately captures this behavior. Notably, only the biaxial strain along [100] crystal directions is modeled here. For all the materials investigated in this thesis, this is the most common substrate orientation and growth direction in epitaxy process.

Importantly, this modeling approach considers the structural strain imposed by the substrate while disregarding the electronic influence, thus eliminating the need for explicit substrate modeling and significantly reducing computational costs. Finally, uniaxial strain, which is often achieved experimentally by applying pressure along a specific crystalline direction [191, 192], effectively aligns with the above uniaxial strain model.

It is important to note that in the above modeling approaches, no structural phase transition is assumed during the application of strain. Moreover, the analyses are specifically constrained within a strain range of 5% tensile and compressive strain for ternary and quaternary systems. This is typically the strain range achievable in epitaxial growth. Strain values beyond this range can lead to the formation of defects; however, this work does not consider the modeling of such defects.

3.1.3 Computational Setup

The DFT calculations are performed using the Vienna ab initio simulation package (VASP 5.4.4) [193–196]. The calculations employ a plane-wave basis set in conjunction with the projector-augmented wave (PAW) approach [139, 140]. To determine the appropriate \mathbf{k} -point density in the Brillouin zone and basis set energy cutoff, comprehensive and systematic convergence tests are conducted, as depicted in Figure S1 of Mondal et al. [146]. Based on the findings from these tests, a $10 \times 10 \times 10$ Γ -centered Monkhorst-Pack \mathbf{k} -point mesh [197] is utilized for calculations involving the primitive cell, and the basis set energy cutoff is chosen within the range of 450–550 eV. The convergence criteria used for electronic energy and force are 10^{-6} – 10^{-7} eV and 10^{-2} eV \AA^{-1} , respectively. The specific values of these convergence criteria can be found in the associated publications listed in the appendix of this thesis. In the case of supercells, given their large size, the reciprocal space is sampled only at the Γ -point.

The geometry optimization of the supercells is performed using the PBE functional [80], including the dispersion-correction method DFT-D3 with Becke-Johnson damping function (DFT-D3(BJ)) [160, 161]. Other approaches, such as Tkatchenko-Scheffler (TS) model [158], TS method with iterative Hirshfeld partitioning (TS/HI) [198, 199], TS with self-consistent screening (TS+SCS) [159], many-body dispersion energy method (MBD) [159, 200], improved vdw-DF method (vdw-DF2) [201] and optB88-vdw method [202], are also tested to describe dispersion interactions. However, PBE-D3(BJ) approach yielded the best agreement between the optimized and experimental lattice parameters. For comprehensive results of these tests, refer to Table S1 and Figure S2 in Mondal et al. [146].

The structure optimization process involves consecutive volume and position optimizations until convergence is achieved. Additional constrained optimizations are performed on the structures obtained from the above geometry optimization to model the different strains, as discussed in Section 3.1.2.

To calculate electronic properties such as bandgaps and bandstructures, the m-BJ functional [88] is utilized, taking into account the effect of spin-orbit coupling. For binary materials, the bandgap values and natures are calculated from the primitive bandstructures. For the ternary and quaternary materials, the bandgap values are calculated by determining the energy difference between the highest occupied VB and the lowest unoccupied CB obtained from folded bands in supercell calculations. The nature of these bandgaps is determined using the BSW-based protocol described in Section 2.8.5. The fold2Bloch program [95] is used to calculate the BSWs. The EBSs are constructed using the BandUP program [169, 170].

3.2 Machine Learning Setup

3.2.1 Model Description

In this thesis, SVM models are employed for ML predictions of bandgaps. In particular, for training and predicting bandgap values, the ε -SVR [175] model is used. To determine the nature of the bandgaps, the SVC model [173, 203] is utilized. Moreover, RBF kernel [204, 205] is applied to introduce a nonlinear transformation to the feature space. All ML algorithms are used as implemented in scikit-learn Python library [206].

3.2.2 Feature Representation

Various feature representations have been proposed for periodic solid-state systems, such as element-specific features [114, 115, 122–124, 207, 208], radial distribution functions [209], Voronoi tessellations [210], representation learning from stoichiometry [211], and property-labeled materials fragments [212]. Considering the analysis involves strained and unstrained structures, a simple descriptor consisting of composition and strain values as input features for ML training is chosen in this thesis. This choice enables faster prediction and training times compared to extensive descriptors while still providing excellent accuracy for this study.

For constructing the composition features, all III- and V-elements in the investigated material system are considered. The strain feature, on the other hand, only consists of the measurement of the considered strain.

Table 3.1: Example of machine learning dataset features for biaxially strained InGaAsPSb. The negative and positive signs in the strain values represent compressive and tensile strains, respectively.

| Sample index | Features | | | | | |
|--------------|----------|--------|--------|-------|--------|------------|
| | In (%) | Ga (%) | As (%) | P (%) | Sb (%) | Strain (%) |
| 1 | 60 | 40 | 50 | 20 | 30 | -2 |
| 2 | 10 | 90 | 1 | 80 | 19 | 5 |

Sample 1: $\text{In}_{60}\text{Ga}_{40}\text{As}_{50}\text{P}_{20}\text{Sb}_{30}$, 2.0% biaxial compressive strain

Sample 2: $\text{In}_{10}\text{Ga}_{90}\text{As}_1\text{P}_{80}\text{Sb}_{19}$, 5.0% biaxial tensile strain

Table 3.2: Machine learning dataset features and labels of biaxially strained GaAsPSb. The negative and positive signs in the strain values indicate the compressive and tensile strains, respectively. Table adapted from Reference [213].

| Sample index | Features | | | | Labels | |
|--------------|----------|-------|--------|------------|--------------|----------|
| | As (%) | P (%) | Sb (%) | Strain (%) | Bandgap (eV) | Nature |
| 1 | 25 | 25 | 50 | 3.0 | 0.629 | direct |
| 2 | 50 | 50 | 0 | -5.0 | 1.243 | indirect |

Sample 1: $\text{Ga}_{100}\text{As}_{25}\text{P}_{25}\text{Sb}_{50}$, 3.0% biaxial tensile strain

Sample 2: $\text{Ga}_{100}\text{As}_{50}\text{P}_{50}\text{Sb}_0$, 5.0% biaxial compressively strain

Table 3.1 provides an example of the feature space for biaxially strained InGaAsPSb compounds. However, it is important to note that the composition features can be reduced when dealing with specific systems. For instance, Table 3.2 illustrates the case of GaAsPSb. In this case, the number of compositional degrees of freedom is three (x , y , and z in $\text{Ga}_{100}\text{As}_x\text{P}_y\text{Sb}_z$). Since the group III site in the lattice is occupied by only one type of element (Ga), it is excluded from the feature vector. Although only x and y are independent compositional degrees of freedom and z can be deduced from x and y ($z = 100 - x - y$), including z in the feature vector ensures the model learns this constraint. With the strain feature, the final feature space is thus four-dimensional in this case. The labels of the ML data in this study consist of the bandgap values and natures obtained from DFT calculations.

Notably, the composition and strain exhibit varying orders of magnitude in variance. Therefore, prior to training the models, the input data are standardized using the StandardScaler class from scikit-learn. Additionally, the bandgap natures, classified as direct and indirect in Table 3.2, are transformed to binary labels, 1 and 0.

3.2.3 Performance Evaluation Metrics

The prediction accuracies of the SVR models are evaluated using several performance metrics, including root-mean-squared error (RMSE), mean absolute error (MAE), maximum error (Max error), and the coefficient of determination (R^2). In the case of SVC models, accuracy-score and balanced-accuracy-score metrics are used. During the hyperparameter optimization of SVR and SVC models, the RMSE and accuracy-score scoring functions are employed, respectively.

It is worth noting that some SVR models predict small negative direct bandgap values (up to -5 meV). However, the studies in this thesis do not consider possible physical effects that could lead to negative direct bandgaps, such as topological band inversion. Consequently, any ML-predicted negative bandgap values are shifted to 0 eV.

3.2.4 Hyperparameter Optimization

Choosing appropriate hyperparameters is crucial for achieving optimal performance and accuracy in the SVM model. To achieve the best hyperparameter settings, a random search over a large number of combinations of hyperparameters, C and γ are conducted. The ML models are trained at each combination of the C and γ values with 5-fold cross-validation. The model with the highest cross-validation score is selected as the final model with the best set of hyperparameters. For SVR models, the ε hyperparameter values are additionally optimized. Throughout, the ranges of the hyperparameter optimization space are carefully fine-tuned to ensure that the selected ranges are comprehensive and capable of capturing the best possible settings for the hyperparameters. To streamline the hyperparameter optimization process, the `RandomizedSearchCV` module from the `scikit-learn` library is utilized.

3.2.5 Model Training

To ensure the proper training of the ML models and the comprehensiveness of the training set, learning curves are constructed. For this purpose, a test set comprising random 25% of the total input dataset is created. The remaining 75% of the data is used to create the training set, with the set size consecutively increasing from 1% up to 75%. This process is repeated multiple times to improve the robustness of the predictions [214]. The train-test splittings are performed using 5-fold `ShuffleSplit` from the `scikit-learn` library. For each ML model training, hyperparameters are re-optimized to ensure optimal performance.

Chapter 4

Results

This chapter presents an overview of the key findings of the thesis. For further reference and detailed discussions, the reprints of the referenced publications are included at the end of the thesis.

4.1 Binary III-V systems

For all the binary III-V compounds, GaP, GaAs, GaSb, InP, InAs, InSb, and Si, the primitive cells are optimized and the bandgaps are calculated following the DFT methodology described in Section 3.1. Notably, this thesis focuses exclusively on materials with zincblende crystal structures. Therefore, compounds such as GaN and InN, which possess wurtzite structures, are excluded from the analysis. Additionally, GaBi and InBi compounds are not included in this study due to their metallic nature.

The optimized lattice parameters of the unstrained compounds from the PBE-D3(BJ) functional agree well with the experiments, with a maximum deviation of only 0.09 Å or 1.3% across the materials. The deviation in the m-BJ calculated bandgap values for these unstrained systems ranges between 20 meV to 50 meV, except for the antimonide systems GaSb and InSb, where the deviation is about 200 meV. The excellent agreement between the experimental and calculated values for both the lattice parameters and bandgaps validates the accuracy of the employed DFT scheme, including the chosen functionals and well-converged computational setups.

Subsequently, constrained optimizations are performed to simulate strain in the systems using the strain models and methodology outlined in Section 3.1.2. The applied strain in the calculations ranges from 10% tensile to 10% compressive. This is in the order of magnitude of pressures (10 to several 100 GPa) achievable in modern experiments [215–222].

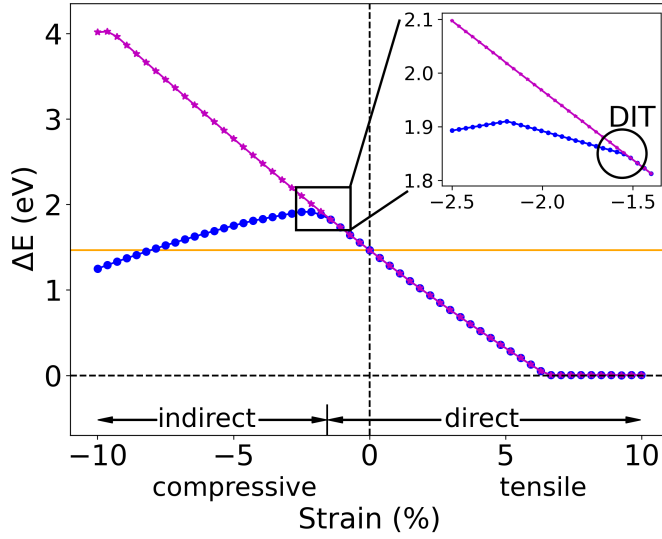


Figure 4.1: Variation of bandgap in isotropically strained GaAs. The positive and negative signs in strain values indicate tensile and compressive strains, respectively. The ΔE_{Γ} (magenta), E_g (blue), and the direct-indirect transition (DIT) are shown. The solid orange line indicates E_g for the unstrained structure (1.47 eV). The strain range where bandgaps are direct and indirect is indicated. The inset shows the region of the DIT with a finer grid of strain calculations. Figure adapted from Reference [146].

Figure 4.1 shows the variation of the energy difference between the CB and the VB at the Γ point (ΔE_{Γ}), as well as the bandgap value (E_g), as a function of isotropic strain in GaAs. For a direct bandgap, both ΔE_{Γ} and E_g have the same value. On the contrary, if the E_g value is smaller than ΔE_{Γ} , that indicates an indirect bandgap.

From the figure, it is clear that when subjected to tensile strain, the bandgap remains direct throughout, as the E_g curve coincides with the ΔE_{Γ} curve. However, under compressive strain, the E_g curve initially overlaps with the ΔE_{Γ} curve until -1.56% strain, where the two curves separate. After this strain, the E_g values are smaller than ΔE_{Γ} values, indicating a transition to indirect bandgap in this region. The strain value where the two curves start deviating marks a direct-indirect transition (DIT) in the bandgap nature. Therefore, a DIT is found in GaAs at -1.56% isotropic strain. The calculated DIT value agrees closely with the experimental value of -2.75% [223], deviating by only 1.19% strain.

Furthermore, the bandstructures for GaAs are calculated at each strain value. Figure 4.2 shows the bandstructures at three different strain values.

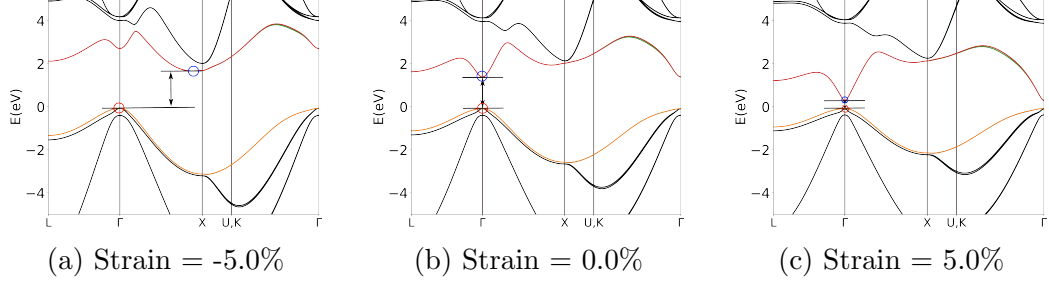


Figure 4.2: Three snapshots of GaAs bandstructure under isotropic strain. The positive and negative signs in strain values indicate tensile and compressive strains, respectively. The bandgaps are indicated by arrows. The VBM positions are shown in red circles. The blue circles indicate the positions of CBM. Figure adapted from Reference [146].

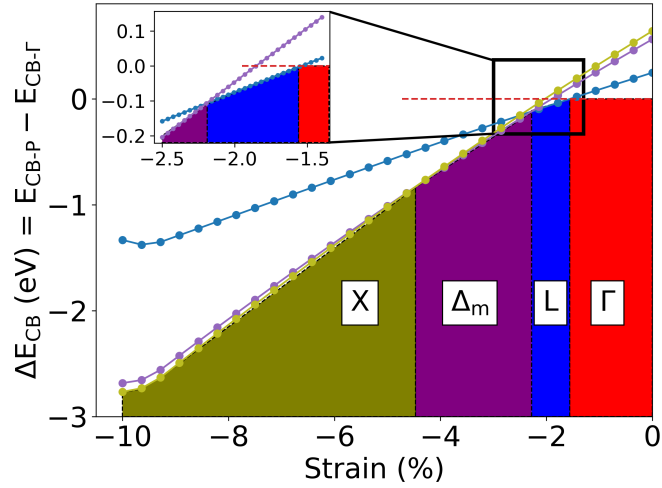


Figure 4.3: Difference between CB energies at the Γ point and other k-points P ($\Delta E_{CB} = E_{CB-P} - E_{CB-\Gamma}$; with P = Γ , L, Δ_m , and X) for isotropically strained GaAs. The negative strains indicate compressive strains. Colored areas indicate at which k-point we find the CBM for the given value of compressive strain. Figure reprinted from Reference [146].

The bandstructures reveal that the VBM is consistently located at the Γ -point across the investigated strain regimes. However, the position of the CBM changes in \mathbf{k} -space when compressive strain is applied, leading to the direct-indirect transition. In the case of tensile strain, the CBM remains at the Γ -point throughout, and only the VBM-CBM gap closes.

Additionally, by analyzing the variation of band energies at different \mathbf{k} -points, it is observed that under compressive strain, the CBM occurs at four high-symmetry \mathbf{k} -points in reciprocal space: Γ , L, near X (referred to as Δ_m), and X points. Comparing the energy differences at these points provides further insights. As shown in Figure 4.3, without strain (0% strain), the CBM is located at the Γ -point. As the strain reaches -1.56% strain, the CBM shifts from Γ to L, marking the DIT point. Subsequently, with increasing strain beyond -2.28% , the CBM shifts to Δ_m , and ultimately to the X-point at -4.47% strain.

The analyses presented above are also applied successfully to other types of strain, including biaxial and uniaxial, as well as to the other mentioned materials. Notably, under isotropic strain application, a transition from an indirect to a direct bandgap is observed for GaP and Si. The calculated transition points, such as the DIT, exhibit good agreement with experimental results. For more comprehensive findings and detailed discussions, refer to the attached first scientific contribution at the end of this thesis [146].

4.2 Ternary III-V systems

Unlike binary III-V compounds, ternary materials exhibit compositional variations. For example, in GaAsP, the group III sites contain only Ga, while the group V sites are occupied by either As or P. This can be represented as $\text{Ga}_{100}\text{As}_{100-x}\text{P}_x$, where the composition x ranges from 0 to 100%. To model these compositions, SQS supercells are utilized. The strain modeling and DFT setups follow the same as described in the previous section. Additionally, the bandgap properties from supercell calculations are determined using the Bloch spectral-based protocol outlined in Section 2.8.5.

The ternary compounds analyzed in this thesis include GaAsP, GaAsN, GaPSb, GaAsSb, GaPBi, and GaAsBi. In the case of GaAsN, the investigation is limited to nitrogen concentrations up to 12%. Higher concentrations of nitrogen, especially under large compressive strain, require larger supercells than the chosen size of $6 \times 6 \times 6$ to avoid unphysical electronic interactions between nitrogen atoms and their periodic images [18]. Similarly, for the bismides GaPBi and GaAsBi, up to 15% bismuth fraction is investigated. These compounds become metallic at higher bismuth fractions.

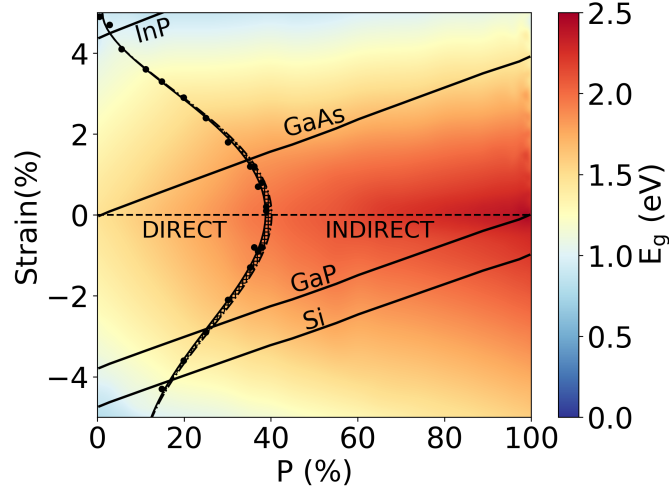


Figure 4.4: Variation of bandgap in GaAsP as a function of composition and biaxial strain. The dashed black horizontal line indicates unstrained GaAsP. The black circles are the calculated DIT points. The DIT points are fitted with a 5th-order polynomial. The labels ‘direct’ and ‘indirect’ indicate the enclosed regions, with the nature of bandgap being direct and indirect, respectively. The hatched pattern region is the ‘partially direct’ bandgap region. Solid black lines indicate the substrate lines under biaxial strain model. Figure reprinted with permission from Reference [171].

Figure 4.4 shows the variation of bandgaps (values and natures) in biaxially strained GaAsP as a function of composition and strain. The strain values range from 5% tensile to 5% compressive strain. The bandgap values are represented by the color scale. The bandgap natures are indicated by enclosed areas labeled as ‘direct’ and ‘indirect’. The black curve represents the DIT line, which separates the bandgap into different regions or phases based on their nature. This representation of composition, strain, and bandgap relationship resembles the phase diagrams commonly used in material science. In this thesis, it is referred to as the “bandgap phase diagram”.

Additionally, the influence of substrates in the epitaxy process is investigated within the biaxial strain model. Each solid line in the figure corresponds to a specific substrate: GaAs, GaP, InP, or Si. These lines represent the amount of biaxial strain that would be induced in the GaAsP layer when it is epitaxially grown on the respective substrates. For example, when growing GaAsP with 100% phosphorus on a GaP substrate, the strain is zero. However, growing GaAs (0% phosphorus) on GaP would result in 3.8% in-plane compressive strain.

Several design strategies are proposed utilizing the bandgap phase diagram as a tool to optimize material selection for specific applications, as illustrated in Figure 4.5.

Figure 4.5a showcases an example of a quantum-well heterostructure (QWH) construction for optoelectronic applications using biaxially strained GaAsP on a GaAs substrate. In this case, as the quantum-well layers are made out of a single material with varied composition only, the epitaxial growth could be performed efficiently. The bandgap phase diagram highlights the compositional phase space where GaAsP achieves a direct bandgap (phosphorus content less than 34%), making it suitable for this application. Higher phosphorus content results in indirect bandgaps, making them unsuitable for this target application.

Figure 4.5b presents an efficient approach for the monolithic integration of multiple QWHs to construct multijunction photovoltaics. In this case, the QWHs are separated by thin indirect bandgap layers of the same material as the QWH but only with a different composition. This would make the integration approach efficient, as no sample transfer is required during the growth process.

In Figure 4.5c, a device with a gradual change in bandgap properties is proposed. The concept leverages the continuous transition in the nature of the bandgap with alloy concentration in the vicinity of the DIT region. By selecting an appropriate range of phosphorus concentration, a GaAsP epitaxial layer can be grown on GaP, with the phosphorus concentration continuously changing from the direct to the indirect bandgap region or vice versa. This enables changes in both the values and nature of the bandgap. Notably, the concentration gradient can be implemented in both the horizontal and vertical directions.

Figure 4.5d demonstrates another application where the choice of the substrate allows tuning the epitaxial layer's bandgap to exhibit either a direct or indirect nature. Depending on the substrate used, GaAs or Si, a specific GaAsP composition indicated by the vertical line will display a direct or indirect bandgap, respectively.

These illustrations highlight how the appropriate selection of substrate, combined with specific compositions, can be used to tune the bandgap values and nature over a wide range. The bandgap phase diagram, in this regard, serves as a valuable tool for efficiently and accurately making these choices.

Finally, note that in this section, only the results for the biaxially strained GaAsP compound are presented. The analysis of other compounds and strain types can be found in the second scientific contribution at the end of this thesis [171].

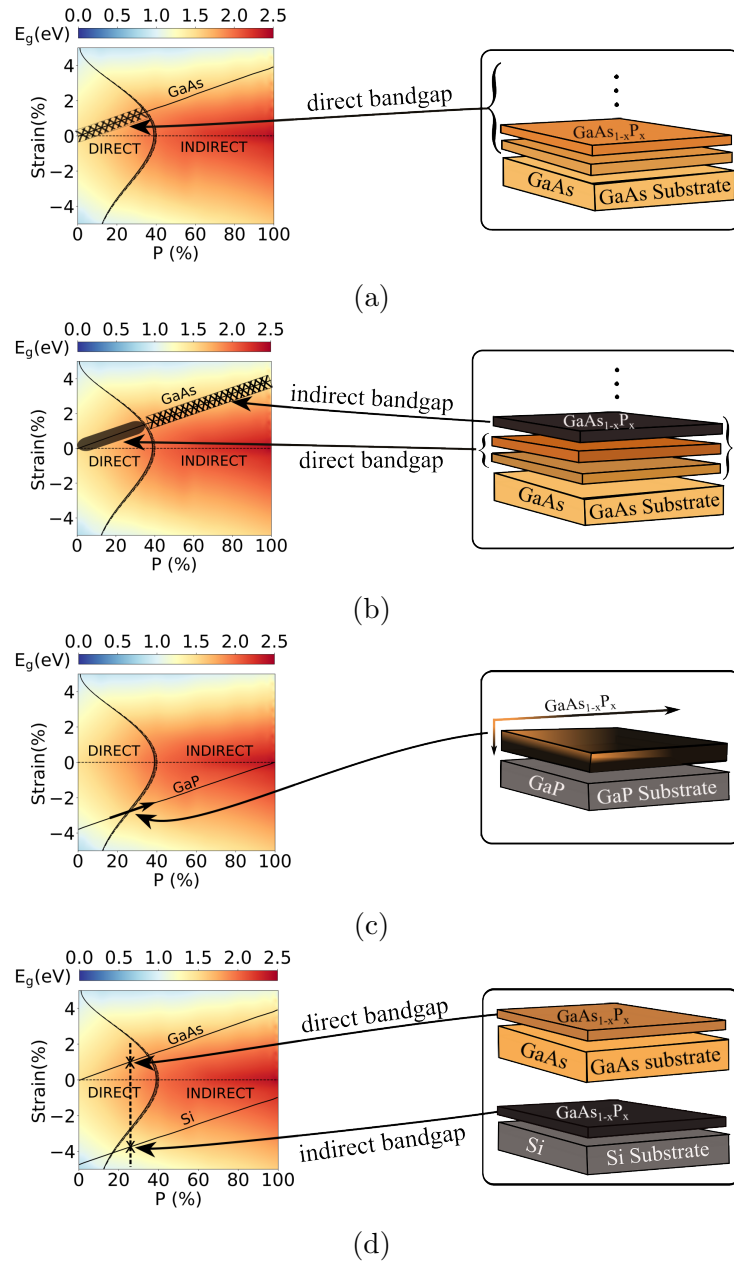


Figure 4.5: Illustration of the application of biaxially strained GaAsP bandgap phase diagram. a) Determining the composition range for creating an optically active QWH of GaAsP on a GaAs substrate. b) Designing a multijunction photovoltaic with successive direct and indirect bandgap cells. c) Modulating the bandgap properties by adjusting the composition near the transition point. d) Tuning the bandgap nature by altering the substrate. Figure reprinted with permission from Reference [171].

4.3 Quaternary III-V systems

This section demonstrates the integration of the ML approach into the DFT approach. The DFT methodologies follow the same as described in the earlier sections. The ML models consist of SVC and SVR models to predict the bandgap nature and bandgap values, respectively. The results presented in this section specifically focus on the biaxially strained GaAsPSb system. The ML models are trained and tested on a comprehensive DFT dataset comprising 4280 data points covering the entire composition range of the GaAsPSb system (As, P, Sb = 0–100%) and biaxial strain values ranging from 5% compressive to 5% tensile strain.

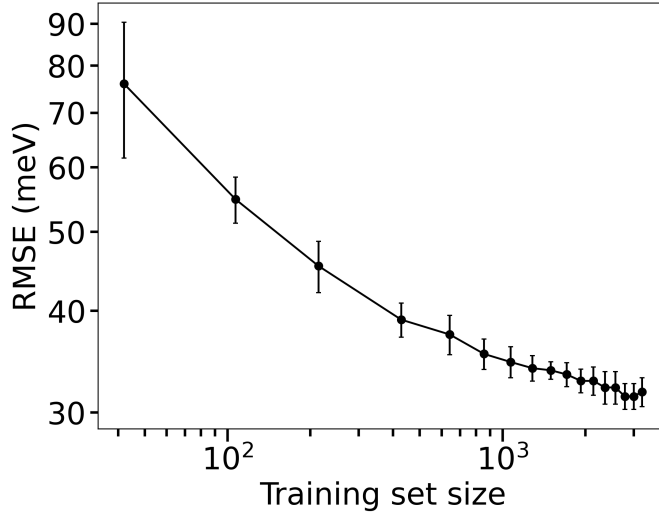


Figure 4.6: Learning curve of SVR model for GaAsPSb, in log–log scale. The plot depicts the RMSE of bandgap value prediction for the test set as a function of the training set size. The error bars represent the standard deviations over five trials. Figure reprinted from Reference [213].

Figure 4.6 shows the learning curve, depicting the dependence of SVR model performance on the size of the training set. The log-log plot exhibits a high degree of linearity, indicating the successful learning of the model. Similar learning curves for the SVC model performance for bandgap nature predictions can be found in Figure 1 of Reference [213]. Notably, the performance of the ML models only marginally improves for training set sizes larger than 1000 (see Figure 4.6). Detail analysis (refer to Figure S4 in Reference [213]) reveals that this performance saturation occurs as the models reach their optimal performance limit.

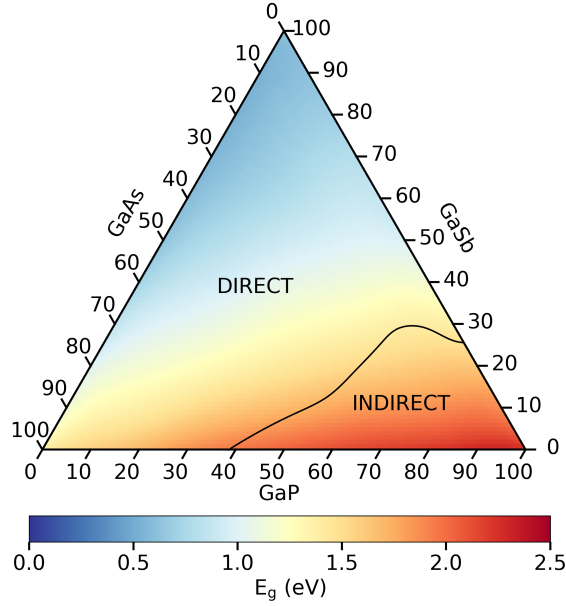


Figure 4.7: Variation of bandgap values (E_g) for unstrained GaAsPSb (0.0% strain). The labels ‘direct’ and ‘indirect’ indicate the enclosed regions, with the nature of bandgap being direct and indirect, respectively. Figure reprinted from Reference [213].

With the largest training set (the last point in Figure 4.6), the SVR models achieve an RMSE of $31(\pm 1)$ meV for bandgap value predictions on the test set. For the bandgap nature predictions with the SVC models, the accuracy is $94(\pm 1)\%$. These errors in bandgap predictions are well within the uncertainty range of the most accurate DFT methods. Consequently, these ML models are employed for predictions in the following analysis.

Figure 4.7 presents the bandgap phase diagram of unstrained GaAsPSb, constructed using the trained ML models mentioned above. The color scale represents the predicted bandgap values. The black curve represents the DIT line, distinguishing regions with direct and indirect bandgaps. The plotted bandgap values are the averages over five predictions, and the bandgap natures correspond to the most frequent outcome over five predictions. Notably, the high antimony content region exhibits direct bandgaps with relatively small bandgap values, while with the high phosphorus content, the bandgap values are the largest and of indirect nature.

The study also investigates the effect of different substrates on the bandgap of GaAsPSb layer in epitaxial growth. For more detailed bandgap phase diagrams with other strain values and an extensive analysis of the substrate effects, refer to the third scientific contribution at the end of this thesis [213].

It should be emphasized that relying on a simple bowing model for bandgap variation [224] in such multinary compounds would require an extensive number of bowing parameters for composition and strains. The specific GaAsPSb system investigated here also lacks extensive experimental data and, thus, the available bowing parameters. Moreover, the variation of bandgap values under strain for various III-V compositions often deviates from the simple quadratic dependence expected from a bowing model [146], and they lack information about the bandgap nature.

The training process for the ML models takes only a few minutes (6-core CPU). Once the training is complete, the models can swiftly predict bandgap properties across the entire composition and strain ranges, typically within a few seconds. Therefore, the developed ML models, while being simple, highly efficient, and accurate, are of significant importance for the accurate determination of bandgap values and natures in these compounds.

It is also important to note that the specific ML models trained here are limited to the selected elements and strain type only. However, as discussed in Section 3.2.2, the descriptor can be extended to encompass all possible chemical elements and strain types, allowing the universal application of the developed ML approach.

Chapter 5

Summary

This thesis presents a comprehensive computational approach that combines density functional theory (DFT) and machine learning (ML) to accurately predict bandgaps in III-V compound semiconductor materials, with a particular focus on strained systems. Throughout the study, computational results are rigorously validated against experimental findings, ensuring the reliability and accuracy of the approach.

First, a DFT-based first-principles methodology is established that accurately predicts bandgaps in strained binary III-V materials (Section 4.1). The study covers a range of materials, including GaAs, GaP, GaSb, InP, InAs, InSb, and Si. These materials not only have a broad range of applications in the field of (opto-)electronics but are of great interest for fundamental research as well. A reliable strain model is developed within the DFT framework to simulate experimental strain application techniques. Subsequently, it is demonstrated that the modified Becke-Johnson (m-BJ) functional, known for its highly efficient and accurate bandgap predictions in unstrained III-V materials, can also effectively predict bandgaps in strained systems. By utilizing the m-BJ functional and developed strain modeling, the strain-induced variations in bandgaps for the aforementioned binary III-V compounds are successfully calculated across a wide range of compressive and tensile strains (up to 10% strain). The investigation reveals that not only do the bandgap values change under strain, but the nature of the bandgap itself can transition from direct to indirect or vice versa. The direct-indirect transitions for all the materials studied are successfully determined.

Furthermore, the critical analysis of the bandstructures of these materials under strain reveals that the valence band maximum (VBM) remains at the Γ -point throughout the applied strain regimes while the conduction band minimum (CBM) shifts positions. The analysis identifies four specific \mathbf{k} -points (namely, Γ , L, Δ_m , and X) that play a crucial role in these transitions.

This work lays the foundation for predictive DFT modeling of bandgap properties in strained III-V systems, encompassing the selection of appropriate DFT functionals, modeling strain applications, and other necessary computational setups to produce reliable and accurate results. It is important to note that the successful application of the m-BJ functional in the strained system in this work is particularly significant. It provides an accurate means to estimate bandgap values that are comparable to more computationally expensive methods, such as hybrid functional or GW methods, but at a moderate computational cost. As a result, it becomes feasible to utilize this functional for large-scale systems where the mentioned higher-level methods would be impractical. This opens up possibilities for exploring the bandgap properties in multinary III-V compound semiconductors under strain.

Next, the approach is extended to the higher-order ternary systems (Section 4.2). The specific systems investigated here include GaAsP, GaAsN, GaPSb, GaAsSb, GaPBi, and GaAsBi, all of which have significant applications in semiconductor-based devices. Unlike binary systems, where primitive cells are sufficient for DFT calculations, ternary systems are modeled using special quasi-random structure (SQS) supercells, resulting in band folding. This presents a challenge in determining bandgap properties within the supercell approach. Specifically, in the folded bands from supercell calculations, the primitive Bloch characters are mixed up, which hinders the determination of bandgap nature. One potential solution to this problem is to use effective bandstructure (EBS). However, constructing EBS for numerous materials is impractical. Nevertheless, the examination of EBSs for a few selected strain values in different ternary compounds reveals similar findings as to the binary compounds, that the VBM remains at the Γ point consistently, while only the CBM changes its position under strain. This shows that only a few specific \mathbf{k} -points in reciprocal space exclusively determine the bandgap nature in ternary III-V semiconductors under various strains. Based on these observations, an efficient approach is developed to determine the bandgap natures from supercell calculation. This approach utilizes the Bloch spectral weights of only the conduction band at a few specific \mathbf{k} -points, enabling the determination of bandgap nature efficiently for a large number of bandgap calculations without the need to construct the complete EBS.

The combination of the m-BJ functional and the newly devised bandgap nature determination protocol from supercell calculations enables efficient determination of complete bandgap properties (value and nature) in ternary III-V semiconductors. Following this approach, the bandgaps of the aforementioned ternary materials are mapped throughout their entire composition range ($x = 0-100\%$ for $\text{Ga}_{100-x}\text{E}_x\text{Y}_{100-x}$ with E, Y = As, P, Sb, Bi) and across a wide range of strain values (up to 5% strain).

Moreover, the practical implications of this comprehensive composition-strain-bandgap relationship mapping in III-V materials, referred to as the “bandgap phase diagram”, are demonstrated in optimizing material combinations for various applications. These bandgap phase diagrams provide valuable insights to select materials with desired bandgap properties, thereby enhancing the performance and functionality of target devices.

Importantly, the bandgap nature determination protocol developed in this work also applies to further higher-order III-V systems, such as quaternary and beyond. With this work, the ultimate groundwork for the predictive DFT-based first-principles modeling of bandgap properties in strained multi-ternary III-V semiconductor systems is established.

However, applying the above DFT approach to higher-order systems, such as quaternary compounds, poses limitations. Despite its efficiency, the substantial number of DFT calculations needed in those systems (\sim millions) enormously increases the computational cost. Consequently, the comprehensive mapping of the bandgaps over the extensive composition-strain space in higher-order systems becomes limited.

To overcome this limitation, a support vector machine (SVM) ML model is developed to complement the standalone DFT approach (Section 4.3). By integrating ML with DFT, the number of DFT calculations required (\sim thousands) is significantly reduced, by a factor of 1000, while maintaining the high accuracy of the predictions. This DFT-ML hybrid computational approach finally enables comprehensive mapping of bandgap values and natures (direct or indirect) in multi-ternary III-V semiconductor systems. It significantly enhances sampling efficiency across the extensive composition-strain space in these systems, which would otherwise be impractical to cover solely with standalone DFT approach.

In particular, by utilizing this DFT-ML hybrid approach, the bandgap phase diagram for GaAsPSb compound is constructed over its entire composition range (As, P, Sb = 0–100%) and covering a wide range of strain values (up to 5% strain). Although this specific quaternary III-V compound has not been extensively studied, its binary and ternary subsystems (GaAs, GaP, GaSb, GaAsP, GaAsSb, and GaPSb), as mentioned above, are important. Moreover, this theoretical analysis will offer valuable insights for future experimental exploration of this material system.

Notably, the presented DFT-ML hybrid computational approach can be easily generalized to other III-V semiconductors and material classes, enabling the rapid estimation of bandgaps for a broad range of materials and strain values. This virtual high-throughput screening capability thus holds significant potential for facilitating the exploration and discovery of new semiconductor materials for (opto-)electronic applications.

In conclusion, this thesis establishes a comprehensive and efficient computational approach for predicting bandgaps in strained III-V semiconductor materials. By combining DFT and ML, a cost-effective protocol for accurate bandgap predictions in those systems is achieved. Valuable insights into bandgap tuning for several III-V materials under strain are provided through the construction of bandgap phase diagrams, facilitating the optimization of material combinations for various III-V semiconductor material-based device applications. The DFT-ML hybrid computational protocol developed can be extended to explore a wide range of multinary III-V materials and beyond. This computational materials design approach thus paves the way for the development of novel strain-engineered semiconductor materials with tailored bandgap characteristics.

Zusammenfassung

In dieser Dissertation wird ein umfassender computergestützter Ansatz vorgestellt, der Dichtefunktionaltheorie (DFT) und maschinelles Lernen (ML) kombiniert, um Bandlücken in III-V-Halbleitermaterialien genau vorherzusagen, wobei ein besonderer Schwerpunkt auf gespannten Systemen liegt. Während der gesamten Studie werden die berechneten Ergebnisse rigoros anhand experimenteller Ergebnisse validiert, um die Zuverlässigkeit und Genauigkeit des Ansatzes zu gewährleisten.

Zunächst wird eine DFT-basierte first-principles Methode entwickelt, die Bandlücken in gespannten binären III-V-Materialien genau vorhersagt (Abschnitt 4.1). Die Studie deckt eine Reihe von Materialien ab, darunter GaAs, GaP, GaSb, InP, InAs, InSb und Si. Diese Materialien haben nicht nur eine breite Palette von Anwendungen im Bereich der (Opto-)Elektronik, sondern sind auch für die Grundlagenforschung von großem Interesse. Es wird ein zuverlässiges Spannungsmodell im Rahmen der DFT-Rechnungen entwickelt, um experimentelle Methoden, bei der es zu Spannungen im Material kommt, zu simulieren. Anschließend wird gezeigt, dass das modifizierte Becke-Johnson (m-BJ) Funktional, welches für seine hocheffizienten und genauen Bandlückenvorhersagen in ungespannten III-V-Materialien bekannt ist, auch effektiv Bandlücken in gespannten Systemen vorhersagen kann. Unter Verwendung des m-BJ Funktionals und des entwickelten Spannungsmodells werden die spannungsinduzierten Variationen der Bandlücken für die oben genannten binären III-V-Verbindungen über einen breiten Bereich von Druck- und Zugspannung (bis zu 10% Spannung) erfolgreich berechnet. Die Untersuchung zeigt, dass sich nicht nur die Werte der Bandlücken unter Spannung ändern, sondern auch die Art der Bandlücke von direkt zu indirekt oder umgekehrt übergehen kann. Die direkt-indirekt Übergänge werden für alle untersuchten Materialien erfolgreich bestimmt.

Darüber hinaus zeigt die kritische Analyse der Bandstrukturen dieser gespannten Materialien, dass die Valenzbandmaximum (VBM) im gesamten verwendeten Spannungsbereich am Γ -Punkt verbleiben, während die Leitungsbandminimum (CBM) ihre Position verschieben. Die Analyse identi-

fiziert vier spezifische \mathbf{k} -Punkte (nämlich Γ , L, Δ_m und X), die bei diesen Übergängen eine entscheidende Rolle spielen.

Diese Arbeit legt den Grundstein für die vorhersagende DFT-Modellierung von Bandlückeneigenschaften in gespannten III-V-Systemen, einschließlich der Auswahl geeigneter DFT-Funktionale, die Modellierung von Spannungsanwendungen sowie andere notwendige Berechnungseinstellungen, um zuverlässige und genaue Ergebnisse zu erzielen. Es ist wichtig darauf hinzuweisen, dass die erfolgreiche Anwendung des m-BJ Funktionals in dem gespannten System in dieser Arbeit besonders wichtig ist. Sie bietet ein genaues Mittel zur Abschätzung von Bandlückenwerten, welche mit rechenaufwändigeren Methoden wie Hybridfunktionalen oder GW-Methoden vergleichbar sind, jedoch zu moderaten Rechenkosten. Dadurch wird es möglich, dieses Funktional für große Systeme zu verwenden, bei denen die genannten komplexeren Methoden unpraktisch wären. Dies eröffnet Möglichkeiten zur Erforschung der Bandlückeneigenschaften in multinären III-V-Halbleitern unter Spannung.

Anschließend wird der Ansatz auf ternäre Systeme ausgedehnt (Abschnitt 4.2). Zu den hier untersuchten Systemen gehören GaAsP, GaAsN, GaPSb, GaAsSb, GaPBi und GaAsBi, die alle wichtige Anwendungen in Halbleiterbauelementen haben. Im Gegensatz zu den binären Systemen, bei denen primitive Einheitszellen für DFT-Berechnungen ausreichen, werden die ternären Systeme durch Superzellen mit einer besonderen quasi-zufälligen Struktur (SQS) modelliert, was zu einer Bandfaltung führt. Dies stellt eine Herausforderung bei der Bestimmung der Bandlückeneigenschaften im Rahmen dieses Superzellenansatzes dar. Insbesondere werden in den gefalteten Bändern aus Superzellenberechnungen die primitiven Bloch-Charakteristika durcheinandergebracht, was die Bestimmung der Art der Bandlücke verkompliziert. Eine mögliche Lösung für dieses Problem ist die Verwendung der effektiven Bandstruktur (EBS). Die Konstruktion von EBS für zahlreiche Materialien ist jedoch unpraktisch. Dennoch zeigt die Untersuchung der EBS für einige ausgewählte Spannungswerte in verschiedenen ternären Verbindungen ähnliche Ergebnisse wie bei den binären Verbindungen, nämlich dass die VBM durchweg am Γ -Punkt bleiben, während nur die CBM ihre Positionen unter Spannung ändern. Dies zeigt, dass nur wenige spezifische \mathbf{k} -Punkte im reziproken Raum die Art der Bandlücke in ternären III-V-Halbleitern unter verschiedenen Spannungen bestimmen. Auf Grundlage dieser Beobachtungen wird ein effizienter Ansatz entwickelt, um die Art der Bandlücke anhand von Superzellenberechnungen zu bestimmen. Dieser Ansatz nutzt die Bloch-Spektralwichtungen des Leitungsbandes an einigen spezifischen \mathbf{k} -Punkten und ermöglicht die effiziente Bestimmung der Art der Bandlücke für eine große Anzahl von Bandlückenberechnungen, ohne dass die vollständige EBS

konstruiert werden muss.

Die Kombination aus dem m-BJ Funktional und dem neu entwickelten Protokoll zur Bestimmung der Art der Bandlücke aus Superzellenrechnungen ermöglicht eine effiziente Bestimmung der vollständigen Bandlückeneigenschaften (Wert und Art) in ternären III-V-Halbleitern. Mit diesem Ansatz werden die Bandlücken der oben genannten ternären Materialien über ihren gesamten Zusammensetzungsbereich ($x = 0\text{--}100\%$ für $\text{Ga}_{100-x}\text{E}_x\text{Y}_{100-x}$ mit E, Y = As, P, Sb, Bi) und über einen breiten Bereich von Spannungswerten (bis zu 5% Spannung) abgebildet.

Darüber hinaus werden die praktischen Auswirkungen dieser umfassenden Abbildung der Zusammensetzung-Spannung-Bandlücken Beziehung in III-V-Materialien, die als "Bandlücken-Phasendiagramm" bezeichnet wird, bei der Optimierung von Materialkombinationen für verschiedene Anwendungen demonstriert. Diese Bandlücken-Phasendiagramme liefern wertvolle Erkenntnisse für die Auswahl von Materialien mit den gewünschten Bandlückeneigenschaften, wodurch die Leistung und Funktionalität der Zielgeräte verbessert wird.

Wichtig ist, dass das in dieser Arbeit entwickelte Protokoll zur Bestimmung der Bandlücke auch für weitere III-V-Systeme höherer Ordnung, wie beispielsweise quaternäre und darüber hinaus, gilt. Mit dieser Arbeit wird die ultimative Grundlage für die vorhersagende DFT-basierte first-principles Modellierung von Bandlückeneigenschaften in gespannten multinären III-V-Halbleitersystemen geschaffen.

Die Anwendung des oben genannten DFT-Ansatzes auf Systeme höherer Ordnung, wie z. B. quaternäre Verbindungen, bringt jedoch Einschränkungen mit sich. Trotz seiner Effizienz erhöht die beträchtliche Anzahl von DFT-Berechnungen, die für diese Systeme erforderlich sind (\sim Millionen), die Rechenkosten enorm. Infolgedessen ist die umfassende Abbildung der Bandlücken über den umfangreichen Raum von Zusammensetzung und Spannungen in Systemen höherer Ordnung begrenzt.

Um diese Einschränkung zu überwinden, wird ein Support-Vektor-Maschine (SVM) ML-Modell entwickelt, das den eigenständigen DFT-Ansatz ergänzt (Abschnitt 4.3). Durch die Integration von ML und DFT wird die Anzahl der erforderlichen DFT-Berechnungen (\sim Tausende) um einen Faktor von 1000 reduziert, wobei die hohe Genauigkeit der Vorhersagen erhalten bleibt. Dieser hybride DFT-ML-Berechnungsansatz ermöglicht schließlich eine umfassende Abbildung der Bandlückenwerte und art (direkt oder indirekt) in multinären III-V-Halbleitersystemen. Er verbessert die Effizienz der Probenahme im umfangreichen Raum der Zusammensetzungen und Spannungen in diesen Systemen erheblich, der andernfalls mit einem alleinigen DFT-Ansatz nicht abgedeckt werden könnte.

Insbesondere wird mit Hilfe dieses DFT-ML-Hybridansatzes das Bandlücken-Phasendiagramm für die GaAsPSb-Verbindung über den gesamten Zusammensetzungsbereich (As, P, Sb = 0–100%) und über einen großen Bereich von Spannungswerten (bis zu 5% Spannung) erstellt. Obwohl diese spezielle quaternäre III-V-Verbindung noch nicht eingehend untersucht wurde, sind ihre binären und ternären Teilsysteme (GaAs, GaP, GaSb, GaAsP, GaAsSb und GaPSb), wie bereits erwähnt, von Bedeutung. Darüber hinaus wird diese theoretische Analyse wertvolle Erkenntnisse für die künftige experimentelle Erforschung dieses Materialsystems liefern.

Der vorgestellte hybride DFT-ML-Berechnungsansatz lässt sich leicht auf andere III-V-Halbleiter und Materialklassen verallgemeinern und ermöglicht die schnelle Abschätzung der Bandlücken für eine breite Palette von Materialien und Spannungswerten. Dieses virtuelle Hochdurchsatz-Screening bringt somit ein erhebliches Potenzial für die Erforschung und Entdeckung neuer Halbleitermaterialien für (opto-)elektronische Anwendungen.

Zusammenfassend lässt sich sagen, dass diese Dissertation einen umfassenden und effizienten Berechnungsansatz für die Vorhersage von Bandlücken in gespannten III-V-Halbleitermaterialien entwickelt hat. Durch die Kombination von DFT und ML wird ein kosteneffektives Protokoll für genaue Bandlückenvorhersagen in diesen Systemen erreicht. Durch die Konstruktion von Bandlücken-Phasendiagrammen werden wertvolle Einblicke in die Bandlückenoptimierung für verschiedene III-V-Materialien unter Spannung gewonnen, was die Optimierung von Materialkombinationen für verschiedene III-V-Halbleitermaterialanwendungen erleichtert. Das entwickelte hybride DFT-ML-Rechenprotokoll kann erweitert werden, um eine breite Palette von multinären III-V-Materialien und Systeme darüber hinaus zu untersuchen. Dieser computergestützte Ansatz für das Materialdesign ebnet somit den Weg für die Entwicklung neuartiger spannungsabhängiger Halbleitermaterialien mit maßgeschneiderten Bandlückeneigenschaften.

Bibliography

- [1] S. Kasap, *Principles of electronic materials and devices*, 4th ed., McGraw-Hill Education, Europe, **2017**.
- [2] S. M. Sze, and M. K. Lee, *Semiconductor devices: physics and technology*, 3rd ed., John Wiley & Sons Inc, New York, **2012**.
- [3] D. A. Neamen, *Semiconductor physics and devices: basic principles*, 4th ed., McGraw-Hill, New York, **2011**.
- [4] S. P. Philipps, F. Dimroth, and A. W. Bett, “High-efficiency III-V multijunction solar cells” in *McEvoy’s Handbook of Photovoltaics, 3rd ed.* (Ed.: S. A. Kalogirou), Academic Press, **2018**, pp. 439–472.
- [5] R. Soref, “The past, present, and future of silicon photonics”, *IEEE J. Sel. Top. Quantum Electron.* **2006**, *12*, 1678–1687.
- [6] P. Bhattacharya, *Semiconductor optoelectronic devices*, 2nd ed., Pearson India Education Services Pvt. Ltd., India, **2017**.
- [7] S. Mokkalapati, and C. Jagadish, “III-V compound SC for optoelectronic devices”, *Mater. Today* **2009**, *12*, 22–32.
- [8] K. Y. Cheng, *III-V compound semiconductors and devices*, 1st ed., Springer International Publishing, Cham, **2020**.
- [9] P. Y. Yu, and M. Cardona, *Fundamentals of semiconductors: physics and materials properties*, 3rd ed., Springer, Berlin, **2005**.
- [10] M. G. Craford, D. L. Keune, W. O. Groves, and A. H. Herzog, “The luminescent properties of nitrogen doped GaAsP light emitting diodes”, *J. Electron. Mater.* **1973**, *2*, 137–158.
- [11] I. D. Henning, and H. Thomas, “Process-induced defect states in GaAsP light emitting diodes”, *Phys. Status Solidi (a)* **1983**, *79*, 567–574.
- [12] Y. Tanaka, and T. Toyama, “Analysis of current-temperature-light characteristics of GaAsP light-emitting diodes”, *IEEE Trans. Electron Devices* **1994**, *41*, 1475–1477.

BIBLIOGRAPHY

- [13] T. Sato, and M. Imai, “Characteristics of nitrogen-doped GaAsP light-emitting diodes”, *Jpn. J. Appl. Phys.* **2002**, *41*, 5995–5998.
- [14] J. F. Geisz, and D. J. Friedman, “III-N-V semiconductors for solar photovoltaic applications”, *Semicond. Sci. Technol.* **2002**, *17*, 769–777.
- [15] J. R. Lang, J. Faucher, S. Tomasulo, K. Nay Yaung, and M. Larry Lee, “Comparison of GaAsP solar cells on GaP and GaP/Si”, *Appl. Phys. Lett.* **2013**, *103*, 092102.
- [16] K. Hayashi, T. Soga, H. Nishikawa, T. Jimbo, and M. Umeno, “MOCVD growth of GaAsP on Si for tandem solar cell application”, *Conf. Rec. IEEE Photovolt. Spec. Conf.* **1994**, *2*, 1890–1893.
- [17] T. J. Grassman, D. J. Chmielewski, S. D. Carnevale, J. A. Carlin, and S. A. Ringel, “GaAs_{0.75}P_{0.25}/Si dual-junction solar cells grown by MBE and MOCVD”, *IEEE J. Photovolt.* **2016**, *6*, 326–331.
- [18] P. Rosenow, L. C. Bannow, E. W. Fischer, W. Stolz, K. Volz, S. W. Koch, and R. Tonner, “Ab initio calculations of the concentration dependent band gap reduction in dilute nitrides”, *Phys. Rev. B* **2018**, *97*, 075201.
- [19] M. Weyers, M. S. Michio Sato, and H. A. Hiroaki Ando, “Red shift of photoluminescence and absorption in dilute GaAsN alloy layers”, *Jpn. J. Appl. Phys.* **1992**, *31*, L853.
- [20] B. Kunert, K. Volz, J. Koch, and W. Stolz, “Direct-band-gap Ga(NAsP)-material system pseudomorphically grown on GaP substrate”, *Appl. Phys. Lett.* **2006**, *88*, 182108.
- [21] Y. Zhao, G. Chen, S. Wang, and S. F. Yoon, “Thermal characterization of gallium arsenic nitride epilayer on gallium arsenide substrate using pulsed photothermal reflectance technique”, *Thin Solid Films* **2004**, *450*, 352–356.
- [22] S. Loualiche, A. Le Corre, S. Salaun, J. Caulet, B. Lambert, M. Gauneau, D. Lecrosnier, and B. Deveaud, “GaPSb: a new ternary material for Schottky diode fabrication on InP”, *Appl. Phys. Lett.* **1998**, *59*, 423.
- [23] H. Shimomura, T. Anan, and S. Sugou, “Growth of AlPSb and GaPSb on InP by gas-source molecular beam epitaxy”, *J. Cryst. Growth* **1996**, *162*, 121–125.

-
- [24] K. Nakajima, T. Ujihara, S. Miyashita, and G. Sazaki, “Thickness dependence of stable structure of the Stranski–Krastanov mode in the GaPSb/GaP system”, *J. Cryst. Growth* **2000**, *209*, 637–647.
- [25] H. B. Russell, A. N. Andriotis, M. Menon, J. B. Jasinski, A. Martinez-Garcia, and M. K. Sunkara, “Direct band gap gallium antimony phosphide ($\text{GaSb}_x\text{P}_{1-x}$) Alloys”, *Sci. Rep.* **2016**, *6*, 20822.
- [26] M. J. Jou, Y. T. Cherng, H. R. Jen, and G. B. Stringfellow, “Organometallic vapor phase epitaxial growth of a new semiconductor alloy: $\text{GaP}_{1-x}\text{Sb}_x$ ”, *Appl. Phys. Lett.* **1988**, *52*, 549–551.
- [27] M. J. Cherng, R. M. Cohen, and G. B. Stringfellow, “GaAs $_{1-x}$ Sb $_x$ growth by OMVPE”, *J. Electron. Mater.* **1984**, *13*, 799–813.
- [28] H. R. Jen, M. J. Cherng, and G. B. Stringfellow, “Ordered structures in GaAs $_{0.5}$ Sb $_{0.5}$ alloys grown by organometallic vapor phase epitaxy”, *Appl. Phys. Lett.* **1998**, *48*, 1603.
- [29] T. M. Christian, D. A. Beaton, A. Mascarenhas, and K. Alberi, “Bismuth incorporation into gallium phosphide”, *Proc. SPIE 10174, Int. Symp. Clust. Nanomater.* **2016**, *10174*, 228–234.
- [30] T. M. Christian, D. A. Beaton, K. Alberi, B. Fluegel, and A. Mascarenhas, “Mysterious absence of pair luminescence in gallium phosphide bismide”, *Appl. Phys. Express* **2015**, *8*, 061202.
- [31] S. J. Sweeney, Z. Batool, K. Hild, S. R. Jin, and T. J. Hosea, “The potential role of Bismide alloys in future photonic devices” in 2011 13th Int. Conf. Transparent Opt. Networks, **2011**, pp. 1–4.
- [32] S. Wang et al., “Novel dilute bismides for IR optoelectronics applications” in Asia Commun. Photonics Conf. 2013, OSA, Washington, D.C., **2013**, AF3B.5.
- [33] D. G. Cooke, F. A. Hegmann, E. C. Young, and T. Tiedje, “Electron mobility in dilute GaAs bismide and nitride alloys measured by time-resolved terahertz spectroscopy”, *Appl. Phys. Lett.* **2006**, *89*, 122103.
- [34] A. Bett, F. Dimroth, G. Stollwerck, and O. Sulima, “III-V compounds for solar cell applications”, *Applied Physics A: Materials Science & Processing* **1999**, *69*, 119–129.
- [35] B. Kunert, K. Volz, and W. Stolz, “Dilute nitride Ga(NAsP)/GaP-heterostructures: toward a material development for novel optoelectronic functionality on Si-substrate”, *Phys. Status Solidi (b)* **2007**, *244*, 2730–2739.

BIBLIOGRAPHY

- [36] K. Volz, J. Koch, F. Höhnsdorf, B. Kunert, and W. Stolz, “MOVPE growth of dilute nitride III/V semiconductors using all liquid metalorganic precursors”, *J. Cryst. Growth* **2009**, *311*, 2418–2426.
- [37] B. Kunert, J. Koch, T. Torunski, K. Volz, and W. Stolz, “MOVPE growth experiments of the novel (GaIn)(NP)/GaP material system”, *J. Cryst. Growth* **2004**, *272*, 753–759.
- [38] B. Kunert, S. Zinnkann, K. Volz, and W. Stolz, “Monolithic integration of Ga(NAsP)/(BGa)P multi-quantum well structures on (0 0 1) silicon substrate by MOVPE”, *J. Cryst. Growth* **2008**, *310*, 4776–4779.
- [39] K. Volz, T. Torunski, B. Kunert, O. Rubel, S. Nau, S. Reinhard, and W. Stolz, “Specific structural and compositional properties of (GaIn)(NAs) and their influence on optoelectronic device performance”, *J. Cryst. Growth* **2004**, *272*, 739–747.
- [40] S. Liebich et al., “Laser operation of Ga(NAsP) lattice-matched to (001) silicon substrate”, *Appl. Phys. Lett.* **2011**, *99*, 071109.
- [41] T. Hepp, L. Nattermann, and K. Volz, “MOVPE growth and device applications of ternary and quaternary dilute bismide alloys on GaAs substrates” in *Bismuth-Containing Alloys and Nanostructures*, (Eds.: S. Wang, and P. Lu), Springer, Singapur, **2019**, pp. 37–58.
- [42] P. E. Van Camp, V. E. Van Doren, and J. T. Devreese, “Pressure dependence of the electronic properties of cubic III-V In compounds”, *Phys. Rev. B* **1990**, *41*, 1598–1602.
- [43] R. F. Potter, “Indirect transitions in indium antimonide”, *Phys. Rev.* **1956**, *103*, 861–862.
- [44] P. A. Alekseev, V. A. Sharov, B. R. Borodin, M. S. Dunaevskiy, R. R. Reznik, and G. E. Cirlin, “Effect of the uniaxial compression on the GaAs nanowire solar cell”, *Micromachines* **2020**, *11*, 581.
- [45] A. K. Katiyar, K. Y. Thai, W. S. Yun, J. Lee, and J.-h. Ahn, “Breaking the absorption limit of Si toward SWIR wavelength range via strain engineering”, *Sci. Adv.* **2020**, *6*, eabb0576.
- [46] B. Lim, X. Y. Cui, and S. P. Ringer, “Strain-mediated bandgap engineering of straight and bent semiconductor nanowires”, *Phys. Chem. Chem. Phys.* **2021**, *23*, 5407–5414.

- [47] G. Signorello, E. Lörtscher, P. Khomyakov, S. Karg, D. Dheeraj, B. Gotsmann, H. Weman, and H. Riel, “Inducing a direct-to-pseudodirect bandgap transition in wurtzite GaAs nanowires with uniaxial stress”, *Nat. Commun.* **2014**, *5*, 3655.
- [48] G. Signorello, S. Karg, M. T. Björk, B. Gotsmann, and H. Riel, “Tuning the Light Emission from GaAs Nanowires over 290 meV with Uniaxial Strain”, *Nano Lett.* **2013**, *13*, 917–924.
- [49] H. Zimmermann, “III–V semiconductor materials on silicon” in *Integrated Silicon Optoelectronics*, Springer Berlin Heidelberg, Berlin, Heidelberg, **2000**, pp. 167–185.
- [50] T. Wegele, A. Beyer, P. Ludewig, P. Rosenow, L. Duschek, K. Jandieri, R. Tonner, W. Stolz, and K. Volz, “Interface morphology and composition of Ga(NAsP) quantum well structures for monolithically integrated LASERS on silicon substrates”, *J. Phys. D. Appl. Phys.* **2016**, *49*, 075108.
- [51] K. Volz, W. Stolz, A. Dadgar, and A. Krost, “Growth of III/Vs on silicon” in *Handbook of Crystal Growth*, Elsevier, **2015**, pp. 1249–1300.
- [52] G. Stringfellow, “Fundamental aspects of MOVPE” in *Metalorganic vapor phase epitaxy (MOVPE): growth, materials properties, and applications*, (Ed.: P. C. Stuart Irvine), John Wiley & Sons Ltd., **2019**.
- [53] A. Beyer, W. Stolz, and K. Volz, “Metastable cubic zinc-blende III/V semiconductors: growth and structural characteristics”, *Prog. Cryst. Growth Charact. Mater.* **2015**, *61*, 46–62.
- [54] O. Supplie et al., “Metalorganic vapor phase epitaxy of III–V-on-silicon: experiment and theory”, *Prog. Cryst. Growth Charact. Mater.* **2018**, *64*, 103–132.
- [55] R. D. Dupuis, “Metalorganic chemical vapor deposition of III-V semiconductors”, *Science* **1984**, *226*, 623–629.
- [56] R. Dupuis, “III-V semiconductor heterojunction devices grown by metalorganic chemical vapor deposition”, *IEEE Journal of Selected Topics in Quantum Electronics* **2000**, *6*, 1040–1050.
- [57] S. Dhar, *Analytical mobility modeling for strained silicon-based devices*, Dissertation, Wien, August 2007, **last accessed 10.07.2023**.
- [58] G. L. Bir, and G. E. Pikus, *Symmetry and strain-induced effects in semiconductors*, John Wiley & Sons, New York, **1974**.

BIBLIOGRAPHY

- [59] Y. Sun, S. E. Thompson, and T. Nishida, “Physics of strain effects in semiconductors and metal-oxide-semiconductor field-effect transistors”, *J. Appl. Phys.* **2007**, *101*, 104503.
- [60] C. P. Kuo, S. K. Vong, R. M. Cohen, and G. B. Stringfellow, “Effect of mismatch strain on band gap in III-V semiconductors”, *J. Appl. Phys.* **1985**, *57*, 5428–5432.
- [61] P. Ludewig, N. Knaub, W. Stolz, and K. Volz, “MOVPE growth of Ga(AsBi)/GaAs multi quantum well structures”, *J. Cryst. Growth* **2013**, *370*, 186–190.
- [62] L. Balaghi, G. Bussone, R. Grifone, R. Hübner, J. Grenzer, M. Ghorbani-Asl, A. V. Krashennnikov, H. Schneider, M. Helm, and E. Dimakis, “Widely tunable GaAs bandgap via strain engineering in core/shell nanowires with large lattice mismatch”, *Nat. Commun.* **2019**, *10*, 2793.
- [63] J. Grönqvist, N. Søndergaard, F. Boxberg, T. Guhr, S. Åberg, and H. Q. Xu, “Strain in semiconductor core-shell nanowires”, *J. Appl. Phys.* **2009**, *106*, 053508.
- [64] M. Hetzl, M. Kraut, J. Winnerl, L. Francaviglia, M. Döblinger, S. Matich, A. FontcubertaMorrall, and M. Stutzmann, “Strain-induced band gap engineering in selectively grown GaN-(Al,Ga)N core-shell nanowire heterostructures”, *Nano Lett.* **2016**, *16*, 7098–7106.
- [65] M. Montazeri et al., “Direct measure of strain and electronic structure in GaAs/GaP core-shell nanowires”, *Nano Lett.* **2010**, *10*, 880–886.
- [66] N. Sköld, L. S. Karlsson, M. W. Larsson, M. E. Pistol, W. Seifert, J. Trägårdh, and L. Samuelson, “Growth and optical properties of strained GaAs-Ga_xIn_{1-x}P core-shell nanowires”, *Nano Lett.* **2005**, *5*, 1943–1947.
- [67] Y.-H. Won, O. Cho, T. Kim, D.-Y. Chung, T. Kim, H. Chung, H. Jang, J. Lee, D. Kim, and E. Jang, “Highly efficient and stable InP/ZnSe/ZnS quantum dot light-emitting diodes”, *Nature* **2019**, *575*, 634–638.
- [68] H. G. Kim et al., “Effects of Al precursors on deposition selectivity of atomic layer deposition of Al₂O₃ using ethanethiol inhibitor”, *Chemistry of Materials* **2020**, *32*, 8921–8929.
- [69] P. Reiss, M. Protière, and L. Li, “Core/shell semiconductor nanocrystals”, *Small* **2009**, *5*, 154–168.

- [70] J. Zhai, T. Dong, Y. Zhou, J. Min, Y. Yan, C. S. Garoufalidis, S. Baskoutas, D. Xu, and Z. Zeng, “Efficient band-edge emission from indirect bandgap semiconductor quantum dots upon shell engineering”, *Nano Lett.* **2023**, *23*, 3239–3244.
- [71] V. Srivastava, V. Kamysbayev, L. Hong, E. Dunietz, R. F. Klie, and D. V. Talapin, “Colloidal chemistry in molten salts: synthesis of luminescent $\text{In}_{1-x}\text{Ga}_x\text{P}$ and $\text{In}_{1-x}\text{Ga}_x\text{As}$ quantum dots”, *J. Am. Chem. Soc.* **2018**, *140*, 12144–12151.
- [72] M. Rusishvili, S. Wippermann, D. V. Talapin, and G. Galli, “Stoichiometry of the core determines the electronic structure of core-shell III-V/II-VI nanoparticles”, *Chem. Mater.* **2020**, *32*, 9798–9804.
- [73] R. Ghosh Chaudhuri, and S. Paria, “Core/shell nanoparticles: classes, properties, synthesis mechanisms, characterization, and applications”, *Chem. Rev.* **2012**, *112*, 2373–2433.
- [74] J. C. Slater, and G. F. Koster, “Simplified LCAO Method for the Periodic Potential Problem”, *Phys. Rev.* **1954**, *94*, 1498–1524.
- [75] N. W. Ashcroft, and N. D. Mermin, *Solid state physics*, Saunders college, Philadelphia, Pa., **1976**.
- [76] W. A. Harrison, *Electronic structure and the properties of solids: the physics of the chemical bond*, Dover Publications, New York, **1989**.
- [77] P. Hohenberg, and W. Kohn, “Inhomogeneous electron gas”, *Phys. Rev.* **1964**, *136*, B864–B871.
- [78] W. Kohn, and L. J. Sham, “Self-consistent equations including exchange and correlation effects”, *Phys. Rev.* **1965**, *140*, A1133–A1138.
- [79] W. Kohn, A. D. Becke, and R. G. Parr, “Density functional theory of electronic structure”, *J. Phys. Chem.* **1996**, *100*, 12974–12980.
- [80] J. P. Perdew, K. Burke, and M. Ernzerhof, “Generalized gradient approximation made simple”, *Phys. Rev. Lett.* **1996**, *77*, 3865–3868.
- [81] L. Hedin, “New method for calculating the one-Particle green’s function with application to the electron-gas problem”, *Phys. Rev.* **1965**, *139*, A796–A823.
- [82] M. S. Hybertsen, and S. G. Louie, “Electron correlation in semiconductors and insulators: band gaps and quasiparticle energies”, *Phys. Rev. B* **1986**, *34*, 5390–5413.
- [83] F. Aryasetiawan, and O. Gunnarsson, “The GW method”, *Rep. Prog. Phys.* **1998**, *61*, 237–312.

- [84] W. G. Aulbur, L. Jönsson, and J. W. Wilkins, “Quasiparticle calculations in solids” in *Solid State Physics, Vol. 54*, (Eds.: H. Ehrenreich, and F. Spaepen), Academic Press, **2000**, pp. 1–218.
- [85] A. V. Krukau, O. A. Vydrov, A. F. Izmaylov, and G. E. Scuseria, “Influence of the exchange screening parameter on the performance of screened hybrid functionals”, *J. Chem. Phys.* **2006**, *125*, 224106.
- [86] J. Heyd, G. E. Scuseria, and M. Ernzerhof, “Hybrid functionals based on a screened Coulomb potential”, *J. Chem. Phys.* **2003**, *118*, 8207–8215.
- [87] M. Marsman, J. Paier, A. Stroppa, and G. Kresse, “Hybrid functionals applied to extended systems”, *J. Phys. Condens. Matter* **2008**, *20*, 064201.
- [88] F. Tran, and P. Blaha, “Accurate band gaps of semiconductors and insulators with a semilocal exchange-correlation potential”, *Phys. Rev. Lett.* **2009**, *102*, 226401.
- [89] R. R. Pela, M. Marques, and L. K. Teles, “Comparing LDA-1/2, HSE03, HSE06 and G 0 W 0 approaches for band gap calculations of alloys”, *J. Phys. Condens. Matter* **2015**, *27*, 505502.
- [90] Y.-S. Kim, M. Marsman, G. Kresse, F. Tran, and P. Blaha, “Towards efficient band structure and effective mass calculations for III-V direct band-gap semiconductors”, *Phys. Rev. B* **2010**, *82*, 205212.
- [91] H. Jiang, “Band gaps from the Tran-Blaha modified Becke-Johnson approach: a systematic investigation”, *J. Chem. Phys.* **2013**, *138*, 134115.
- [92] D. Koller, F. Tran, and P. Blaha, “Improving the modified Becke-Johnson exchange potential”, *Phys. Rev. B* **2012**, *85*, 155109.
- [93] M. I. Ziane, Z. Bensaad, B. Labdelli, and H. Bennacer, “First-principles study of structural, electronic and optical properties of III-arsenide binary GaAs and InAs, and III-nitrides binary GaN and InN: improved density-functional-theory Study”, *Sensors & transducers* **2014**, *27*, 374.
- [94] G. Rehman, M. Shafiq, Saifullah, R. Ahmad, S. Jalali-Asadabadi, M. Maqbool, I. Khan, H. Rahnamaye-Aliabad, and I. Ahmad, “Electronic band structures of the highly desirable III–V semiconductors: TB-mBJ DFT studies”, *J. Electron. Mater.* **2016**, *45*, 3314–3323.

-
- [95] O. Rubel, A. Bokhanchuk, S. J. Ahmed, and E. Assmann, “Unfolding the band structure of disordered solids: from bound states to high-mobility Kane fermions”, *Phys. Rev. B* **2014**, *90*, 115202.
- [96] L. C. Bannow, P. Rosenow, P. Springer, E. W. Fischer, J. Hader, J. V. Moloney, R. Tonner, and S. W. Koch, “An ab initio based approach to optical properties of semiconductor heterostructures”, *Model. Simul. Mater. Sci. Eng.* **2017**, *25*, 065001.
- [97] L. C. Bannow, P. Rosenow, P. Springer, E. W. Fischer, J. Hader, J. V. Moloney, R. Tonner, and S. W. Koch, “An ab initio based approach to optical properties of semiconductor heterostructures”, *Model. Simul. Mater. Sci. Eng.* **2017**, *25*, 065001.
- [98] S. B. Zhang, S.-H. Wei, and A. Zunger, “Stabilization of ternary compounds via ordered arrays of defect pairs”, *Phys. Rev. Lett.* **1997**, *78*, 4059–4062.
- [99] M. Asta, V. Ozolins, and C. Woodward, “A first-principles approach to modeling alloy phase equilibria”, *JOM* **2001**, *53*, 16–19.
- [100] A. Walle, and G. Ceder, “Automating first-principles phase diagram calculations”, *J. Phase Equil.* **2002**, *23*, 348–359.
- [101] R. Arroyave, A. Van De Walle, and Z. K. Liu, “First-principles calculations of the Zn-Zr system”, *Acta Mater.* **2006**, *54*, 473–482.
- [102] A. van de Walle, “Multicomponent multisublattice alloys, nonconfigurational entropy and other additions to the Alloy Theoretic Automated Toolkit”, *Calphad* **2009**, *33*, 266–278.
- [103] Z.-K. Liu, “First-Principles Calculations and CALPHAD Modeling of Thermodynamics”, *J. Phase Equilibria Diffus.* **2009**, *30*, 517–534.
- [104] R. Chinnappan, B. Panigrahi, and A. van de Walle, “First-principles study of phase equilibrium in Ti–V, Ti–Nb, and Ti–Ta alloys”, *Calphad* **2016**, *54*, 125–133.
- [105] S. H. Wei, L. G. Ferreira, and A. Zunger, “First-principles calculation of temperature-composition phase diagrams of semiconductor alloys”, *Phys. Rev. B* **1990**, *41*, 8240–8269.
- [106] A. Mujica, R. J. Needs, and A. Muñoz, “First-principles pseudopotential study of the phase stability of the III-V semiconductors GaAs and AlAs”, *Phys. Rev. B* **1995**, *52*, 8881–8892.
- [107] H. Meradji, S. Drablia, S. Ghemid, H. Belkhir, B. Bouhaf, and A. Tadjer, “First-principles elastic constants and electronic structure of BP, BAs, and BSb”, *Phys. status solidi* **2004**, *241*, 2881–2885.

BIBLIOGRAPHY

- [108] S. Q. Wang, and H. Q. Ye, “First-principles study on elastic properties and phase stability of III–V compounds”, *Phys. status solidi* **2003**, *240*, 45–54.
- [109] H. Salehi, H. A. Badehian, and M. Farbod, “First principle study of the physical properties of semiconducting binary antimonide compounds under hydrostatic pressures”, *Mater. Sci. Semicond. Process.* **2014**, *26*, 477–490.
- [110] C. Zhu, R. Yang, Q. Wei, and D. Zhang, “Theoretical investigations of phases of AIAs by first-principles”, *Chinese J. Phys.* **2018**, *56*, 2119–2128.
- [111] T. Hastie, R. Tibshirani, and J. Friedman, *The elements of statistical learning: data Mining, inference, and prediction*, 2nd ed., Springer, New York, **2009**.
- [112] C. M. Bishop, *Pattern recognition and machine learning*, 1st ed., Springer, New York, **2006**.
- [113] Kevin P. Murphy, *Machine learning: a probabilistic perspective*, MIT press, Cambridge, Massachusetts, **2012**.
- [114] G. Pilania, A. Mannodi-Kanakkithodi, B. P. Uberuaga, R. Ramprasad, J. E. Gubernatis, and T. Lookman, “Machine learning bandgaps of double perovskites”, *Sci. Rep.* **2016**, *6*, 19375.
- [115] V. Gladkikh, D. Y. Kim, A. Hajibabaei, A. Jana, C. W. Myung, and K. S. Kim, “Machine learning for predicting the band gaps of ABX₃ perovskites from elemental properties”, *J. Phys. Chem. C* **2020**, *124*, 8905–8918.
- [116] W. Setyawan, R. M. Gaume, S. Lam, R. S. Feigelson, and S. Curtarolo, “High-throughput combinatorial database of electronic band structures for inorganic scintillator materials”, *ACS Comb. Sci.* **2011**, *13*, 382–390.
- [117] P. Dey, J. Bible, S. Datta, S. Broderick, J. Jasinski, M. Sunkara, M. Menon, and K. Rajan, “Informatics-aided bandgap engineering for solar materials”, *Comput. Mater. Sci.* **2014**, *83*, 185–195.
- [118] A. C. Rajan, A. Mishra, S. Satsangi, R. Vaish, H. Mizuseki, K. R. Lee, and A. K. Singh, “Machine-learning-assisted accurate band gap predictions of functionalized mxene”, *Chem. Mater.* **2018**, *30*, 4031–4038.

- [119] L. Weston, and C. Stampfl, “Machine learning the band gap properties of kesterite I2-II-IV- V4 quaternary compounds for photovoltaics applications”, *Phys. Rev. Mater.* **2018**, *2*, 085407.
- [120] K. L. Heng, S. J. Chua, and P. Wu, “Prediction of semiconductor material properties by the properties of their constituent chemical elements”, *Chem. Mater.* **2000**, *12*, 1648–1653.
- [121] J. Lee, A. Seko, K. Shitara, K. Nakayama, and I. Tanaka, “Prediction model of band gap for inorganic compounds by combination of density functional theory calculations and machine learning techniques”, *Phys. Rev. B* **2016**, *93*, 115104.
- [122] Y. Zhuo, A. Mansouri Tehrani, and J. Brgoch, “Predicting the band gaps of inorganic solids by machine learning”, *J. Phys. Chem. Lett.* **2018**, *9*, 1668–1673.
- [123] Z. Zhu, B. Dong, H. Guo, T. Yang, and Z. Zhang, “Fundamental band gap and alignment of two-dimensional semiconductors explored by machine learning”, *Chin. Phys. B* **2020**, *29*, 046101.
- [124] T. Gu, W. Lu, X. Bao, and N. Chen, “Using support vector regression for the prediction of the band gap and melting point of binary and ternary compound semiconductors”, *Solid State Sci.* **2006**, *8*, 129–136.
- [125] Y. Huang, C. Yu, W. Chen, Y. Liu, C. Li, C. Niu, F. Wang, and Y. Jia, “Band gap and band alignment prediction of nitride-based semiconductors using machine learning”, *J. Mater. Chem. C* **2019**, *7*, 3238–3245.
- [126] F. Jensen, *Introduction to computational chemistry*, 2nd ed., John Wiley & Sons, **2007**.
- [127] A. Szabo, and N. S. Ostlund, *Modern quantum chemistry: introduction to advanced electronic structure theory*. Dover Publications, McGraw-Hill, New York, **1996**.
- [128] R. G. Parr, and W. Yang, *Density-functional theory of atoms and molecules*, (Ed.: International Series of Monographs on Chemistry), Oxford University Press, New York, NY, **1994**.
- [129] R. M. Martin, *Electronic structure: basic theory and practical methods*, 2nd, Cambridge University Press, Cambridge, England, **2020**.
- [130] Gerd Czycholl, *Theoretische festkörperphysik*, 3rd ed., Springer, Berlin Heidelberg, **2008**.

BIBLIOGRAPHY

- [131] D. Frenkel, and B. Smit, *Understanding molecular simulation: from algorithms to applications*, 2nd ed., Academic Press, **2002**.
- [132] M. Levy, “Universal variational functionals of electron densities, first-order density matrices, and natural spin-orbitals and solution of the v-representability problem”, *Proc. Natl. Acad. Sci.* **1979**, *76*, 6062–6065.
- [133] S.-E. Ungersböck, *Advanced modeling of strained CMOS technology*, Dissertation, Wien, April 2007, **last accessed 10.07.2023**.
- [134] Brillouin zone, Wikipedia, **last accessed 10.07.2023**.
- [135] VASP ENCUT, <https://www.vasp.at/wiki/index.php/ENCUT>, **last accessed 10.07.2023**.
- [136] H. J. Monkhorst, and J. D. Pack, “Special points for Brillouin-zone integrations”, *Phys. Rev. B* **1976**, *13*, 5188–5192.
- [137] J. Ihm, A. Zunger, and M. L. Cohen, “Momentum-space formalism for the total energy of solids”, *J. Phys. C Solid State Phys.* **1979**, *12*, 4409–4422.
- [138] R. M. Martin, L. Reining, and D. M. Ceperley, *Interacting electrons: theory and computational approaches*, Cambridge University Press, Cambridge, **2016**.
- [139] P. E. Blöchl, “Projector augmented-wave method”, *Phys. Rev. B* **1994**, *50*, 17953–17979.
- [140] G. Kresse, and D. Joubert, “From ultrasoft pseudopotentials to the projector augmented-wave method”, *Phys. Rev. B* **1999**, *59*, 1758–1775.
- [141] C. Rostgaard, “The projector augmented-wave method”, **2009**, DOI 10.48550/arXiv.0910.1921.
- [142] J. Wilhelm, *Computational electronic structure theory of solids and applications*, Lecture note, <https://www.ur.de/physik/evers/wt21-22-cest/index.html>, **last accessed 01.12.2021**.
- [143] R. J. Elliott, “Spin-Orbit coupling in band theory—character tables for some ”double” space groups”, *Phys. Rev.* **1954**, *96*, 280–287.
- [144] J. P. Perdew, and M. Levy, “Physical content of the exact Kohn-Sham orbital energies: band gaps and derivative discontinuities”, *Phys. Rev. Lett.* **1983**, *51*, 1884–1887.

-
- [145] S. Hamel, P. Duffy, M. E. Casida, and D. R. Salahub, “Kohn–Sham orbitals and orbital energies: fictitious constructs but good approximations all the same”, *J. Electron Spectros. Relat. Phenomena* **2002**, *123*, 345–363.
- [146] B. Mondal, and R. Tonner-Zech, “Systematic strain-induced bandgap tuning in binary III-V semiconductors from density functional theory”, *Phys. Scr.* **2023**, *98*, 065924.
- [147] P. Mori-Sánchez, A. J. Cohen, and W. Yang, “Localization and delocalization errors in density functional theory and implications for band-gap prediction”, *Phys. Rev. Lett.* **2008**, *100*, 146401.
- [148] D. Koller, F. Tran, and P. Blaha, “Merits and limits of the modified Becke-Johnson exchange potential”, *Phys. Rev. B* **2011**, *83*, 195134.
- [149] A. D. Becke, and E. R. Johnson, “A simple effective potential for exchange”, *J. Chem. Phys.* **2006**, *124*, 221101.
- [150] A. D. Becke, and M. R. Roussel, “Exchange holes in inhomogeneous systems: a coordinate-space model”, *Phys. Rev. A* **1989**, *39*, 3761–3767.
- [151] E. Caldeweyher, J.-M. Mewes, S. Ehlert, and S. Grimme, “Extension and evaluation of the D4 London-dispersion model for periodic systems”, *Phys. Chem. Chem. Phys.* **2020**, *22*, 8499–8512.
- [152] M. Dion, H. Rydberg, E. Schröder, D. C. Langreth, and B. I. Lundqvist, “Van der Waals density functional for general geometries”, *Phys. Rev. Lett.* **2004**, *92*, 246401.
- [153] K. Berland, V. R. Cooper, K. Lee, E. Schröder, T. Thonhauser, P. Hyldgaard, and B. I. Lundqvist, “van der Waals forces in density functional theory: a review of the vdW-DF method”, *Reports Prog. Phys.* **2015**, *78*, 066501.
- [154] O. A. Vydrov, and T. Van Voorhis, “Nonlocal van der Waals density functional made simple”, *Phys. Rev. Lett.* **2009**, *103*, 063004.
- [155] O. A. Vydrov, and T. Van Voorhis, “Improving the accuracy of the nonlocal van der Waals density functional with minimal empiricism”, *J. Chem. Phys.* **2009**, *130*, 104105.
- [156] A. D. Becke, and E. R. Johnson, “Exchange-hole dipole moment and the dispersion interaction”, *J. Chem. Phys.* **2005**, *122*, 154104.
- [157] A. D. Becke, and E. R. Johnson, “A density-functional model of the dispersion interaction”, *J. Chem. Phys.* **2005**, *123*, 154101.

- [158] A. Tkatchenko, and M. Scheffler, “Accurate molecular van der Waals interactions from ground-state electron density and free-atom reference data”, *Phys. Rev. Lett.* **2009**, *102*, 073005.
- [159] A. Tkatchenko, R. A. DiStasio, R. Car, and M. Scheffler, “Accurate and efficient method for many-body van der Waals interactions”, *Phys. Rev. Lett.* **2012**, *108*, 236402.
- [160] S. Grimme, J. Antony, S. Ehrlich, and H. Krieg, “A consistent and accurate ab initio parametrization of density functional dispersion correction (DFT-D) for the 94 elements H-Pu”, *J. Chem. Phys.* **2010**, *132*, 154104.
- [161] S. Grimme, S. Ehrlich, and L. Goerigk, “Effect of the damping function in dispersion corrected density functional theory”, *J. Comput. Chem.* **2011**, *32*, 1456–1465.
- [162] A. Zunger, S. H. Wei, L. G. Ferreira, and J. E. Bernard, “Special quasirandom structures”, *Phys. Rev. Lett.* **1990**, *65*, 353.
- [163] A. van de Walle, P. Tiwary, M. de Jong, D. Olmsted, M. Asta, A. Dick, D. Shin, Y. Wang, L.-Q. Chen, and Z.-K. Liu, “Efficient stochastic generation of special quasirandom structures”, *Calphad* **2013**, *42*, 13–18.
- [164] W. Ku, T. Berlijn, and C.-C. Lee, “Unfolding first-principles band structures”, *Phys. Rev. Lett.* **2010**, *104*, 216401.
- [165] S.-Y. Yang, H. Yang, E. Derunova, S. S. P. Parkin, B. Yan, and M. N. Ali, “Symmetry demanded topological nodal-line materials”, *Adv. Phys. X* **2018**, *3*, 1414631.
- [166] L. W. Wang, L. Bellaiche, S. H. Wei, and A. Zunger, ““Majority representation” of alloy electronic states”, *Phys. Rev. Lett.* **1998**, *80*, 4725–4728.
- [167] V. Popescu, and A. Zunger, “Extracting E versus \vec{k} effective band structure from supercell calculations on alloys and impurities”, *Phys. Rev. B* **2012**, *85*, 085201.
- [168] V. Popescu, and A. Zunger, “Effective band structure of random alloys”, *Phys. Rev. Lett.* **2010**, *104*, 236403.
- [169] P. V. C. Medeiros, S. Stafström, and J. Björk, “Effects of extrinsic and intrinsic perturbations on the electronic structure of graphene: Retaining an effective primitive cell band structure by band unfolding”, *Phys. Rev. B* **2014**, *89*, 041407(R).

- [170] P. V. C. Medeiros, S. S. Tsirkin, S. Stafström, and J. Björk, “Unfolding spinor wave functions and expectation values of general operators: introducing the unfolding-density operator”, *Phys. Rev. B* **2015**, *91*, 041116(R).
- [171] B. Mondal, M. Kröner, T. Hepp, K. Volz, and R. Tonner-Zech, “Accurate first principles band gap predictions in strain engineered ternary III-V semiconductors”, *Phys. Rev. B* **2023**, *108*, 035202.
- [172] Machine learning, <https://www.javatpoint.com/supervised-machine-learning>, **last accessed 10.07.2023**.
- [173] C. Cortes, and V. Vapnik, “Support-Vector Networks”, *Mach. Learn.* **1995**, *20*, 273–297.
- [174] B. E. Boser, I. M. Guyon, and V. N. Vapnik, “A training algorithm for optimal margin classifiers” in Proceedings of the Fifth Annual Workshop on Computational Learning Theory, Association for Computing Machinery, Pittsburgh, Pennsylvania, USA, **1992**, pp. 144–152.
- [175] A. J. Smola, and B. Schölkopf, “A tutorial on support vector regression”, *Stat. Comput.* **2004**, *14*, 199–222.
- [176] O. A. von Lilienfeld, “Quantum machine learning in chemical compound space”, *Angew. Chemie Int. Ed.* **2018**, *57*, 4164–4169.
- [177] T. Viering, and M. Loog, “The shape of learning curves: a review”, *IEEE Trans. Pattern Anal. Mach. Intell.* **2023**, *45*, 7799–7819.
- [178] M. Jaros, “Electronic properties of semiconductor alloy systems”, *Reports Prog. Phys.* **1985**, *48*, 1091–1154.
- [179] L. Bellaiche, S. H. Wei, and A. Zunger, “Band gaps of GaPN and GaAsN alloys”, *Appl. Phys. Lett.* **1997**, *70*, 3558–3560.
- [180] G. Ghosh, A. van de Walle, and M. Asta, “First-principles calculations of the structural and thermodynamic properties of bcc, fcc and hcp solid solutions in the Al–TM (TM=Ti, Zr and Hf) systems: a comparison of cluster expansion and supercell methods”, *Acta Mater.* **2008**, *56*, 3202–3221.
- [181] D. Shin, R. Arróyave, Z.-K. Liu, and A. Van de Walle, “Thermodynamic properties of binary hcp solution phases from special quasirandom structures”, *Phys. Rev. B* **2006**, *74*, 024204.
- [182] D. Shin, A. van de Walle, Y. Wang, and Z.-K. Liu, “First-principles study of ternary fcc solution phases from special quasirandom structures”, *Phys. Rev. B* **2007**, *76*, 144204.

- [183] D. Shin, and Z.-K. Liu, “Enthalpy of mixing for ternary fcc solid solutions from special quasirandom structures”, *Calphad* **2008**, *32*, 74–81.
- [184] C. Jiang, C. R. Stanek, K. E. Sickafus, and B. P. Uberuaga, “First-principles prediction of disordering tendencies in pyrochlore oxides”, *Phys. Rev. B* **2009**, *79*, 104203.
- [185] A. van de Walle, M. Asta, and G. Ceder, “The alloy theoretic automated toolkit: a user guide”, *Calphad* **2002**, *26*, 539–553.
- [186] B. Welber, M. Cardona, C. K. Kim, and S. Rodriguez, “Dependence of the direct energy gap of GaAs on hydrostatic pressure”, *Phys. Rev. B* **1975**, *12*, 5729–5738.
- [187] B. Welber, C. Kim, M. Cardona, and S. Rodriguez, “Dependence of the indirect energy gap of silicon on hydrostatic pressure”, *Solid State Commun.* **1975**, *17*, 1021–1024.
- [188] P. Y. Yu, and B. Welber, “High pressure photoluminescence and resonant Raman study of GaAs”, *Solid State Commun.* **1978**, *25*, 209–211.
- [189] J.-S. Park, M. Tang, S. Chen, and H. Liu, “Heteroepitaxial growth of III-V semiconductors on silicon”, *Crystals* **2020**, *10*, 1163.
- [190] P. Ludewig, M. Diederich, K. Jandieri, and W. Stolz, “Growth of high N containing GaNAs/GaP/BGaAsP multi quantum well structures on Si (0 0 1) substrates”, *J. Cryst. Growth* **2017**, *467*, 61–64.
- [191] P. Grivickas, M. D. McCluskey, and Y. M. Gupta, “Transformation of GaAs into an indirect L -band-gap semiconductor under uniaxial strain”, *Phys. Rev. B* **2009**, *80*, 073201.
- [192] P. Grivickas, M. D. McCluskey, and Y. M. Gupta, “Band-gap luminescence of GaP:S shock compressed to 5GPa”, *Appl. Phys. Lett.* **2008**, *92*, 142104.
- [193] G. Kresse, and J. Hafner, “Ab initio molecular dynamics for liquid metals”, *Phys. Rev. B* **1993**, *47*, 558–561.
- [194] G. Kresse, and J. Hafner, “Ab initio molecular-dynamics simulation of the liquid-metal–amorphous-semiconductor transition in germanium”, *Phys. Rev. B* **1994**, *49*, 14251–14269.
- [195] G. Kresse, and J. Furthmüller, “Efficient iterative schemes for ab initio total-energy calculations using a plane-wave basis set”, *Phys. Rev. B* **1996**, *54*, 11169–11186.

- [196] G. Kresse, and J. Furthmüller, “Efficiency of ab-initio total energy calculations for metals and semiconductors using a plane-wave basis set”, *Comput. Mater. Sci.* **1996**, *6*, 15–50.
- [197] H. J. Monkhorst, and J. D. Pack, “Special points for Brillouin-zone integrations”, *Phys. Rev. B* **1976**, *13*, 5188–5192.
- [198] T. Bučko, S. Lebègue, J. Hafner, and J. G. Ángyán, “Improved density dependent correction for the description of London dispersion forces”, *J. Chem. Theory Comput.* **2013**, *9*, 4293–4299.
- [199] P. Bultinck, C. Van Alsenoy, P. W. Ayers, and R. Carbó-Dorca, “Critical analysis and extension of the Hirshfeld atoms in molecules”, *J. Chem. Phys.* **2007**, *126*, 144111.
- [200] A. Ambrosetti, A. M. Reilly, R. A. Distasio, and A. Tkatchenko, “Long-range correlation energy calculated from coupled atomic response functions”, *J. Chem. Phys.* **2014**, *140*, 18A508.
- [201] K. Lee, É. D. Murray, L. Kong, B. I. Lundqvist, and D. C. Langreth, “Higher-accuracy van der Waals density functional”, *Phys. Rev. B* **2010**, *82*, 081101.
- [202] J. Klimeš, D. R. Bowler, and A. Michaelides, “Chemical accuracy for the van der Waals density functional”, *J. Phys. Condens. Matter* **2009**, *22*, 022201.
- [203] C. J. Burges, “A tutorial on support vector machines for pattern recognition”, *Data Min. Knowl. Discov.* **1998**, *2*, 121–167.
- [204] B. Scholkopf, and A. J. Smola, *Learning with kernels: support vector machines, regularization, optimization, and beyond*, MIT Press, Cambridge, Massachusetts, **2018**.
- [205] S. Vempati, A. Vedaldi, A. Zisserman, and C. V. Jawahar, “Generalized RBF feature maps for efficient detection” in Proceedings Br. Mach. Vis. Conf. 2010, British Machine Vision Association, **2010**, pp. 2.1–2.11.
- [206] F. Pedregosa *et al.*, “Scikit-learn: machine learning in Python”, *J. Mach. Learn. Res.* **2011**, *12*, 2825–2830.
- [207] J. Schmidt, J. Shi, P. Borlido, L. Chen, S. Botti, and M. A. L. Marques, “Predicting the thermodynamic stability of solids combining density functional theory and machine learning”, *Chem. Mater.* **2017**, *29*, 5090–5103.
- [208] L. Ward, A. Agrawal, A. Choudhary, and C. Wolverton, “A general-purpose machine learning framework for predicting properties of inorganic materials”, *Npj Comput. Mater.* **2016**, *2*, 16028.

BIBLIOGRAPHY

- [209] K. T. Schütt, H. Glawe, F. Brockherde, A. Sanna, K. R. Müller, and E. K. U. Gross, “How to represent crystal structures for machine learning: towards fast prediction of electronic properties”, *Phys. Rev. B* **2014**, *89*, 205118.
- [210] L. Ward, R. Liu, A. Krishna, V. I. Hegde, A. Agrawal, A. Choudhary, and C. Wolverton, “Including crystal structure attributes in machine learning models of formation energies via Voronoi tessellations”, *Phys. Rev. B* **2017**, *96*, 024104.
- [211] R. E. Goodall, and A. A. Lee, “Predicting materials properties without crystal structure: deep representation learning from stoichiometry”, *Nat. Commun.* **2020**, *11*, 6280.
- [212] O. Isayev, C. Oses, C. Toher, E. Gossett, S. Curtarolo, and A. Tropsha, “Universal fragment descriptors for predicting properties of inorganic crystals”, *Nat. Commun.* **2017**, *8*, 15679.
- [213] B. Mondal, J. Westermayr, and R. Tonner-Zech, “Machine learning for accelerated bandgap prediction in strain-engineered quaternary III-V semiconductors”, *J. Chem. Phys.* **2023**, *159*, 104702.
- [214] M. Gastegger, J. Behler, and P. Marquetand, “Machine learning molecular dynamics for the simulation of infrared spectra”, *Chem. Sci.* **2017**, *8*, 6924–6935.
- [215] A. Prins, A. Adams, and S. Sweeney, “Pressure studies” in *Semiconductor research: experimental techniques*, (Eds.: A. Patane, and N. Balkan), Springer, Berlin, Heidelberg, **2012**, pp. 171–195.
- [216] M. Cardona, “12th International Conference on High Pressure Semiconductor Physics (HPSP-12): concluding remarks”, *Phys. Status Solidi (b)* **2007**, *244*, 481–487.
- [217] D. E. Fratanduono et al., “Establishing gold and platinum standards to 1 terapascal using shockless compression”, *Science* **2021**, *372*, 1063–1068.
- [218] L. Dubrovinsky et al., “The most incompressible metal osmium at static pressures above 750 gigapascals”, *Nature* **2015**, *525*, 226–229.
- [219] P. Y. Yu, “High pressure semiconductor physics: looking toward the future on the shoulder of the past”, *Phys. Status Solidi (b)* **2011**, *248*, 1077–1082.

- [220] E. Snider, N. Dasenbrock-Gammon, R. McBride, M. Debessai, H. Vindana, K. Vencatasamy, K. V. Lawler, A. Salamat, and R. P. Dias, “Room-temperature superconductivity in a carbonaceous sulfur hydride”, *Nature* **2020**, *586*, 373–377.
- [221] C. Dang et al., “Achieving large uniform tensile elasticity in micro-fabricated diamond”, *Science* **2021**, *371*, 76–78.
- [222] Z. Shi, M. Dao, E. Tsymbalov, A. Shapeev, J. Li, and S. Suresh, “Metallization of diamond”, *Proc. Natl. Acad. Sci.* **2020**, *117*, 24634–24639.
- [223] A. L. Edwards, and H. G. Drickamer, “Effect of pressure on the absorption edges of some III-V, II-VI, and I-VII compounds”, *Phys. Rev.* **1961**, *122*, 1149–1157.
- [224] I. Vurgaftman, J. R. Meyer, and L. R. Ram-Mohan, “Band parameters for III–V compound semiconductors and their alloys”, *J. Appl. Phys.* **2001**, *89*, 5815–5875.

Scientific Contributions

This chapter presents the research manuscripts to be considered for the cumulative part of this dissertation. First, a brief overview of the manuscripts is provided, consisting of the abstracts of the publications and my contributions to these publications. Subsequently, the reprints of the complete articles and supporting informations are attached.

Systematic strain-induced bandgap tuning in binary III-V semiconductors from density functional theory

Authors: Badal Mondal and Ralf Tonner-Zech

Publication: *Phys. Scr.* **2023**, 98, 065924

DOI: 10.1088/1402-4896/acd08b

arXiv ID: 2208.10596

Abstract

The modification of the nature and size of bandgaps for III-V semiconductors is of strong interest for optoelectronic applications. Strain can be used to systematically tune the bandgap over a wide range of values and induce indirect-to-direct transition (IDT), direct-to-indirect transition (DIT), and other changes in bandgap nature. Here, we establish a predictive first-principles approach, based on density functional theory, to analyze the effect of uniaxial, biaxial, and isotropic strain on the bandgap. We show that systematic variation is possible. For GaAs, DITs are observed at 1.56% isotropic compressive strain and 3.52% biaxial tensile strain, while for GaP an IDT is found at 2.63% isotropic tensile strain. We additionally propose a strategy for the realization of direct-to-indirect transition by combining biaxial strain with uniaxial strain. Further transition points are identified for strained GaSb, InP, InAs, and InSb and compared to the elemental semiconductor silicon. Our analyses thus provide a systematic and predictive approach to strain-induced bandgap tuning in binary III-V semiconductors.

Author's Contributions

I conceived and designed the research, laying the foundation for the investigation. I conducted all the calculations, collected data, and performed a comprehensive formal analysis of the results. I took the lead in interpreting the computational outcomes, and through extensive discussions with my supervisor and co-author, Ralf Tonner-Zech, I refined and enhanced the interpretations. Ralf Tonner-Zech proposed the fundamental methodologies and computational software tools employed in this research, which I adeptly adapted to meet the specific requirements of the project. I compiled the figures and tables included in the article. I drafted the manuscript, presenting the research in a clear and coherent manner. The initial draft was then critically reviewed and revised by Ralf Tonner-Zech, who provided valuable insights and suggestions to improve the overall quality and clarity of the manuscript. Throughout the review process, I actively engaged in editing the manuscript alongside my co-author to ensure accuracy and consistency.

Accurate first principles band gap predictions in strain engineered ternary III-V semiconductors

Authors: Badal Mondal, Marcel Kröner, Thilo Hepp, Kerstin Volz, and Ralf Tonner-Zech

Publication: *Phys. Rev. B* **2023**, *108*, 035202

DOI: 10.1103/PhysRevB.108.035202

arXiv ID: 2302.14547

Abstract

Tuning the bandgap in ternary III-V semiconductors via modification of the composition or the strain in the material is a major approach for the design of optoelectronic materials. Experimental approaches screening a large range of possible target structures are hampered by the tremendous effort to optimize the material synthesis for every target structure. We present an approach based on density functional theory efficiently capable of providing the bandgap as a function of composition and strain. Using a specific density functional designed for accurate bandgap computation (TB09) together with a band unfolding procedure and special quasirandom structures, we develop a computational protocol to predict bandgaps. The approach's accuracy is validated by comparison to selected experimental data. We thus map the bandgap over the phase space of composition and strain (we call this the 'bandgap phase diagram') for several important III-V compound semicon-

ductors: GaAsP, GaAsN, GaPSb, GaAsSb, GaPBi, and GaAsBi. We show the application of these diagrams for identifying the most promising materials for device design. Furthermore, our computational protocol can easily be generalized to explore the vast chemical space of III-V materials with all other possible combinations of III- and V-elements.

Author's Contributions

I conceptualized and designed the study along with my supervisor and co-author of this paper, Ralf Tonner-Zech. The initial research question of this project was posed by Kerstin Volz. I conducted all the calculations, collected data, and performed a comprehensive formal analysis of the results. Initial interpretations of the computational results were conducted by me and further refined by Ralf Tonner-Zech. I compiled the figures and tables included in the article. Ralf Tonner-Zech proposed the fundamental methodologies and computational software tools used in this research, which I adeptly adapted to meet the specific project requirements. However, I also initiated some methods. Our experimental collaborators Marcel Kröner, Thilo Hepp, and Kerstin Volz assisted in compiling the experimental results presented in the paper. I took the lead in drafting the manuscript, which underwent thorough review and revision by all the co-authors. Throughout the review process, I actively engaged in editing the manuscript alongside my co-authors to ensure accuracy and consistency.

Machine learning for accelerated bandgap prediction in strain-engineered quaternary III-V semiconductors

Authors: Badal Mondal, Julia Westermayr, and Ralf Tonner-Zech

Publication: *J. Chem. Phys.* **2023**, *159*, 104702

DOI: 10.1063/5.0159604

arXiv ID: 2305.03666

Abstract

Quaternary III-V semiconductors are one of the major promising material classes in optoelectronics. The bandgap and its character, direct or indirect, are the most important fundamental properties determining the performance and characteristics of optoelectronic devices. Experimental approaches screening a large range of possible combinations of III- and V-elements with variations in composition and strain are impractical for every

target application. We present a combination of accurate first-principles calculations and machine learning based approaches to predict the properties of the bandgap for quaternary III-V semiconductors. By learning bandgap magnitudes and their nature at density functional theory accuracy based solely on the composition and strain features of the materials as an input, we develop a computationally efficient yet highly accurate machine learning approach that can be applied to a large number of compositions and strain values. This allows for a computationally efficient prediction of a vast range of materials under different strains, offering the possibility for virtual screening of multinary III-V materials for optoelectronic applications.

Author's Contributions

I conceived and designed the study along with my supervisor and co-author of this paper, Ralf Tonner-Zech. I proposed the fundamental methodology and software tools, which were then refined by all the co-authors to meet the project requirements. I conducted all the calculations, collected data, and performed the formal analysis in this study. Initial interpretations of the computational results were performed by me and subsequently refined by all the co-authors. I compiled the figures and tables included in this article, which were further critically refined by the co-authors. I drafted the manuscript, which was then thoroughly reviewed and revised by the co-authors. Throughout the review process, I actively engaged in editing the manuscript alongside the co-authors.

Data Availability Statement

All the DFT and ML calculations performed, as well as the data used in this thesis, are freely accessible in the following repositories:

1. The DFT calculations are available in the following NOMAD repositories (open- access):
 - Badal Mondal and Ralf Tonner-Zech (2022).
“III-V binary semiconductors strain study”, NOMAD.
DOI: 10.17172/NOMAD/2022.08.20-2.
 - Badal Mondal and R. Tonner-Zech (2023).
“III-V ternary semiconductors strain study”, NOMAD.
DOI: 10.17172/NOMAD/2023.02.27-1.
 - Badal Mondal, Julia Westermayr, and R. Tonner-Zech (2023).
“GaAsPSb bandgap phase diagram”, NOMAD.
DOI: 10.17172/NOMAD/2023.05.03-1.
2. The Python scripts implementing the ML models and the corresponding databases can be found in the GitHub repository:
[https:// bmondal94.github.io/Bandgap-Phase-Diagram/](https://bmondal94.github.io/Bandgap-Phase-Diagram/)
(last accessed July 2023). Additionally, they can be found in the supplementary attachment of the corresponding publications.
3. The GitHub repository [https:// bmondal94.github.io/Bandgap-Phase-Diagram/](https://bmondal94.github.io/Bandgap-Phase-Diagram/) (last accessed July 2023) additionally contains all the collective results of this thesis. In addition to the supplementary attachment of the corresponding papers, the interactive bandgap phase diagrams can be found directly on this page (open access).

PAPER • OPEN ACCESS

Systematic strain-induced bandgap tuning in binary III–V semiconductors from density functional theory

To cite this article: Badal Mondal and Ralf Tonner-Zech 2023 *Phys. Scr.* **98** 065924

View the [article online](#) for updates and enhancements.

You may also like

- [Phonon propagation dynamics in band-engineered one-dimensional phononic crystal waveguides](#)
Daiki Hatanaka, Amaury Dodel, Imran Mahboob et al.
- [Floquet engineering of optical lattices with spatial features and periodicity below the diffraction limit](#)
S Subhankar, P Bienias, P Titum et al.
- [Novel attributes of bandstructure effect on the performance of germanium Schottky barrier MOSFET](#)
Zahra Ahangari



PAPER

Systematic strain-induced bandgap tuning in binary III–V semiconductors from density functional theory

OPEN ACCESS

RECEIVED

1 September 2022

REVISED

11 April 2023

ACCEPTED FOR PUBLICATION

26 April 2023

PUBLISHED

23 May 2023

Original content from this work may be used under the terms of the [Creative Commons Attribution 4.0 licence](#).

Any further distribution of this work must maintain attribution to the author(s) and the title of the work, journal citation and DOI.

Badal Mondal^{1,2} and Ralf Tonner-Zech¹ ¹ Wilhelm-Ostwald-Institut für Physikalische und Theoretische Chemie, Universität Leipzig, 04103 Leipzig, Germany² Fachbereich Physik, Philipps-Universität Marburg, 35032 Marburg, GermanyE-mail: ralf.tonner@uni-leipzig.de**Keywords:** III-V semiconductors, direct-indirect transition, density functional theory, optical properties, bandgap engineering, strain engineeringSupplementary material for this article is available [online](#)**Abstract**

The modification of the nature and size of bandgaps for III-V semiconductors is of strong interest for optoelectronic applications. Strain can be used to systematically tune the bandgap over a wide range of values and induce indirect-to-direct transition (IDT), direct-to-indirect transition (DIT), and other changes in bandgap nature. Here, we establish a predictive first-principles approach, based on density functional theory, to analyze the effect of uniaxial, biaxial, and isotropic strain on the bandgap. We show that systematic variation is possible. For GaAs, DITs are observed at 1.56% isotropic compressive strain and 3.52% biaxial tensile strain, while for GaP an IDT is found at 2.63% isotropic tensile strain. We additionally propose a strategy for the realization of direct-to-indirect transition by combining biaxial strain with uniaxial strain. Further transition points are identified for strained GaSb, InP, InAs, and InSb and compared to the elemental semiconductor silicon. Our analyses thus provide a systematic and predictive approach to strain-induced bandgap tuning in binary III-V semiconductors.

1. Introduction

Semiconductor compounds attract a great amount of attention, both in science and technology, due to their immense application range in areas such as optoelectronics and integrated circuits [1, 2]. One of the major goals in basic and applied research is to tailor the optical properties of semiconductor materials to a target application. The most important fundamental property determining these properties is the material's bandgap. For example, materials for optical telecommunication applications require direct bandgaps in the range of 0.80–0.95 eV [3–5], while a range of 0.5–2.0 eV is necessary for materials used in efficient solar cells [6–9]. One material class that is especially versatile in this respect are compound semiconductors, specifically the III-V semiconductors composed of elements from group 13 and 15 of the periodic table of elements [2, 5, 10–22]. In the last decades, the optical properties of this material class have been intensively investigated [2, 10–14, 22–36] and several strategies have emerged to fine-tune the bandgap. Changing the nature of the chemical elements and their relative composition is a powerful approach to vary the gap over a wide range of energies [37–44]. However, changing the chemical composition is not always possible. One reason for this lies in the constraints in the growth characteristics of precursor molecules for the chemical vapor deposition techniques often used to grow these materials. Another reason is the thermodynamic instabilities of some elemental compositions [3, 14, 37, 44–48].

An alternative and sometimes also complementary approach to vary the bandgap is strain engineering. This can be achieved through external effects such as: applying pressure on the system [23, 24, 27–36], altering the temperature of the system, or changing the substrate in epitaxial growth processes [13, 16, 19, 37–42, 45, 46, 49–62]. All of these approaches result in structural strain in the system because of the deviation of one or several lattice parameters of the material from their equilibrium values. The effects on the electronic structure from

straining the material are shifts in valence-band maximum (VBM) and conduction-band minimum (CBM), and thus, the variation in the bandgap.

Many attempts have been made to understand the effect of strain from theoretical perspectives. The electronic properties of semiconductor materials have been previously analyzed by: (a) empirical or semi-empirical methods such as the local/nonlocal empirical pseudopotential method [63–71], the semi-empirical tight-binding method [72–84], the $k\cdot p$ method [85–90]; or by (b) first-principles methods [91–98] such as density functional theory (DFT) [91, 99–104]. Although empirical and semi-empirical methods are computationally efficient and often easy to apply, they rely on many empirical fitting parameters. This strongly lowers their ability to predict properties for new materials, which is a core goal in computational materials design [105]. In contrast, first-principles methods allow the calculation of the electronic structure without the need for empirical fitting parameters.

One of the most widely used first-principles approaches in material science is DFT. The crucial ingredient here is the density functional. Functionals following the generalized gradient approximation (GGA) often lead to an excellent agreement of computed lattice parameters with experimental data. However, they are known to show very large errors for bandgaps [105–109]. Hybrid functionals such as HSE06 [110] and GW-based methods [95–98] can solve this issue but are computationally expensive. Previously, we and others successfully used the exchange-correlation functional, developed by Tran and Blaha, to predict the electronic properties of unstrained III-V compound semiconductors without empirical adjustments or application of scissor operators [105, 111–117]. Although this functional contains one global system-dependent parameter, this parameter is derived from the density and two fitted parameters only without adjustment to experimental values. Here, we will show that this approach can also successfully be used for predicting properties when applying a wide range of strains to these materials.

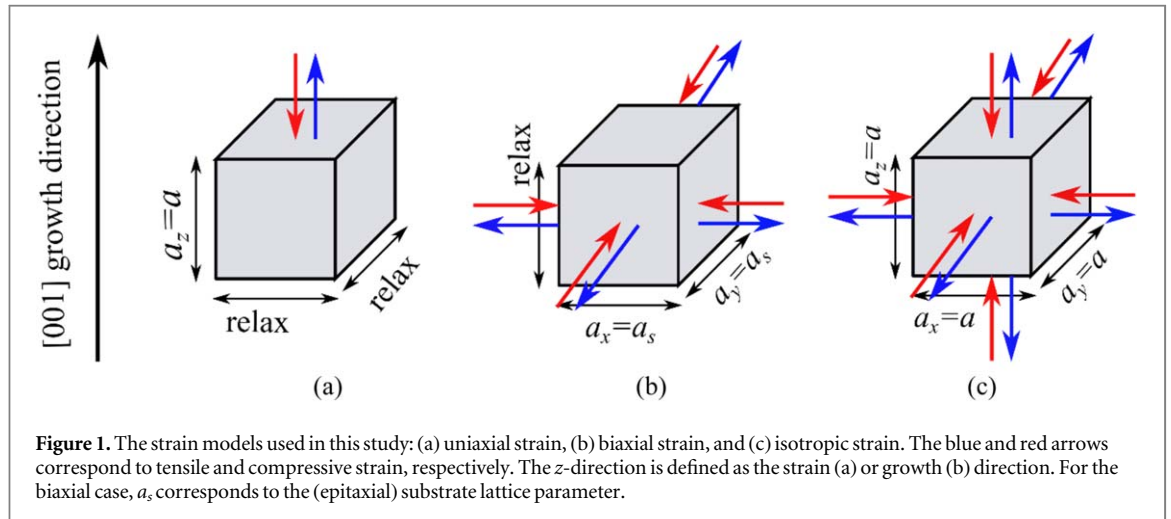
Although strain engineering is an established field for III-V semiconductors [2, 45, 87, 118, 119], the investigation of strain effects has recently found renewed interest in the field of nanowires [120–128]. Furthermore, no systematic theoretical study is yet available that predicts optical properties of strained materials of this kind without empirical adjustments. We now set out to reliably predict the optical properties of strained materials over a wide range of strains. This will ultimately enable computational materials design approaches in strain engineering of established and upcoming materials.

This work will establish the methodology and highlight the challenges of predictive modelling. Thus, we focus our analysis of strain effects on the electronic structure of the most widely investigated binary III-V semiconductors: GaAs and GaP. These materials are not only interesting for basic research but also support a wide range of applications (either as binary materials or as a host material for multinary compounds) in microelectronics, solar cells, laser technology, and LEDs [2–9, 14–21]. To show the general applicability of our approach, selected data on the materials Si, GaSb, InP, InAs, and InSb are included.

In this work, we present and validate a computational approach predicting the size and nature of the bandgap of III-V semiconductor materials over a wide range of strain values. The ultimate goal is to provide guidelines for future experimental work on strained materials.

2. Model

In this study we model uniaxial, biaxial, and isotropic strain. Figure 1 schematically shows which lattice parameters are kept fixed and which are relaxed in the modelling of these three types of strain. The materials investigated are all feature zincblende structures. The growth direction in the ‘theoretical epitaxy’ approach applied (see below) is taken to be [001] in this study and is defined as the z -direction in our modelling approach. We limit our analysis of uniaxial strain to the application of strain along the growth direction only. This uniaxial (compressive) strain is experimentally realized most often by applying pressure. Here, we model this by varying the lattice parameter in the z -direction while relaxing the in-plane lattice parameters (figure 1(a)). In the spirit of a systematic study, we also study uniaxial tensile strain over the same range of values. However, the experimental realization of expanding lattice parameters is typically limited to small strain values (e.g. by increasing the temperature or applying shear stress). The major approach to produce biaxially strained materials is epitaxial growth on a substrate with a different lattice parameter (a_s). We thus fix the in-plane lattice parameters (a_x, a_y) to the lattice parameter of an (imaginary) substrate (a_s) while varying the parameter in the growth direction (figure 1(b)). In this case, we consider the structural strain imposed by a substrate but neglect the electronic influence for the modelling (theoretical epitaxy) [45, 119]. Isotropic strain is then consequently modelled by not constraining any lattice parameter and increasing (decreasing) all lattice parameters by the same amount (figure 1(c)).



3. Computational details

Computations were carried out with DFT-based approaches as implemented in the Vienna *Ab initio* Simulation Package (VASP 5.4.4) [101, 130–133], using plane-wave basis sets in conjunction with the projector augmented wave (PAW) method [134, 135]. The primitive zincblende cell was used throughout. The basis set energy cutoff of 450 eV, the electronic energy convergence criteria of 10^{-6} eV, and the force convergence of 10^{-2} eV/Å were used. Reciprocal space was sampled with a $10 \times 10 \times 10$ Γ -centered Monkhorst-Pack k-point mesh [136]. We used these settings for all the solids studied in this work. The convergence test for k-mesh and plane wave cutoff are presented in figure S1. Optimizations of the primitive cells were performed using the Perdew–Burke–Ernzerhof (PBE) exchange–correlation functional [106] with the semi-empirical dispersion correction scheme DFT-D3 with a Becke–Johnson type damping function [137, 138]. We also tested other approaches to describe dispersion interactions (table S1, figure S2). The best agreement between the optimized and experimental lattice parameters were found using PBE-D3(BJ) approach. Other methods to treat dispersion interaction delivered less good agreement. The geometry optimizations were carried out by the consecutive volume and position optimization until convergence was reached. For every set of lattice parameter values investigated, all atomic positions were optimized.

For the bandgap and band structure calculations, the TB09 functional was used [111] including spin–orbit coupling. This had previously been used to give an excellent agreement with the experimental bandgaps for this compound class [105, 111–116]. The band energies for all the different configurations were re-normalized to the respective VBM. We limited our calculations to a range of $\pm 10\%$ strain by applying constrained optimizations as outlined in the previous section. This is in the order of magnitude of pressures (10 to several 100 GPa) achievable in modern experiments [33, 139–150]. We indicate tensile strain with a ‘+’ sign to emphasize the positive strain value and to make it easier for the reader to distinguish it from compressive strain values, which are denoted with a ‘–’ sign.

The contribution of the atomic orbitals at the different k-points on the bands was calculated by projecting the plane waves on the minimal basis set using LOBSTER [151, 152].

4. Results

4.1. Unstrained structures

Before we discuss the influence of strain, the unstrained materials investigated here shall briefly be presented. Regarding the sign convention, we define positive strain to correspond to expansion (tensile strain) and negative strain as compression (compressive strain). The strain values were calculated according to equation (1).

$$\text{strain}(\%) = (a_f - a_{eqm})/a_{eqm} \times 100 \quad (1)$$

Here, a_f is the lattice parameter in the strained structure while a_{eqm} is the equilibrium lattice parameter. The equilibrium lattice parameters for all materials investigated were computed with the PBE-D3(BJ) approach and are given in table 1. The good agreement with the experimental lattice parameters (maximum deviation of 0.09 Å or 1.3%) lends confidence to the accuracy of the theoretical approach.

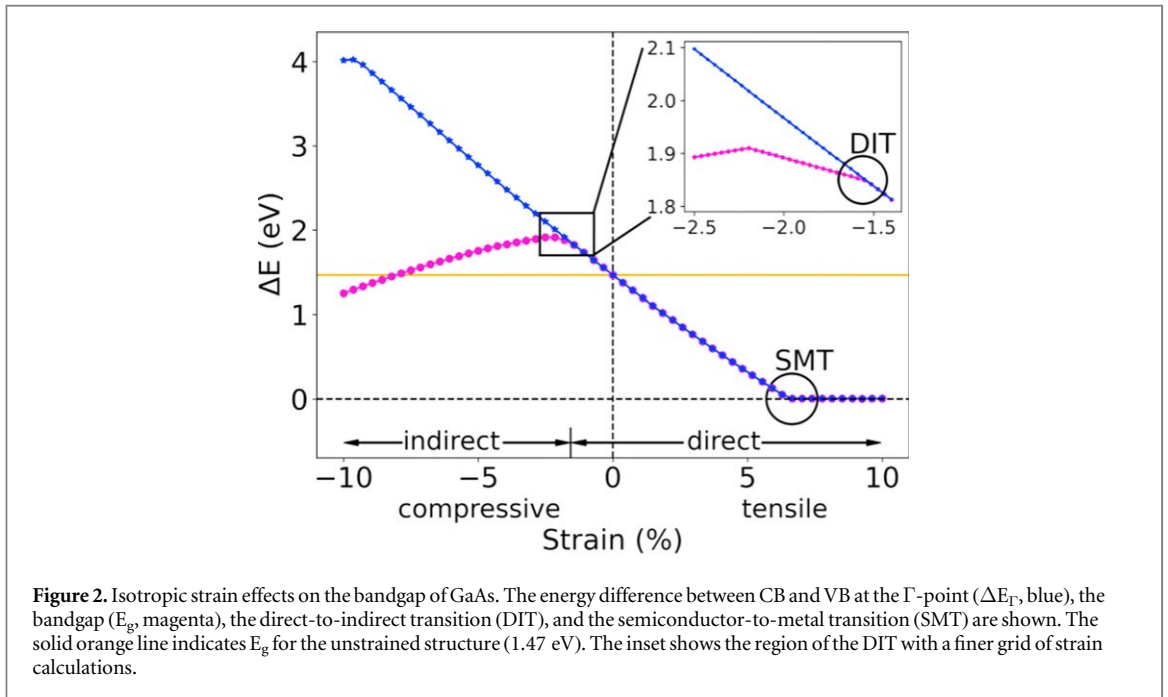


Figure 2. Isotropic strain effects on the bandgap of GaAs. The energy difference between CB and VB at the Γ -point (ΔE_{Γ} , blue), the bandgap (E_g , magenta), the direct-to-indirect transition (DIT), and the semiconductor-to-metal transition (SMT) are shown. The solid orange line indicates E_g for the unstrained structure (1.47 eV). The inset shows the region of the DIT with a finer grid of strain calculations.

Table 1. Computed (PBE-D3(BJ)) optimized unstrained lattice parameters (\AA) for the materials investigated in comparison to experimental reference values at 0 K.

| System | Si | GaP | GaAs | GaSb | InP | InAs | InSb |
|----------------------|-------|-------|-------|-------|-------|-------|-------|
| Calculation | 5.421 | 5.474 | 5.689 | 6.134 | 5.939 | 6.138 | 6.556 |
| Experiment [38, 129] | 5.430 | 5.442 | 5.642 | 6.082 | 5.861 | 6.050 | 6.469 |

4.2. Gallium arsenide

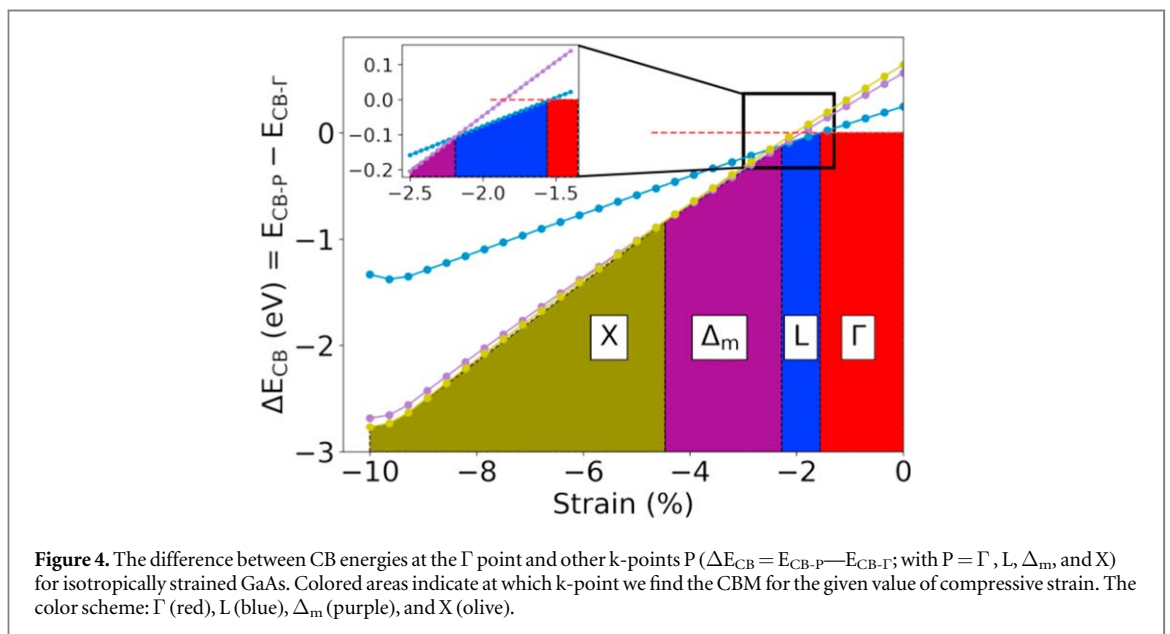
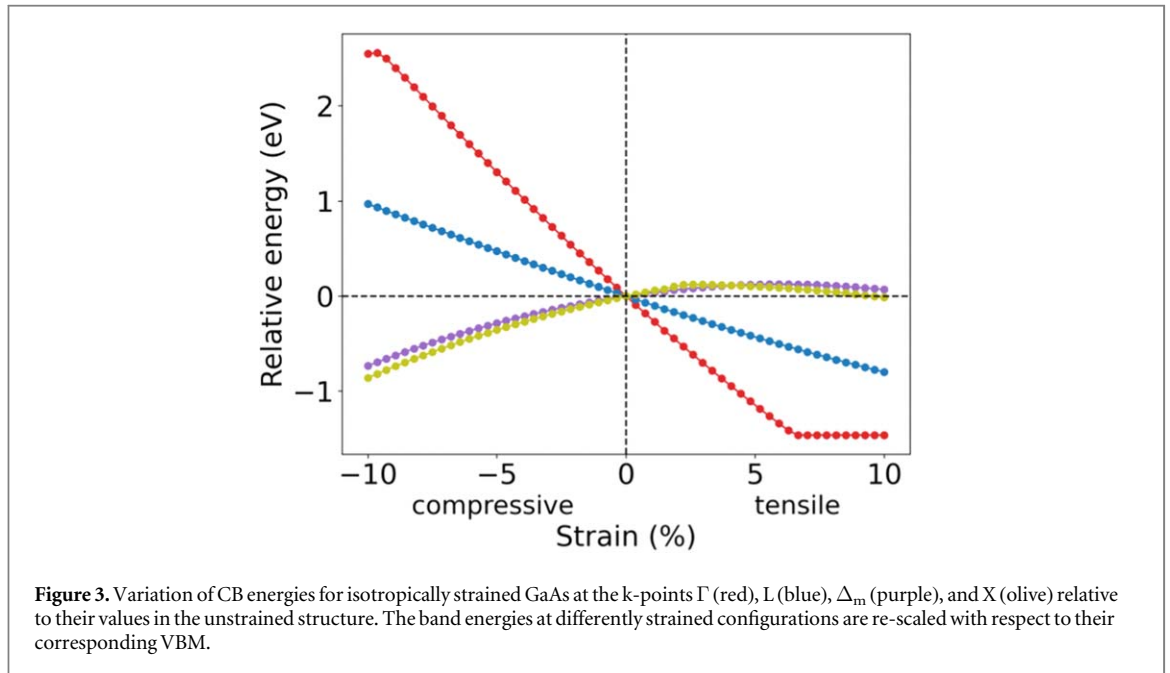
4.2.1. Isotropic strain

First, we present the bandgap variation of GaAs under the application of isotropic strain in a range of $\pm 10\%$ around the unstrained lattice parameter. Figure 2 shows the variation of the energy difference between the conduction band (CB) and the valence band (VB) at the Γ point (ΔE_{Γ}), as well as the bandgap (E_g), as a function of strain. Here, and throughout the manuscript, we distinguish between these two energy differences. For a direct bandgap material, both values are the same. If E_g is smaller than ΔE_{Γ} this indicates an indirect bandgap. A strain value where the two curves start deviating thus indicates a direct-to-indirect (DIT) bandgap transition point.

Under tensile strain, E_g decreases until, at $+6.78\%$ strain, the bandgap vanishes, corresponding to a semiconductor-to-metal transition (SMT). In this case, the E_g curve coincides with the ΔE_{Γ} curve throughout, indicating a direct bandgap. Under compressive strain, however, the E_g curve initially follows the ΔE_{Γ} curve until -1.56% strain, where the E_g curve then separates from the ΔE_{Γ} curve. Although ΔE_{Γ} still increases under further strain, the bandgap starts to decrease. Thus, we have a DIT point here.

To understand the origin of this deviation, we look at the band structures computed at each strain value. The band structures can be found in the supporting information (figures S3(a), (b)). We find that the VBM remains at the Γ point not only here but for all materials and strain regimes investigated. Only the CBM changes its position in k-space when strain is applied. Thus, the change in CBM under compressive strain determines the change in the nature of bandgap. Figure 3 shows the change in CB energies for strained GaAs relative to their values for the unstrained structure at four high-symmetry points in reciprocal space: Γ , L, Δ_m , and X points. This shows that the CB energies at the Γ and L points decrease under tensile strain with a slight increase for Δ_m and X points. The largest change is found at the Γ point, followed by L, Δ_m , and X. As unstrained GaAs is a direct bandgap semiconductor, this signifies that the bandgap remains direct under tensile strain, to begin with. Subsequently, at $+6.78\%$ strain, the CBM and VBM become degenerate, which results in the SMT.

For compressive strain, however, the CB energies at the Γ and L point increase while a slight decrease is found at the Δ_m and X points (figure 3). This results in an increase in the direct bandgap for small strain values. Since CB at the Γ point changes the most with strain, beyond -1.56% strain it supersedes the energy at the L point. This results in the CBM shifting from the Γ to the L point and a DIT. CB energy at the Γ point increases

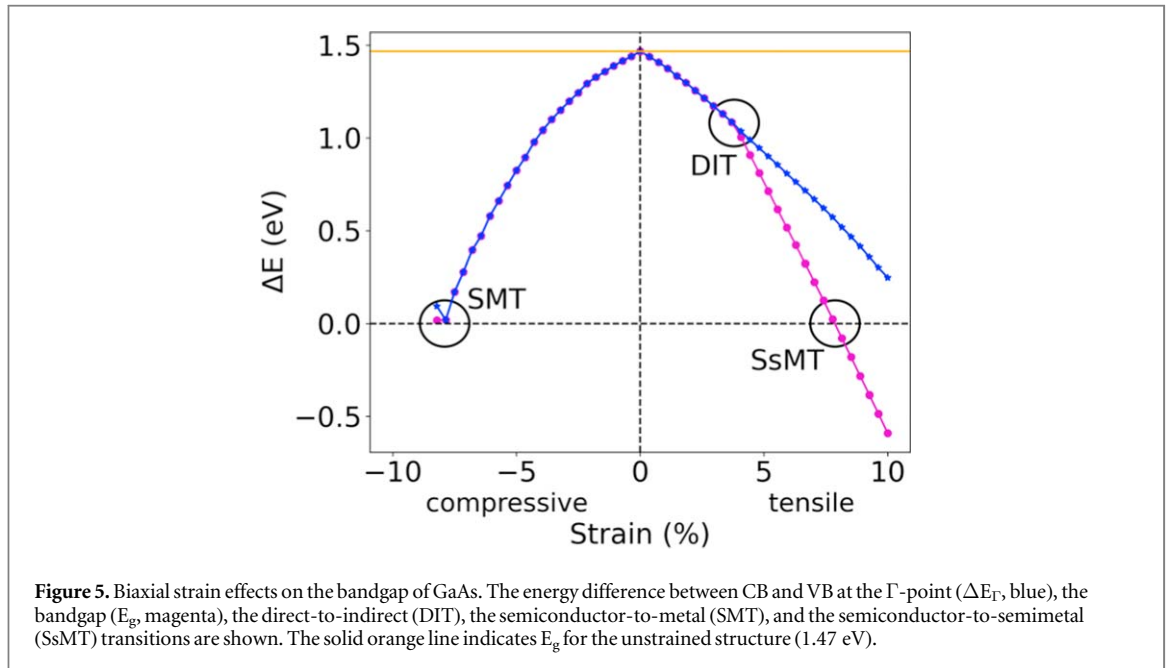


further resulting in a steep increase of ΔE_{Γ} for high strain values (figure 2). CB at the L point increases much slower in energy, flattening the E_g curve and even producing bandgap decrease at high compressive strain (figure 2).

Further, by comparing the difference in CB energies at the Γ , L, Δ_m , and X points, different ‘transition points’ are estimated (figure 4). The first transition is from Γ to L at -1.56% strain (DIT), the second from L to Δ_m at -2.28% strain, and the third from Δ_m to X at -4.47% strain. Increasing the resolution in the k points further reveal that, unlike the sharp first and second transitions, the third is much smoother (figure S3(c)). During the third transition, the CBM start to flatten out with strain, until at -6.78% when the X point also become part of the CBM-plateau. After that, the plateau start to shrink towards the X point.

4.2.2. Biaxial strain

The effect of the biaxial strain on the bandgap is shown in figure 5 (band structures are shown in figures S3(d), (e)). The bandgap decreases under both compressive and tensile strain. During compression, the E_g curve coincides with ΔE_{Γ} throughout. The CBM always remains at the Γ point, and hence, the bandgap remains direct. Only for very high compressive strain values (beyond -7.86%), the CBM and VBM become degenerate,



leading to an SMT. For tensile strain, a DIT is found at + 3.52% strain, exemplified by the E_g curve splitting from ΔE_{Γ} in figure 5.

Under further tensile strain, the bandgap continues to decrease until GaAs become a semimetal at + 8.00% strain. Thus, we observe a semiconductor to semimetal transition (SsMT). By comparing the difference in CB energies at the Γ , L, Δ_m , and X points (figure S4) we find the DIT to correspond to a Γ to Δ_m transition. No further transition points are found here.

4.2.3. Uniaxial strain

The uniaxial strain model in our case is equivalent to the biaxial strain model. This is true because we consider the [001] crystal orientation in the zincblende crystal grown on the [001] surface of another zincblende substrate, and the uniaxial strain is then applied in the $\langle 100 \rangle$ direction (figure 1(a)). In this configuration, relaxing the lattice parameter in the z-direction at fixed in-plane (x and y) lattice parameters (a_x) is equivalent to fixing it in the z-direction at the value a , and relaxing the in-plane parameters. For the uniaxial strain in other crystal orientations or directions, this equivalence is not true, because of finite off-diagonal stress tensor elements [118, 153, 154].

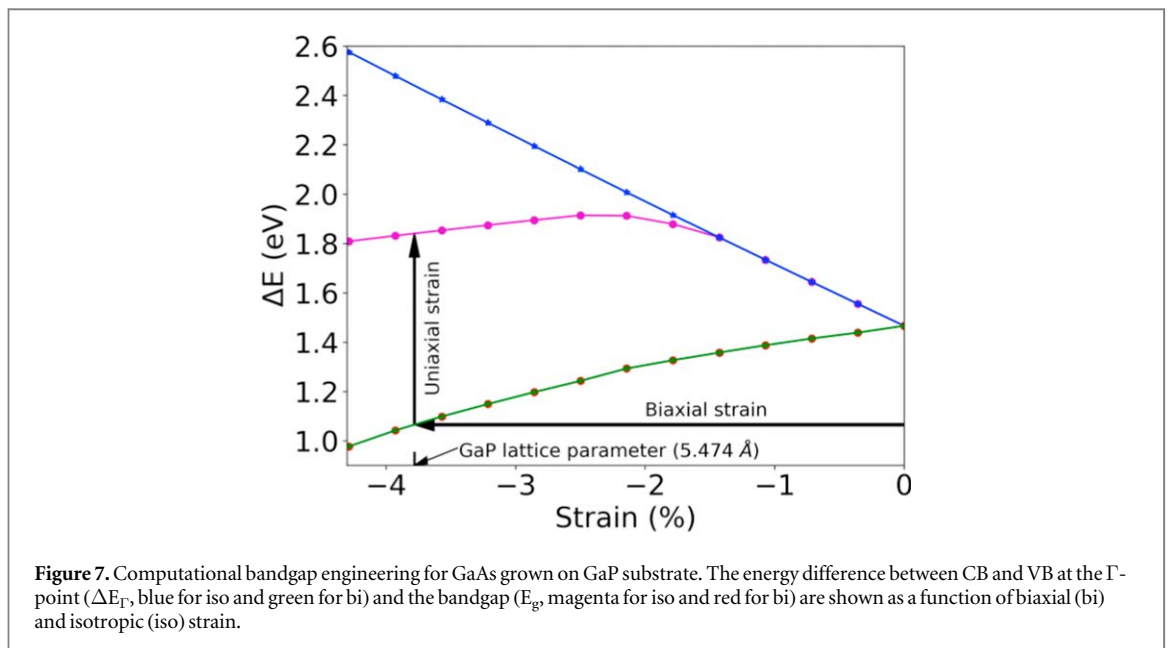
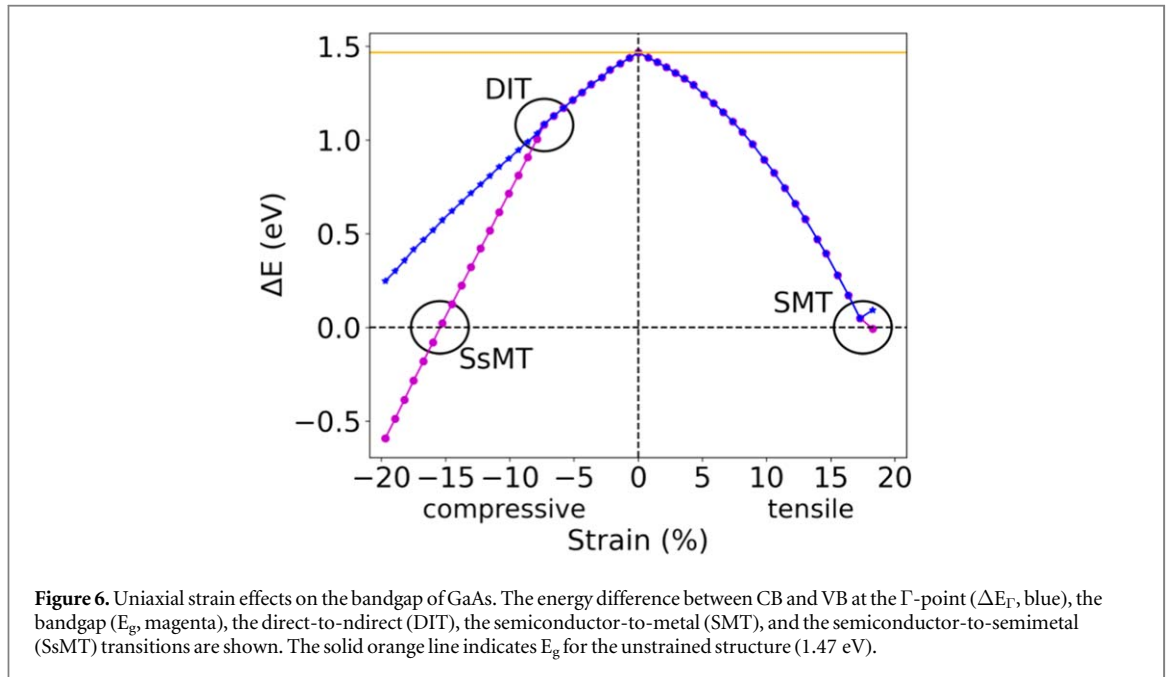
Therefore, we use the data from the previous subsection and now present them as a function of the out-of-plane lattice parameter (figure 6). This is essentially a mirrored version of figure 5 with a changed scaling of the x -axis. Now, we find the DIT at -7.30% strain, the SsMT at -15.43% strain, and the SMT at $+17.73\%$ strain, respectively.

4.2.4. Combining biaxial and uniaxial strain

Uniaxial and biaxial strain are shown in the previous sections to be useful strategies to tune the magnitude of the bandgap. However, one major goal in tuning the electronic structure is changing the nature of the bandgap. As shown in the previous subsection, this however, can not be achieved via biaxial compressive strain, which is one of the most common experimental realizations of strain via epitaxial growth. We will now show that in a new strategy by combining this biaxial compressive strain with uniaxial strain changes in the nature of the bandgap can in fact be achieved.

In a thought experiment (figures 7, S5), the desired material (GaAs) is first ‘grown’ epitaxially on a substrate with a smaller lattice constant (e.g., GaP), resulting in compressive biaxial strain (here: -3.78%). Such epitaxial growth would lead to expansion of the z-lattice parameter. Subsequently, uniaxial compressive strain (e.g., pressure) could be applied along the z-direction to compress the z-lattice parameter. We assume that the in-plane lattice parameters would not relax upon compression of the z-lattice parameter. We thus model a case here where strain is accumulated inside the epitaxial layer without creating defects. In this case, we find a DIT point at -3.2% uniaxial strain (figure 8).

Next, we further generalize this strategy. Figure 9 shows the required uniaxial compressive strain for the DIT in biaxial compressively strained GaAs. No transition can be achieved for biaxial compressive strain below 1.56%, as both the biaxial and isotropic strain would have the same direct nature of the bandgap (figures 7, S6).



A similar strategy can be applied for the indirect to direct transition (IDT) in biaxial tensile strained GaAs (figure S6). In this case, one would need to expand the z -lattice parameter for the transition. Experimentally, this can be achieved e.g., by thermal expansion. As shown in figure S7, this however, is only reasonable for biaxial strain smaller than 4.5%. For higher biaxial strain the large required amount of uniaxial tensile strain can not be achieved by thermal expansion only.

4.3. Gallium phosphide

Gallium phosphide is an indirect bandgap semiconductor. Next, we demonstrate the application of strain on the bandgap engineering. Figure 10 shows the variation in CB energy for GaP under isotropic strain at the Γ , L, Δ_m , and X points relative to their unstrained values (band structures are shown in figures S3(f), (g)).

For compressive strain, the CB at Γ and L point increases in energy, while it decreases at the Δ_m and X points. As GaP is an indirect bandgap semiconductor at equilibrium, the nature of the bandgap thus does not change. For tensile strain, the CB energy at the Γ and L points decreases strongly while we find a small increase at the Δ_m and X points. This lead to a shift of the indirect bandgap from Δ_m to L at + 1.43% tensile strain (figure 11). As

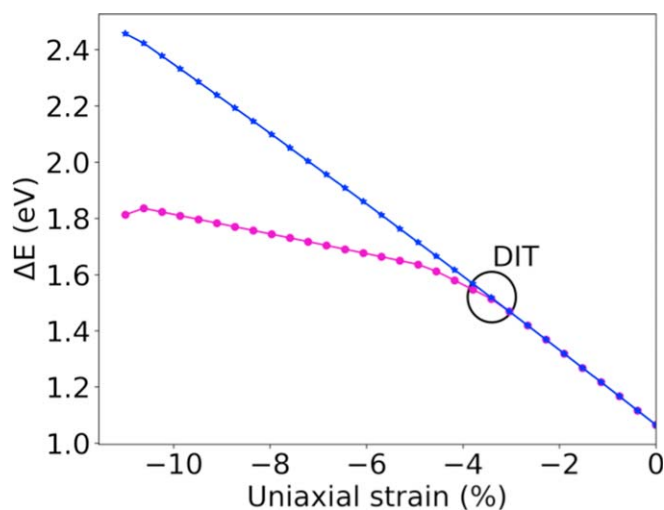


Figure 8. Change in bandgap as a function of uniaxial compressive strain along z -lattice parameter for GaAs grown on GaP [001] substrate. The energy difference between CB and VB at the Γ -point (ΔE_{Γ} , blue), the bandgap (E_g , magenta), and the direct-to-indirect (DIT) transition are shown.

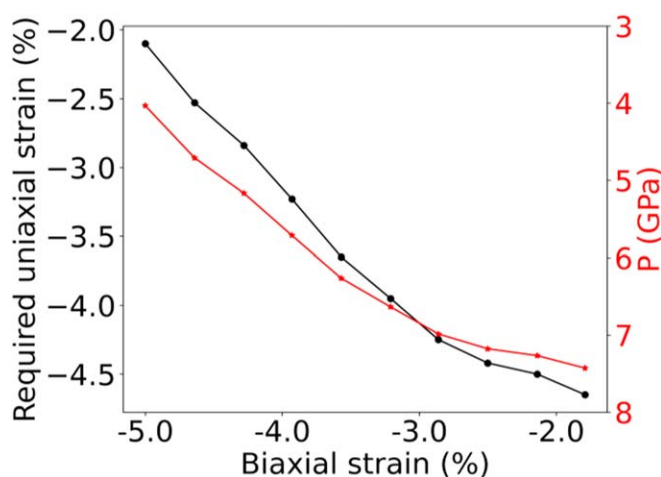


Figure 9. Variation of required uniaxial compressive strain for the direct to indirect transition (DIT) in biaxially compressively strained GaAs. 3rd order Birch-Murnaghan equation [155] is used for the strain to pressure conversion. We use reference [156, 157] for the bulk modulus and its first derivative data for the conversion.

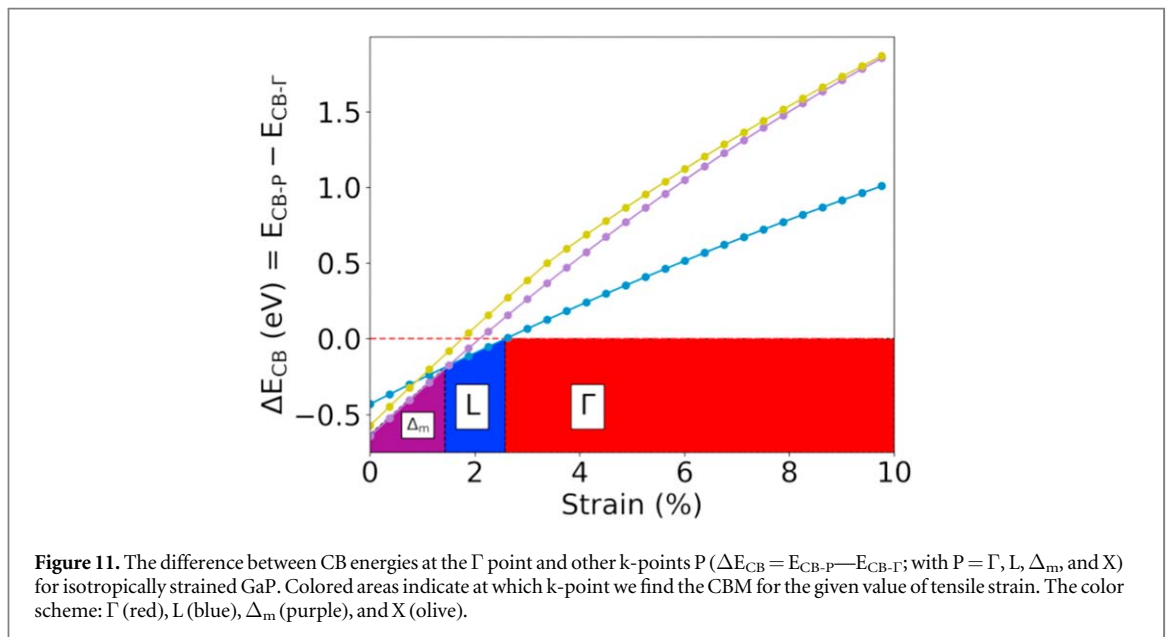
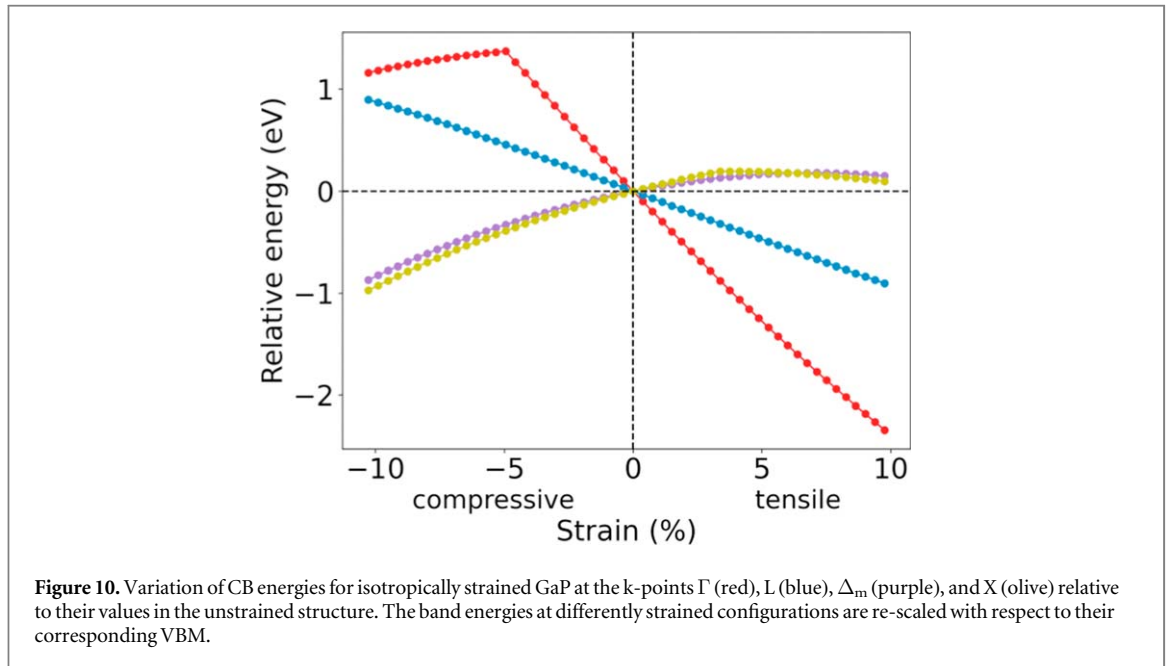
the slope for the energy at the Γ point is largest (figure 10), we find an indirect to direct transition (IDT) at +2.63% strain (figures 11, S8).

The result for biaxial strain is shown in figure 12 (band structures are shown in figures S3(h), (i)). Here, we find no change in the nature of the bandgap throughout the entire range of compressive and tensile strain. The bandgap remains indirect throughout. For very high strain values, we find SsMTs at +8.45% and -9.83% strain.

The uniaxial conversion of the data in figure 12, as is explained for GaAs case, would not have any further special interest (figure S9). Similar to GaAs, by combining biaxial and uniaxial strain in GaP one can in principle achieve IDT. However, this would require large uniaxial tensile strain ($> 8\%$), which can not be realized by thermal expansion (figure S10).

4.4. Silicon, GaSb, InP, InAs, and InSb

We also applied the approach outlined in detail for GaAs and GaP to other interesting semiconductor materials. Tables 2 and 3 summarizes the main results for Si, GaSb, InP, InAs, and InSb. In all cases, the VBM stays at the Γ point throughout the strain regimes applied. Thus, the position of the CBM in reciprocal space determines the nature of the bandgap.



Si and GaP are indirect bandgap semiconductors in their equilibrium structure while the other materials discussed show direct bandgaps. Accordingly, Si and GaP show IDTs while the other materials show DITs. The strain values where these transitions are found, for isotropic and biaxial strain, are shown in columns 3 and 4 of table 2. For the isotropic strain case, the IDTs are found for tensile strain as already discussed for GaP in the previous section. The value for Si is so high (+ 10.31%) that it will certainly be out of range for any experiment. The DITs are found for isotropic compressive strain throughout, with strain values ranging from -1.00% (GaSb) to -7.41% (InAs).

For biaxial strain, DITs are found only for GaAs, GaSb, and InP. In all cases, a significant tensile strain would be necessary. For many materials, transitions are found to other k-points in reciprocal space where the nature of the bandgap stays indirect. This is shown in the right-hand part of the table. [more details are shown in figures S11, S12, and S13.]

Notably, In-based compound semiconductors show the DIT points at much higher strain values compared to Ga-based materials. Figure 13 shows the contribution of the atomic orbitals to the CB for unstrained GaAs and InAs. At the decisive points in k-space (Γ , L, and X points) the group III elements show the major orbital contributions to CB. Furthermore, while the s-orbital contributions (Ga(4s), In(5s)) dominate at the Γ point, the L point and the X point show high p-orbital contributions (Ga(4p), In(5p)). Since the energy gap between 5s and

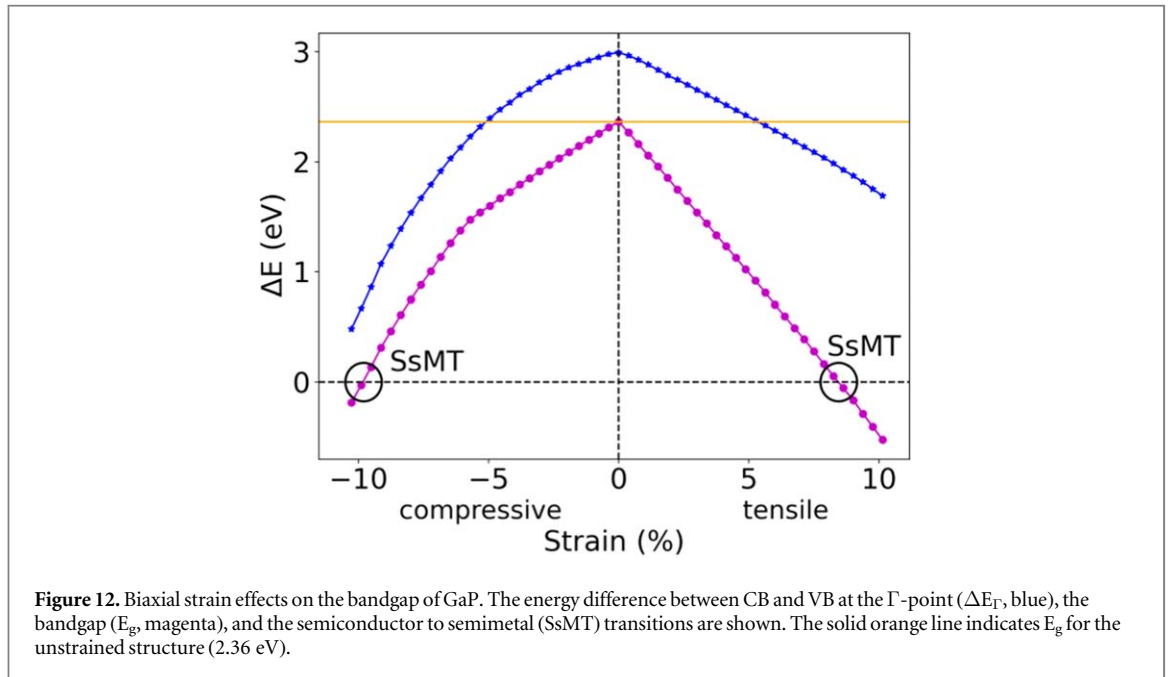


Figure 12. Biaxial strain effects on the bandgap of GaP. The energy difference between CB and VB at the Γ -point (ΔE_{Γ} , blue), the bandgap (E_g , magenta), and the semiconductor to semimetal (SsMT) transitions are shown. The solid orange line indicates E_g for the unstrained structure (2.36 eV).

Table 2. Change in the nature of bandgap for different III-V semiconductor materials for isotropic and biaxial strain.

| System | Type ^a | Transition | | CBM transition path | |
|--------|-------------------|---------------------|-------------|---|--|
| | | Isotropic (%) | Biaxial (%) | Isotropic | Biaxial |
| Si | IDT | +10.31 ^b | × | $\Delta_m \rightarrow L \rightarrow \Gamma$ | $\Delta_m \rightarrow K \rightarrow L$ |
| GaP | IDT | +2.63 | × | $\Delta_m \rightarrow L \rightarrow \Gamma$ | $\Delta_m \rightarrow L$ |
| GaAs | DIT | -1.56 | +3.52 | $\Gamma \rightarrow L \rightarrow \Delta_m \rightarrow X$ | $\Gamma \rightarrow \Delta_m$ |
| GaSb | DIT | -1.00 | +3.71 | $\Gamma \rightarrow L \rightarrow \Delta_m$ | $\Gamma \rightarrow \Delta_m$ |
| InP | DIT | -4.40 | +7.66 | $\Gamma \rightarrow X$ | $\Gamma \rightarrow \Delta_m$ |
| InAs | DIT | -7.41 | × | $\Gamma \rightarrow X$ | × |
| InSb | DIT | -5.18 | × | $\Gamma \rightarrow L \rightarrow \Delta_m$ | × |

^a Direct to indirect transition (DIT) and indirect to direct transition (IDT).

^b Estimated using linear extrapolation.

× No transitions within $\pm 10\%$ strain.

Table 3. Semiconductor to metal transition (SMT) and semiconductor to semimetal transition (SsMT) points for different III-V semiconductor materials under isotropic and biaxial strain. ΔE_{Γ} corresponds to the energy difference between CB and VB at the Γ point.

| System | ΔE_{Γ} (eV) | SMT | | SsMT | |
|--------|--------------------------|---------------------|--------------|---------------|--------------|
| | | Isotropic (%) | Biaxial (%) | Isotropic (%) | Biaxial (%) |
| Si | 3.14 | +15.00 ^a | × | × | +3.70, -6.50 |
| GaP | 2.99 | +13.00 ^a | × | × | +8.45, -9.83 |
| GaAs | 1.81 | +6.67 | -7.86 | × | +8.00 |
| GaSb | 0.64 | +2.85 | -5.00 | × | +5.07 |
| InP | 1.43 | +8.20 | -9.90 | × | +10.38 |
| InAs | 0.36 | +2.10 | +4.74, -4.36 | × | × |
| InSb | 0.03 | +0.34 | +0.34, -0.34 | × | × |

^a Estimated using linear extrapolation.

× No transitions within $\pm 10\%$ strain.

5p orbital in In is much higher than 4s and 4p in Ga, changing group III from Ga to In increases the energy difference between Γ & X and Γ & L, respectively (see figure 14). Under strain, the decrease of these energy differences ultimately results in the shift of CBM from the Γ to the L and/or X point (figures S3, S14). Therefore, the higher this relative energy difference, the higher the requirement of the amount of strain needed to reach the

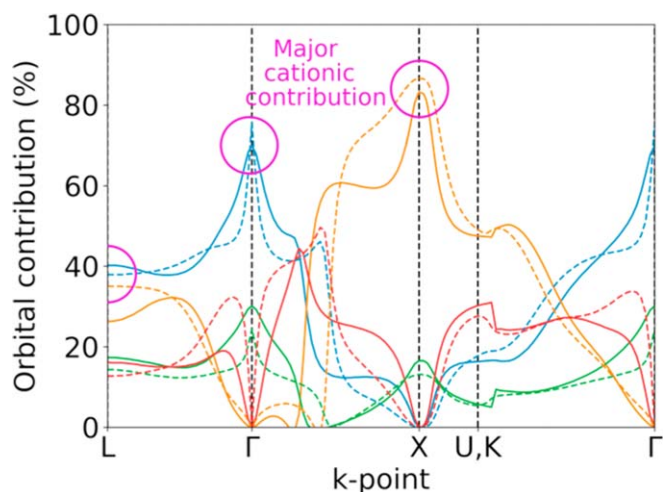


Figure 13. Atom resolved orbital contributions for unstrained GaAs and InAs CB. Solid sky blue: Ga(4s), dotted sky blue: In(5s), solid orange: Ga(4p), dotted orange: In(5p), solid green: As(4s) in GaAs, dotted green: As(4s) in InAs, solid red: As(4p) in GaAs, dotted red: As(4p) in InAs.

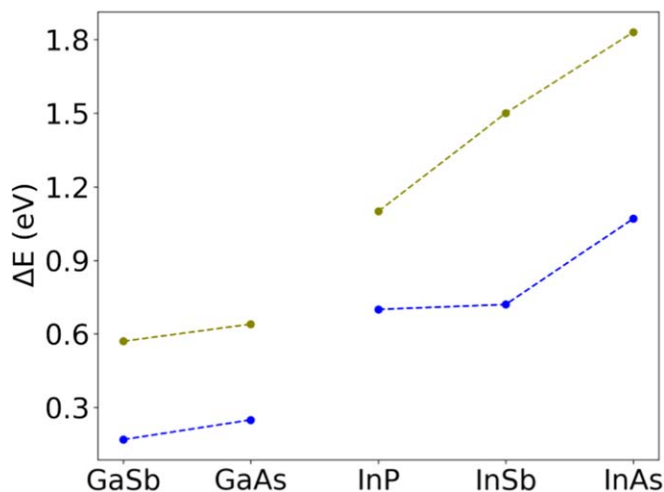


Figure 14. The relative energy differences between Γ & X (olive) and Γ & L (blue) at the CB for unstrained Ga and In series binaries (figure S15).

DIT point (figures S12, S13). This results in DIT points at larger strain values for In-based compounds in comparison to the Ga-based compounds. Note that, as the above reasoning is qualitative, for simplicity, we do not consider the Δ_m point here.

Table 3 summarizes the SMTs and SsMTs for the compound semiconductors investigated. These transitions depend on the closing of the CBM and VBM gaps. As the VBM always remains at the Γ point, these transition points therefore depend on ΔE_{Γ} . Figure 15 shows the SMTs under isotropic strain for different systems in relation to their corresponding ΔE_{Γ} . As the ΔE_{Γ} increases, so does the S(s)MT values.

In table 4, we compare our calculated results with the available experimental findings. The results match quite well. In experiments, the DIT points were measured in terms of applied hydrostatic pressure. Using the third-order Birch-Murnaghan equation [155] we converted the measurement in terms of strains. We used reference [156, 157] for the bulk modulus and its first derivative data for the conversion. For GaAs, the strain region when CBM is visible at the L point is very small (only 0.72% strain window), figure 4. Therefore, we conclude that in the experiment this region was most likely missed (table 4, 3rd row last column). For InSb a deviation of 0.21 eV was found for the equilibrium bandgap. This, in turn, would result in the overestimation of the DIT point in our calculation (table 4, 7th row last column).

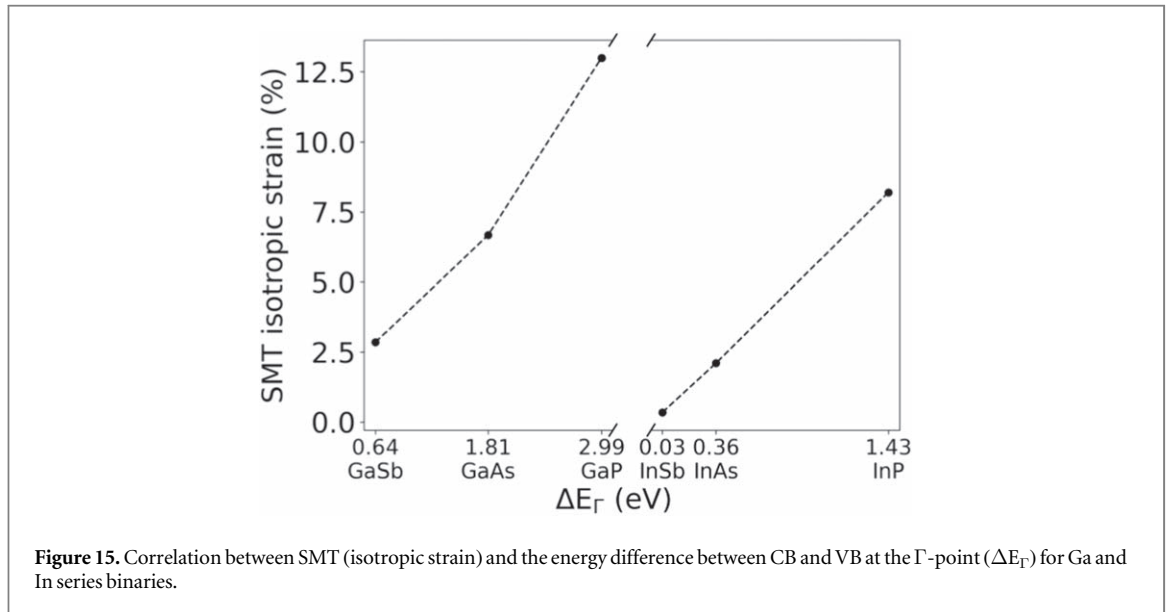


Figure 15. Correlation between SMT (isotropic strain) and the energy difference between CB and VB at the Γ -point (ΔE_{Γ}) for Ga and In series binaries.

Table 4. The calculated equilibrium (unstrained) bandgaps, DIT points, and the DIT transitions compared with the experiments.

| System | Equilibrium bandgap (eV) | | Isotropic strain DIT (%) | | Transitions | |
|--------|--------------------------|-------------------------|--------------------------|--------------------|------------------------|--------------------------|
| | Calculated | Experiment ^a | Calculated | Experiment | Calculated | Experiment |
| Si | 1.19 | 1.17 | — | — | — | — |
| GaP | 2.36 | 2.34 | — | — | — | — |
| GaAs | 1.47 | 1.52 | -1.56 | -2.75 ^b | $\Gamma \rightarrow L$ | $\Gamma \rightarrow X^b$ |
| GaSb | 0.64 | 0.81 | -1.00 | -1.54 ^b | $\Gamma \rightarrow L$ | $\Gamma \rightarrow L^b$ |
| InP | 1.43 | 1.42 | -4.40 | -5.16 ^c | $\Gamma \rightarrow X$ | $\Gamma \rightarrow X^c$ |
| InAs | 0.36 | 0.41 | -7.41 | -8.17 ^c | $\Gamma \rightarrow X$ | $\Gamma \rightarrow X^c$ |
| InSb | 0.03 | 0.24 | -5.18 | -4.23 ^c | $\Gamma \rightarrow L$ | $\Gamma \rightarrow X^c$ |

^a Experimental bandgaps are at 0 K [38, 129].

^b Reference [28].

^c Reference [28, 157, 158].

— For Si and GaP IDTs are in the tensile strain region.

No experimental data are available.

5. Conclusions

We calculated the strain-induced bandgap variation for various III-V binary compounds focusing on GaAs and GaP for a detailed analysis. We investigated compressive and tensile strain in the range of $\pm 10\%$ around the unstrained structure, which enabled the tuning of the bandgap over a wide range. Furthermore, we showed the presence of direct-to-indirect and indirect-to-direct transitions in the nature of bandgap of these materials based on the analyses of differences between valence and conduction band energies at the Γ -point (ΔE_{Γ}) and the bandgap (E_g). Only 4 special k-points were found to be responsible for the direct-indirect transitions: Γ , L, Δ_m , and X. The valence band maximum stayed at the Γ point throughout the strain regimes applied. Thus, the position of the conduction band minimum alone in reciprocal space determined the nature of the band gap. By combining the biaxial and uniaxial strain, we proposed a strategy for the realization of direct-indirect transitions in the regions where otherwise no transition could be achieved by single type of strain. With this work, we laid the foundation for further efforts with multinary compound semiconductors under strain.

Acknowledgments

We thank the German Research Foundation (DFG) for funding via the Research Training Group 'Functionalization of Semiconductors' (GRK 1782). We acknowledge computational resources provided by HRZ Marburg, GOETHE-CSC Frankfurt, ZIH Dresden & HLR Stuttgart. We thank Prof. Dr. Kerstin Volz from Philipps-Universität Marburg for discussions and continued support.

Data availability statement

The data that support the findings of this study are openly available at the following URL/DOI: <https://doi.org/10.17172/NOMAD/2022.08.20-2>.

ORCID iDs

Badal Mondal  <https://orcid.org/0000-0002-0522-1254>

Ralf Tonner-Zech  <https://orcid.org/0000-0002-6759-8559>

References

- [1] Soref R A 1993 Silicon-based optoelectronics *Proc. IEEE* **81** 1687–706
- [2] Yu P Y and Cardona M 2010 *Fundamentals of Semiconductors* (Berlin, Heidelberg: Springer Berlin Heidelberg)
- [3] Hepp T, Lehr J, Güntel R, Maßmeyer O, Glowatzki J, Ruiz Perez A, Reinhard S, Stolz W and Volz K 2022 Room-temperature laser operation of a (Ga,In)As/Ga(As,Bi)/(Ga,In)As W-type laser diode *Electron. Lett.* **58** 70–2
- [4] Fuchs C *et al* 2018 High-temperature operation of electrical injection type-II (GaIn)As/Ga(AsSb)/(GaIn)As ‘W’-quantum well lasers emitting at 1.3 μm *Sci. Rep.* **8** 1422
- [5] Mokkapatil S and Jagadish C 2009 III-V compound SC for optoelectronic devices *Mater. Today* **12** 22–32
- [6] Dimroth F *et al* 2016 Four-Junction Wafer-Bonded Concentrator solar cells *IEEE J. Photovoltaics* **6** 343–9
- [7] Létay G and Bett A 2001 EtaOpt—a program for calculating limiting efficiency and optimum bandgap structure for multi-bandgap solar cells and TPV cells *Proc. of the 17th European Photovoltaic Solar Energy Conf. (2001)* 178–81
- [8] Mitchell B, Peharz G, Siefer G, Peters M, Gandy T, Goldschmidt J C, Benick J, Glunz S W, Bett A W and Dimroth F 2011 Four-junction spectral beam-splitting photovoltaic receiver with high optical efficiency *Prog. Photovoltaics Res. Appl.* **19** 61–72
- [9] Philipps S P, Dimroth F and Bett A W 2018 High-Efficiency III–V multijunction solar cells *McEvoy’s Handbook of Photovoltaics* ed S A Kalogirou (Amsterdam: Elsevier) 439–72
- [10] Kneissl M, Seong T-Y, Han J and Amano H 2019 The emergence and prospects of deep-ultraviolet light-emitting diode technologies *Nat. Photonics* **13** 233–44
- [11] Asif Khan M, Bhattarai A, Kuznia J N and Olson D T 1993 High electron mobility transistor based on a GaN-Al_xGa_{1-x}N heterojunction *Appl. Phys. Lett.* **63** 1214–5
- [12] Wu J, Chen S, Seeds A and Liu H 2015 Quantum dot optoelectronic devices: lasers, photodetectors and solar cells *J. Phys. D: Appl. Phys.* **48** 363001
- [13] Nakamura S, Mukai T and Senoh M 1991 High-power GaN P-N junction blue-light-emitting diodes *Jpn. J. Appl. Phys.* **30** L1998–2001
- [14] Park J-S, Tang M, Chen S and Liu H 2020 Heteroepitaxial growth of III-V semiconductors on silicon *Crystals* **10** 1163
- [15] Bett A W, Dimroth F, Stollwerck G and Sulima O V 1999 III-V compounds for solar cell applications *Appl. Phys. A Mater. Sci. Process.* **69** 119–29
- [16] Zimmermann H 2000 III–V semiconductor materials on silicon *Integrated Silicon Optoelectronics* (Berlin, Heidelberg: Springer Berlin Heidelberg) 167–85
- [17] Stillman G E, Robbins V M and Tabatabaie N 1984 III-V compound semiconductor devices: optical detectors *IEEE Trans. Electron Devices* **31** 1643–55
- [18] Shah N J and Pei S-S 1989 III-V device technologies for electronic applications *AT&T Tech. J.* **68** 19–28
- [19] Kuech T F 2016 III-V compound semiconductors: growth and structures *Prog. Cryst. Growth Charact. Mater.* **62** 352–70
- [20] Yu E T and Manasreh M O 2002 *III-V Nitride Semiconductors: Applications and Devices* (Boca Raton London New York: CRC Press, Taylor & Francis group) 978-1560329749
- [21] Cheng K Y 2020 *III-V Compound Semiconductors and Devices* (Cham: Springer International Publishing)
- [22] Kosten E D, Atwater J H, Parsons J, Polman A and Atwater H A 2013 Highly efficient GaAs solar cells by limiting light emission angle *Light: Sci. Appl.* **2** e45–45
- [23] Goni A R, Strössner K, Syassen K and Cardona M 1987 Pressure dependence of direct and indirect optical absorption in GaAs *Phys. Rev. B* **36** 1581
- [24] Tsay Y-F and Bendow B 1976 Pressure dependence of the direct energy gap of GaAs *Phys. Rev. B* **14** 2681–2
- [25] Jayaraman A, Kosicki B B and Irvin J C 1968 $\Delta 1$ Conduction-Band minimum of Ge from high-pressure studies on p-n junctions *Phys. Rev.* **171** 836
- [26] Müller H, Trommer R, Cardona M and Vogl P 1980 Pressure dependence of the direct absorption edge of InP *Phys. Rev. B* **21** 4879
- [27] Welber B, Kim C K, Cardona M and Rodriguez S 1975 Dependence of the indirect energy gap of silicon on hydrostatic pressure *Solid State Commun.* **17** 1021
- [28] Edwards A L and Drickamer H G 1961 Effect of pressure on the absorption edges of some III-V, II-VI, and I-VII compounds *Phys. Rev.* **122** 1149–57
- [29] Strössner K, Ves S, Kim C K and Cardona M 1987 Pressure dependence of the lowest direct absorption edge of ZnTe *Solid State Commun.* **61** 275
- [30] Zallen R and Paul W 1964 Band structure of gallium phosphide from optical experiments at high pressure *Phys. Rev.* **134** A1628–41
- [31] Grivickas P, McCluskey M D and Gupta Y M 2007 Indirect band-gap transitions in GaP shocked along the [100], [110], and [111] axes *Phys. Rev.* **75** 235207
- [32] Grivickas P, McCluskey M D and Gupta Y M 2008 Band-gap luminescence of GaP:S shock compressed to 5GPa *Appl. Phys. Lett.* **92** 142104
- [33] Paul W 1998 *High Pressure in Semiconductor Physics Semiconductors and Semimetals* ed T Suski and W Paul (Amsterdam: Elsevier) 54, 1–48
- [34] Yu P Y and Welber B 1978 High pressure photoluminescence and resonant Raman study of GaAs *Solid State Commun.* **25** 209–11
- [35] Olego D, Cardona M and Müller H 1980 Photoluminescence in heavily doped GaAs. II. Hydrostatic pressure dependence *Phys. Rev. B* **22** 894–903
- [36] Welber B, Cardona M, Kim C K and Rodriguez S 1975 Dependence of the direct energy gap of GaAs on hydrostatic pressure *Phys. Rev. B* **12** 5729–38

- [37] Beyer A, Stolz W, Volz K, Wegele T, Beyer A, Ludewig P and Rosenow P 2015 Metastable cubic zinc-blende III/V semiconductors: Growth and structural characteristics *Prog. Cryst. Growth Charact. Mater.* **61** 46–62
- [38] Vurgafman I, Meyer J R and Ram-Mohan L R 2001 Band parameters for III-V compound semiconductors and their alloys *J. Appl. Phys.* **89** 5815
- [39] Stringfellow G B 2019 Fundamental Aspects of MOVPE *Metalorganic Vapor Phase Epitaxy (MOVPE)* (New York: Wiley) 19–69
- [40] Volz K, Koch J, Höhnsdorf F, Kunert B and Stolz W 2009 MOVPE growth of dilute nitride III/V semiconductors using all liquid metalorganic precursors *J. Cryst. Growth* **311** 2418–26
- [41] Feifel M *et al* 2017 MOVPE grown gallium phosphide–silicon heterojunction solar cells *IEEE J. Photovoltaics* **7** 502–7
- [42] Kunert B, Koch J, Torunski T, Volz K and Stolz W 2004 MOVPE growth experiments of the novel (GaIn)(NP)/GaP material system *J. Cryst. Growth* **272** 753–9
- [43] Volz K, Torunski T, Kunert B, Rubel O, Nau S, Reinhard S and Stolz W 2004 Specific structural and compositional properties of (GaIn)(NAs) and their influence on optoelectronic device performance *J. Cryst. Growth* **272** 739–47
- [44] Veletas J, Hepp T, Volz K and Chatterjee S 2019 Bismuth surface segregation and disorder analysis of quaternary (Ga,In)(As,Bi)/InP alloys *J. Appl. Phys.* **126** 135705
- [45] Wegele T, Beyer A, Ludewig P, Rosenow P, Duschek L, Jandieri K, Tonner R, Stolz W and Volz K 2016 Interface morphology and composition of Ga(NAsP) quantum well structures for monolithically integrated LASERs on silicon substrates *J. Phys. D: Appl. Phys.* **49** 075108
- [46] Hepp T, Nattermann L and Volz K 2019 MOVPE growth and device applications of ternary and quaternary dilute bismide alloys on GaAs substrates *Bismuth-Containing Alloys and Nanostructures* ed S Wang and P Lu (Singapore: Springer) 37–58
- [47] Beyer A, Knaub N, Rosenow P, Jandieri K, Ludewig P, Bannow L, Koch S W, Tonner R and Volz K 2017 Local Bi ordering in MOVPE grown Ga(As,Bi) investigated by high resolution scanning transmission electron microscopy *Appl. Mater. Today* **6** 22–8
- [48] Kükhelhan P, Firoozabadi S, Beyer A, Duschek L, Fuchs C, Oelerich J O, Stolz W and Volz K 2019 Segregation at interfaces in (GaIn)As/Ga(AsSb)/(GaIn)As- quantum well heterostructures explored by atomic resolution STEM *J. Cryst. Growth* **524** 125180
- [49] Volz K, Beyer A, Witte W, Ohlmann J, Németh I, Kunert B and Stolz W 2011 GaP-nucleation on exact Si (001) substrates for III/V device integration *J. Cryst. Growth* **315** 37–47
- [50] Cho A Y 1983 Growth of III–V semiconductors by molecular beam epitaxy and their properties *Thin Solid Films* **100** 291–317
- [51] Dupuis R D 1997 Epitaxial growth of III–V nitride semiconductors by metalorganic chemical vapor deposition *J. Cryst. Growth* **178** 56–73
- [52] Dupuis R D 1984 Metalorganic chemical vapor deposition of III-V semiconductors *Science* **226** 623–9
- [53] Stringfellow G B 1978 VPE growth of III/V semiconductors *Annu. Rev. Mater. Sci.* **8** 73–98
- [54] Dupuis R D 2000 III-V semiconductor heterojunction devices grown by metalorganic chemical vapor deposition *IEEE J. Sel. Top. Quantum Electron.* **6** 1040–50
- [55] Stringfellow G B 2017 Thermodynamic considerations for epitaxial growth of III/V alloys *J. Cryst. Growth* **468** 11–6
- [56] Behet M, Hövel R, Kohl A, Küsters A M, Opitz B and Heime K 1996 MOVPE growth of III–V compounds for optoelectronic and electronic applications *Microelectronics J.* **27** 297–334
- [57] Volz K, Stolz W, Dadgar A and Krost A 2015 Growth of III/Vs on silicon *Handbook of Crystal Growth* (Amsterdam: Elsevier) 1249–300
- [58] Ludewig P, Reinhard S, Jandieri K, Wegele T, Beyer A, Tapfer L, Volz K and Stolz W 2016 MOVPE growth studies of Ga(NAsP)/(BGa)(AsP) multi quantum well heterostructures (MQWH) for the monolithic integration of laser structures on (001) Si-substrates *J. Cryst. Growth* **438** 63–9
- [59] Németh I, Kunert B, Stolz W and Volz K 2008 Heteroepitaxy of GaP on Si: correlation of morphology, anti-phase-domain structure and MOVPE growth conditions *J. Cryst. Growth* **310** 1595–601
- [60] Liebich S *et al* 2011 Laser operation of Ga(NAsP) lattice-matched to (001) silicon substrate *Appl. Phys. Lett.* **99** 071109
- [61] Volk M and Stolz W 2017 Determination of refractive index and direct bandgap of lattice matched BGaP and (BGa)(AsP) materials on exact oriented silicon *J. Appl. Phys.* **122** 235702
- [62] Supple O *et al* 2018 Metalorganic vapor phase epitaxy of III–V-on-silicon: experiment and theory *Prog. Cryst. Growth Charact. Mater.* **64** 103–32
- [63] Chelikowsky J R and Cohen M L 1976 Nonlocal pseudopotential calculations for the electronic structure of eleven diamond and zinc-blende semiconductors *Phys. Rev.* **14** 556–82
- [64] Xiao Z, Goldsman N and Dhar N K 2015 Simulation of Indirect-Direct transformation phenomenon of germanium under uniaxial and biaxial strain along arbitrary orientations *2015 Int. Conf. on Simulation of Semiconductor Processes and Devices (SISPAD) (IEEE)* 397–400
- [65] Fischetti M V and Laux S E 1996 Band structure, deformation potentials, and carrier mobility in strained Si, Ge, and SiGe alloys *J. Appl. Phys.* **80** 2234–52
- [66] Cohen M L and Bergstresser T K 1966 Band structures and pseudopotential form factors for fourteen semiconductors of the diamond and zinc-blende structures *Phys. Rev.* **141** 789–96
- [67] Gonzalez S, Vasileska D and Demkov A A 2002 Empirical pseudopotential method for the band structure calculation of strained-silicon germanium materials *J. Comput. Electron.* **1** 179–83
- [68] Kim J and Fischetti M V 2010 Electronic band structure calculations for biaxially strained Si, Ge, and III–V semiconductors *J. Appl. Phys.* **108** 013710
- [69] Tsay Y F, Gong B, Mitra S S and Vetelino J F 1972 Temperature dependence of energy gaps of some III-V semiconductors *Phys. Rev. B* **6** 2330–6
- [70] Bechiri A, Benmakhlouf F and Bouarissa N 2003 Band structure of III–V ternary semiconductor alloys beyond the VCA *Mater. Chem. Phys.* **77** 507–10
- [71] Cohen M L and Chelikowsky J R 1988 *Electronic Structure and Optical Properties of Semiconductors* (Berlin, Heidelberg: Springer Berlin Heidelberg) 75
- [72] Boykin T B, Klimeck G, Bowen R C and Lake R 1997 Effective-mass reproducibility of the nearest-neighbor models: analytic results *Phys. Rev. B* **56** 4102–7
- [73] Anderson N G and Jones S D 1991 Optimized tight-binding valence bands and heterojunction offsets in strained III-V semiconductors *J. Appl. Phys.* **70** 4342–56
- [74] Boykin T B, Klimeck G and Oyafuso F 2004 Valence band effective-mass expressions in the sp³d⁵s* empirical tight-binding model applied to a Si and Ge parametrization *Phys. Rev. B* **69** 115201
- [75] Tan Y, Povolotskyi M, Kubis T, Boykin T B and Klimeck G 2016 Transferable tight-binding model for strained group IV and III-V materials and heterostructures *Phys. Rev. B* **94** 045311

- [76] Nestoklon M O, Benchamekh R and Voisin P 2016 Virtual crystal description of III–V semiconductor alloys in the tight binding approach *J. Phys. Condens. Matter* **28** 305801
- [77] Slater J C and Koster G F 1954 Simplified LCAO method for the periodic potential problem *Phys. Rev.* **94** 1498–524
- [78] Harrison W A 1989 *Electronic structure and the properties of solids : the physics of the chemical bond* (New York: Dover Publications)
- [79] Chadi D J and Cohen M L 1975 Tight-binding calculations of the valence bands of diamond and zincblende crystals *Phys. Status Solidi* **68** 405–19
- [80] Vogl P, Hjalmarson H P and Dow J D 1983 A Semi-empirical tight-binding theory of the electronic structure of semiconductors *J. Phys. Chem. Solids* **44** 365–78
- [81] Jancu J M, Scholz R, Beltram F and Bassani F 1998 Empirical tight-binding calculation for cubic semiconductors: general method and material parameters *Phys. Rev. B* **57** 6493–507
- [82] Gürel H H, Akinci Ö and Ünlü H 2006 Semiempirical tight-binding modelling of III-N-based heterostructures *Superlattices Microstruct.* **40** 588–97
- [83] Klimeck G, Bowen R C, Boykin T B, Salazar-Lazaro C, Cwik T A and Stoica A 2000 Si tight-binding parameters from genetic algorithm fitting *Superlattices Microstruct.* **27** 77–88
- [84] Boykin T B, Klimeck G, Bowen R C and Oyafulo F 2002 Diagonal parameter shifts due to nearest-neighbor displacements in empirical tight-binding theory *Phys. Rev. B* **66** 125207
- [85] Cavassilas N, Aniel F, Boujdaria K and Fishman G 2001 Energy-band structure of GaAs and Si: a sp³ k-p method *Phys. Rev. B* **64** 1152071–5
- [86] Cardona M and Pollak F H 1966 Energy-band structure of germanium and silicon: the k-p method *Phys. Rev.* **142** 530–43
- [87] Bir G L and Pikus G E 1974 *Symmetry and strain-induced effects in semiconductors* (New York: Wiley) 0470073217
- [88] Chuang S L and Chang C S 1996 k-p method for strained wurtzite semiconductors *Phys. Rev. B* **54** 2491–504
- [89] Luttinger J M and Kohn W 1955 Motion of electrons and holes in perturbed periodic fields *Phys. Rev.* **97** 869–83
- [90] Luttinger J M 1956 Quantum theory of cyclotron resonance in semiconductors: general theory *Phys. Rev.* **102** 1030–41
- [91] Hohenberg P and Kohn W 1964 Inhomogeneous electron gas *Phys. Rev.* **136** B864–71
- [92] Car R and Parrinello M 1985 Unified approach for molecular dynamics and density-functional theory *Phys. Rev. Lett.* **55** 2471–4
- [93] Georges A, Kotliar G, Krauth W and Rozenberg M J 1996 Dynamical mean-field theory of strongly correlated fermion systems and the limit of infinite dimensions *Rev. Mod. Phys.* **68** 13–125
- [94] Hedin L and Lundqvist S 1969 *Solid State Phys.* ed H Ehenreich and F T D Seitz (New York: Academic) 23
- [95] Hybertsen M S and Louie S G 1986 Electron correlation in semiconductors and insulators: band gaps and quasiparticle energies *Phys. Rev. B* **34** 5390–413
- [96] Hedin L 1965 New method for calculating the one-particle Green's function with application to the electron-Gas problem *Phys. Rev.* **139** A796–823
- [97] Aulbur W G, Jönsson L and Wilkins J W 2000 *Quasiparticle calculations in solids solid state physics* ed H Ehrenreich and F Spaepen (New York: Academic) 54, 1–218
- [98] Aryasetiawan F and Gunnarsson O 1998 The GW method *Reports Prog. Phys.* **61** 237–312
- [99] Kohn W and Sham L J 1965 Self-consistent equations including exchange and correlation effects *Phys. Rev.* **140** A1133
- [100] Kohn W, Becke A D and Parr R G 1996 Density functional theory of electronic structure *J. Phys. Chem.* **100** 12974
- [101] Hafner J 2008 Ab-initio simulations of materials using VASP: density-functional theory and beyond *J. Comput. Chem.* **29** 2044–78
- [102] Hafner J, Wolverson C and Ceder G 2006 Toward computational materials design: the impact of density functional theory on materials research *MRS Bull.* **31** 659–68
- [103] Van Doren V E, Van Alsenoy C and Geerlings P 2001 *Density functional theory and its application to materials* ed V E Van Doren, C Van Alsenoy and P Geerlings (Antwerp, Belgium: American Institute of Physics) (AIP conference proceedings) 9780735400160
- [104] Fiolhais C, Nogueira F and Marques M A L 2003 *A Primer in Density Functional Theory* ed C Fiolhais, F Nogueira and M A L Marques (Berlin, Heidelberg: Springer Berlin Heidelberg) 620978-3-540-37072-7 (<https://doi.org/10.1007/3-540-37072-2>)
- [105] Rosenow P, Bannow L C, Fischer E W, Stolz W, Volz K, Koch S W and Tonner R 2018 Ab initio calculations of the concentration dependent band gap reduction in dilute nitrides *Phys. Rev. B* **97** 075201
- [106] Perdew J P, Burke K and Ernzerhof M 1996 Generalized gradient approximation made simple *Phys. Rev. Lett.* **77** 3865–8
- [107] Perdew J P and Wang Y 1992 Accurate and simple analytic representation of the electron-gas correlation energy *Phys. Rev. B* **45** 13244–9
- [108] Perdew J P 1985 Density functional theory and the band gap problem *Int. J. Quantum Chem.* **28** 497–523
- [109] Koller D, Tran F and Blaha P 2011 Merits and limits of the modified Becke-Johnson exchange potential *Phys. Rev. B* **83** 195134
- [110] Krukau A V, Vydrov O A, Izmaylov A F and Scuseria G E 2006 Influence of the exchange screening parameter on the performance of screened hybrid functionals *J. Chem. Phys.* **125** 224106
- [111] Tran F and Blaha P 2009 Accurate band gaps of semiconductors and insulators with a semilocal exchange-correlation potential *Phys. Rev. Lett.* **102** 226401
- [112] Kim Y S, Marsman M, Kresse G, Tran F and Blaha P 2010 Towards efficient band structure and effective mass calculations for III-V direct band-gap semiconductors *Phys. Rev. B* **82** 205212
- [113] Jiang H 2013 Band gaps from the Tran-Blaha modified Becke-Johnson approach: a systematic investigation *J. Chem. Phys.* **138** 134115
- [114] Bannow L C, Rosenow P, Springer P, Fischer E W, Hader J, Moloney J V, Tonner R and Koch S W 2017 An ab initio based approach to optical properties of semiconductor heterostructures *Model. Simul. Mater. Sci. Eng.* **25** 065001
- [115] Rehman G, Shafiq M, Saifullah, Ahmad R, Jalali-Asadabadi S, Maqbool M, Khan I, Rahnamaye-Aliabad H and Ahmad I 2016 Electronic band structures of the highly desirable III–V semiconductors: TB-mBJ DFT studies *J. Electron. Mater.* **45** 3314–23
- [116] Koller D, Tran F and Blaha P 2012 Improving the modified Becke-Johnson exchange potential *Phys. Rev. B* **85** 155109
- [117] Ziane M I, Bensaad Z, Labdelli B and Bennacer H 2014 First-principles study of structural, electronic and optical properties of III-arsenide binary GaAs and InAs, and III-nitrides binary GaN and InN: Improved density-functional-theory study *Sensors & transducers* 27 374 Special IssueP_SL_531
- [118] Sun Y, Thompson S E and Nishida T 2007 Physics of strain effects in semiconductors and metal-oxide-semiconductor field-effect transistors *J. Appl. Phys.* **101** 104503
- [119] Beyer A, Stegmüller A, Oelerich J O, Jandieri K, Werner K, Mette G, Stolz W, Baranovskii S D, Tonner R and Volz K 2016 Pyramidal structure formation at the interface between III/V semiconductors and silicon *Chem. Mater.* **28** 3265–75
- [120] Balaghi L, Bussone G, Grifone R, Hübner R, Grenzer J, Ghorbani-Asl M, Krasheninnikov A V, Schneider H, Helm M and Dimakis E 2019 Widely tunable GaAs bandgap via strain engineering in core/shell nanowires with large lattice mismatch *Nat. Commun.* **10** 2793

- [121] Alekseev P A, Sharov V A, Borodin B R, Dunaevskiy M S, Reznik R R and Cirlin G E 2020 Effect of the uniaxial compression on the GaAs nanowire solar cell *Micromachines* **11** 581
- [122] Lim B, Cui X Y and Ringer S P 2021 Strain-mediated bandgap engineering of straight and bent semiconductor nanowires *Phys. Chem. Chem. Phys.* **23** 5407–14
- [123] Signorello G, Karg S, Björk M T, Gotsmann B and Riel H 2013 Tuning the light emission from GaAs nanowires over 290 meV with uniaxial strain *Nano Lett.* **13** 917
- [124] Grönqvist J, Søndergaard N, Boxberg F, Guhr T, Åberg S and Xu H Q 2009 Strain in semiconductor core-shell nanowires *J. Appl. Phys.* **106** 053508
- [125] Signorello G, Lörtscher E, Khomyakov P A, Karg S, Dheeraj D L, Gotsmann B, Weman H and Riel H 2014 Inducing a direct-to-pseudodirect bandgap transition in wurtzite GaAs nanowires with uniaxial stress *Nat. Commun.* **5** 3655
- [126] Copple A, Ralston N and Peng X 2012 Engineering direct-indirect band gap transition in wurtzite GaAs nanowires through size and uniaxial strain *Appl. Phys. Lett.* **100** 193108
- [127] Assali S *et al* 2013 Direct band gap wurtzite gallium phosphide nanowires *Nano Lett.* **13** 1559–63
- [128] Peng X and Copple A 2013 Origination of the direct-indirect band gap transition in strained wurtzite and zinc-blende GaAs nanowires: a first principles study *Phys. Rev. B* **87** 115308
- [129] New Semiconductor Materials Biology systems. Characteristics and Properties, www.matprop.ru, last accessed 22.08.2022
- [130] Kresse G and Hafner J 1993 *Ab initio* molecular dynamics for liquid metals *Phys. Rev. B* **47** 558–61
- [131] Kresse G and Hafner J 1994 *Ab initio* molecular-dynamics simulation of the liquid-metal-amorphous-semiconductor transition in germanium *Phys. Rev. B* **49** 14251–69
- [132] Kresse G and Furthmüller J 1996 Efficiency of *ab-initio* total energy calculations for metals and semiconductors using a plane-wave basis set *Comput. Mater. Sci.* **6** 15–50
- [133] Kresse G and Furthmüller J 1996 Efficient iterative schemes for *ab initio* total-energy calculations using a plane-wave basis set *Phys. Rev. B* **54** 11169–86
- [134] Blöchl P E 1994 Projector augmented-wave method *Phys. Rev. B* **50** 17953–79
- [135] Kresse G and Joubert D 1999 From ultrasoft pseudopotentials to the projector augmented-wave method *Phys. Rev. B* **59** 1758–75
- [136] Monkhorst H J and Pack J D 1976 Special points for Brillouin-zone integrations *Phys. Rev. B* **13** 5188–92
- [137] Grimme S, Ehrlich S and Goerigk L 2011 Effect of the damping function in dispersion corrected density functional theory *J. Comput. Chem.* **32** 1456–65
- [138] Grimme S, Antony J, Ehrlich S and Krieg H 2010 A consistent and accurate *ab initio* parametrization of density functional dispersion correction (DFT-D) for the 94 elements H–Pu *J. Chem. Phys.* **132** 154104
- [139] Prins A, Adams A and Sweeney S 2012 Pressure studies *Semiconductor Research: Experimental Techniques* ed A Patane and N Balkan (Berlin, Heidelberg: Springer Berlin Heidelberg) 171–95
- [140] Fratanduono D E *et al* 2021 Establishing gold and platinum standards to 1 terapascal using shockless compression *Science* **372** 1063–8
- [141] Dubrovinsky L, Dubrovinskaia N, Prakapenka V B and Abakumov A M 2012 Implementation of micro-ball nanodiamond anvils for high-pressure studies above 6 Mbar *Nat. Commun.* **3** 1163
- [142] Dubrovinsky L *et al* 2015 The most incompressible metal osmium at static pressures above 750 gigapascals *Nature* **525** 226–9
- [143] Katiyar A K, Thai K Y, Yun W S, Lee J and Ahn J 2020 Breaking the absorption limit of Si toward SWIR wavelength range via strain engineering *Sci. Adv.* **6** eabb0576
- [144] Yu P Y 2011 High pressure semiconductor physics: looking toward the future on the shoulder of the past *Phys. Status Solidi* **248** 1077–82
- [145] Snider E, Dasenbrock-Gammon N, McBride R, Debessai M, Vindana H, Vencatasamy K, Lawler K V, Salamat A and Dias R P 2020 Room-temperature superconductivity in a carbonaceous sulfur hydride *Nature* **586** 373–7
- [146] Dang C *et al* 2021 Achieving large uniform tensile elasticity in microfabricated diamond *Science* **371** 76–8
- [147] Shi Z, Dao M, Tsymbalov E, Shapeev A, Li J and Suresh S 2020 Metallization of diamond *Proc. Natl Acad. Sci.* **117** 24634
- [148] Cardona M 2007 12th international conference on high pressure semiconductor physics (HPSP-12): concluding remarks *Phys. Status Solidi* **244** 481–7
- [149] Almonacid G *et al* 2016 Structural metastability and quantum confinement in $Zn_{1-x}Co_xO$ nanoparticles *Nano Lett.* **16** 5204–12
- [150] Adler P, Schwarz U, Syassen K, Rozenberg G K, Machavariani G Y, Milner A P, Pasternak M P and Hanfland M 1999 Collapse of the charge disproportionation and covalency-driven insulator-metal transition in $Sr_3Fe_2O_7$ under pressure *Phys. Rev. B* **60** 4609–17
- [151] Nelson R, Ertural C, George J, Deringer V L, Hautier G and Dronskowski R 2020 LOBSTER: local orbital projections, atomic charges, and chemical-bonding analysis from projector-augmented-wave-based density-functional theory *J. Comput. Chem.* **41** 1931
- [152] Maintz S, Deringer V L, Tchougréeff A L and Dronskowski R 2016 LOBSTER: a tool to extract chemical bonding from plane-wave based DFT *J. Comput. Chem.* **37** 1030–5
- [153] Grivickas P, McCluskey M D and Gupta Y M 2009 Transformation of GaAs into an indirect L-band-gap semiconductor under uniaxial strain *Phys. Rev. B* **80** 073201
- [154] Yan Q, Rinke P, Scheffler M and de Walle C G 2009 Strain effects in group-III nitrides: deformation potentials for AlN, GaN, and InN *Appl. Phys. Lett.* **95** 121111
- [155] Birch F 1947 Finite elastic strain of cubic crystals *Phys. Rev.* **71** 809–24
- [156] Misra G, Tripathi P and Goyal S C 2007 Bulk modulus of semiconductors and its pressure derivatives *Philos. Mag. Lett.* **87** 393–401
- [157] Van Camp P E, Van Doren V E and Devreese J T 1990 Pressure dependence of the electronic properties of cubic III-V In compounds *Phys. Rev.* **41** 1598–602
- [158] Potter R F 1956 Indirect transitions in indium antimonide *Phys. Rev.* **103** 861–2

Supplementary Material

Systematic strain-induced bandgap tuning in binary III–V semiconductors from density functional theory

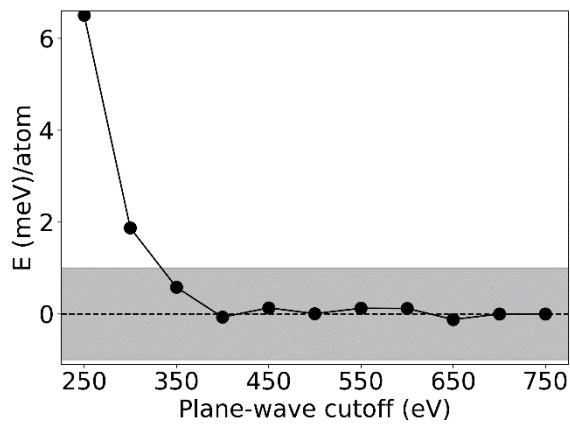
Badal Mondal^{1,2}, Ralf Tonner-Zech^{1*}

¹*Wilhelm-Ostwald-Institut für Physikalische und Theoretische Chemie,
Universität Leipzig, 04103 Leipzig, Germany*

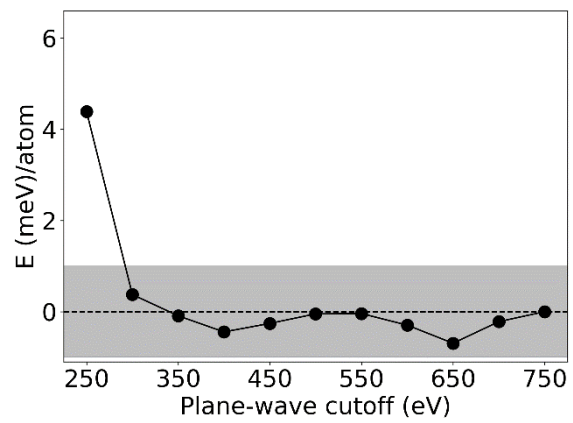
²*Fachbereich Physik, Philipps-Universität Marburg, 35032 Marburg, Germany*

e-mail: ralf.tonner@uni-leipzig.de

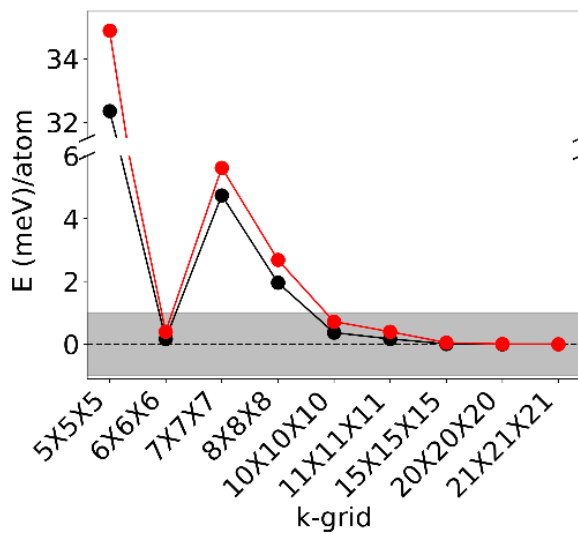
S I Plane wave cut-off energy and k-mesh convergence for Si and GaP



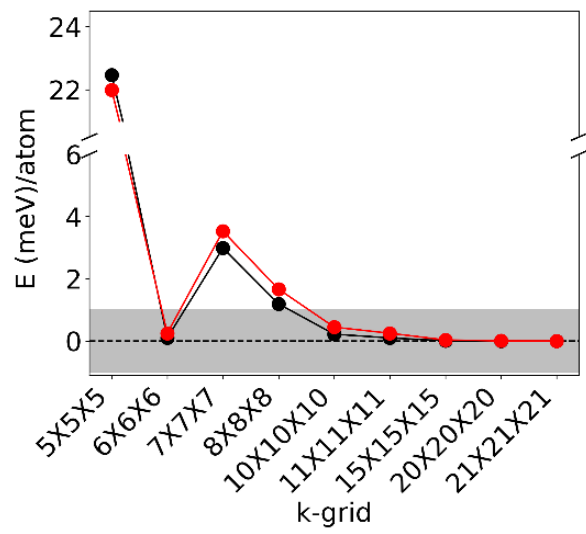
(a)



(b)



(c)



(d)

Figure S1: Results of the convergence test for (a, b) the plane wave cut-off and (c, d) the k-mesh. The data points are given with respect to the most accurate setting (750 eV, $21 \times 21 \times 21$). The range of energy scales within the commonly accepted target accuracy of ± 1 meV/atom are shown by gray areas. (a) and (b) are the plane wave cut-off convergence test for unstrained Si and GaP, respectively. (c) and (d) are the k-mesh convergence test for Si and GaP, respectively (black: strain=0%, red: strain= -10%).

For the plane wave cut-off energy convergence test we present the results for Si and GaP. We chose GaP because among the family of III-V compounds we addressed in the paper, Ga & P has the highest default plane wave cut-off in the PAW potentials we used in VASP calculations. Figure S1a and S1b show the plane wave cut-off energy convergence results for unstrained Si and GaP. The energies per atom were calculated from the optimized geometry at each plane wave cut-off energy. For all the calculations here, we used $10 \times 10 \times 10$ k-mesh. From the results clearly, the 450 eV plane wave cut-off energy can be used as the converged value for the optimal choice.

Figure S1c and S1d show the k-mesh convergence results for Si and GaP. As strain changes the lattice parameters, we also checked the k-mesh convergence for the isotropically compressively strained system. The largest strain we considered in this paper is 10% strain. As GaP has the lowest lattice constant among the family of III-V compounds we addressed in the paper, the converged parameters for GaP should be valid for other III-V as well. The energies per atom were calculated from the optimized geometry at each k-mesh value. For all the calculations here, we used 450 eV plane wave cut-off energy. From the results clearly, $10 \times 10 \times 10$ k-mesh can be used as the converged value for the optimal choice.

After the analyses of the above convergence results, we ultimately chose to use $10 \times 10 \times 10$ k-mesh and 450 eV plane wave cut-off energy value as the optimal setup for all the solids studied in the main manuscript.

S II Effect of dispersion interactions on the equilibrium lattice parameters

Table S1: Effect of the type of dispersion interaction treatment on the computed equilibrium lattice parameters (Å) for the materials investigated in this article. Mean absolute error (MAE) indicates the relative absolute deviation in the calculated lattice parameters with respect to their experimental values, averaged over the materials investigated. The experimental reference values are at 0 K.

| | Si | GaP | GaAs | GaSb | InP | InAs | InSb | MAE(%) |
|------------|-------|-------|-------|-------|-------|-------|-------|--------|
| Experiment | 5.430 | 5.442 | 5.642 | 6.082 | 5.861 | 6.050 | 6.469 | |
| PBE-D3(BJ) | 5.421 | 5.474 | 5.689 | 6.134 | 5.939 | 6.138 | 6.556 | 0.94 |
| PBE-TS | 5.446 | 5.508 | 5.726 | 6.138 | 5.954 | 6.138 | 6.527 | 1.12 |
| PBE-TS/HI | 5.446 | 5.474 | 5.689 | 6.155 | 5.935 | 6.138 | 6.591 | 1.07 |
| PBE-TS+SCS | 5.437 | 5.504 | 5.716 | 6.150 | 5.959 | 6.152 | 6.574 | 1.24 |
| PBE-MBD | 5.432 | 5.481 | 5.702 | 6.154 | 5.945 | 6.146 | 6.579 | 1.10 |
| optB88-vdW | 5.469 | 5.535 | 5.763 | 6.219 | 6.000 | 6.207 | 6.635 | 2.05 |
| vdW-DF2 | 5.539 | 5.650 | 5.930 | 6.421 | 6.140 | 6.391 | 6.850 | 4.68 |

The data shown in Table S1 are the optimized lattice parameters calculated using the Perdew-Burke-Ernzerhof (PBE) exchange-correlation functional combined with the dispersion interaction energy correction of Grimme’s D3 scheme with Becke-Johnson damping (DFT-D3(BJ)) [1], Tkatchenko-Scheffler (TS) model [2], Tkatchenko-Scheffler method with iterative Hirshfeld partitioning (TS/HI) [3,4], Tkatchenko-Scheffler with self-consistent screening (TS+SCS) [5], and the many-body dispersion energy method [5,6]. The results using the nonlocal van der Waals density functional are shown for the improved vdW-DF method (vdW-DF2) [7] and optB88-vdW method [8]. Mean absolute errors (MAE) indicate the relative absolute deviation in the calculated lattice parameters (a_{calc}) from the experimental values (a_{exp}) [9,10], averaged over the materials investigated:

$$MAE = [\sum_{\text{materials}} \text{abs}(a_{calc} - a_{exp}) / a_{exp} \times 100] / n_{\text{materials}}$$

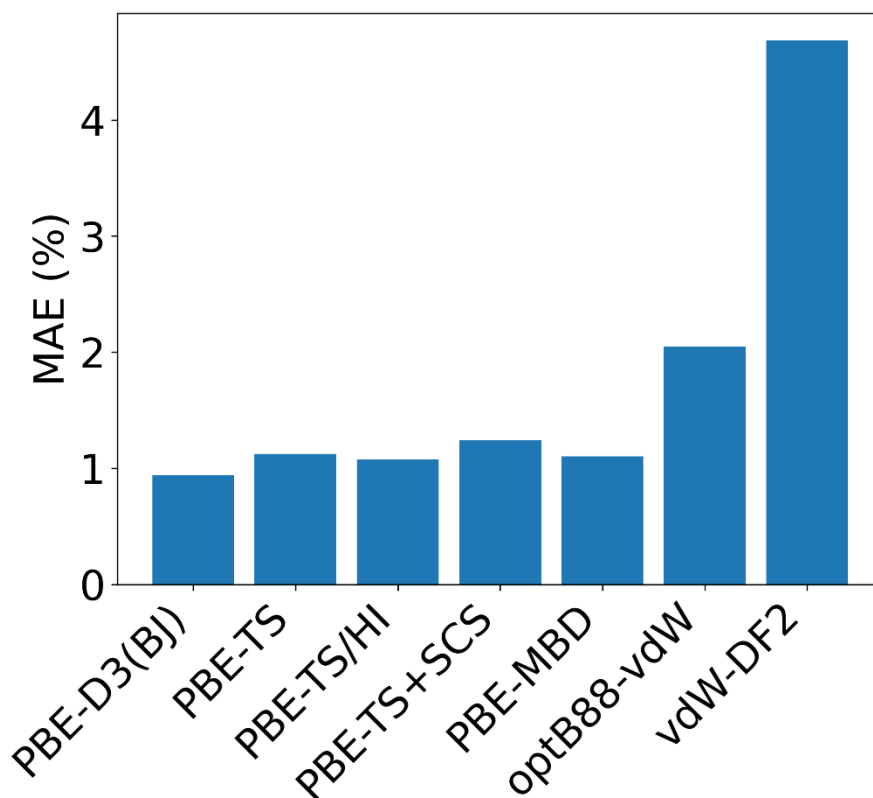


Figure S2: Effect of the type of dispersion interaction treatment on the computed equilibrium lattice parameters (\AA) for the materials investigated in this article. Mean absolute error (MAE) indicates the relative absolute deviation in the calculated lattice parameters with respect to their experimental values, averaged over the materials investigated. The experimental reference values are at 0 K.

Table S1 shows the effect of dispersion interaction correction on the optimized lattice parameters for the compounds addressed in this article. Different approaches to describe the dispersion interaction within the density functional theory framework are shown. Minimum mean absolute error (MAE) is found for DFT-D3(BJ) approach, figure S2. This is therefore, we used for the rest of the calculations. Note, that DFT-D3(DJ) adds a correction to total energy only and hence, will not have any effect on electronic properties calculation with TB09 functional.

S III Movies

The movies referenced here show the evolution of band structure in GaAs and GaP under different strain regimes. The band structures were calculated along the high symmetry path of zincblende structures. In all cases, the band energies were rescaled with respect to their corresponding VBM.

Figure S3a: GaAs under isotropic tensile strain

Figure S3b: GaAs under isotropic compressive strain

Figure S3c: GaAs under isotropic compressive strain zoomed in CB region

Figure S3d: GaAs under biaxial tensile strain

Figure S3e: GaAs under biaxial compressive strain

Figure S3f: GaP under isotropic tensile strain

Figure S3g: GaP under isotropic compressive strain

Figure S3h: GaP under biaxial tensile strain

Figure S3i : GaP under biaxial compressive strain

S IV Direct-to-indirect (DIT) transition in GaAs under biaxial strain

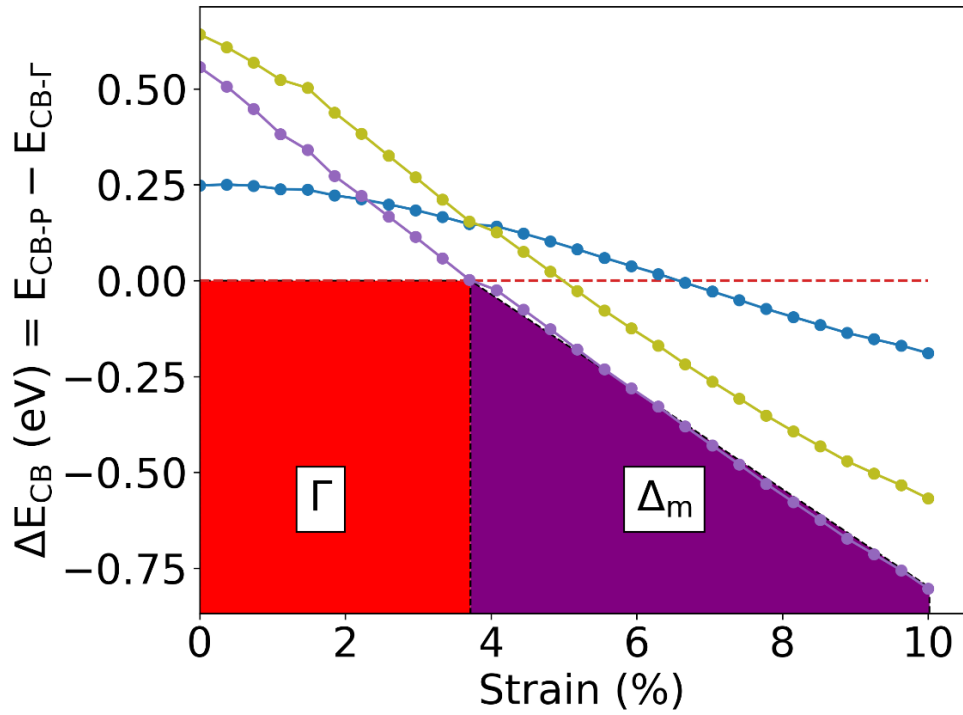
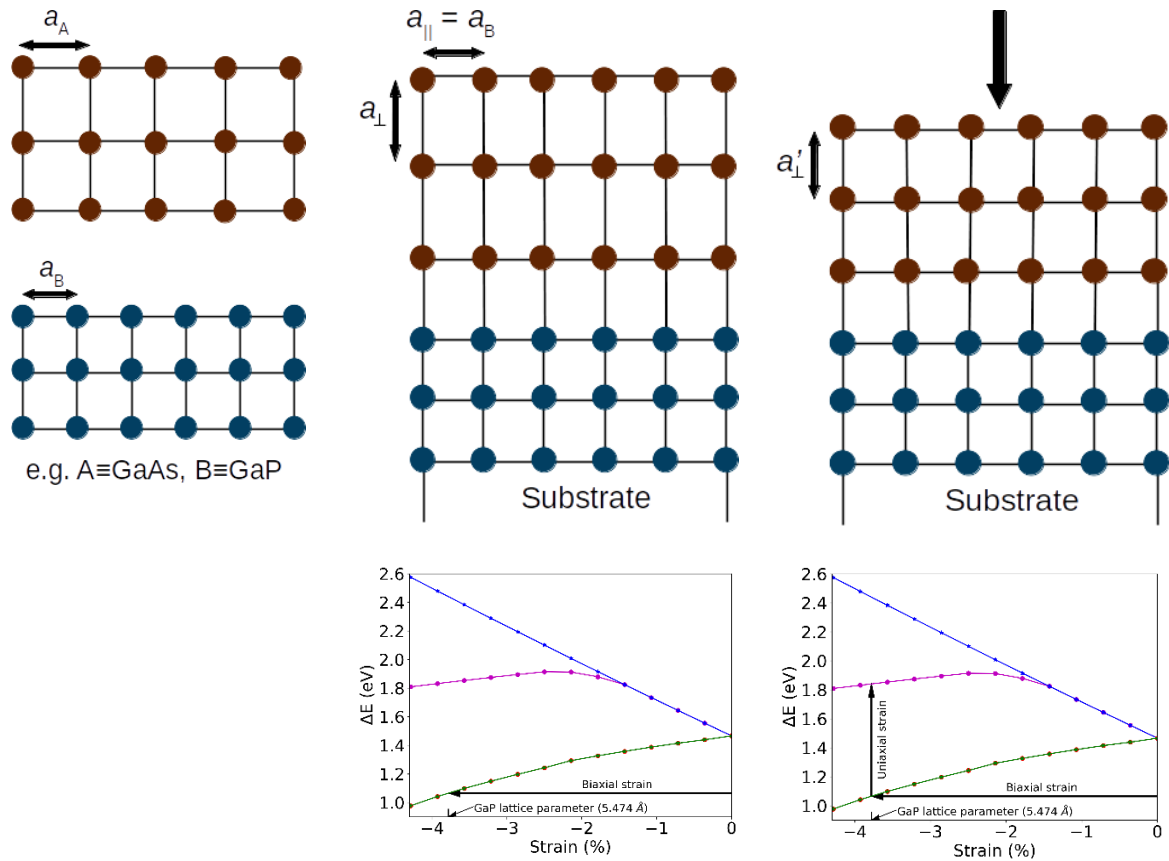


Figure S4: The difference between CB energies at the Γ point and other k-points P ($\Delta E_{CB} = E_{CB-P} - E_{CB-\Gamma}$; with P = Γ , L, Δ_m , and X) for biaxially strained GaAs. Colored areas indicate at which k-point we found the CBM for the given value of tensile strain. The color scheme: Γ (red), L (blue), Δ_m (purple), and X (olive).

S V The schematic of combining uniaxial and biaxial strain



(a) No contact between the systems. Individual systems are in their unstrained configuration. In this condition, GaAs is a direct bandgap semiconductor.

(b) GaAs is epitaxially grown on GaP substrate. Therefore, GaAs layer is in-plane compressively strained. This is the source of biaxial compressive strain. In this condition, strained GaAs is a direct bandgap semiconductor.

(c) Uniaxial compressive strain is applied along the z-direction of biaxially strained GaAs grown on GaP-substrate. In this case, after 3.2% uniaxial strain the strained GaAs shows an indirect bandgap.

Figure S5: The schematic of thought experiment as described in section 4.2.4 of the manuscript. Here, (b) GaAs is grown epitaxially on a substrate with smaller lattice constant, GaP. This results in an in-plane compressive biaxial strain (3.78%) and an expansion of z-lattice parameter in the GaAs epilayer. (c) Then, the application of subsequent uniaxial compressive strain (e.g. pressure) compresses the z-lattice parameter. We assume that the in-plane lattice parameters do not relax upon compression of z-lattice parameter due to the strain exerted by the substrate.

S VI Generalization of the bandgap transition in GaAs by combining uniaxial and biaxial strain

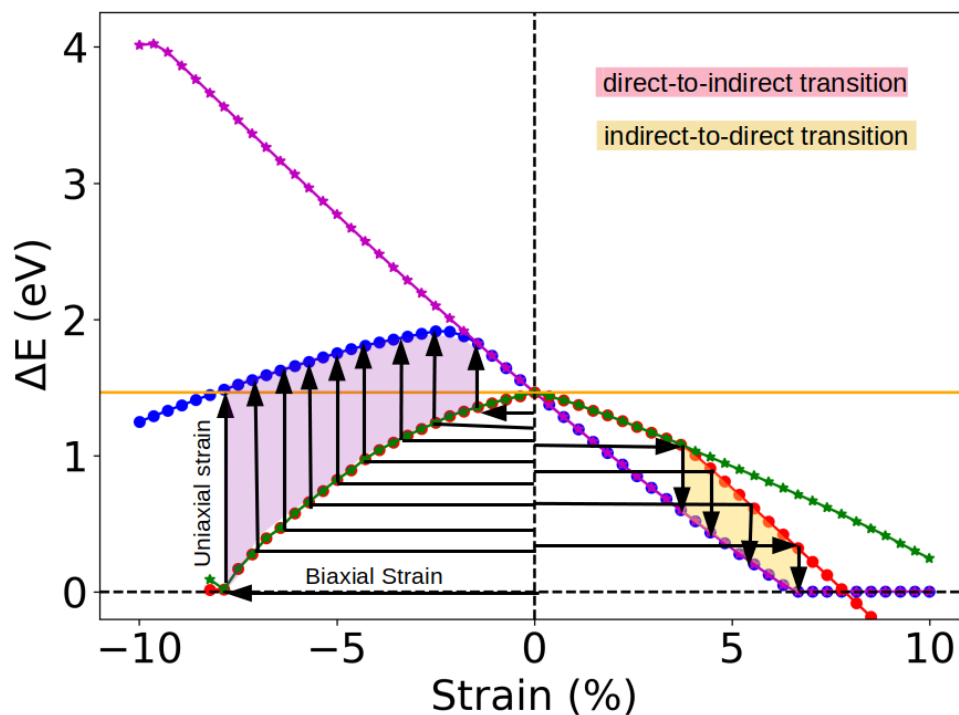


Figure S6: Bandgap variation with strain for GaAs. The energy difference between conduction and valence band at the Γ point (ΔE_{Γ} , magenta for isotropic and green for biaxial strain) and the bandgap (E_g , blue for isotropic and red for biaxial strain) are shown as a function of biaxial (bi) and isotropic (iso) strain. The solid orange line indicate E_g for the unstrained GaAs. The shaded regions indicate the strain regime, only where one can achieve the direct-indirect transition in the bandgap nature by applying uniaxial strain on the biaxially strained GaAs.

S VII Indirect-to-direct (IDT) transition by applying uniaxial tensile strain in biaxially strained GaAs

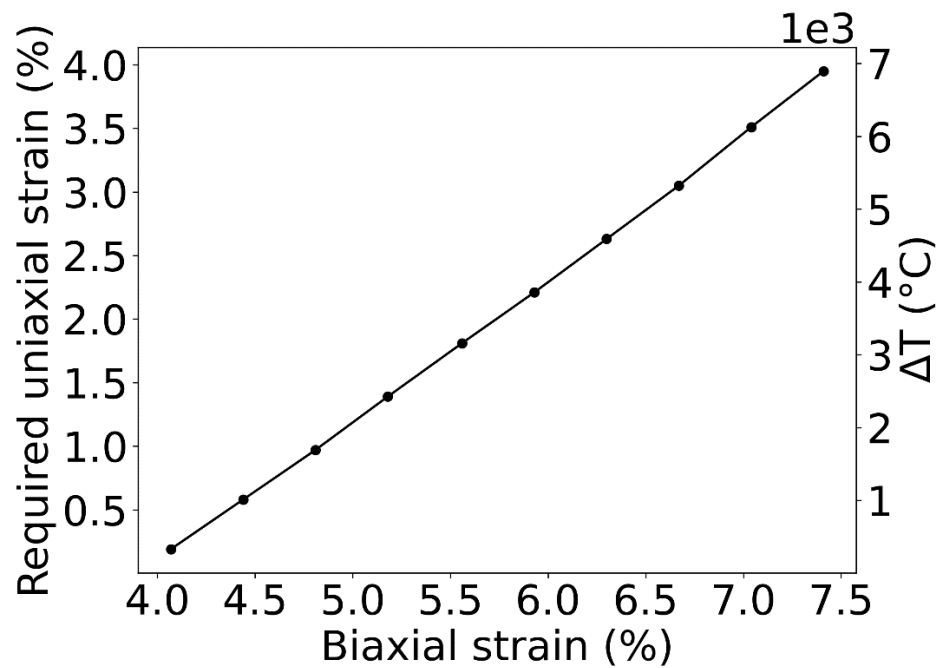


Figure S7: Variation of required uniaxial tensile strain for the indirect to direct transition (IDT) in biaxial tensile strained GaAs. The temperature increase (ΔT) required for the thermal expansion was calculated using the linear thermal expansion coefficient of GaAs ($5.73 \times 10^{-6} \text{ }^{\circ}\text{C}^{-1}$ [10]).

S VIII Indirect-to-direct (IDT) transition in GaP

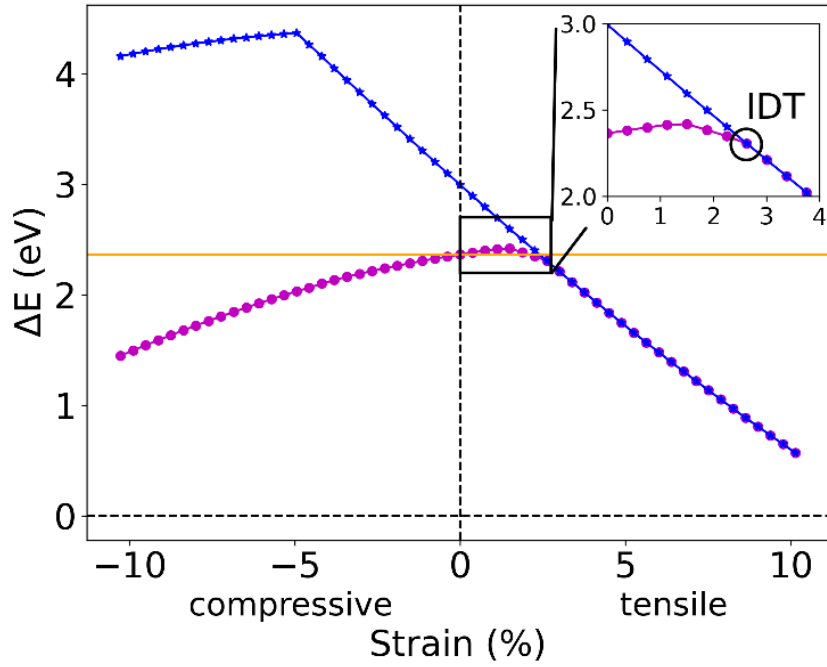


Figure S8: Isotropic strain effects on the bandgap of GaP. The energy difference between CB and VB at the Γ -point (ΔE_{Γ} , blue), the bandgap (E_g , magenta), and the indirect to direct transition (IDT) are shown. The solid orange line indicates E_g for the equilibrium structure (2.36 eV). The inset shows the region of the IDT with a finer grid of strain calculations resulting in higher resolution.

S IX Uniaxial strain effect on bandgap of GaP

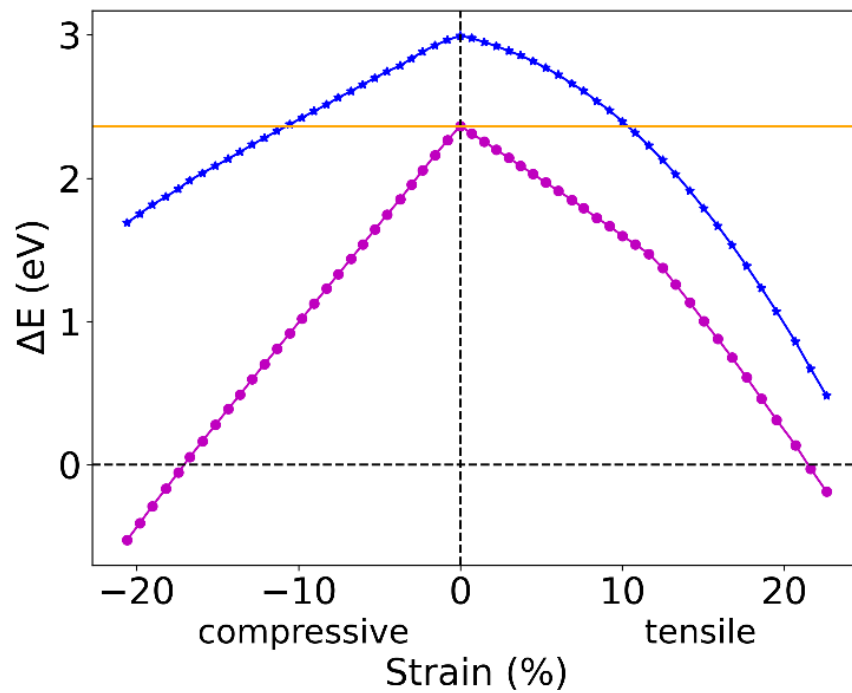


Figure S9: Uniaxial strain effects on the bandgap of GaP. The energy difference between CB and VB at the Γ -point (ΔE_{Γ} , blue) and the bandgap (E_g , magenta) are shown. The solid orange line indicates E_g for the equilibrium structure (2.36 eV).

S X Indirect-to-direct (IDT) transition in GaP by combining biaxial and uniaxial strain

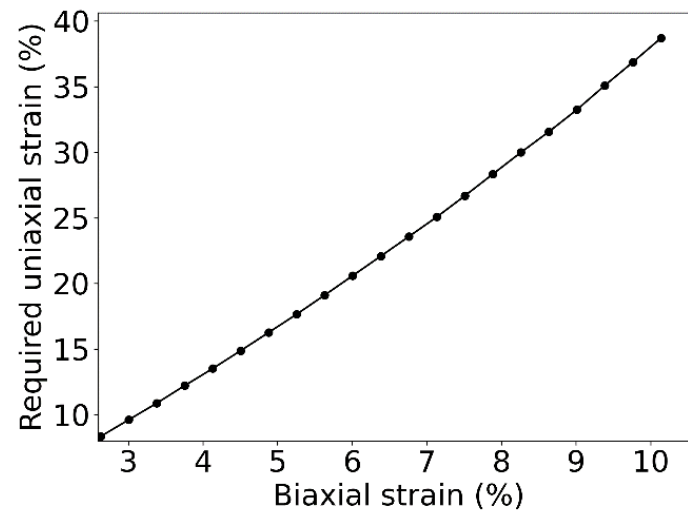
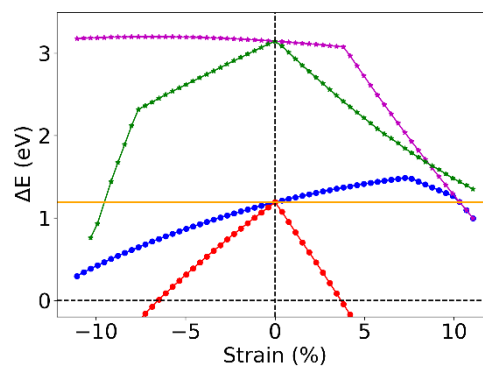
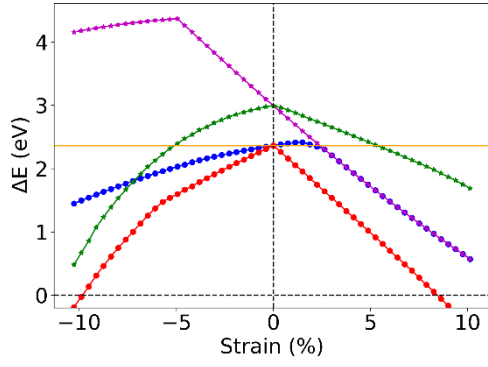


Figure S10: Variation of required uniaxial tensile strain for the indirect to direct transition (IDT) to take place in biaxial tensile strained GaP.

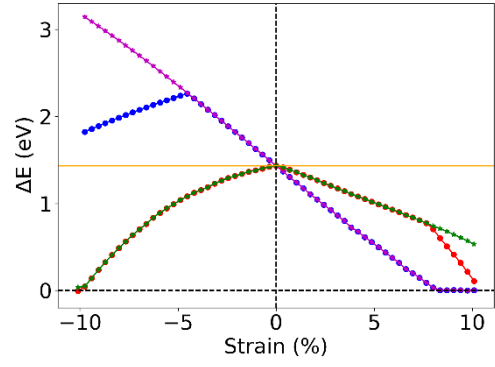
S XI Bandgap variation with strain for III–V semiconductors



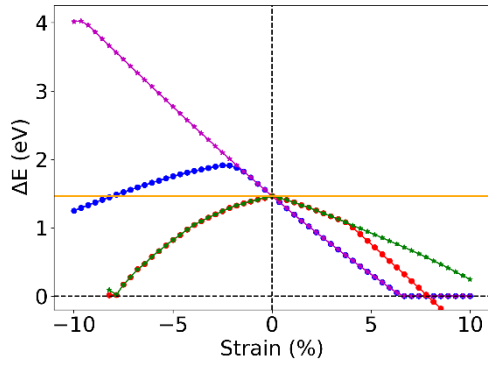
(a) Si



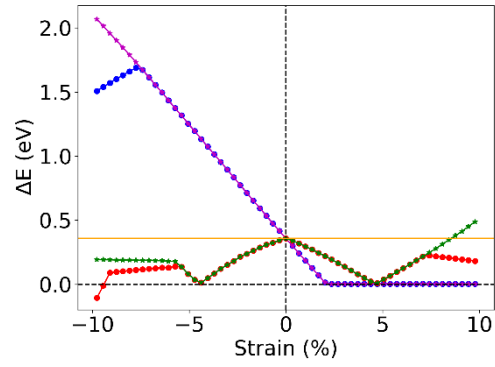
(b) GaP



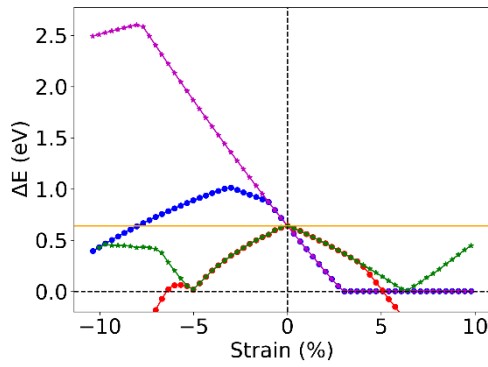
(e) InP



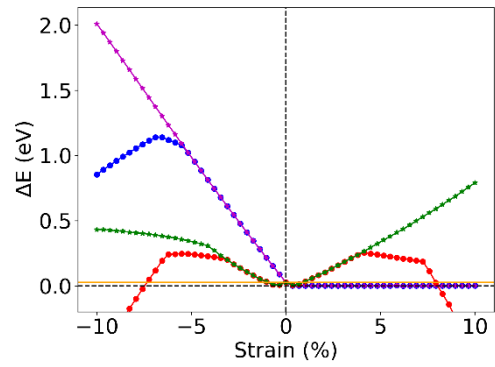
(c) GaAs



(f) InAs



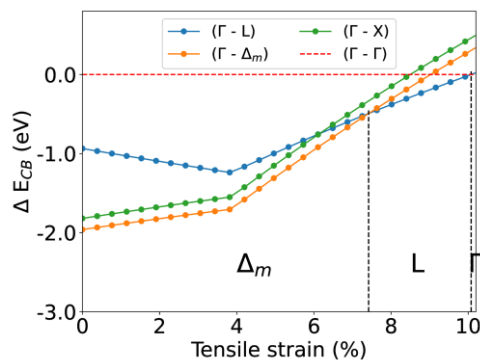
(d) GaSb



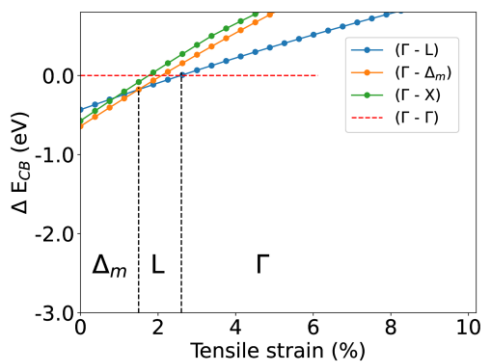
(g) InSb

Figure S11: Bandgap variation with strain for different III-V binary semiconductors. The energy difference between conduction and valence band at the Γ point (ΔE_{Γ} , magenta for iso and green for bi) and the bandgap (E_g , blue for iso and red for bi) are shown as a function of biaxial (bi) and isotropic (iso) strain. The solid orange lines indicate E_g for the equilibrium structures.

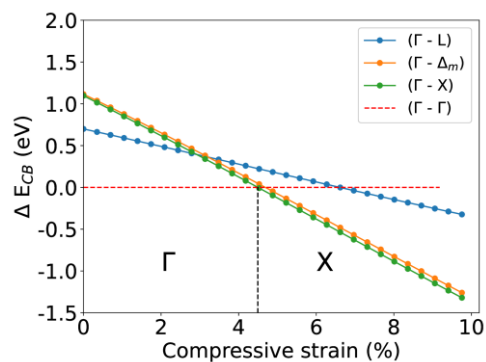
S XII CBM transition path for different III–V semiconductors



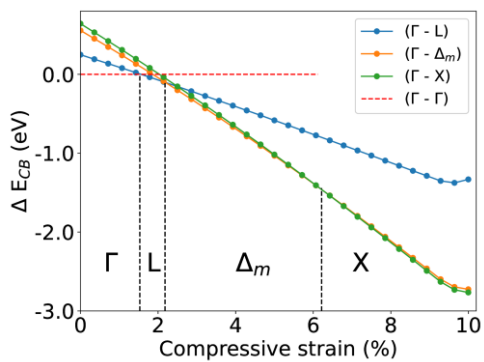
(a) Si



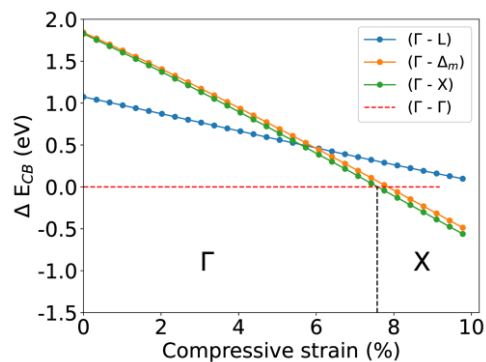
(b) GaP



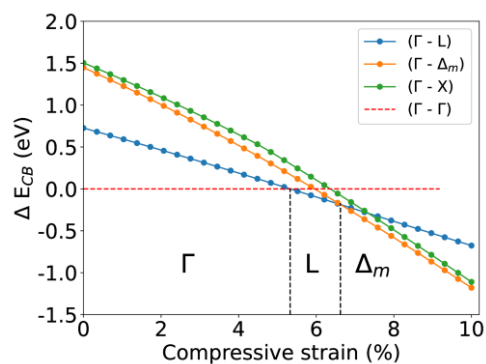
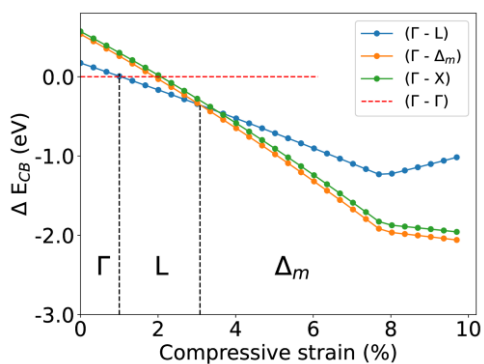
(e) InP



(c) GaAs



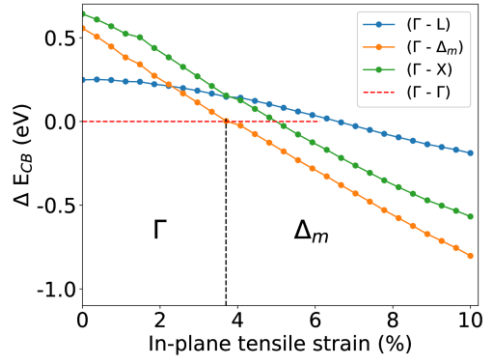
(f) InAs



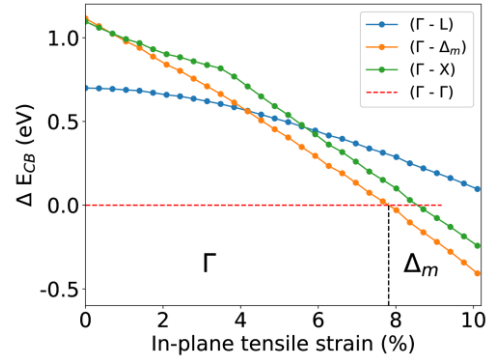
(d) GaSb

(g) InSb

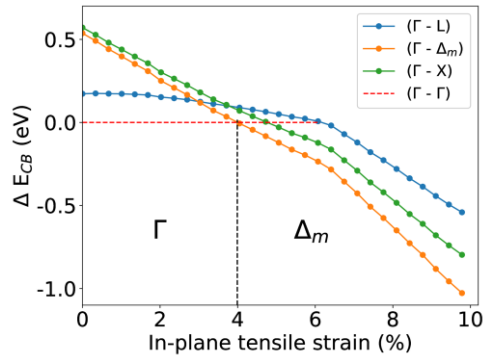
Figure S12: The difference between conduction energies at the Γ point and other k points P ($\Delta E_{CB} = E_{CB-P} - E_{CB-\Gamma}$; with P = L, Δ_m , and X) for isotropically strained III-V binary semiconductors. The enclosed areas between the lines and the x-axis indicate at which k-point we find the conduction band minima for the given values of strains.



(a) GaAs



(c) InP



(b) GaSb

Figure S13: The difference between conduction energies at the Γ point and other k points P ($\Delta E_{CB} = E_{CB-P} - E_{CB-\Gamma}$; with P = Γ , L, Δ_m , and X) for biaxially strained III-V binary semiconductors. The enclosed areas between the lines and the x-axis indicate at which k-point we find the conduction band minima for the given values of strains.

S XIII Evolution of GaAs bandstructure under isotropic compressive strain

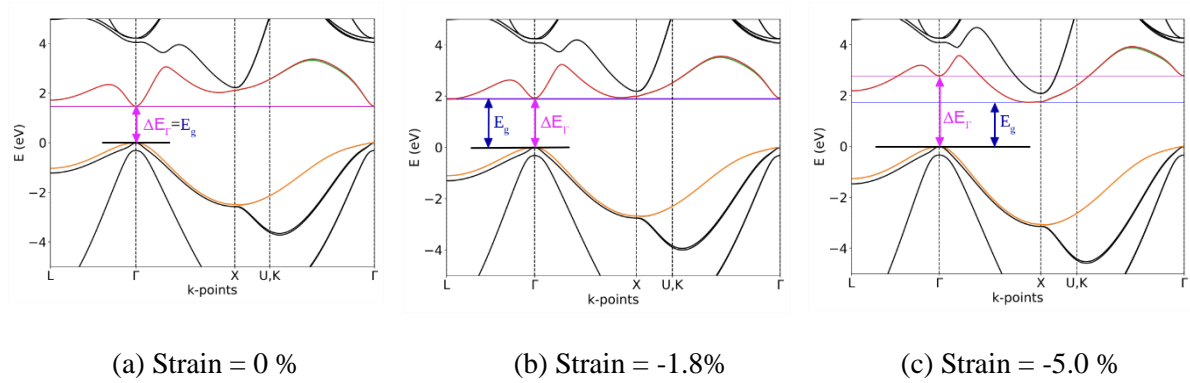


Figure S14: The 3 snapshots around the direct-indirect transition points of the evolution of GaAs bandstructure under isotropic compressive strain. The energy difference between CB and VB at the Γ -point (ΔE_{Γ} , blue) and the bandgap (E_g , magenta) are shown. Only 4 special k-points were found to be responsible for the direct-indirect transitions: Γ , L, Δ_m , and X. For more details see section SIII.

S XIV Schematic of energy difference between Γ & X and Γ & L

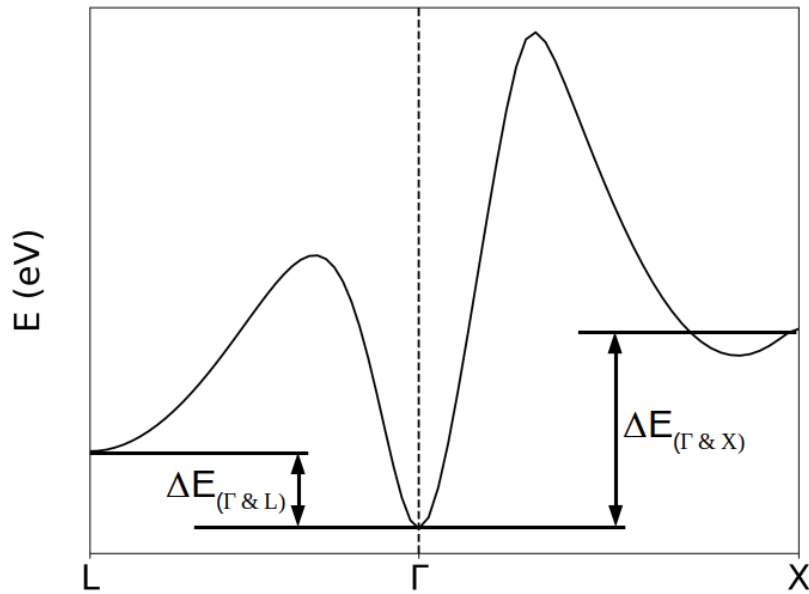



Figure S15: The schematic of the difference between conduction band energies at the Γ point and other k-points P ($\Delta E_{(\Gamma \& P)} = E_{CB-P} - E_{CB-\Gamma}$; with P = L and X). For simplicity, $\Delta E_{(\Gamma \& \Delta_m)}$ is not shown.

References

- [1] Grimme S, Ehrlich S and Goerigk L 2011 Effect of the damping function in dispersion corrected density functional theory *J. Comput. Chem.* **32** 1456–65
- [2] Tkatchenko A and Scheffler M 2009 Accurate Molecular Van Der Waals Interactions from Ground-State Electron Density and Free-Atom Reference Data *Phys. Rev. Lett.* **102** 073005
- [3] Bučko T, Lebègue S, Hafner J and Ángyán J G 2013 Improved density dependent correction for the description of London dispersion forces *J. Chem. Theory Comput.* **9** 4293–9
- [4] Bultinck P, Van Alsenoy C, Ayers P W and Carbó-Dorca R 2007 Critical analysis and extension of the Hirshfeld atoms in molecules *J. Chem. Phys.* **126** 144111
- [5] Tkatchenko A, DiStasio R A, Car R and Scheffler M 2012 Accurate and Efficient Method for Many-Body van der Waals Interactions *Phys. Rev. Lett.* **108** 236402
- [6] Ambrosetti A, Reilly A M, DiStasio R A and Tkatchenko A 2014 Long-range correlation energy calculated from coupled atomic response functions *J. Chem. Phys.* **140** 18A508
- [7] Lee K, Murray É D, Kong L, Lundqvist B I and Langreth D C 2010 Higher-accuracy van der Waals density functional *Phys. Rev. B* **82** 081101
- [8] Klimeš J, Bowler D R and Michaelides A 2009 Chemical accuracy for the van der Waals density functional *J. Phys. Condens. Matter* **22** 022201
- [9] Vurgaftman I, Meyer J R and Ram-Mohan L R 2001 Band parameters for III–V compound semiconductors and their alloys *J. Appl. Phys.* **89** 5815–75
- [10] New Semiconductor Materials. Biology systems. Characteristics and Properties, www.matprop.ru, last accessed 22.08.2022

Accurate first principles band gap predictions in strain engineered ternary III-V semiconductorsBadal Mondal *Wilhelm-Ostwald-Institut für Physikalische und Theoretische Chemie, Universität Leipzig, 04103 Leipzig, Germany
and Fachbereich Physik, Philipps-Universität Marburg, 35032 Marburg, Germany*Marcel Kröner, Thilo Hepp , and Kerstin Volz *Material Science Center and Department of Physics, Philipps-Universität Marburg, D-35043 Marburg, Germany*Ralf Tonner-Zech **Wilhelm-Ostwald-Institut für Physikalische und Theoretische Chemie, Universität Leipzig, 04103 Leipzig, Germany*

(Received 7 March 2023; revised 10 May 2023; accepted 14 June 2023; published 7 July 2023)

Tuning the band gap in ternary III-V semiconductors via modification of the composition or the strain in the material is a major approach for the design of optoelectronic materials. Experimental approaches screening a large range of possible target structures are hampered by the tremendous effort to optimize the material synthesis for every target structure. We present an approach based on density functional theory efficiently capable of providing the band gap as a function of composition and strain. Using a specific density functional designed for accurate band gap computation (TB09) together with a band unfolding procedure and special quasirandom structures, we develop a computational protocol to predict band gaps. The approach's accuracy is validated by comparison to selected experimental data. We thus map the band gap over the phase space of composition and strain (we call this the “band gap phase diagram”) for several important III-V compound semiconductors: GaAsP, GaAsN, GaPSb, GaAsSb, GaPBi, and GaAsBi. We show the application of these diagrams for identifying the most promising materials for device design. Furthermore, our computational protocol can easily be generalized to explore the vast chemical space of III-V materials with all other possible combinations of III and V elements.

DOI: [10.1103/PhysRevB.108.035202](https://doi.org/10.1103/PhysRevB.108.035202)**I. INTRODUCTION**

Materials based on III-V semiconductor compounds are attracting much attention in science and engineering due to their diverse applications in fields such as optoelectronics [1,2]. One of the main goals of basic and applied research is to tailor materials' optical properties to a specific application [3–8]. One of the most critical fundamental properties in this respect is the band gap, both in terms of size and type (direct or indirect). For example, optical telecommunication applications require materials with direct band gaps in the range of 0.80–0.95 eV [3–5], while solar cell applications require a range of 0.5–2.0 eV [6–8]. Composition engineering, i.e., changing the relative composition of group 13 and 15 elements in ternary III-V compounds, is one of the most important approaches to adjusting the band gap [9–22]. Systematic application of strain such as mechanical strain (e.g., external pressure [23–26], mechanical bending of nanowires [27–29]) or strain due to lattice mismatch (e.g., core-shell mismatch in nanowires [30–34]) on a system are alternative strategies to tailor the band gap. Combining composition and strain engineering, the band gap can be tuned over a wide range of values, and direct or indirect semiconductors can be designed. In thin-layer heteroepitaxy, choosing the substrate-layer

combination with minimum lattice mismatch is often desirable to minimize the strain effect from the substrate. However, in practice, perfect lattice matching is rarely possible. In such cases, not only the composition but the effect of inherent strain from the substrate also substantially affects the active layer's band gap [9–22,35–39]. Therefore, one requires a complete knowledge of the material-specific dependence of the band gap on composition and strain to guide the optimal choice of materials. However, exploring the vast chemical space of all possible combinations of III and V elements with variation in composition and strain is experimentally not feasible. Additionally, growing a new material is often challenging because of thermodynamic or kinetic limitations, such as phase separation or surface roughening, in addition to the demanding task of optimizing the growth conditions [9,13,16,19,21,22]. This makes an experimental screening approach of vast compound and strain spaces unrealistic. We thus aim in this study to develop a reliable and predictive theoretical approach.

Two major theoretical approaches that have been used to analyze strain effects on the band gap of III-V materials are (semi-)empirical methods and *ab initio* approaches. Although (semi-)empirical methods such as $k \cdot p$ theory [36,40] and tight-binding methods [36,41–43] are computationally efficient, they rely on empirical parameters which require system-specific experimental input data. This strongly limits the predictive ability of these methods for new or yet unknown materials. Additionally, in case of a large

*ralf.tonner@uni-leipzig.de

mismatch in atomic sizes of the constituting elements, the ternary material shows local strain effects, severely affecting the band gap [44]. These local strain effects, however, can not be included in empirical approaches and, hence, are neglected. Then again, *ab initio* approaches such as density functional theory (DFT) [40,45–50] allow for the calculation of electronic properties from first principles and are thus predictive if accurate density functionals are used. The relaxation of the atomic positions also allows to properly include and investigate the effect of the local strain on the electronic properties in these approaches. Additionally, recent advancements in the modeling strategies of alloy systems using quasirandom supercells [51–55] allow for electronic properties calculations in the *ab initio* approaches, even for diluted and disordered materials. An accurate alternative to DFT approaches is the use of GW-based methods, which are nevertheless too computationally demanding for screening approaches as intended here [44–46,56].

In a previous study, we established a computational protocol for predictive modeling based on DFT for binary III-V compounds over a wide range of strain values [45]. In this study, we are now extending this approach to ternary III-V compounds, which then allow the combination of strain and composition to fully explore a band gap design approach. For ternary systems, only the effects of composition variations on the band gap in unstrained materials have been studied [40,41,44,51–55]. For strained materials, a suitable theoretical framework is still lacking. We present here a predictive first-principles protocol for a complete mapping of the mutual correlation of composition, strain, and band gap in ternary III-V semiconductor systems. The goal is to provide guidelines for assessing and identifying the most promising target materials for experimental investigations in the future.

We start by describing the computational methods in Sec. II. Next, we describe the protocol for determining the nature of the band gap from supercell calculations using GaAsP as an example in Sec. III. We further present the composition-strain-band gap correlation results for different ternary III-V semiconductors in Sec. IV. We start with GaAsP, an experimentally well-studied and promising candidate for LEDs, detectors, and Si-based multijunction solar cells [57–64]. The results for the GaAsN compound, a promising laser-active material [44,65–67], are presented next. To show the general applicability of our approach, we then show selected results for (i) GaPSb, a candidate for vertical cavity emitting surface laser [68–72]; (ii) GaAsSb, a material for tandem solar cell application [73,74]; (iii) GaPBi, a promising material for nearinfrared photonic device application on Si [75,76]; and (iv) GaAsBi, another material discussed for near and midinfrared photonic device application [77–79]. We then discuss the comparison of our computations with experimental data in Sec. V, underlining the accuracy and predictive capability of our computational approach.

II. COMPUTATIONAL DETAILS

The calculations were performed with DFT-based approaches as implemented in the Vienna *ab initio* simulation package (VASP 5.4.4) [80–83], using plane wave basis sets in conjunction with the projector-augmented wave (PAW)

approach [84,85]. The ternary materials were generated using the special quasirandom structures (SQS) approach [86] with a supercell of size $6 \times 6 \times 6$. The SQS cells were generated using the alloy theoretic automated toolkit (ATAT) [87–89]. For all the materials except GaAsN, one SQS cell was used per composition. In GaAsN, in agreement with the previous observation [44], we found that the size of the band gap strongly depends on the distribution of N atoms in the supercell, even in the SQS approach. We thus used 10 SQS cells for each composition in this case.

Geometry optimization of the supercells was performed using the PBE functional [90], including the dispersion-correction method DFT-D3 with an improved damping function [91,92]. The basis set energy cutoff was set to 450 eV. The electronic energy convergence criteria of 10^{-6} eV and the force convergence of 10^{-2} eVÅ⁻¹ were used. The reciprocal space was sampled at the Γ point only, given the large supercells used [93]. The meta-GGA functional TB09 [47] was used to calculate the electronic properties (band gaps and band structures). The effects of spin-orbit coupling were considered in the TB09 calculations. For the meta-GGA calculations, the energy cutoff of the basis set and the convergence criterion for the electronic energy were lowered to 350 eV and 10^{-4} eV, respectively, to reduce the computational costs. Structure optimizations were carried out by consecutive volume and position optimization until convergence was reached. This setup was previously used to generate band gaps in excellent agreement with experimental data [44].

All the materials within the composition range investigated here feature the zincblende-type structure only. Moreover, [100] crystal direction is the most common choice of substrate orientation and growth direction in epitaxy. Therefore, we modeled the strain application along [100] directions only. The isotropic strain was modeled by increasing (decreasing) all the lattice parameters of the unstrained structure by the same amount. In this case, only the atomic positions of the strained structure were optimized, keeping the volume fixed. For biaxial strain, the in-plane lattice parameters were kept fixed, and the lattice parameter in the out-of-plane direction was optimized. No structural phase transition is assumed under strain application. More details on the strain modeling can be found in Ref. [45]. In the following, we indicate tensile strain with a positive sign and compressive strain with a negative sign.

DFT calculations were performed at discrete points in composition-strain space (Fig. S6 [94]). The calculated band gap values were then interpolated to create the final images in Figs. 2–6. Noticeably, for the systems we addressed in this article, the variations of band gap values with concentration and strain are mostly nonmonotonic (Fig. S6 [94]). This resulted in nonsmooth interpolation in Figs. 2–6. It is to be stressed that the origin of the nonsmooth patterns is neither an interpolation artifact nor a deficiency of our DFT protocol. This solely originated because of the nonmonotonic variation of the band gap values (in the composition-strain space) of the SQS cells that we used to calculate band gaps. A choice of positive smoothing during interpolation (e.g., bivariate B-spline, gaussian filtering) could mitigate the problem but significantly increased the deviation of the interpolated band gap values from the calculated DFT values and was thus not

chosen. Further detail of the interpolation procedures can be found in Sec. SVI [94]. Moreover, the nature of band gaps can solely be deduced from the direct-indirect transition lines and thus requires no interpolation.

III. PROTOCOL FOR DETERMINING BAND GAP NATURE

Supercell calculations, as required for modeling ternary semiconductors, lead to the folding of band structures [104,105]. The size of the band gap can be well extracted from the folded band structure, which represents the energy difference between the highest occupied VB and the lowest unoccupied CB obtained from supercell calculations (folded bands). However, determining the band gap's nature requires the primitive Bloch character of the bands to be known, which gets mixed up in the supercell eigenstates. With the band unfolding method, one projects these supercell eigenstates on the eigenstates of a suitable reference primitive cell. This requires the calculation of Bloch spectral weights (BSW), which measure the fraction of the primitive Bloch character in a supercell eigenstate. The result is an effective band structure (EBS) [51–55]. The spectral weights, $w_{n,\mathbf{K}}(\mathbf{k})$, can be calculated from the plane wave coefficients as described in Ref. [55]:

$$w_{n,\mathbf{K}}(\mathbf{k}_j) = \sum_{\mathbf{g}} |C_{n,\mathbf{K}}(\mathbf{g} + \mathbf{G}_j)|^2, \quad (1)$$

where n represents the band index, and the reciprocal lattice vectors of the primitive and supercell are denoted by \mathbf{g} and \mathbf{G}_j , respectively. The index j accounts for the series of primitive vectors, $\mathbf{k}_j = \mathbf{K} + \mathbf{G}_j$. The code “fold2Bloch” from Ref. [54] was used to calculate the BSW values.

In our previous study on binary III-V systems [45], we have shown that the valence band maxima (VBM) always remain at the Γ point, and only the conduction band minima (CBM) change their position in reciprocal space under strain. We have also shown that the CBM occurs only at the Γ , L, and (near) X point in the band structure under strain. Therefore, it is sufficient to trace the conduction band (CB) at these points to determine the nature of the band gap. As in our previous study on binary systems, we focus here on analyzing ternary III-V compounds with zincblende structures. For these structures in the $6 \times 6 \times 6$ supercell dimensions chosen here, the Γ , L, and X point of the primitive band structure fold to the Γ point in the supercell [53–55]. Therefore, it is sufficient to calculate the BSWs of solely the CB at the Γ point in the supercell calculation to determine the nature of the band gap. Consequently, we performed the supercell calculations by sampling the reciprocal space only at the Γ point and unfolded the CB.

Figure 1 shows the steps for determining the band gap nature from supercell calculations more clearly. Figure 1(a) shows the band gap variation for GaAs_{0.963}P_{0.037} with 3.7% P concentration under isotropic compressive strain. The Γ , L, and X BSWs of the folded supercell CB are given in parentheses. This shows 100% Γ BSW for the unstrained structure in line with the direct band gap. With increasing strain, the Γ BSW decreases (first number in brackets), and the L BSW increases (second number in brackets). After a certain amount of strain, the L character of the CB dominates. The band gap

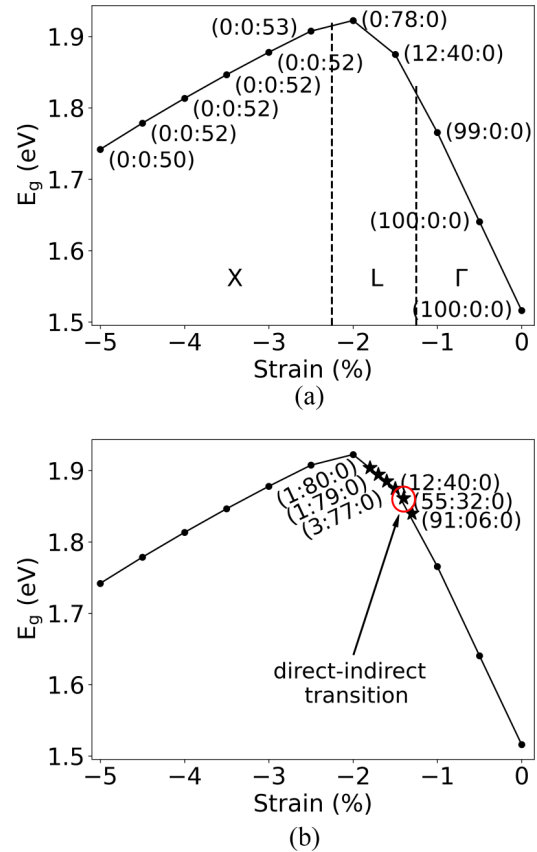


FIG. 1. Variation of the band gap under isotropic compressive strain for GaAs_{0.963}P_{0.037}. The Γ , L, and X BSW of the folded supercell conduction band are given in parentheses in the format (Γ :L:X). The vertical lines in (a) separate regions where the CBM changes character. In (b), the strain resolution is increased to determine the point of direct-indirect transition more accurately, indicated by the red circle (where the highest BSW changes from Γ to L).

becomes indirect in nature. Notably, once the strain values reach the point of direct-indirect transition (DIT) in the band gap nature (around -1.5% strain), the band gap values begin to decrease further with additional strain. This trend is like what we previously observed in binary III-V semiconductor systems, where a strong dependence of the band energies (E) on the wavevectors (\mathbf{k}) under strain was found, leading to a nonmonotonic variation of band gap values with strain [45]. Moreover, we found that such nonmonotonic behavior in band gap values under strain points to a DIT [45]. In ternary III-V semiconductor systems, we have now found that similar nonmonotonic behavior in band gap values under strain also indicates a DIT. Further compressing the system then leads to a transition of the CB character from L to X.

In Fig. 1(b), we show calculations with increased resolution in strain to accurately determine the transition to L corresponding to the sought point of DIT at -1.4% strain. We define the last strained structure with band gap of direct nature before the transition to the indirect band gap as the transition point [the red circle in Fig. 1(b)]. In the Supplemental Material (Fig. S1 [94]), we have given the EBSs of GaAs_{0.963}P_{0.037} for different strain values. These confirm our analyses.

If the difference in BSW between different points in k -space is large, the nature of the band gap can be unanimously determined. However, close to the transition points, in some cases, the differences are more subtle (Fig. S2 [94]). We, therefore, set a cutoff criterion of 20% BSW. If the Γ BSW is larger than the cutoff criterion, then the direct transition has a finite probability even if the L or X BSW is larger than the Γ BSW. In such cases, the band gap is called “partially direct.” This defines a “region of uncertainty” in the band gap nature. We chose the 20% cutoff criterion because this produces results that agree best when compared to the experiments for several systems. For the GaPBi system, however, the 10% BSW cutoff criterion produces the best agreement.

In some systems such as GaAsN, the band originating from the added nitrogen atoms, the so-called “defect N state” [54,106–109], is strongly dispersed under strain (Figs. S3b and S4b [94]). Therefore, we set another cutoff criterion of 20% BSW as a minimum limit for a (defect) eigenstate to be considered an eigenstate (Fig. S5 [94]). Starting from the lowest unoccupied CB, we search for eigenstates until the cutoff BSW criterion is met, at which point we consider it to be the redefined CB. If none of the CBs satisfy the cutoff criterion, we use the lowest CB for determining the band gap nature. Accordingly, in these cases, we calculate the band gap values as the energy difference between the highest VB and the redefined CB. When redefining, unoccupied CB states that do not satisfy the cutoff criteria are disregarded. This led to an increase in the band gap values, as is observed in Fig. S5 [94].

IV. RESULTS

In this section, we present the band gaps calculated for different materials and determine their nature according to the above protocol. We mapped the band gaps in terms of their size and nature for various strained ternary III-V compounds. We start with two important ternary III-V semiconductor materials, GaAsP and GaAsN. Then we show selected data for the material systems GaPSb, GaAsSb, GaPBi, and GaAsBi.

A. GaAsP

For the case of isotropic strain, Fig. 2 shows the band gap as a function of composition ($x = 0$ –100% in $\text{GaAs}_{1-x}\text{P}_x$) from 5% tensile to 5% compressive strain. The band gap value varies between 0.32 and 2.42 eV in the strain regime investigated. For the same amount of P concentration, the band gap primarily increases in moving from tensile to compressive. Furthermore, the figure shows that in going from compressive to tensile strain, the DIT occurs at a higher concentration of P atoms. The dashed horizontal line marks the data corresponding to the unstrained structures for different fractions of P. The intersection of this line with the DIT line shows at which percentage of phosphorous contribution the unstrained structure shows a DIT. This transition occurs at $x = 37\%$. Here, the band gap shows a value of 1.96 eV. The terms direct and indirect in the figure correspond to the area where the band gap is direct and indirect, respectively. Due to the similarity with commonly used phase diagrams, we call this representation a “band gap phase diagram.” This and the

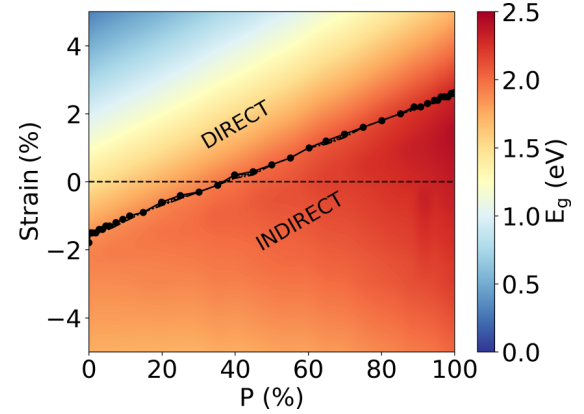


FIG. 2. Isotropic strain for GaAsP. The variation of band gap magnitudes (E_g) and type as a function of composition and strain. The dashed black horizontal line indicates unstrained GaAsP. The black circles are the calculated DIT points. The direct and indirect enclosed regions describe the nature of band gap being direct and indirect, respectively. The hatched pattern region is the “uncertainty region” (see Sec. III).

following figures thus provide a 2D representation of the band gap phase diagram for the ternary materials.

For the biaxial strain regime, Fig. 3 shows the band gap phase diagram for GaAsP as a function of composition from 5% tensile to 5% compressive strain. The value of the band gap varies in a range of 0.82–2.42 eV. For the same amount of P atoms, the band gap reaches a maximum around the unstrained structure and gets smaller for tensile as well as compressive strain. This is different from the isotropic strain case. For unstrained GaP, the band gap value is 2.36 eV. The nature of the band gap also shows a different trend compared to Fig. 2. The range of strain around the unstrained structure where a direct band gap is found gets smaller for higher

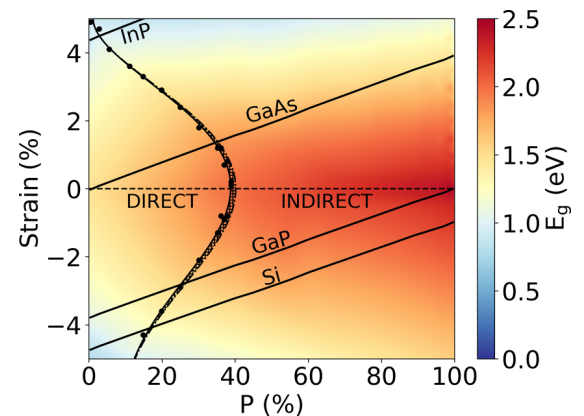


FIG. 3. Biaxial strain for GaAsP. The variation of band gap magnitudes (E_g) and type as a function of composition and strain. The dashed black horizontal line indicates unstrained GaAsP. The black circles are the calculated DIT points. The DIT points are fitted with a fifth-order polynomial. The direct and indirect enclosed regions describe the nature of band gap being direct and indirect, respectively. The hatched pattern region is the “uncertainty region” (see Sec. III). Solid black lines indicate the substrate lines under “epitaxial growth” model.

amounts of P. This is in line with GaAs (0% P) being a direct and GaP (100% P) being an indirect semiconductor. The largest amount of P concentration where a direct semiconductor is found is 39–40% P in the unstrained structure. This is similar to the previous experimental result (45% P) [10,110].

One of the most common approaches to experimentally realize biaxial strain in III-V semiconductors is epitaxial growth. As pointed out in Ref. [45], biaxial strain can be used to model epitaxial growth. We thus investigate the effect of different substrates in our band gap phase diagram (Fig. 3), where each solid line corresponds to one substrate: GaAs, GaP, InP, or Si. These solid lines indicate how much biaxial strain would develop in the GaAsP system as the respective value of % P when grown on the respective substrates under idealized conditions. The (substrate) strains are calculated according to Eq. (2):

$$\text{Substrate strain(\%)} = \frac{a_{\text{sub}} - a}{a} \times 100, \quad (2)$$

where a_{sub} is the equilibrium lattice parameters of the substrates, and a is the lattice parameters of unstrained GaAsP systems at their respective P concentrations, e.g., for 100% P, the strain on the GaP substrate is zero, while growing GaAs (0% P) on GaP would result in 3.8% in-plane compressive strain. This, of course, neglects defect formation and strain relaxations and assumes perfect epitaxial growth. Clearly, by choosing different substrates, the nature can be changed, and the size of the band gap can be tuned over a wide range. We refer to the next section for a comparison of our calculations to experimental data.

B. GaAsN

As the next material, we investigate GaAsN. First, we show results for isotropic strain, which results in the band gap phase diagram shown in Fig. 4. The results are markedly different from GaAsP, and the data set is much more limited. In this case, we found a strong dependency of the band gap on the N atoms distribution in the supercell [44]. We thus used 10 SQS cells for each data point in the figure and averaged the resulting band gaps. This results in an error bar for the DIT points, which is rather large for medium amounts of nitrogen atoms due to the formation of small clusters and chains. Calculations were only possible for up to 12% N. For higher concentration and/or high compressive strain, our chosen supercell is not large enough to avoid the unphysical electronic interaction of N atoms with their images in the periodic boundary condition approach. This effect has already been discussed in Ref. [44]. For the strain and composition regions where computation was possible, an indirect gap is only found for low values of % N and rather large compressive strain values. The EBSs for selected % N and strain values are shown in Figs. S3 and S4 [94].

For biaxial strain in GaAsN, the data are shown in Fig. 5. In contrast to GaAsP, the band gap gets smaller with the increasing amount of nitrogen in the system, from 1.47 eV for the unstrained case of GaAs to 0.10 eV for the highly strained systems with a large number of N atoms. All band gaps computed are direct. Epitaxial growth on GaAs is reasonably

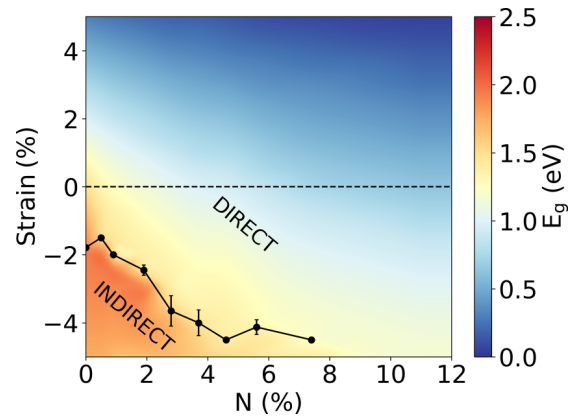


FIG. 4. Isotropic strain for GaAsN (up to 12% N). The variation of band gap magnitudes (E_g) and type as a function of composition and strain. The dashed black horizontal line indicates unstrained GaAsN. The black circles are the calculated DIT points. Beyond 7% N, the DIT is outside the investigated strain regime. 10 SQS cells are used for each configuration and strain point. The band gaps plotted are the average band gaps. The error bars indicate the standard deviation in DIT points estimation. The direct and indirect enclosed regions describe the nature of band gap being direct and indirect, respectively.

possible for moderate strain values and results in a variation of band gap from 1.47 eV to 0.45 eV. For GaP and Si substrates, a large strain would be exerted on the system, and mostly lower band gap values are found.

C. GaPSb, GaAsSb, GaPBi, GaAsBi

The approach outlined here can be extended to other combinations of elements in III-V semiconductor materials. Exemplarily, we present the band gap phase diagrams for four other important ternary compounds in Fig. 6. Since epitaxial growth is the most interesting experimental realization method for these compounds, we only present the data for biaxial strain.

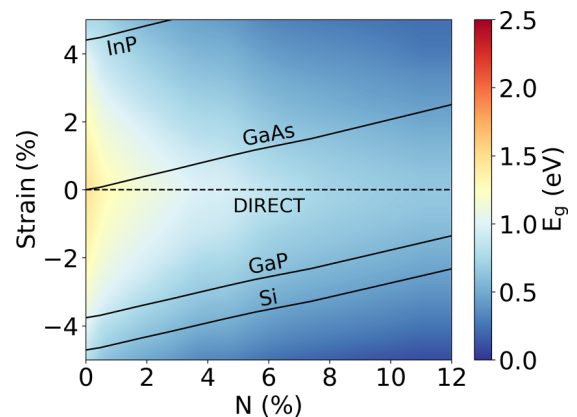


FIG. 5. Biaxial strain for GaAsN (up to 12% N). The variation of band gap magnitudes (E_g) and type as a function of composition and strain. The dashed black horizontal line indicates unstrained GaAsN. 10 SQS cells are used for each configuration and strain point. The band gaps plotted are the average band gaps. All the band gaps are direct in nature. Solid black lines indicate the substrate lines under the “epitaxial growth” model.

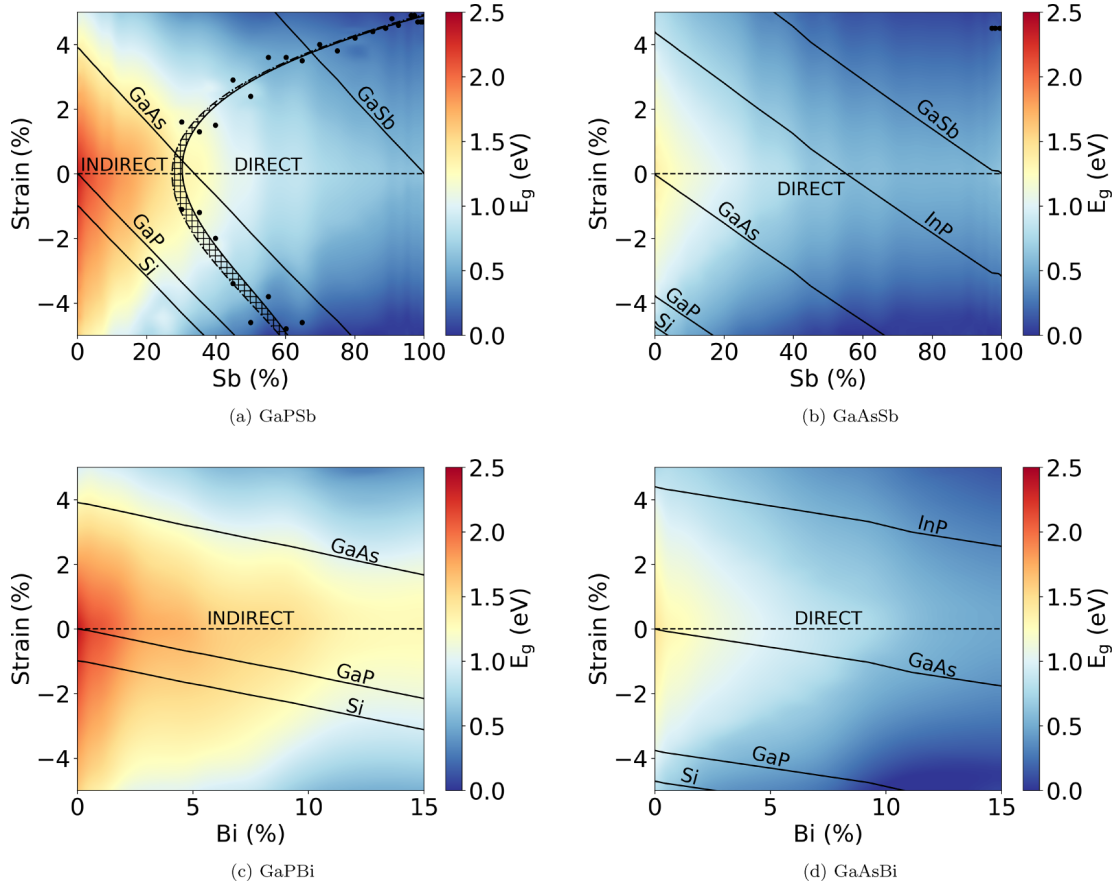


FIG. 6. Band gap phase diagram for ternary III-V semiconductors GaEY ($E = \text{P, As}$; $Y = \text{Sb, Bi}$) under biaxial strain. The band gap magnitudes (E_g) are shown in the color bar. The dashed black horizontal line indicates unstrained structures. The black circles are the calculated DIT points. The direct and indirect enclosed regions describe the nature of band gap being direct and indirect, respectively. The hatched pattern region is the “uncertainty region” (see Sec. III). Solid black lines indicate the substrate lines under the “epitaxial growth” model.

For all compounds investigated, we find a band gap range of 0.00–2.36 eV, with the largest values found for the host materials GaP and GaAs in the unstrained case. The alloys with Sb could be investigated over the full range of 0–100% Sb in GaPSb and GaAsSb [Figs. 6(a) and 6(b)]. We find a DIT for unstrained GaPSb at 30% Sb concentration [Fig. 6(a)]. For this compound, the DIT is shown as a region, including the uncertainty in determining the nature of the band gap, as outlined in Sec. III. With the increase in the Sb fraction, the strain at which the DITs take place increases. For GaAsSb and GaAsBi, the band gap is direct throughout the range investigated [Figs. 6(b) and 6(d)], while it is indirect for GaPBi [Fig. 6(c)]. Notably, we only investigate the bismides up to a fraction of 15% Bi. The reason is that, similar to GaAsN (Fig. S4 [94]), for structures with large Bi content, the strongly dispersed bands decrease the reliability in the determination of band gap nature. Additionally, GaPBi and GaAsBi become metallic for higher Bi fractions. Although we find no transition within 15% Bi, it can not be excluded that the DIT appears at higher percentages of bismuth.

Again, we indicate the strain values associated with different typical substrates for epitaxial growth by solid black lines in the figures. The data show that deviating from the substrate-layer lattice-matching condition quickly leads to high strain,

and defects are highly likely to occur during growth. Also, Si can be used as a substrate for GaPSb and GaPBi epitaxial growth if the Sb or Bi content is not too large. The epitaxial growth of the respective GaAs-based materials (GaAsP, GaAsN, GaAsSb, GaAsBi) will give rise to high strain on Si substrate throughout the whole composition region. A noticeable change in the slope in substrate lines is found close to 10% Bi and 40% Sb concentration in GaAsBi and GaAsSb, respectively. Although we did not find any structural phase transition in those regions, the origin of the change in the slope is not clear to us yet.

From the above discussions, it becomes clear that band gap phase diagrams can be a valuable aid in deciding which substrates are good choices for targeting a specific band gap size and nature for a given ternary material. And vice versa, which material to grow for a specific application and a given substrate? We will discuss this further in the next section.

V. DISCUSSION

All data were derived from DFT computations to this point. In Table I, we now compare our calculated band gaps with experimental data from measurements on heteroepitaxial layer structures. The GaAsP/GaAs samples were grown

TABLE I. Comparison of the calculated band gaps for investigated ternary III-V semiconductors under biaxial strain with experiments. The experimental data are for the heteroepitaxial layer structures, and the band gaps are determined from photoluminescence (PL) measurements. The “I” in the brackets indicate the indirect nature of the band gap. The remaining band gaps are direct. (RT-PL: room temperature PL)

| System | Substrate | $x(\%)$ | Layer Thickness (nm) | Band gap (eV) | | Deviation (eV) | Percentage Deviation (%) | RMSD ^a (eV) | |
|---|-----------|---------|----------------------|---------------|------------|-------------------|--------------------------|------------------------|------|
| | | | | Calculated | Experiment | | | | |
| GaAs _{1-x} P _x [111] | GaAs | 18.0 | 9000 | 1.65 | 1.66 | 0.01 | 0.6 | 0.01 | |
| | | 25.0 | 12250 | 1.72 | 1.72 | 0.00 | 0.0 | | |
| | | 28.0 | 13000 | 1.75 | 1.76 | 0.01 | 0.6 | | |
| GaP _{1-x} Sb _x ^b [72] | GaP | 14.0 | – | 1.66(I) | 1.61(I) | –0.05 | –3.1 | 0.10 | |
| | | GaAs | 29.0 | – | 1.33(I) | 1.39(I) | 0.06 | | 4.3 |
| | | | 32.0 | – | 1.30 | 1.31 | 0.01 | | 0.8 |
| | | | 37.0 | – | 1.24 | 1.33 | 0.09 | | 6.8 |
| | GaSb | 93.0 | – | 0.56 | 0.74 | 0.18 | 24.3 | | |
| GaAs _{1-x} Sb _x | GaAs | 5.5 | 46.3 | 1.22 | 1.34 | 0.12 | 9.0 | 0.13 | |
| | | 7.0 | 51.2 | 1.17 | 1.31 | 0.14 | 10.7 | | |
| GaAs _{1-x} Bi _x [112,113,115] [116–118] | GaAs | 0.9 | 75.0 | 1.28 | 1.33 | 0.05 | 3.8 | 0.10 | |
| | | 1.9 | 67.0 | 1.19 | 1.26 | 0.07 | 5.6 | | |
| | | 2.9 | 60.0 | 1.10 | 1.20 | 0.10 | 8.3 | | |
| | | 3.2 | 59.0 | 1.08 | 1.18 | 0.10 | 8.5 | | |
| | | 3.8 | 54.0 | 1.04 | 1.14 | 0.10 | 8.8 | | |
| | | 4.8 | 25.0 | 0.98 | 1.11 | 0.13 | 11.7 | | |
| | | 5.3 | 50.0 | 0.95 | 1.07 | 0.12 | 11.2 | | |
| 6.0 | 25.0 | 0.91 | 1.04 | 0.13 | 12.5 | | | | |
| GaAs _{1-x} N _x [10,44,114] | GaAs | 1.2 | 6.3 | 1.20 | 1.25 | 0.05 | 4.0 | 0.12 | |
| | | 2.0 | 17.0 | 1.10 | 1.16 | 0.06 | 5.2 | | |
| | | 2.3 | 7.0 | 1.06 | 1.17 | 0.11 | 9.4 | | |
| | | 2.9 | 7.0 | 1.00 | 1.11 | 0.11 | 9.9 | | |
| | | 5.0 | 4.0 | 0.82 | 1.01 | 0.19 | 18.8 | | |
| GaAs _{1-x} Sb _x | GaAs | 27.8 | 3.7 | 0.67 | 1.10 | 0.43 | 39.1 | 0.42 | |
| | | 28.0 | 4.1 | 0.66 | 1.07 | 0.41 | 38.3 | | |
| GaAs _{1-x} N _x [10,44,114] | GaP | 4.9 | 6.0 | 0.66 | 1.18 | 0.52 | 44.1 | 0.66 | |
| | | Si | 6.9 | 5.5 | 0.47 | 1.21 | 0.74 | | 61.2 |
| | 8.9 | | 5.5 | 0.46 | 1.17 | 0.71 | 60.7 | | |
| | 9.5 | | 6.0 | 0.45 | 1.11 | 0.66 | 59.5 | | |
| | 10.9 | 5.4 | 0.45 | 1.11 | 0.66 | 59.5 | | | |
| GaP _{1-x} Sb _x | Si | ≤17.5 | 7–9 | 1.91–1.36(I) | | No RT-PL observed | | | |
| GaP _{1-x} Bi _x [112] | GaP | ≤12.0 | 17–73 | 2.03–1.18(I) | | No RT-PL observed | | | |

^aCalculated from all samples per system.

^bFor GaPSb samples, no specific thicknesses were reported in the reference.

by low-pressure hydride vapor phase epitaxy (LP-HVPE). Further details can be found in Ref. [111]. The remaining samples were grown by metalorganic vapor phase epitaxy (MOVPE). The details of the growth characteristics of the MOVPE samples can be found in Refs. [22,72,112–117]. Experimentally, the layer thickness and band gaps of the MOVPE samples were determined using x-ray diffraction and room-temperature photoluminescence (RT-PL), respectively. Except for GaPSb samples from Ref. [72], in which cases, the PL were measured at 10 K.

The comparison of the experimental band gaps with our computed results shows good agreement. The deviation is

determined with respect to the root-mean-square deviation (RMSD) from all available experimental samples. For most structures, the RMSD is around 0.1 eV. Most computed values deviate by less than 10% from the experimental values (exceptions are discussed separately); in the case of GaAsP, the deviation is even more accurate (< 1%). This confirms our previous findings on unstrained structures that the DFT protocol we developed gives excellent agreement to experimental band gaps [11,40,44,45]. In this study, we show that it is also applicable to compound semiconductors under strain. For samples with very small layer thickness, the matching of experiment and computation is less good. This can be observed

for GaAsSb/GaAs thin samples with RMSD of ca. 0.4 eV. We attribute this to the 2D quantum confinement effect, which is found for thin samples. This confinement effect leads to an increase in the band gap with respect to thicker samples [119]. This effect is not captured in our computational model as the calculations were performed for 3D periodic strained structures. The large deviation observed for GaAsN/GaP and GaAsN/Si samples can not be explained by this effect alone, though. An additional effect here is the strong dependency of the band gap on the distribution of N atoms which has been found for unstrained GaAsN before [44]. The dependency is further amplified under large strain (around 3%, see Fig. 5) in those samples. In the case of GaAsN/GaAs samples, where the N concentration investigated was around 1–5%, the strain is relatively small ($< 1\%$), resulting in better agreement with the experiment as compared to the GaAsN/GaP and GaAsN/Si samples. No RT-PL was observed for GaPSb/Si and GaPBi/GaP samples. This is consistent with our findings that those materials show indirect band gaps [Figs. 6(a) and 6(c)]. Experimental measurements of the magnitude of the indirect band gaps are not available yet.

The consistent agreement between the experiment and calculated band gaps (both in magnitude and in nature) suggests that we are able to quantitatively predict the band gap over a wide range of compounds, compositions, and strain regions. However, as discussed above, the effect of 2D confinement is also crucial for relatively thin quantum well heterostructures and, hence, needs further investigation.

Finally, based on the band gap phase diagram, we propose several design strategies to optimize the selection of material combinations for achieving specific optical applications and new design principles for devices (Fig. 7).

In Fig. 7(a), we propose a quantum-well heterostructure (QWH) composed of biaxially strained GaAsP on GaAs substrate. As the QW layers are made out of a single material with varied composition only, the epitaxial growth could be performed efficiently. The band gap phase diagram shows the areas in compositional phase space where a direct band gap in $\text{GaAs}_{1-x}\text{P}_x$ can be achieved ($x < 34\%$). For $x > 35\%$, the band gaps are indirect and hence, are inappropriate for the heterostructure.

Figure 7(b) shows an efficient approach for the monolithic integration of multiple QWH to construct multijunction photovoltaics. In this case, the QWHs are separated by thin indirect band gap layers of the same material as QWH but only with a different composition. This would make the integration approach efficient, as no sample transfer is required during growth.

In Fig. 7(c), we propose a device with a gradual change in the band gap properties. The concept utilizes the continuous transition in the nature of band gap with alloy concentration in the vicinity of the DIT region. At the amount of P chosen here ($x = 15\text{--}35\%$), we propose to grow the GaAsP epitaxial layer on GaP with P concentration continuously changing from the direct to indirect band gap region or vice versa. This way, changes in the band gap magnitude, as well as the nature of the band gap, are possible. Note that the concentration gradient can be implemented both in the horizontal and vertical directions.

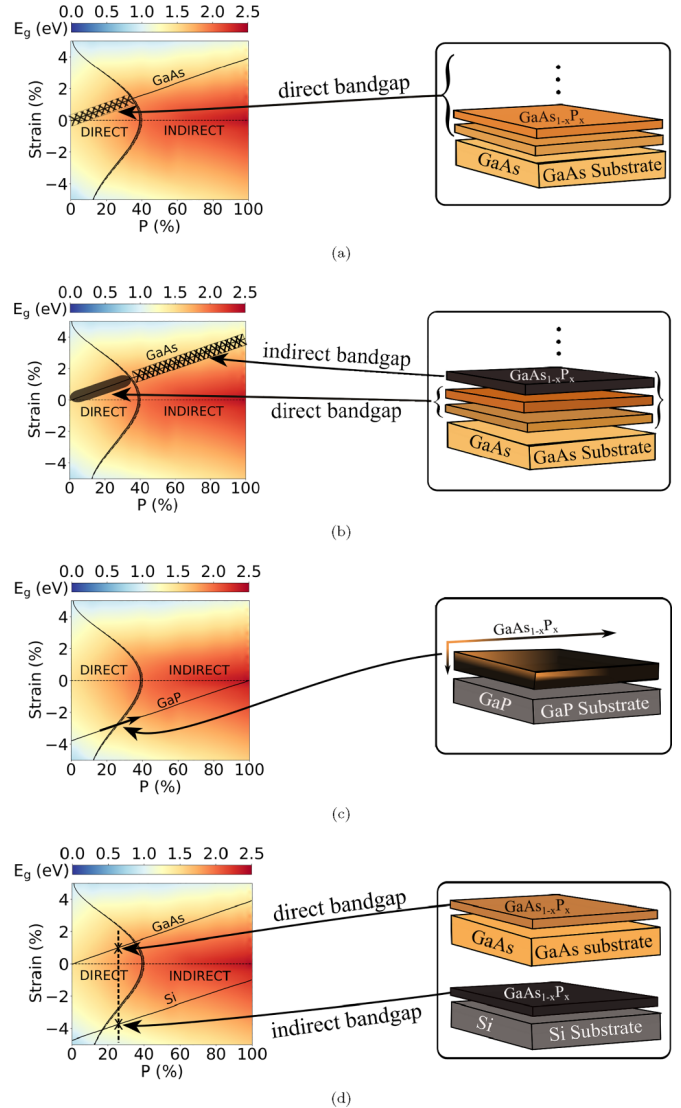


FIG. 7. Proposals on how the band gap phase diagram of biaxially strained GaAsP can be used in designing optoelectronic devices. (a) Defines the bound of composition region for creating a QWH with direct band gap GaAsP on GaAs substrate. (b) Choosing the different composition regions appropriately to make a multijunction photovoltaic with successive direct and indirect cells on the GaAs substrate. (c) In the vicinity of the transition point, the band gap properties of the GaAsP epilayer on the GaP substrate can be changed by appropriately varying the composition. (d) Depending on the choice of substrate, GaAs or Si, the particular composition indicated by the vertical line can be made direct or indirect band gap, respectively.

Figure 7(d) shows another application of this concept. By appropriately choosing the substrate, we can tune the epitaxial layer (here: GaAsP) to show either a direct or indirect band gap. Depending on the substrate, GaAs or Si, the particular composition indicated by the vertical line will show direct or indirect band gap, respectively.

VI. SUMMARY

Using density functional theory and the concept of band unfolding, we developed a first-principles computational protocol for the comprehensive mapping of the band gap magni-

tude and type over a wide range of composition and strain values for several ternary III-V semiconductors. We constructed the composition-strain-band gap relationship, the band gap phase diagram, for several ternary III-V semiconductors: GaAsP, GaAsN, GaPSb, GaAsSb, GaPBi, and GaAsBi. We showed that this way of mapping the effect of strain could be used to choose application-specific best-suited material systems and hence, is highly beneficial to device design. In addition, we developed an efficient approach based on Bloch spectral density for determining the nature of band gap from supercell calculation. Notably, our computational protocol can be generalized to explore the vast chemical space of III-V materials with all other possible combinations of III and V elements. The comparison to experimental band gap data underlines the accuracy of the computational approach chosen. This approach will be extended to more complex materials in the future.

The density functional theory calculations data are openly available in the NOMAD repository [120]. The interactive band gap phase diagrams (in HTML format) are available in the Supplemental Material [94]. To view the diagrams, open the HTML files in a web browser. Alternatively, the diagrams can be viewed directly on GitHub [121], last accessed 10.05.2023).

ACKNOWLEDGMENTS

We thank the Deutsche Forschungsgemeinschaft (DFG) in the framework of the Research Training Group “Functionalization of Semiconductors” (GRK 1782) for funding this project and to HRZ Marburg, GOETHE-CSC Frankfurt, ZIH Dresden, and HLR Stuttgart for providing the computational resources.

-
- [1] R. Soref, *Proc. IEEE* **81**, 1687 (1993).
- [2] P. Y. Yu and M. Cardona, *Fundamentals of Semiconductors: Physics and Materials Properties*, Graduate Texts in Physics (Springer Berlin Heidelberg, 2010).
- [3] T. Hepp, J. Lehr, R. Günkel, O. Maßmeyer, J. Glowatzki, A. Ruiz Perez, S. Reinhard, W. Stolz, and K. Volz, *Electron. Lett.* **58**, 70 (2022).
- [4] C. Fuchs, A. Brüggemann, M. J. Weseloh, C. Berger, C. Möller, S. Reinhard, J. Hader, J. V. Moloney, A. Bäumner, S. W. Koch, and W. Stolz, *Sci. Rep.* **8**, 1422 (2018).
- [5] S. Mokkaapati and C. Jagadish, *Mater. Today* **12**, 22 (2009).
- [6] F. Dimroth, T. N. D. Tibbits, M. Niemeyer, F. Predan, P. Beutel, C. Karcher, E. Oliva, G. Siefer, D. Lackner, P. Fuß-Kailuweit, A. W. Bett, R. Krause, C. Drazek, E. Guiot, J. Wasselin, A. Tauzin, and T. Signamarcheix, *IEEE J. Photovolt.* **6**, 343 (2016).
- [7] B. Mitchell, G. Peharz, G. Siefer, M. Peters, T. Gandy, J. C. Goldschmidt, J. Benick, S. W. Glunz, A. W. Bett, and F. Dimroth, *Prog. Photovolt: Res. Appl.* **19**, 61 (2011).
- [8] S. P. Philipps, F. Dimroth, and A. W. Bett, in *McEvoy's Handbook of Photovoltaics*, edited by S. A. Kalogirou (Elsevier, 2018), 3rd Ed., pp. 439–472.
- [9] A. Beyer, W. Stolz, and K. Volz, *Prog. Cryst. Growth Charact. Mater.* **61**, 46 (2015).
- [10] I. Vurgaftman, J. R. Meyer, and L. R. Ram-Mohan, *J. Appl. Phys.* **89**, 5815 (2001).
- [11] A. Beyer, N. Knaub, P. Rosenow, K. Jandieri, P. Ludewig, L. Bannow, S. W. Koch, R. Tonner, and K. Volz, *Appl. Mater. Today* **6**, 22 (2017).
- [12] P. Ludewig, S. Reinhard, K. Jandieri, T. Wegele, A. Beyer, L. Tapfer, K. Volz, and W. Stolz, *J. Cryst. Growth* **438**, 63 (2016).
- [13] S. Liebich, M. Zimprich, A. Beyer, C. Lange, D. J. Franzbach, S. Chatterjee, N. Hossain, S. J. Sweeney, K. Volz, B. Kunert, and W. Stolz, *Appl. Phys. Lett.* **99**, 071109 (2011).
- [14] O. Supplie, O. Romanyuk, C. Koppka, M. Steidl, A. Nägelein, A. Paszuk, L. Winterfeld, A. Dobrich, P. Kleinschmidt, E. Runge, and T. Hannappel, *Prog. Cryst. Growth Charact. Mater.* **64**, 103 (2018).
- [15] G. Stringfellow, in *Metalorganic Vapor Phase Epitaxy (MOVPE): Growth, Materials Properties, and Applications* (Wiley, 2019), pp. 19–69.
- [16] K. Volz, J. Koch, F. Höhnsdorf, B. Kunert, and W. Stolz, *J. Cryst. Growth* **311**, 2418 (2009).
- [17] M. Feifel, J. Ohlmann, J. Benick, T. Rachow, S. Janz, M. Hermle, F. Dimroth, J. Belz, A. Beyer, K. Volz, and D. Lackner, *IEEE J. Photovolt.* **7**, 502 (2017).
- [18] B. Kunert, J. Koch, T. Torunski, K. Volz, and W. Stolz, *J. Cryst. Growth* **272**, 753 (2004).
- [19] K. Volz, T. Torunski, B. Kunert, O. Rubel, S. Nau, S. Reinhard, and W. Stolz, *J. Cryst. Growth* **272**, 739 (2004).
- [20] J. Veletas, T. Hepp, K. Volz, and S. Chatterjee, *J. Appl. Phys.* **126**, 135705 (2019).
- [21] T. Wegele, A. Beyer, P. Ludewig, P. Rosenow, L. Duschek, K. Jandieri, R. Tonner, W. Stolz, and K. Volz, *J. Phys. D: Appl. Phys.* **49**, 075108 (2016).
- [22] T. Hepp, L. Nattermann, and K. Volz, in *Bismuth-Containing Alloys and Nanostructures*, edited by S. Wang and P. Lu, Springer Series in Materials Science, Vol. 285 (Springer, Singapore, 2019), pp. 37–58.
- [23] P. E. Van Camp, V. E. Van Doren, and J. T. Devreese, *Phys. Rev. B* **41**, 1598 (1990).
- [24] R. F. Potter, *Phys. Rev.* **103**, 861 (1956).
- [25] P. A. Alekseev, V. A. Sharov, B. R. Borodin, M. S. Dunaevskiy, R. R. Reznik, and G. E. Cirlin, *Micromachines* **11**, 581 (2020).
- [26] A. K. Katiyar, K. Y. Thai, W. S. Yun, J. Lee, and J.-H. Ahn, *Sci. Adv.* **6**, eabb0576 (2020).
- [27] B. Lim, X. Y. Cui, and S. P. Ringer, *Phys. Chem. Chem. Phys.* **23**, 5407 (2021).
- [28] G. Signorello, E. Lörtscher, P. Khomyakov, S. Karg, D. Dheeraj, B. Gotsmann, H. Weman, and H. Riel, *Nat. Commun.* **5**, 3655 (2014).
- [29] G. Signorello, S. Karg, M. T. Björk, B. Gotsmann, and H. Riel, *Nano Lett.* **13**, 917 (2013).
- [30] L. Balaghi, G. Bussone, R. Grifone, R. Hübner, J. Grenzer, M. Ghorbani-Asl, A. V. Krashenninnikov, H. Schneider, M. Helm, and E. Dimakis, *Nat. Commun.* **10**, 2793 (2019).

- [31] J. Grönqvist, N. Söndergaard, F. Boxberg, T. Guhr, S. Åberg, and H. Q. Xu, *J. Appl. Phys.* **106**, 053508 (2009).
- [32] M. Hetzl, M. Kraut, J. Winnerl, L. Francaviglia, M. Döblinger, S. Matich, A. FontcubertaMorral, and M. Stutzmann, *Nano Lett.* **16**, 7098 (2016).
- [33] M. Montazeri, M. Fickenscher, L. M. Smith, H. E. Jackson, J. Yarrison-Rice, J. H. Kang, Q. Gao, H. Hoe Tan, C. Jagadish, Y. Guo, J. Zou, M. E. Pistol, and C. E. Pryor, *Nano Lett.* **10**, 880 (2010).
- [34] N. Sköld, L. S. Karlsson, M. W. Larsson, M.-E. Pistol, W. Seifert, J. Trägårdh, and L. Samuelson, *Nano Lett.* **5**, 1943 (2005).
- [35] G. Bir and G. Pikus, *Symmetry and Strain-induced Effects in Semiconductors*, A Halsted Press book (Wiley, 1974).
- [36] Y. Sun, S. E. Thompson, and T. Nishida, *J. Appl. Phys.* **101**, 104503 (2007).
- [37] L. Tao, W. Ou, Y. Li, H. Liao, J. Zhang, F. Gan, and X. Ou, *Semicond. Sci. Technol.* **35**, 103002 (2020).
- [38] G. Tsutsui, S. Mochizuki, N. Loubet, S. W. Bedell, and D. K. Sadana, *AIP Adv.* **9**, 030701 (2019).
- [39] H. Fang, M. Madsen, C. Carraro, K. Takei, H. S. Kim, E. Plis, S. Y. Chen, S. Krishna, Y. L. Chueh, R. Maboudian, and A. Javey, *Appl. Phys. Lett.* **98**, 012111 (2011).
- [40] L. C. Bannow, P. Rosenow, P. Springer, E. W. Fischer, J. Hader, J. V. Moloney, R. Tonner, and S. W. Koch, *Modell. Simul. Mater. Sci. Eng.* **25**, 065001 (2017).
- [41] N. G. Anderson and S. D. Jones, *J. Appl. Phys.* **70**, 4342 (1991).
- [42] Y. Tan, M. Povolotskiy, T. Kubis, T. B. Boykin, and G. Klimeck, *Phys. Rev. B* **94**, 045311 (2016).
- [43] J. M. Jancu, R. Scholz, F. Beltram, and F. Bassani, *Phys. Rev. B* **57**, 6493 (1998).
- [44] P. Rosenow, L. C. Bannow, E. W. Fischer, W. Stolz, K. Volz, S. W. Koch, and R. Tonner, *Phys. Rev. B* **97**, 075201 (2018).
- [45] B. Mondal and R. Tonner-Zech, *Phys. Scr.* **98**, 065924 (2023).
- [46] Y.-S. Kim, M. Marsman, G. Kresse, F. Tran, and P. Blaha, *Phys. Rev. B* **82**, 205212 (2010).
- [47] F. Tran and P. Blaha, *Phys. Rev. Lett.* **102**, 226401 (2009).
- [48] H. Jiang, *J. Chem. Phys.* **138**, 134115 (2013).
- [49] G. Rehman, M. Shafiq, Saifullah, R. Ahmad, S. Jalali-Asadabadi, M. Maqbool, I. Khan, H. Rahnamaye-Aliabad, and I. Ahmad, *J. Electron. Mater.* **45**, 3314 (2016).
- [50] D. Koller, F. Tran, and P. Blaha, *Phys. Rev. B* **85**, 155109 (2012).
- [51] L. W. Wang, L. Bellaiche, S. H. Wei, and A. Zunger, *Phys. Rev. Lett.* **80**, 4725 (1998).
- [52] P. V. C. Medeiros, S. S. Tsirkin, S. Stafström, and J. Björk, *Phys. Rev. B* **91**, 041116(R) (2015).
- [53] V. Popescu and A. Zunger, *Phys. Rev. Lett.* **104**, 236403 (2010).
- [54] O. Rubel, A. Bokhanchuk, S. J. Ahmed, and E. Assmann, *Phys. Rev. B* **90**, 115202 (2014).
- [55] V. Popescu and A. Zunger, *Phys. Rev. B* **85**, 085201 (2012).
- [56] Y. Hinuma, A. Grüneis, G. Kresse, and F. Oba, *Phys. Rev. B* **90**, 155405 (2014).
- [57] M. G. Craford, D. L. Keune, W. O. Groves, and A. H. Herzog, *J. Electron. Mater.* **2**, 137 (1973).
- [58] I. D. Henning and H. Thomas, *Phys. Status Solidi A* **79**, 567 (1983).
- [59] Y. Tanaka and T. Toyama, *IEEE Trans. Electron Devices* **41**, 1475 (1994).
- [60] T. Sato and M. Imai, *Jpn. J. Appl. Phys.* **41**, 5995 (2002).
- [61] J. F. Geisz and D. J. Friedman, *Semicond. Sci. Technol.* **17**, 769 (2002).
- [62] J. R. Lang, J. Faucher, S. Tomasulo, K. Nay Young, and M. Larry Lee, *Appl. Phys. Lett.* **103**, 092102 (2013).
- [63] K. Hayashi, T. Soga, H. Nishikawa, T. Jimbo, and M. Umeno, *Conf. Rec. IEEE Photovoltaic Spec. Conf.* **2**, 1890 (1994).
- [64] T. J. Grassman, D. J. Chmielewski, S. D. Carnevale, J. A. Carlin, and S. A. Ringel, *IEEE J. Photovolt.* **6**, 326 (2016).
- [65] M. Weyers, M. S. Michio Sato, and H. A. Hiroaki Ando, *Jpn. J. Appl. Phys.* **31**, L853 (1992).
- [66] B. Kunert, K. Volz, J. Koch, and W. Stolz, *Appl. Phys. Lett.* **88**, 182108 (2006).
- [67] Y. Zhao, G. Chen, S. Wang, and S. F. Yoon, *Thin Solid Films* **450**, 352 (2004).
- [68] S. Loualiche, A. Le Corre, S. Salaun, J. Caulet, B. Lambert, M. Gauneau, D. Lecrosnier, and B. Deveaud, *Appl. Phys. Lett.* **59**, 423 (1991).
- [69] H. Shimomura, T. Anan, and S. Sugou, *J. Cryst. Growth* **162**, 121 (1996).
- [70] K. Nakajima, T. Ujihara, S. Miyashita, and G. Sazaki, *J. Cryst. Growth* **209**, 637 (2000).
- [71] H. B. Russell, A. N. Andriotis, M. Menon, J. B. Jasinski, A. Martinez-Garcia, and M. K. Sunkara, *Sci. Rep.* **6**, 20822 (2016).
- [72] M. J. Jou, Y. T. Cherg, H. R. Jen, and G. B. Stringfellow, *Appl. Phys. Lett.* **52**, 549 (1988).
- [73] M. J. Cherg, R. M. Cohen, and G. B. Stringfellow, *J. Electron. Mater.* **13**, 799 (1984).
- [74] H. R. Jen, M. J. Cherg, and G. B. Stringfellow, *Appl. Phys. Lett.* **48**, 1603 (1986).
- [75] T. M. Christian, D. A. Beaton, A. Mascarenhas, and K. Alberi, *Proc. SPIE 10174, Int. Symp. Clust. Nanomater.* **10174**, 101740F (2016).
- [76] T. M. Christian, D. A. Beaton, K. Alberi, B. Fluegel, and A. Mascarenhas, *Appl. Phys. Express* **8**, 061202 (2015).
- [77] S. J. Sweeney, Z. Batool, K. Hild, S. R. Jin, and T. J. C. Hosea, in *2011 13th International Conference on Transparent Optical Networks, Stockholm, Sweden* (IEEE, Piscataway, NJ, 2011), pp. 1–4.
- [78] S. Wang, Y. Song, K. Wang, Y. Gu, H. Zhao, X. Chen, H. Ye, H. Zhou, C. Kang, Y. Li, C. Cao, L. Zhang, J. Shao, Q. Gong, and Y. Zhang, in *Asia Communications and Photonics Conference 2013* (OSA, Washington, D.C., 2013), p. AF3B.5.
- [79] D. G. Cooke, F. A. Hegmann, E. C. Young, and T. Tiedje, *Appl. Phys. Lett.* **89**, 122103 (2006).
- [80] G. Kresse and J. Hafner, *Phys. Rev. B* **47**, 558 (1993).
- [81] G. Kresse and J. Hafner, *Phys. Rev. B* **49**, 14251 (1994).
- [82] G. Kresse and J. Furthmüller, *Phys. Rev. B* **54**, 11169 (1996).
- [83] G. Kresse and J. Furthmüller, *Comput. Mater. Sci.* **6**, 15 (1996).
- [84] G. Kresse and D. Joubert, *Phys. Rev. B* **59**, 1758 (1999).
- [85] P. E. Blöchl, *Phys. Rev. B* **50**, 17953 (1994).
- [86] A. Zunger, S. H. Wei, L. G. Ferreira, and J. E. Bernard, *Phys. Rev. Lett.* **65**, 353 (1990).
- [87] A. van de Walle, M. Asta, and G. Ceder, *Calphad* **26**, 539 (2002).
- [88] A. van de Walle, *Calphad* **33**, 266 (2009).

- [89] A. van de Walle, P. Tiwary, M. de Jong, D. Olmsted, M. Asta, A. Dick, D. Shin, Y. Wang, L.-Q. Chen, and Z.-K. Liu, *Calphad* **42**, 13 (2013).
- [90] J. P. Perdew, K. Burke, and M. Ernzerhof, *Phys. Rev. Lett.* **77**, 3865 (1996).
- [91] S. Grimme, J. Antony, S. Ehrlich, and H. Krieg, *J. Chem. Phys.* **132**, 154104 (2010).
- [92] S. Grimme, S. Ehrlich, and L. Goerigk, *J. Comput. Chem.* **32**, 1456 (2011).
- [93] H. J. Monkhorst and J. D. Pack, *Phys. Rev. B* **13**, 5188 (1976).
- [94] See Supplemental Material at <http://link.aps.org/supplemental/10.1103/PhysRevB.108.035202> for the effective band structures of GaAsP, GaAsN, and GaAsN under selected isotropic strain values; a visual representation of the assessment of uncertainty in the band gap nature near the direct-indirect transition region; the DFT calculated band gap values for all the systems described in the manuscript; the details of the interpolation procedure; and the band gap phase diagrams. The Supplemental Material also contains Refs. [45,52,95–103].
- [95] P. V. C. Medeiros, S. Stafström, and J. Björk, *Phys. Rev. B* **89**, 041407(R) (2014).
- [96] P. Virtanen, R. Gommers, T. E. Oliphant, M. Haberland, T. Reddy, D. Cournapeau, E. Burovski, P. Peterson, W. Weckesser, J. Bright, S. J. van der Walt, M. Brett, J. Wilson, K. J. Millman, N. Mayorov, A. R. J. Nelson, E. Jones, R. Kern, E. Larson, C. J. Carey *et al.*, *Nat. Methods* **17**, 261 (2020).
- [97] G. M. Nielson, *Math. Comput.* **40**, 253 (1983).
- [98] R. Renka and A. Cline, *Rocky Mt. J. Math.* **14**, 223 (1984).
- [99] Qhull code for convex hull, delaunay triangulation, Voronoi diagram and halfspace intersection about a point, www.qhull.org.
- [100] P. Alfeld, *Comput. Aided Geom. Des.* **1**, 169 (1984).
- [101] G. Farin, *Comput. Aided Geom. Des.* **3**, 83 (1986).
- [102] J. D. Hunter, *Comput. Sci. Eng.* **9**, 90 (2007).
- [103] T. A. Caswell, A. Lee, M. Droettboom, E. S. de Andrade, T. Hoffmann, J. Klymak, J. Hunter, E. Firing, D. Stansby, N. Varoquaux, J. H. Nielsen, B. Root, R. May, P. Elson, J. K. Seppänen, D. Dale, J.-J. Lee, D. McDougall, A. Straw, P. Hobson *et al.*, *matplotlib/matplotlib: REL: v3.6.0* (2022).
- [104] W. Ku, T. Berlijn, and C.-C. Lee, *Phys. Rev. Lett.* **104**, 216401 (2010).
- [105] S. Y. Yang, H. Yang, E. Derunova, S. S. Parkin, B. Yan, and M. N. Ali, *Adv. Phys.* **X 3**, 1414631 (2018).
- [106] J. C. Goodrich, D. Borovac, C. K. Tan, and N. Tansu, *Sci. Rep.* **9**, 5128 (2019).
- [107] S.-H. Wei and A. Zunger, *Phys. Rev. Lett.* **76**, 664 (1996).
- [108] J. Wu, W. Walukiewicz, K. M. Yu, J. D. Denlinger, W. Shan, J. W. Ager, A. Kimura, H. F. Tang, and T. F. Kuech, *Phys. Rev. B* **70**, 115214 (2004).
- [109] J. Misiewicz, R. Kudrawiec, and G. Sek, in *Dilute Nitride Semiconductors* (Elsevier, 2005) pp. 279–324.
- [110] M. Capizzi, S. Modesti, F. Martelli, and A. Frova, *Solid State Commun.* **39**, 333 (1981).
- [111] A. Strömberg, G. Omanakuttan, Y. Liu, T. Mu, Z. Xu, S. Lourduoss, and Y.-T. Sun, *J. Cryst. Growth* **540**, 125623 (2020).
- [112] L. Nattermann, A. Beyer, P. Ludewig, T. Hepp, E. Sterzer, and K. Volz, *J. Cryst. Growth* **463**, 151 (2017).
- [113] P. Ludewig, N. Knaub, W. Stolz, and K. Volz, *J. Cryst. Growth* **370**, 186 (2013).
- [114] P. Ludewig, M. Diederich, K. Jandieri, and W. Stolz, *J. Cryst. Growth* **467**, 61 (2017).
- [115] R. B. Lewis, M. Masnadi-Shirazi, and T. Tiedje, *Appl. Phys. Lett.* **101**, 082112 (2012).
- [116] M. Masnadi-Shirazi, R. B. Lewis, V. Bahrami-Yekta, T. Tiedje, M. Chicoine, and P. Servati, *J. Appl. Phys.* **116**, 223506 (2014).
- [117] P. Ludewig, Z. L. Bushell, L. Nattermann, N. Knaub, W. Stolz, and K. Volz, *J. Cryst. Growth* **396**, 95 (2014).
- [118] A. R. Mohmad, F. Bastiman, C. J. Hunter, J. S. Ng, S. J. Sweeney, and J. P. David, *Appl. Phys. Lett.* **99**, 042107 (2011).
- [119] L. A. Cipriano, G. Di Liberto, S. Tosoni, and G. Pacchioni, *Nanoscale* **12**, 17494 (2020).
- [120] <https://doi.org/10.17172/NOMAD/2023.02.27-1>.
- [121] <https://bmondal94.github.io/Bandgap-Phase-Diagram/>.

Supplemental Material

Accurate first-principles bandgap predictions in strain-engineered ternary III-V semiconductors

Badal Mondal

*Wilhelm-Ostwald-Institut für Physikalische und Theoretische Chemie,
Universität Leipzig, 04103 Leipzig, Germany and
Fachbereich Physik, Philipps-Universität Marburg, 35032 Marburg, Germany*

Marcel Kröner, Thilo Hepp, and Kerstin Volz

*Material Science Center and Department of Physics,
Philipps-Universität Marburg, D-35043 Marburg, Germany*

Ralf Tonner-Zech*

Wilhelm-Ostwald-Institut für Physikalische und Theoretische Chemie, Universität Leipzig, 04103 Leipzig, Germany

(Dated: June 15, 2023)

* ralf.tonner@uni-leipzig.de

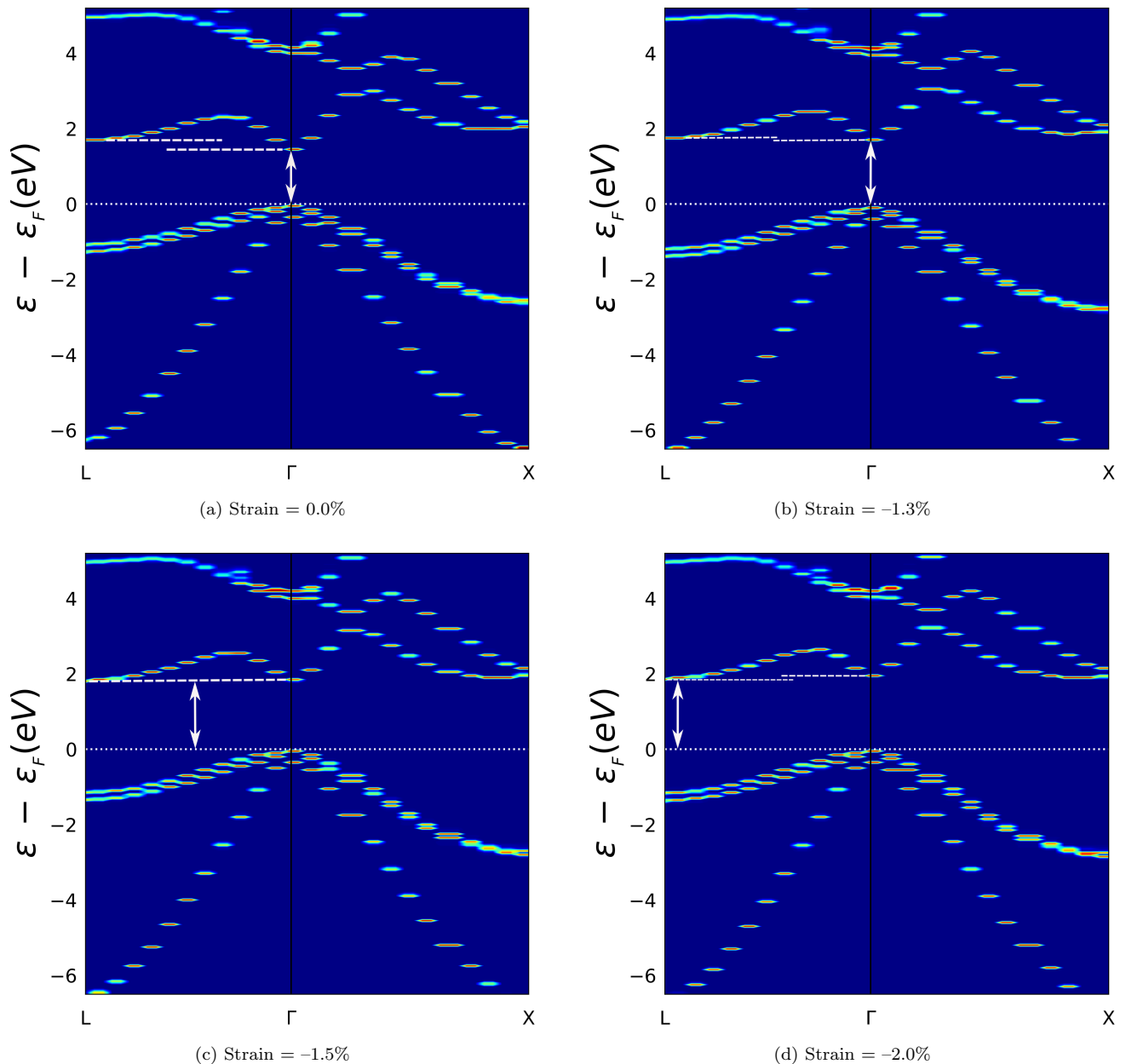
S I. EFFECTIVE BANDSTRUCTURES OF $\text{GaAs}_{0.963}\text{P}_{0.037}$ UNDER ISOTROPIC STRAIN


FIG. S1. Effective bandstructures of $\text{GaAs}_{0.963}\text{P}_{0.037}$ under isotropic strain. The bandstructures were plotted using ‘BandUP’ [1, 2]. In (a) and (b), the bandgaps are direct. (c) The conduction band minima are degenerate at the Γ - and L-point. This is the direct-indirect transition point. (d) The bandgap becomes an indirect bandgap. The positive and negative strains correspond to the tensile and compressive strains, respectively. For simplicity, only the $L \rightarrow \Gamma \rightarrow X$ high symmetry path is shown.

S II. DETERMINING THE NATURE OF BANDGAP USING BLOCH SPECTRAL WEIGHTS

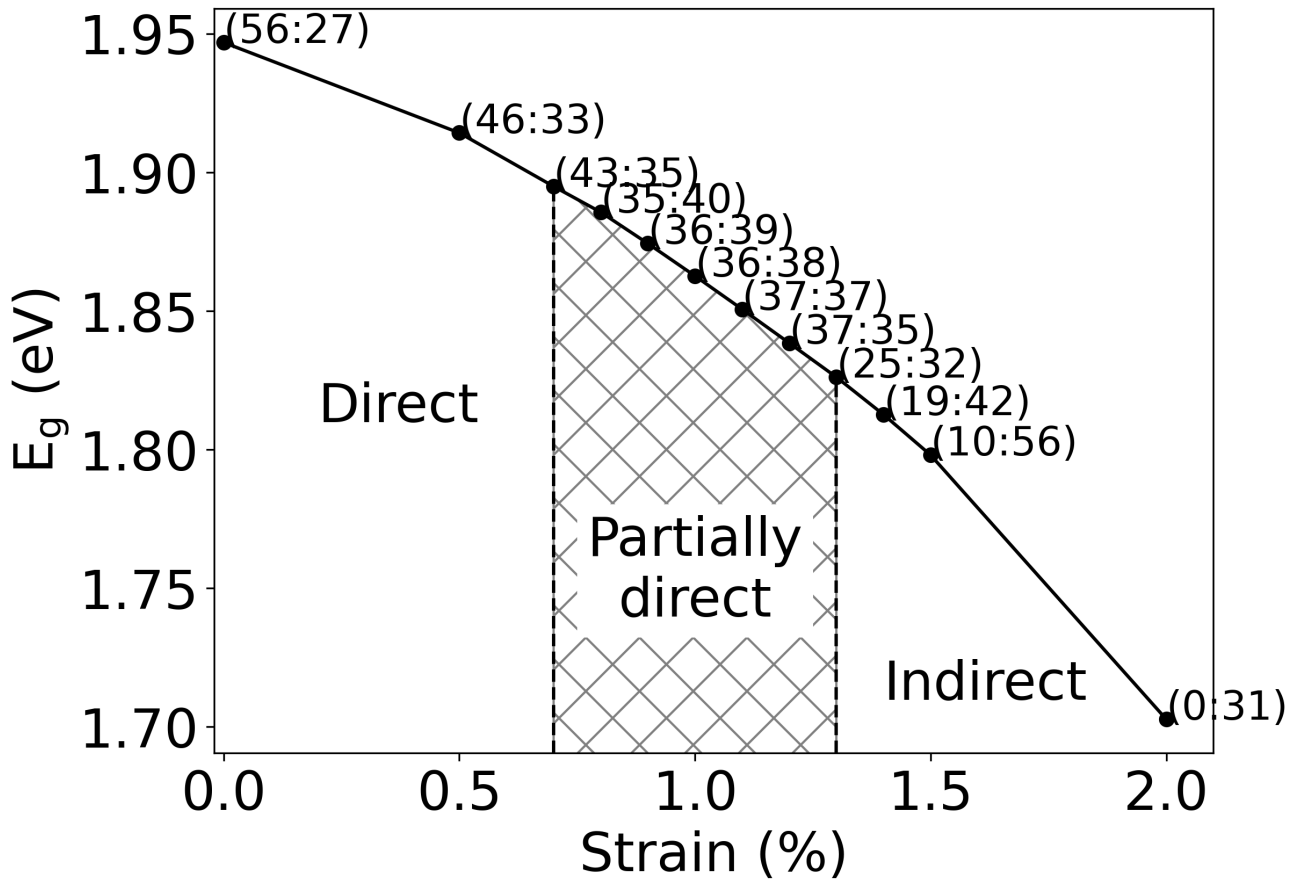


FIG. S2. Variation of the bandgap (E_g) under biaxial tensile strain for $\text{GaAs}_{0.63}\text{P}_{0.37}$. The Bloch spectral weights (BSW) are given for the conduction band at the Γ and L or X point [$\Gamma : (\text{L or X})$]. The vertical lines separate regions where the CBM changes character. As we are only interested in the direct and indirect character of the bandgap, here, we do not explicitly show the L and X BSWs.

S III. EFFECTIVE BANDSTRUCTURES OF $\text{GaAs}_{0.995}\text{N}_{0.005}$ UNDER ISOTROPIC STRAIN

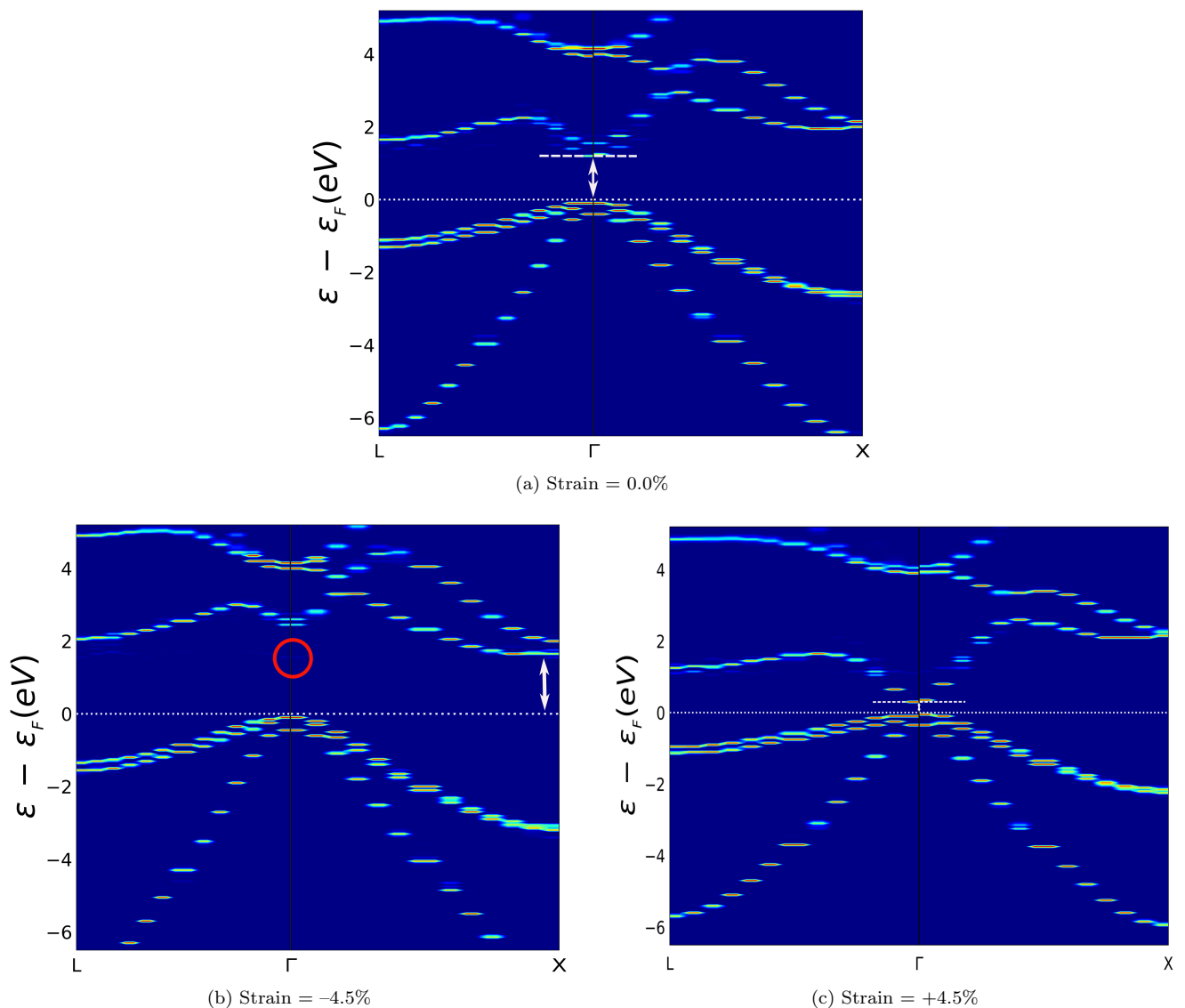


FIG. S3. Effective bandstructures of $\text{GaAs}_{0.995}\text{N}_{0.005}$ under isotropic strain. The bandstructures were plotted using ‘BandUP’ [1, 2]. In (a) and (c), the bandgaps are direct. In (b), the Bloch spectral weight of the ‘N-defect state’ at the conduction band Γ -point is very small, indicated by red circle. Therefore, the bandgap is categorized as an indirect bandgap. The positive and negative strains correspond to the tensile and compressive strains, respectively. For simplicity, only the $L \rightarrow \Gamma \rightarrow X$ high symmetry path is shown.

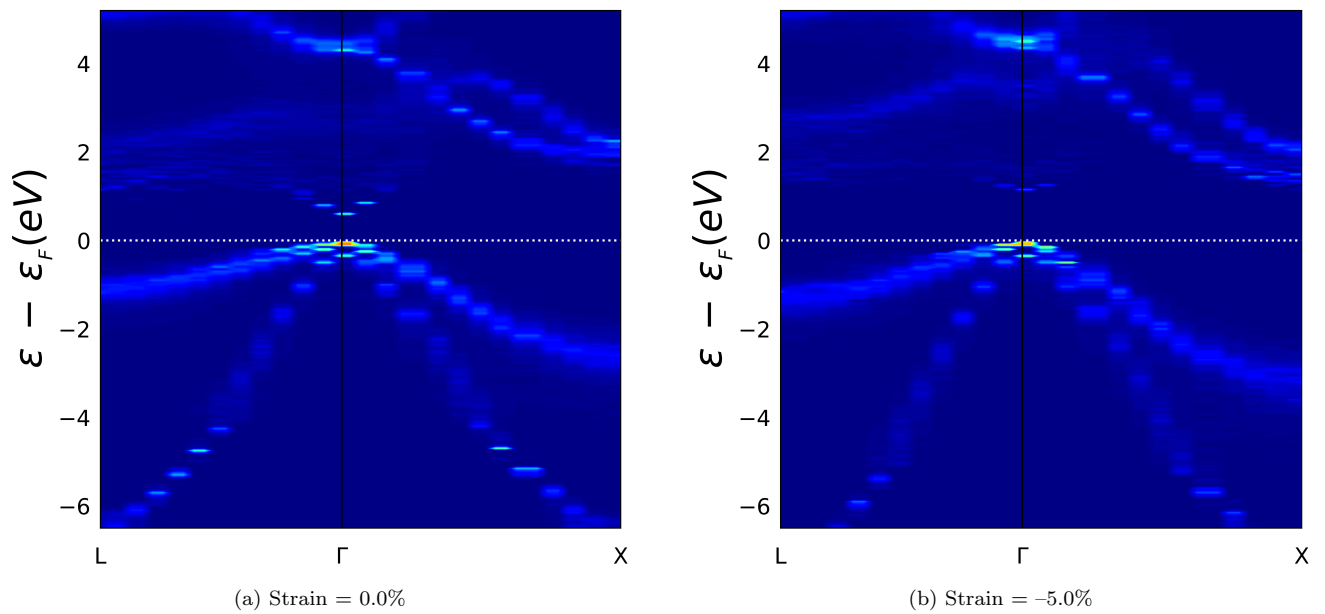


FIG. S4. Effective bandstructures of GaAs_{0.889}N_{0.111} under isotropic strain. The bandstructures were plotted using ‘BandUP’ [1, 2]. The bands are strongly dispersed for high N concentrations. The positive and negative strains correspond to the tensile and compressive strains, respectively. For simplicity, only the L → Γ → X high symmetry path is shown.

S IV. CONDUCTION BAND REDEFINITION BASED ON MINIMUM CUT-OFF BLOCH SPECTRAL WEIGHTS CRITERION

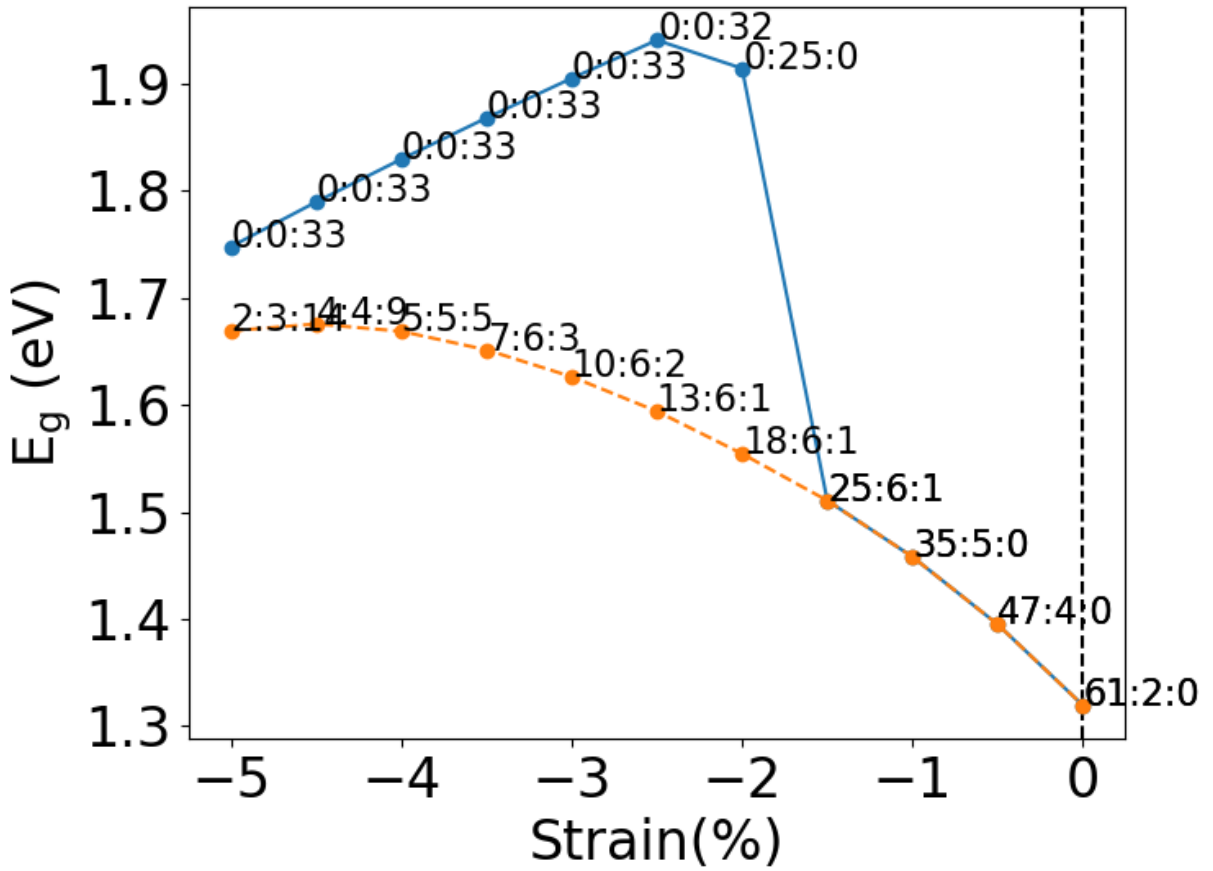
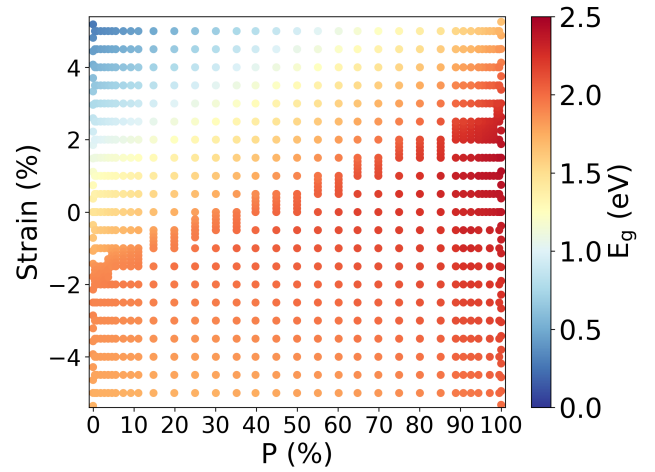
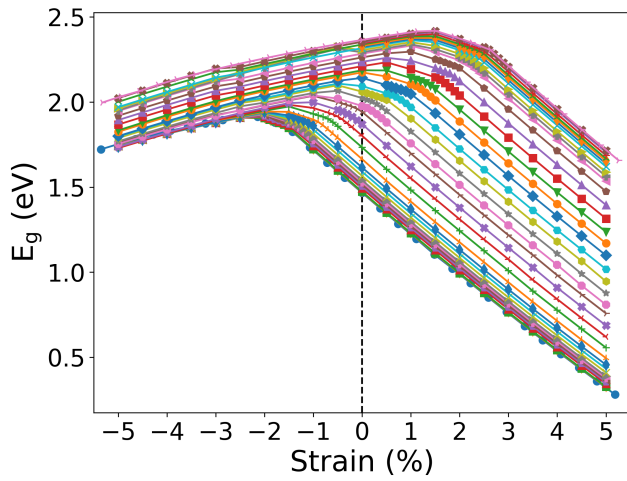
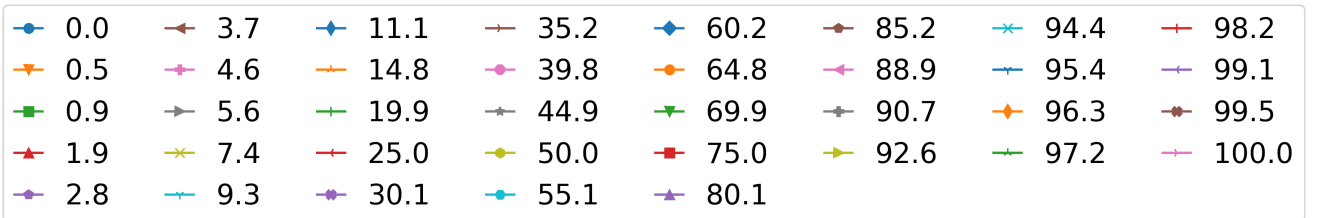
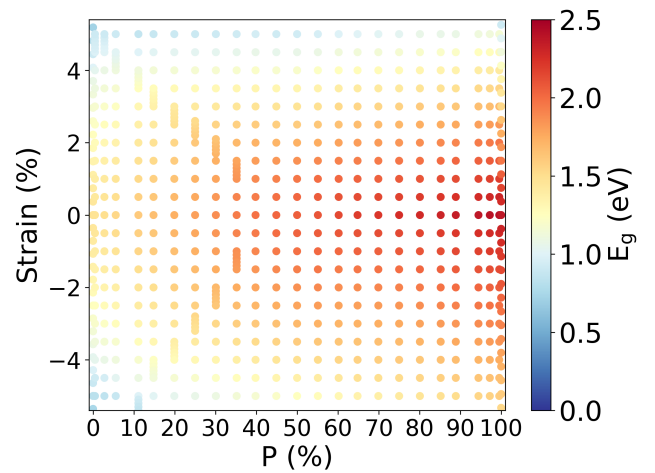
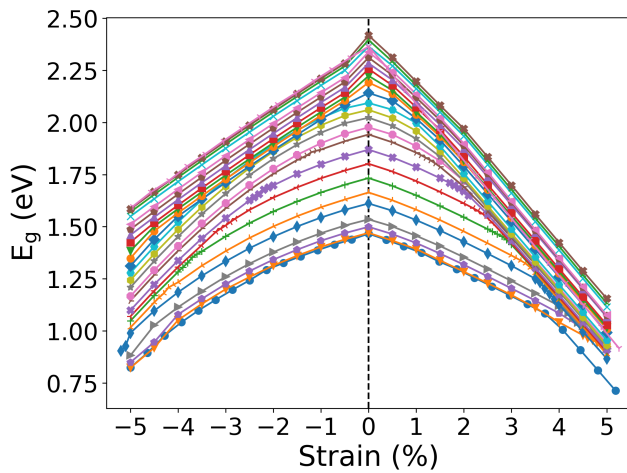


FIG. S5. Variation of the bandgap (E_g) under biaxial compressive strain for $\text{GaAs}_{0.995}\text{N}_{0.005}$. The folded supercell conduction bands' Γ -, L-, and X-BSWs are given at each point. The blue and orange lines are the E_g with and without redefinition of the CBM. 20% BSW is the cut-off criterion for redefining an eigenstate.

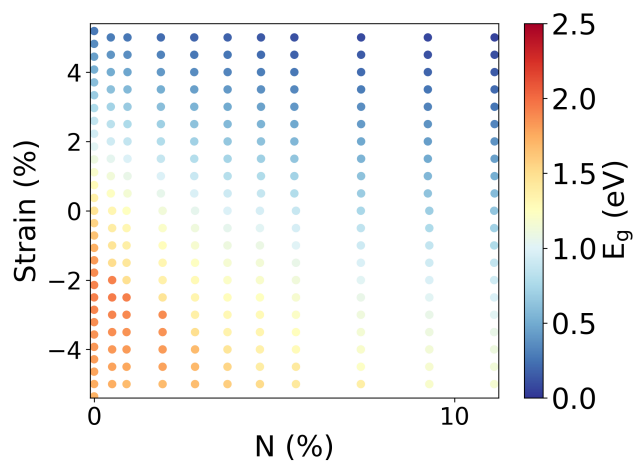
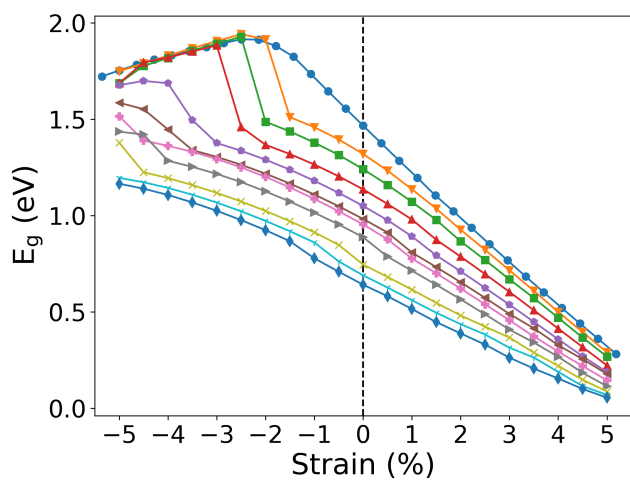
S V. THE DENSITY FUNCTIONAL THEORY BANDGAP VALUES (WITHOUT INTERPOLATION)



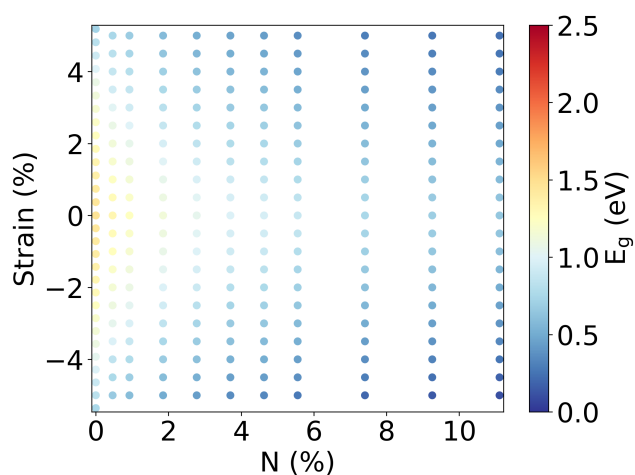
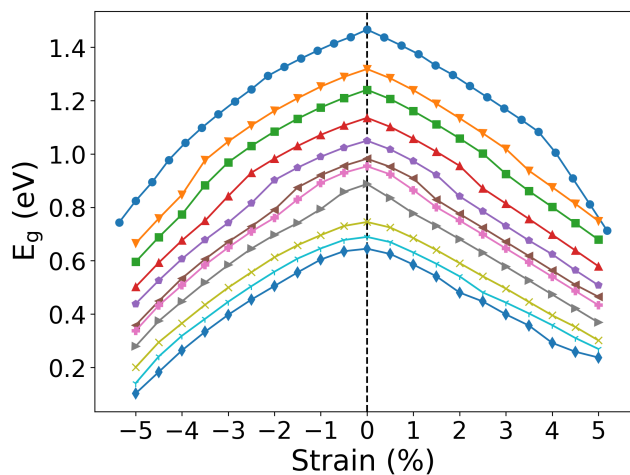
(a) Isotropic strain for GaAsP



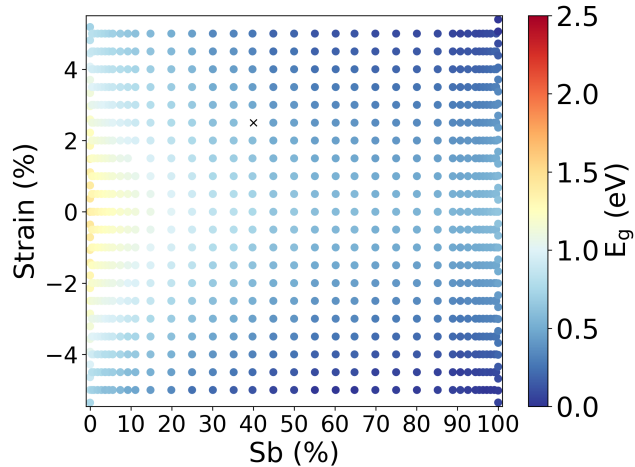
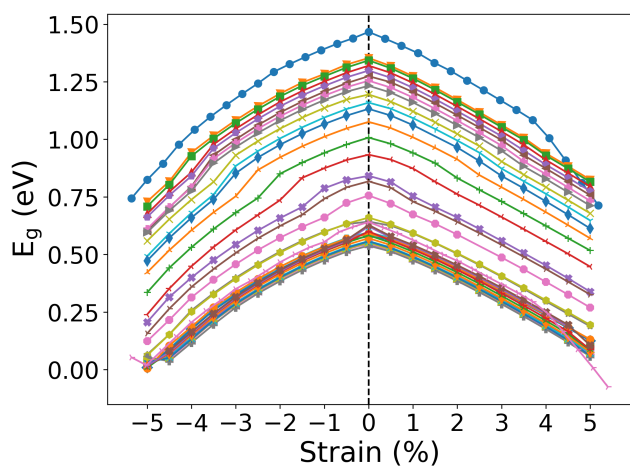
(b) Biaxial strain for GaAsP



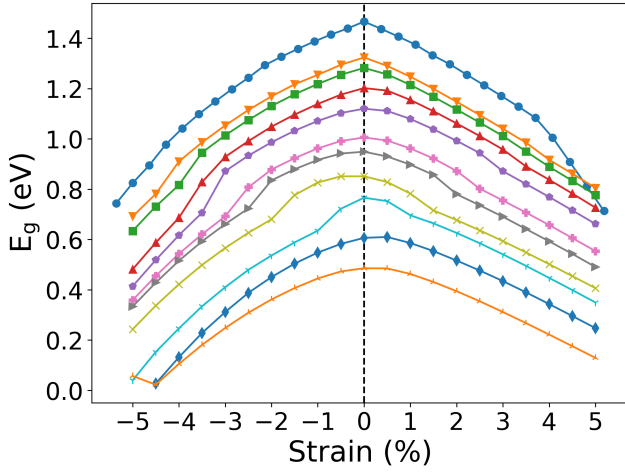
(c) Isotropic strain for GaAsN



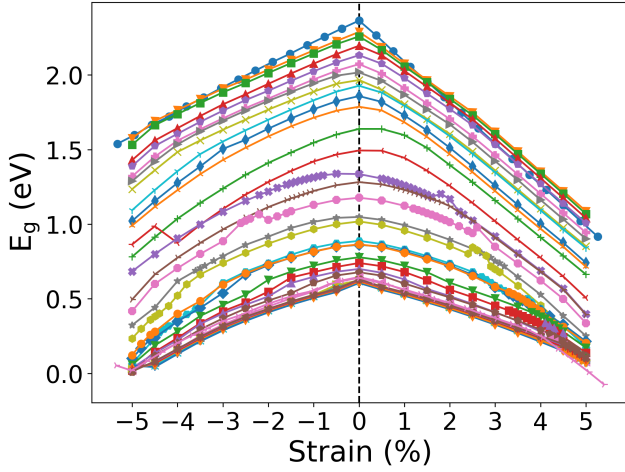
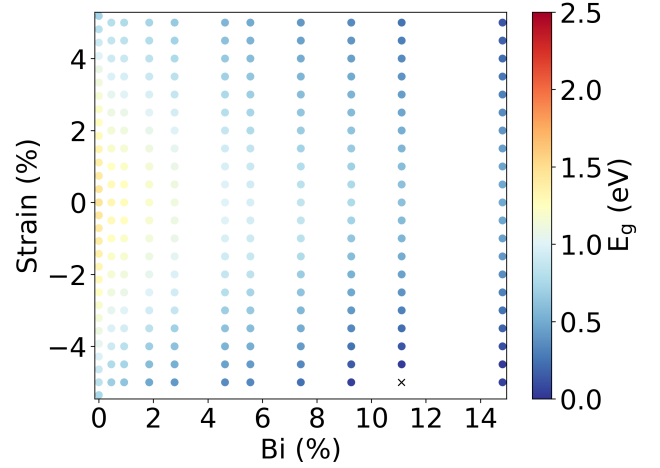
(d) Biaxial strain for GaAsN



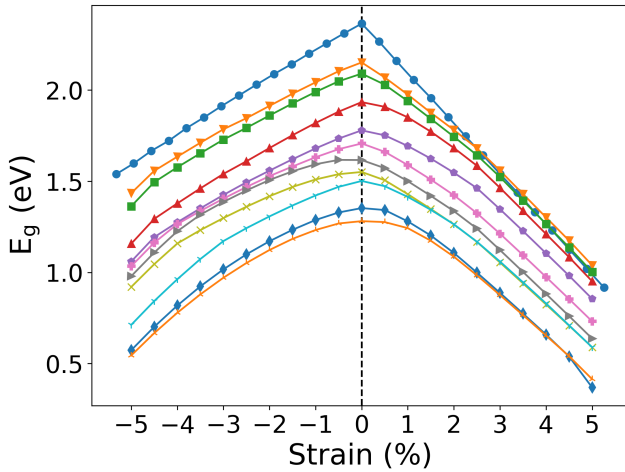
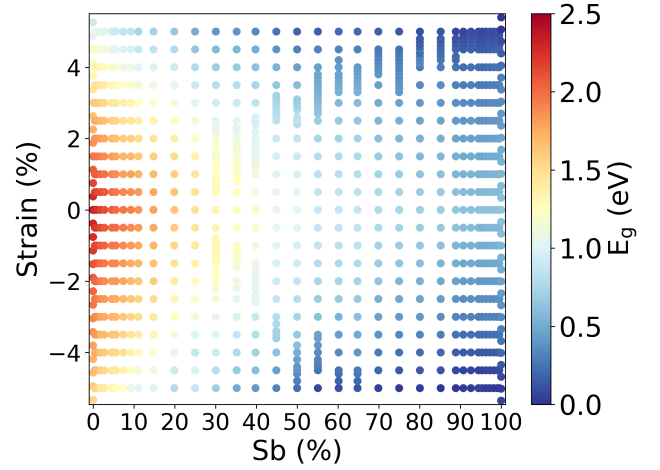
(e) Biaxial strain for GaAsSb



(f) Biaxial strain for GaAsBi



(g) Biaxial strain for GaPSb



(h) Biaxial strain for GaPBi

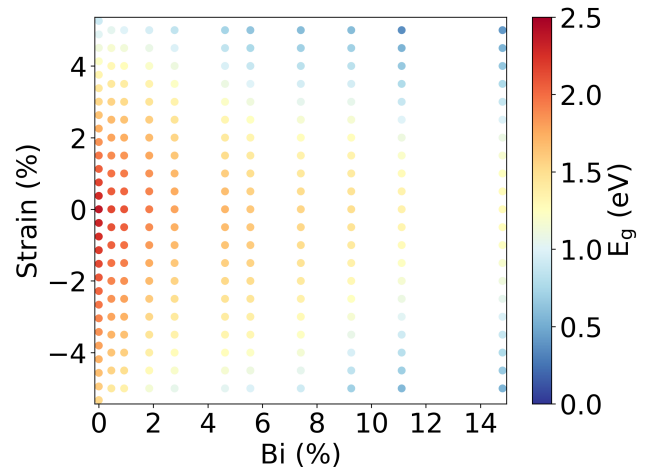


FIG. S6. Effect of strain on the bandgap of $\text{GaE}_{1-x}\text{Y}_x$ ($\text{E}=\text{As}, \text{P}$; $\text{Y}=\text{P}, \text{N}, \text{Sb}, \text{Bi}$). The left column shows the variation of bandgap magnitudes (E_g) as a function of strain at different compositions for the systems. The composition ($x\%$) legends are shown at the top. In the right column, we project the E_g on the composition-strain space. The E_g from these figures is interpolated to create Figs. 2–6 of the manuscript. We chose the same color bar scale for all the systems for consistency. The black crosses in (e) and (f) indicate the bandgap calculations that did not converge.

In Fig. S6, for the binary compounds (GaAs, GaP, and GaSb), we used the bandgap values from the ‘III-V binary semiconductors strain study’ dataset of Ref. [3]. The strain axes were sampled primarily on the regular interval of 0.5%. For GaAsP and GaPSb systems, sampling resolutions were increased close to the direct-indirect transition regions, as explained in Sec. III of the manuscript. For binaries, the intervals were not regular in the reference dataset. The composition axes were sampled in non-regular intervals. Because of the finite supercell size, the compositions could not be sampled in regular intervals. Note, however, the choice of compositions was arbitrary. Also, some of the DFT calculations at high strain could not be converged to the required accuracy and hence, are excluded. For GaAsN, under isotropic strain because of the effective conduction band redefinition (Fig. S5), as explained in Sec. III of the manuscript, the sudden rapid increase in bandgap values under compressive strain are noticeable (Fig. S6c). The sudden increase in band energies due to band redefinition is also visible for compressively strained GaPSb at 25% Sb concentration (Fig. S6g).

S VI. INTERPOLATION DETAILS

The E_g from the right column figures of Fig. S6 were interpolated over a fine grid to create Figs. 2–6 of the manuscript. We chose 0.1 grid resolution in both composition and strain for all the systems. We used Clough-Tocher piecewise cubic, C1 smooth, curvature-minimizing 2D interpolator from python `scipy.interpolate` class [4]. The interpolation scheme follows:

- Step 1: The input data are first triangulated with `Qhull` [5] (Fig. S7b).
- Step 2: The interpolant then constructs a piecewise cubic interpolating Bézier polynomial on each triangle using the Clough-Tocher scheme [6, 7] (Fig. S7c). The interpolant is guaranteed to be continuously differentiable. The interpolant gradients are determined such that the interpolating surface curvature is approximately minimized [8, 9].
- Step 3: In the end, nearest-neighbor extrapolation is performed on the remaining points that can not be covered via `Qhull` (Fig. S7d). Note that mostly the boundary points beyond the x and y limits of input points can not be triangulated under `Qhull`. As long as those points are not far away from the available input points, the nearest-neighbor extrapolations to those points are acceptable.
- Step 4: Finally, bicubic interpolation, as implemented in python `matplotlib.pyplot.imshow` class [10, 11] is applied to smoothen the grid image (Fig. S7e).

Note both the input data and interpolation grid are rescaled to unit square during interpolation to eliminate the effect of incommensurable units and/or large differences between the x & y scales.

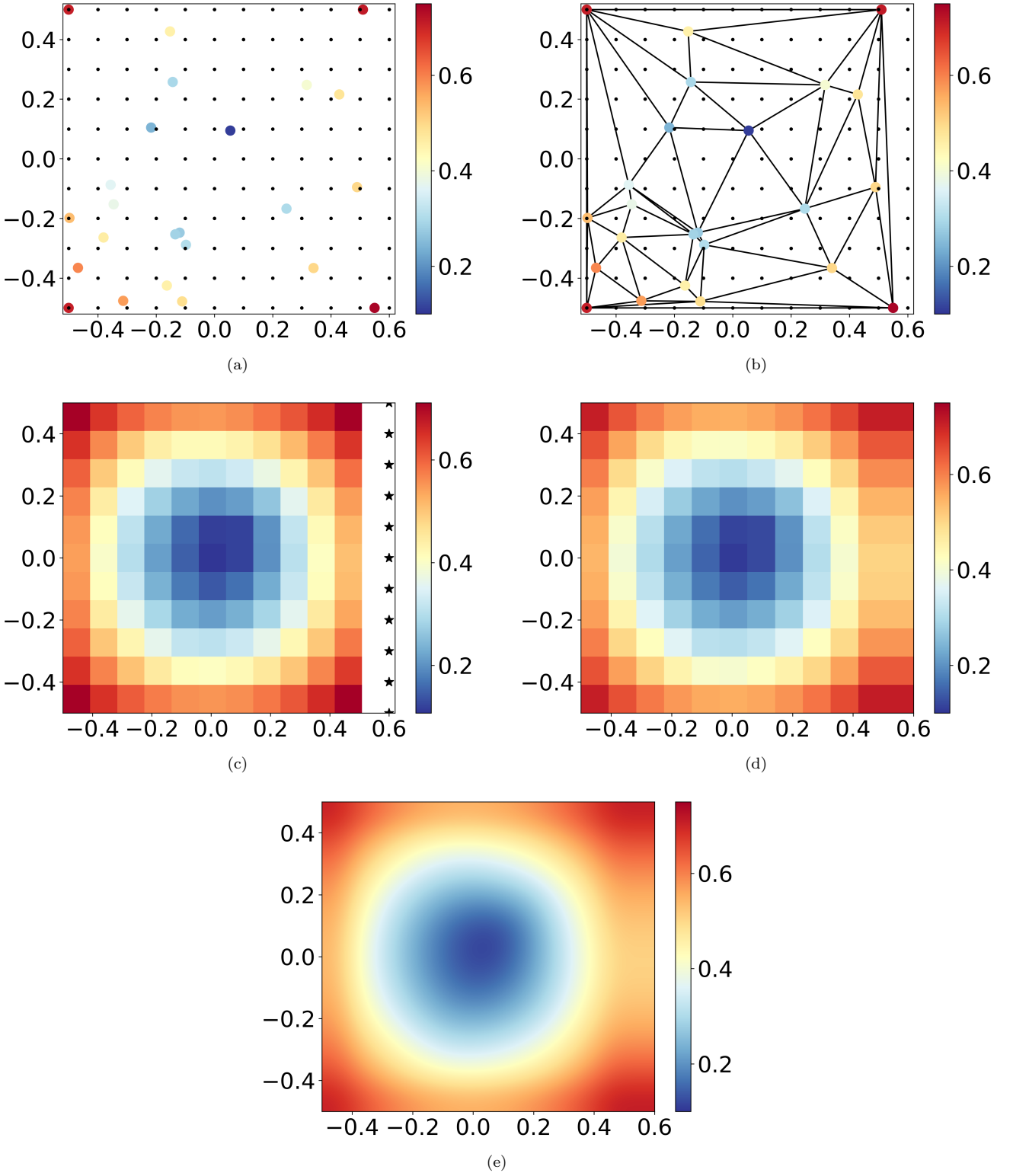


FIG. S7. The Clough-Tocher piecewise cubic, C1 smooth, curvature-minimizing 2D interpolation scheme. The color dots are the input points. The black dots indicate the interpolation grid. (a) Input data. (b) Delaunay triangulation, indicated by black triangles. (c) Nearest-neighbor interpolation points, indicated by the black stars. These points could not be triangulated. (d) Nearest-neighbor interpolation. (e) Bicubic interpolation over (d).

-
- [1] P. V. C. Medeiros, S. S. Tsirkin, S. Stafström, and J. Björk, Unfolding spinor wave functions and expectation values of general operators: Introducing the unfolding-density operator, *Physical Review B* **91**, 041116(R) (2015).
- [2] P. V. C. Medeiros, S. Stafström, and J. Björk, Effects of extrinsic and intrinsic perturbations on the electronic structure of graphene: Retaining an effective primitive cell band structure by band unfolding, *Physical Review B* **89**, 041407(R) (2014).
- [3] B. Mondal and R. Tonner-Zech, Systematic strain-induced bandgap tuning in binary III-V semiconductors from density functional theory, *Phys. Scr.* **98**, 065924 (2023).
- [4] P. Virtanen, R. Gommers, T. E. Oliphant, M. Haberland, T. Reddy, D. Cournapeau, E. Burovski, P. Peterson, W. Weckesser, J. Bright, S. J. van der Walt, M. Brett, J. Wilson, K. J. Millman, N. Mayorov, A. R. J. Nelson, E. Jones, R. Kern, E. Larson, C. J. Carey, I. Polat, Y. Feng, E. W. Moore, J. VanderPlas, D. Laxalde, J. Perktold, R. Cimrman, I. Henriksen, E. A. Quintero, C. R. Harris, A. M. Archibald, A. H. Ribeiro, F. Pedregosa, P. van Mulbregt, A. Vijaykumar, A. P. Bardelli, A. Rothberg, A. Hilboll, A. Kloeckner, A. Scopatz, A. Lee, A. Rokem, C. N. Woods, C. Fulton, C. Masson, C. Häggström, C. Fitzgerald, D. A. Nicholson, D. R. Hagen, D. V. Pasechnik, E. Olivetti, E. Martin, E. Wieser, F. Silva, F. Lenders, F. Wilhelm, G. Young, G. A. Price, G.-L. Ingold, G. E. Allen, G. R. Lee, H. Audren, I. Probst, J. P. Dietrich, J. Silterra, J. T. Webber, J. Slavič, J. Nothman, J. Buchner, J. Kulick, J. L. Schönberger, J. V. de Miranda Cardoso, J. Reimer, J. Harrington, J. L. C. Rodríguez, J. Nunez-Iglesias, J. Kuczynski, K. Tritz, M. Thoma, M. Newville, M. Kümmerer, M. Bolingbroke, M. Tartre, M. Pak, N. J. Smith, N. Nowaczyk, N. Shebanov, O. Pavlyk, P. A. Brodtkorb, P. Lee, R. T. McGibbon, R. Feldbauer, S. Lewis, S. Tygier, S. Sievert, S. Vigna, S. Peterson, S. More, T. Pudlik, T. Oshima, T. J. Pingel, T. P. Robitaille, T. Spura, T. R. Jones, T. Cera, T. Leslie, T. Zito, T. Krauss, U. Upadhyay, Y. O. Halchenko, and Y. Vázquez-Baeza, SciPy 1.0: fundamental algorithms for scientific computing in Python, *Nature Methods* **17**, 261 (2020).
- [5] Qhull code for convex hull, delaunay triangulation, Voronoi diagram and halfspace intersection about a point, <http://www.qhull.org/>.
- [6] P. Alfeld, A trivariate clough—tocher scheme for tetrahedral data, *Computer Aided Geometric Design* **1**, 169 (1984).
- [7] G. Farin, Triangular Bernstein-Bézier patches, *Computer Aided Geometric Design* **3**, 83 (1986).
- [8] G. M. Nielson, A method for interpolating scattered data based upon a minimum norm network, *Mathematics of Computation* **40**, 253 (1983).
- [9] R. Renka and A. Cline, A triangle-based C^1 interpolation method, *Rocky Mountain Journal of Mathematics* **14**, 223 (1984).
- [10] J. D. Hunter, Matplotlib: A 2D Graphics Environment, *Computing in Science & Engineering* **9**, 90 (2007).
- [11] T. A. Caswell, A. Lee, M. Droettboom, E. S. de Andrade, T. Hoffmann, J. Klymak, J. Hunter, E. Firing, D. Stansby, N. Varoquaux, J. H. Nielsen, B. Root, R. May, P. Elson, J. K. Seppänen, D. Dale, J.-J. Lee, D. McDougall, A. Straw, P. Hobson, hannah, O. Gustafsson, G. Lucas, C. Gohlke, A. F. Vincent, T. S. Yu, E. Ma, S. Silvester, C. Moad, and N. Kniazev, [matplotlib/matplotlib](https://pypi.org/project/matplotlib/): REL: v3.6.0 (2022).

Machine learning for accelerated bandgap prediction in strain-engineered quaternary III–V semiconductors

Cite as: J. Chem. Phys. **159**, 104702 (2023); doi: 10.1063/5.0159604

Submitted: 25 May 2023 • Accepted: 16 August 2023 •

Published Online: 8 September 2023



View Online



Export Citation



CrossMark

Badal Mondal,^{1,2}  Julia Westermayr,^{1,3}  and Ralf Tonner-Zech^{1,a)} 

AFFILIATIONS

¹Wilhelm-Ostwald-Institut für Physikalische und Theoretische Chemie, Universität Leipzig, 04103 Leipzig, Germany

²Fachbereich Physik, Philipps-Universität Marburg, 35032 Marburg, Germany

³Center for Scalable Data Analytics and Artificial Intelligence, Dresden/Leipzig, Germany

^{a)}Author to whom correspondence should be addressed: ralf.tonner@uni-leipzig.de

ABSTRACT

Quaternary III–V semiconductors are one of the most promising material classes in optoelectronics. The bandgap and its character, direct or indirect, are the most important fundamental properties determining the performance and characteristics of optoelectronic devices. Experimental approaches screening a large range of possible combinations of III- and V-elements with variations in composition and strain are impractical for every target application. We present a combination of accurate first-principles calculations and machine learning based approaches to predict the properties of the bandgap for quaternary III–V semiconductors. By learning bandgap magnitudes and their nature at density functional theory accuracy based solely on the composition and strain features of the materials as an input, we develop a computationally efficient yet highly accurate machine learning approach that can be applied to a large number of compositions and strain values. This allows for a computationally efficient prediction of a vast range of materials under different strains, offering the possibility of virtual screening of multinary III–V materials for optoelectronic applications.

© 2023 Author(s). All article content, except where otherwise noted, is licensed under a Creative Commons Attribution (CC BY) license (<http://creativecommons.org/licenses/by/4.0/>). <https://doi.org/10.1063/5.0159604>

I. INTRODUCTION

Semiconductor compounds are central to modern optoelectronics and find applications in various fields, such as solar cells, light-emitting diodes, optical telecommunication, and photovoltaics.^{1–11} One of the fundamental properties determining the performance of such optoelectronic devices is the bandgap. The tuning of the size and type of bandgaps is one of the major goals in the field of optoelectronics. Varying the relative composition of compound semiconductors is one of the major approaches here.^{12–25} Alternatively, straining the system can be used to modify the bandgaps.^{26–37} By combining these two approaches, bandgaps can be tailored over a wide range of values, enabling enormous diversity in device applications.^{12–25,38–42} Due to their vast composition space, quaternary III–V semiconductors offer a unique opportunity in material design.⁴³ However, identifying tailored materials for each target application requires assessing the dependence of

the bandgap on composition and strain for a large set of materials. Because of the tremendous effort necessary for the synthesis of unknown materials, experimental approaches to screening the vast chemical space of all possible combinations of III-(or group 13) and V-(or group 15) elements with variation in composition and strain are not practical.^{12,16,19,22,24,25} Therefore, theoretical models that are both accurate and computationally efficient are often the only viable choice for high-throughput virtual screening for material design.^{44,45}

In recent years, density functional theory (DFT) methods based on computationally efficient density functionals such as those based on the local density approximation (LDA)⁴⁶ or generalized gradient approximation (GGA)⁴⁷ have proven to be powerful and successful tools for such high-throughput material screening. However, large errors in semiconductor bandgaps, which can be in the range of 50% of the bandgap value,^{48–50} are common. Better accuracy can be achieved with methods such as hybrid functionals,^{51,52} many-

body perturbation theory (GW),^{53–55} or meta-GGA functionals such as the modified Becke–Johnson functional (TB09).⁵⁶ Our previous study on mapping bandgaps for binary and ternary III–V semiconductors using the TB09 functional over a large range of composition and strain values showed excellent agreement with the experiment at moderate computational costs.^{57,58} However, due to the large composition space of quaternary III–V semiconductor materials, which leads to an estimated 10 000 000⁵⁹ calculations per combination element, the computational costs of these methods are still too large to enable high-throughput studies.

To speed up the exploration of chemical space, machine learning (ML) techniques have been applied in various fields of material science, such as the prediction and classification of crystal structures,^{60–66} thermal properties,^{63,65,67,68} electronic properties,^{65,66,68–83} and the stability of materials.^{65,68,74,84,85} Among the most widely used ML models in the field of bandgap predictions of semiconductor materials are support vector machine (SVM) models.^{65,76,77,80,86,87} However, for III–V semiconductors, the previous reports using ML methods predicted the bandgap values of unstrained compounds only.^{65,74,76,77,86,87} No ML study on strained systems is available so far. Moreover, due to the large compositional space, the bandgap values of only a few selected III–V ternary and quaternary compositions have been predicted so far with ML methods.^{74,76,86}

In this work, we go beyond previous approaches and develop an ML model for bandgap predictions in biaxially strained quaternary III–V materials ($AB_xC_yD_{100-x-y}$; with A = III elements; B, C, and D = V elements) over the complete composition range ($x, y = 0–100$) and a compressive and tensile strain range of 5% around the unstrained structures. The excellent performance of the approach is demonstrated. Subsequently, we construct the composition-strain-bandgap relationship, the “bandgap phase diagram,”^{58,88} for GaAsPSb using our ML model. Although many of the binary and ternary subsystems of GaAsPSb, namely GaAs, GaP, GaSb, GaAsP, GaAsSb, and GaPSb, have been successfully synthesized and found special applications in different research fields,^{4,7,49,89–104} this particular quaternary compound has not been studied yet. Therefore, our theoretical predictions can provide insights for future experimental exploration of this material system.

We emphasize that the predictive capability of the ML models relies on the quality of the reference method used in the generation of ML training data. Given the lack of sufficient experimental data, we opted to use DFT-based methods to create the training dataset for our ML model in this instance. Since our DFT computational setup, as used here, has consistently demonstrated high accuracy in generating bandgaps that align well with experimental data,^{49,50,56–58} our ML model serves as a valuable tool for the initial screening of the vast composition-strain space to guide the next computational and experimental steps. Additionally, our approach allows for straightforward extension to other III–V quaternary systems and, thus, provides a general theoretical basis for targeted exploration of this compound class. The integrated first-principles calculations and ML techniques provide a powerful approach for future computational material design. The ultimate goal of this work is to provide comprehensive guidelines for studying bandgap properties in strained materials.

The article is organized as follows: In Sec. II, we discuss the methodology: details of DFT calculations (Sec. II A) and an

overview of ML methods (Sec. II B). Next, we present the results in Sec. III and establish the best ML models and hyperparameters for predicting the bandgaps of strained GaAsSbP. Using these methods, a complete bandgap phase diagram is constructed for GaAsSbP in Sec. III A. Finally, we summarize our key findings in Sec. IV.

II. METHODS

A. First-principle computational details

First, we created a dataset of 4280 data points obtained from DFT encompassing the whole composition and strain range of GaAsPSb investigated. The dataset comprises 88 calculations of the corresponding strained binary subsystems of GaAsSbP, namely, GaAs, GaP, and GaSb in total (taken from Ref. 57); 2272 composition-strain data points corresponding to the ternary subsystems of GaAsPSb, namely, GaAsP, GaPSb, and GaAsSb (taken from Ref. 58); and 1920 randomly chosen points in the composition-strain space of GaAsPSb, containing a non-zero percentage of all elements As, P, and Sb. Notably, only the data for biaxially strained structures is collected from Refs. 57 and 58. More details on the data features are discussed in Sec. II B 4. The complete dataset can be found in the supplementary material attachment. For convenience, in the following, we label the above three datasets as binary, ternary, and quaternary datasets, respectively.

The DFT computational setup for the quaternary calculations follows the approach used in the binary and ternary dataset calculations in our previous studies.^{57,58} The computations are performed using the projector-augmented wave (PAW) method^{105,106} as implemented in the Vienna *ab initio* simulation package (VASP).^{107–110} The generalized gradient approximation (GGA) based exchange-correlation functional by Perdew, Burke, and Ernzerhof (PBE)⁴⁷ with a cut-off energy of 550 eV for the plane-wave basis set is chosen in all calculations. Corrections for missing dispersion interactions are calculated using the semiempirical DFT-D3 approach with an improved damping function.^{111,112} The electronic energy convergence criteria of 10^{-7} eV and the force convergence of 10^{-2} eV \AA^{-1} are used, respectively. The quaternary materials are modeled using special quasirandom structures (SQS)¹¹³ with a supercell of size $6 \times 6 \times 6$. The SQS cells are generated using the alloy-theoretic automatic toolkit (ATAT).^{114–116} The reciprocal space is sampled at the Γ -point only, which is sufficient due to the large real-space cell size. Geometry optimizations are carried out by consecutive volume and position optimizations until convergence is reached. For the bandgap calculations, the meta-GGA functional TB09⁵⁶ is used, including spin-orbit coupling. The bandgap natures are determined using the Bloch-spectral-weight-based protocol as described in Ref. 58. The “fold2Bloch”¹¹⁷ code is used to determine the Bloch spectral weights.

The materials investigated here all feature zincblende-type structures. Moreover, since these compounds can only be experimentally realized through epitaxy, we only consider the effect of biaxial strain. As [100] crystal direction is the most common choice of substrate orientation and crystal growth direction in epitaxy, we model the strain application along [100] directions. The in-plane lattice parameters ([100] and [010] directions) are kept fixed at the chosen strain values while the out-of-plane direction [001] is

relaxed. The strained in-plane lattice parameters (a_f) are calculated using the following formula [Eq. (1)]:

$$a_f = a_{eqm} \times \left(1 + \frac{\text{biaxial strain (\%)}}{100} \right), \quad (1)$$

where a_{eqm} is the equilibrium lattice parameter of the specific structure that will be strained.^{57,58} Following the convention from Refs. 57 and 58, in the following, we indicate tensile strain with a positive sign and compressive strain with a negative sign. No structural phase transition is assumed under strain application. Notably, we limit our analyses within the compressive and tensile strain ranges of 5%. This is typically the strain range achievable via epitaxial growth. Moreover, our analysis assumes perfect epitaxial growth and does not account for defects.

B. Machine learning details

1. ML model choice

We use the support vector regression (SVR)¹¹⁸ model to train and predict bandgap values. For learning and predicting the bandgap nature, we use the support vector classification (SVC) model.^{119,120} Below, we present the key features of each of these SVM models. All the ML algorithms are used as implemented in `scikit-learn`.¹²¹

The fundamental feature of SVM is that it constructs a (set of) hyper-plane(s) in a high dimensional space. The main objective here is to optimize the positions of these hyper-planes to effectively separate the training data points based on their classes. A good separation is defined when the hyper-plane has the largest distance to the nearest training data points of any class, the so-called functional margin, since maximizing the margin lowers the model's generalization error. However, achieving a perfect separation is not always feasible in real-world datasets. Therefore, an additional regularization parameter, C , is introduced to construct the so-called "soft margin."

Moreover, a nonlinear transformation is applied to the feature space by the so-called "kernel trick."¹²²⁻¹²⁴ The kernel trick simplified the learning task by efficiently mapping the original feature space of the considered data into the new space using a kernel function, thus significantly reducing the cost of learning with large datasets. Here, we use the radial basis function (RBF) kernel,^{122,124} which is defined as follows:

$$k(\mathbf{x}_i, \mathbf{x}_j) = e^{-\gamma \|\mathbf{x}_i - \mathbf{x}_j\|^2}. \quad (2)$$

The parameter γ determines the inverse of the area of influence of the i th data and decays with the distance to another j th data. A low value of γ means the influence reached "far," and a high value means "close." The behavior of the model is very sensitive to the γ values and can be tuned to optimize predictions.

This defines a constrained optimization problem for SVM classification (SVC),

$$\text{minimize}_{\omega, b, \xi} \quad \frac{1}{2} \|\omega\|^2 + C \sum_{i=1}^N \xi_i, \quad (3)$$

$$\text{subject to} \quad y_i (\langle \omega, \phi(\mathbf{x}_i) \rangle + b) \geq 1 - \xi_i \\ \xi_i \geq 0, \quad i = 1, \dots, N, \quad (4)$$

where \mathbf{x}_i is the feature vector (see Sec. II B 4) and y_i refers to the original value of the i th data point from a dataset $\{(\mathbf{x}_i; y_i)\}_{i=1}^N$. In our context, y_i takes on the values of either +1 or -1, indicating whether the bandgaps obtained from quantum chemistry calculations are direct or indirect. The nonlinear mapping function ϕ maps the features \mathbf{x}_i to the higher-dimensional space, which can be efficiently performed using the kernel trick. The misclassification error for the i th data point during optimization is measured by ξ_i . Its value is zero if the data point is correctly classified. Otherwise, the data points on the wrong side get a penalty. The ω and b define the weight vector and offset values, respectively, which are optimized as indicated in Eq. (3). The minimization of $\frac{1}{2} \|\omega\|^2$ maximizes the margin. The C parameter, thus, trades off the misclassification penalty of training samples against the maximization of the margin.

Similarly, in the case of regression (SVR), the optimization problem is formulated as follows:

$$\text{minimize}_{\omega, b, \xi, \xi^*} \quad \frac{1}{2} \|\omega\|^2 + C \sum_{i=1}^N (\xi_i + \xi_i^*), \quad (5)$$

$$\text{subject to} \quad y_i - (\langle \omega, \phi(\mathbf{x}_i) \rangle + b) \leq \varepsilon + \xi_i \\ (\langle \omega, \phi(\mathbf{x}_i) \rangle + b) - y_i \leq \varepsilon + \xi_i^* \\ \xi_i, \xi_i^* \geq 0. \quad (6)$$

Here, an additional parameter, ε , is introduced to define the margin size around the predicted regression function. It determines the tolerance for errors in the regression model. Data points for which predictions $(\langle \omega, \phi(\mathbf{x}_i) \rangle + b)$ are within the ε -tube are considered to have acceptable errors and do not contribute to the penalty term in the objective function. Otherwise, a penalty is added, determined by ξ or ξ^* , depending on whether their predictions lie above or below the ε -tube.

Once the optimization problem is solved, the prediction (\hat{y}) for a (new) sample \mathbf{z} can be performed using the optimized ω and b ,

$$\hat{y} = \langle \omega, \phi(\mathbf{z}) \rangle + b. \quad (7)$$

For classification, the predicted class corresponds to the sign of prediction $[\text{sign}(\hat{y})]$.

2. Hyperparameter optimization

A proper choice of hyperparameters is critical to the SVM model's performance and accuracy. We thus train multiple ML models with five-fold cross-validation at several random combinations of the hyperparameters (C and γ for SVC-RBF; C , γ , and ε for SVR-RBF) values. The model exhibiting the highest cross-validation score is then picked as the final model holding the best set of hyperparameters. We utilize the `RandomizedSearchCV` from `scikit-learn` to automate this hyperparameter optimization routine.

It is important to note that the specific combination of optimized hyperparameter values (C , γ , and ε combinations) may vary upon rerunning the hyperparameter optimization routine due to the stochastic nature of the random search and the random splitting of training and validation datasets within the cross-validation routine. We thus start with a hyperparameter optimization space expanding large C , γ , and ε intervals and carefully tune the ranges

until the optimal ranges are found, covering the regimes with the best hyperparameters set. This ensures consistent performance of the final best models (i.e., cross-validation scores do not change significantly) despite changes in the exact combination of optimized hyperparameter values upon rerunning the optimization routine.

Figure S1 in the supplementary material shows an example of the tuning of hyperparameter space for the SVR-RBF model. We perform a random search over uniformly distributed (in log-scale) 1000 random combinations of the C , γ , and ϵ values. In this case, the optimal ranges found are 0.01–1000, 0.01–10, and 0.01–1 for the C , γ , and ϵ ranges, respectively [the supplementary material, Fig. S1(d)].

3. Performance metric

The prediction accuracies of the SVR-RBF learning models are evaluated by means of root-mean-squared error (RMSE), mean absolute error (MAE), maximum error (Max error), and the coefficient of determination (R^2) metric. The SVC-RBF models are tested using accuracy-score and balanced-accuracy-score performance metrics. The hyperparameters are optimized using the RMSE and accuracy-score scoring functions for the SVR-RBF and SVC-RBF models, respectively. We find some of the SVR-RBF models predict small negative direct bandgap values, up to -5 meV (see the left-bottom corner in the supplementary material, Fig. S2). In this manuscript, we do not consider possible physical effects leading to negative bandgaps, such as topological band inversion, in our DFT dataset. We thus shift all the ML predicted negative bandgap values to 0 eV (the supplementary material, Fig. S2).

4. Feature space and data preprocessing

Alongside the choice of an appropriate model, another crucial part of ML is the choice of descriptors to represent the system under investigation. A number of different feature representations have been proposed for periodic solid-state systems, such as element-specific features,^{65,68,73,75,76,85,87} radial distribution functions,⁶⁹ Voronoi tessellations,¹²⁵ representation learning from stoichiometry,¹²⁶ and property-labeled material fragments.¹²⁷ As our analysis consists of the prediction of strained and unstrained structures, we resort to keeping the descriptor as simple as possible and have chosen the composition and strain values as input features for the ML training. This allows for fast prediction and training times compared to the use of extensive descriptors and is found to be accurate enough for this study. The composition features can generally be constructed considering all the III- and V-elements. However, in the present article, we only present the results for GaAsPSb. In this case, the number of compositional degrees of freedom is reduced to only 3 (x , y , and z in GaAs $_x$ P $_y$ Sb $_z$). Although only x and y are independent compositional degrees of freedom here and z can be deduced from x and y ($z = 100 - x - y$), adding z to the feature vector ensures the model learns this constraint. Together with the measure of biaxial strain, the final feature space is thus only four-dimensional (see the supplementary material, Sec. S3). As shown in Sec. III, this four-dimensional feature space performs exceptionally well. We note that, as a drawback, the above ML model is limited to the elements and type of strain (biaxial strain) chosen. Still, in principle, the descriptor could simply be extended to cover all possible chemical elements and strain types, allowing for universal application of the model.

Moreover, the features in our dataset, namely composition and strain, have different orders of magnitude of variance. Therefore, before training the models, the input data are standardized using the `StandardScaler` class from `scikit-learn`.

5. Dataset size convergence

We construct the learning curve to ensure the proper training of models and the comprehensiveness of the training set. Therefore, we create a test set consisting of random 25% of the total input dataset, comprising 4280 data points. We create the training set from the rest (75% of the data), consecutively increasing the set size from 1% up to 75%. The series is repeated five times. We use five-fold `ShuffleSplit` from `scikit-learn` to perform the above train-test splittings. For each ML model training, hyperparameters are re-optimized.

III. RESULTS AND DISCUSSION

Figure 1 shows the dependence of SVM-RBF model out-of-sample performances on the training set size. As the training set size increases, the RMSE of the SVR-RBF model decreases by ~ 45 meV [Fig. 1(a)]. Eventually, it reaches ~ 30 meV with the largest training set. The log-log plot demonstrates a high degree of linearity, indicating that the model learns properly.^{128,129} The corresponding MAE and Max error values of predictions are shown in the supplementary material, Fig. S3. The values decrease by about 35 and 160 meV, respectively. The R^2 score reaches a maximum of about 1.00 as the training set size increases [the supplementary material, Fig. S3(b)]. Notably, with about 1000 data points, the RMSE is already ~ 35 meV. Further increases in the training set size (>1000) result in only marginal improvements in model performance.

To eliminate the possibility of deteriorating model performance due to noise in the data, we further investigate SVR-RBF models trained on separate direct and indirect bandgap datasets via learning curves [the supplementary material, Figs. S4(a) and S4(b)]. As we find that most of the incorrect predictions in the bandgap nature occur in the vicinity of direct-indirect transition (DIT) regions, we additionally remove all data points predicted incorrectly by the classification model and retrain SVR-RBF models with the reduced dataset [the supplementary material, Fig. S4(c)]. The figures (the supplementary material, Fig. S4) demonstrate that the learning behavior does not change significantly, leading to the conclusion that performance saturation is not due to the severe noise in the data but rather due to models reaching their maximum capacity to capture the patterns and relationships in the data given.^{128,129} The errors in the bandgap value predictions are spread over the entire composition-strain space. These results indicate that learning both direct and indirect bandgaps simultaneously does not lead to confusion in the SVR-RBF model training.

The prediction accuracy-score of the nature of bandgaps from SVC-RBF models increases by about 12% as the training set size reaches the largest size [Fig. 1(b)]. The highest accuracy-score that could be reached is ~ 0.94 [the last point in Fig. 1(b)]. The corresponding balanced-accuracy-score values follow the same pattern (the supplementary material, Fig. S5). The model's performance again saturates at about 1000 data points. These results indicate that the training set is adequate, and around 1000 data points should be sufficient for screening the system being studied.

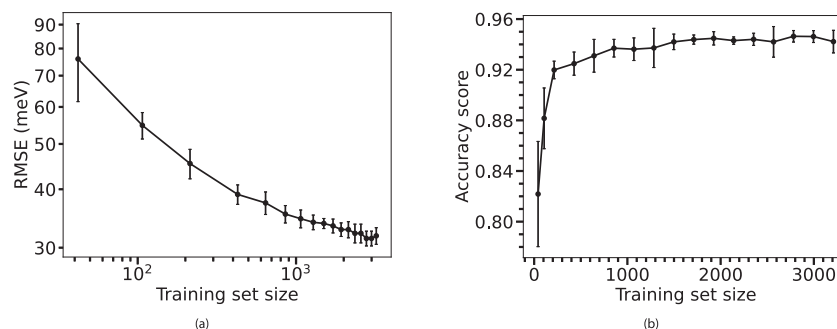


FIG. 1. Dependence of SVM-RBF models out-of-sample performances on the training set size. (a) Bandgap magnitude prediction RMSE from the SVR-RBF model in log-log scale. The hyperparameters are optimized with the RMSE metric. (b) Bandgap nature prediction accuracy from the SVC-RBF model. The hyperparameters are optimized with the accuracy-score metric. The error bars show standard deviations over five trials.

TABLE I. Out-of-sample bandgap prediction accuracy for the SVM-RBF models from the trial set of the last point in Fig. 1.

| Model | Metric ^a | |
|---------|-------------------------|---------------------|
| SVR-RBF | RMSE | 31 (± 1) |
| | MAE | 22 (± 0) |
| | Max error | 155 (± 16) |
| | R ² | 1.00 (± 0.00) |
| SVC-RBF | Accuracy score | 0.94 (± 0.01) |
| | Balanced accuracy score | 0.94 (± 0.01) |

^aValues in brackets state the standard deviation. Error measures (RMSE, MAE, and Max error) are given in meV. For MAE and R², the standard deviations are below 0.5 and 0.005, respectively.

Moreover, the ML models exhibit excellent efficiency. The process of model training, including hyperparameter optimization, with the largest dataset (3210 training data points) takes only a few minutes on a six-core central processing unit (CPU).

Table I summarizes the out-of-sample prediction accuracy of the final SVM-RBF models (the last point in Fig. 1). The RMSE of the bandgap magnitude predictions of the corresponding SVR-RBF models is 31 (± 1) meV. For the classification task, the accuracy-score is 0.94 (± 0.01). The comparison of all the DFT calculated and the ML-predicted bandgap values and types is presented in the supplementary material, Figs. S6 and S7. The final trained models and the list of optimized hyperparameter values for the corresponding models are attached in the supplementary material.

Overall, the errors in bandgap predictions are well within the uncertainty of the most accurate DFT results. We thus use the models from the last point in Fig. 1 to construct the bandgap phase diagram for GaAsPSb over the complete composition range (As, P, Sb = 0%–100%) and up to 5% strain.

We emphasize that relying on a simple bowing model for bandgap variation¹³ in such multinary compounds would require an extensive number of bowing parameters for composition and strains. As stated in the introduction, there is a lack of extensive experimental data or bowing parameters available specifically for GaAsPSb. Furthermore, the variation of bandgap values under strain

for different III–V compositions often deviates from the simple quadratic dependence expected from a bowing model,³⁷ and they lack information about the bandgap nature. Therefore, the combined accurate DFT-ML hybrid approach developed in the article is necessary for an accurate determination of bandgap values and natures.

A. GaAsPSb bandgap phase diagram

Figure 2 shows the bandgap phase diagram for unstrained GaAsPSb. The bandgap values shown are the average values obtained from the predictions of five models. The small standard deviations (<35 meV) of the five model predictions (as shown in the supplementary material, Fig. S8) indicate that the training set covers the whole phase space sufficiently and that the predictions made

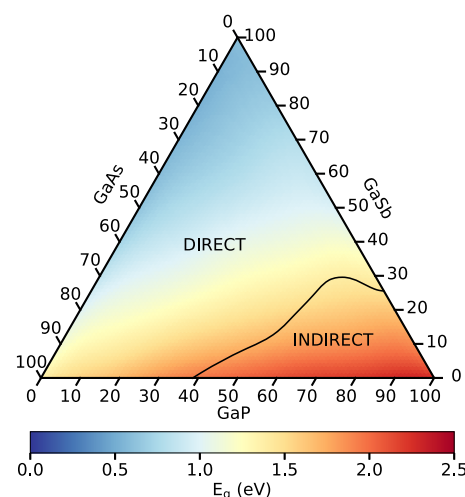


FIG. 2. Variation of bandgap values (E_g) for unstrained GaAsPSb (0.0% strain). The labels “direct” and “indirect” describe the enclosed regions, with the nature of the bandgap being direct and indirect, respectively. The bandgap values are the average values over the five model predictions from the trial set of the last point in Fig. 1(a). The nature of the bandgaps is the most frequent outcome over the five predictions (mode value) from the trial set of the last point in Fig. 1(b).

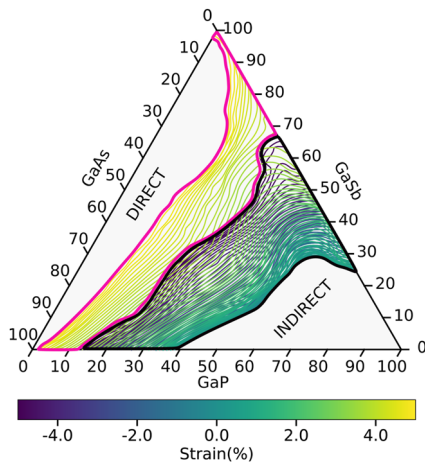


FIG. 3. DIT lines for strained GaAsPSb (up to 5% strain). The labels “direct” and “indirect” describe the enclosed regions, with the nature of the bandgap being direct and indirect, respectively. The DITs occur under both tensile and compressive strain in the area enclosed by the bold black solid line. In the region enclosed by the magenta curve, DITs are possible only under tensile strain. No DIT occurs in the other regions.

across the entire phase space sampled are accurate. In addition, the use of multiple models for prediction increases the robustness of the predictions of regression models by a factor of the square root of the number of models,¹³⁰ making predictions, in general, more precise and less noisy. For the nature of bandgaps, we use the most frequent outcomes over the five predictions (mode value). The labels “direct” and “indirect” in the figure indicate the areas where the

nature of bandgaps is direct and indirect, respectively. These areas are separated by the DIT line (black curve). We smooth the calculated DIT points with the B-spline function¹³¹ (for details, see the supplementary material, Sec. S7). The complete movie of the corresponding diagrams for other strain values is available in the supplementary material. Figure 2 shows that the largest bandgaps, which are indirect in nature, are found at high %P. The bandgaps become smaller as more %As and %Sb are added. The bandgap values also decrease with an increase in tensile as well as compressive strain (the supplementary material, Fig. S10).

Further, we group the composition space DIT curves for all the strain values investigated, as shown in Fig. 3. We find that within the strain regime investigated here, in the area indicated by the magenta box in Fig. 3, DITs are only possible under tensile strain. In the area indicated by the bold black box, the DITs can be achieved using both tensile and compressive strain. No DITs are found in other regions.

B. Modeling GaAsPSb epitaxy

One of the most common approaches to experimentally realizing quaternary III–V semiconductors is epitaxial growth. As pointed out in Ref. 58, biaxial strain can be used to model epitaxial growth (“theoretical epitaxy”). Thus, we also investigate the effects of different substrates. We first calculate the equilibrium lattice parameters of the unstrained quaternary compositions using Vegard’s law,^{132,133} Eq. (8),

$$a_{\text{GaAs}_x\text{P}_y\text{Sb}_{100-x-y}} = \frac{1}{100} [x \times a_{\text{GaAs}} + y \times a_{\text{GaP}} + (100 - x - y) \times a_{\text{GaSb}}] \quad (8)$$

with $a_{\text{GaP}} = 5.475 \text{ \AA}$, $a_{\text{GaAs}} = 5.689 \text{ \AA}$, $a_{\text{GaSb}} = 6.134 \text{ \AA}$.⁵⁷

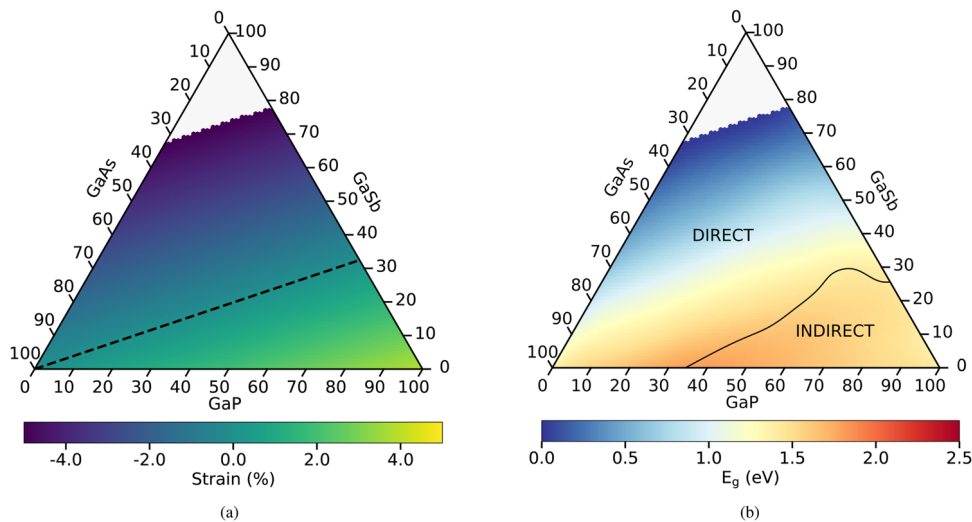


FIG. 4. Effect of GaAs-substrate on GaAsPSb epi-layer under the “theoretical epitaxy” model^{57,58} (up to 5% strain). (a) The calculated biaxial strain values from Eqs. (8) and (9). The black dotted line indicates the perfect lattice matching (no strain) compositions. (b) The predicted bandgap values in color (E_g). The labels “direct” and “indirect” describe the enclosed regions, with the nature of the bandgap being direct and indirect, respectively. The bandgap values are the average values over the five model predictions from the trial set of the last point in Fig. 1(a). The nature of the bandgaps is the most frequent outcome over the five predictions (mode value) from the trial set of the last point in Fig. 1(b).

The biaxial strain values are then computed using Eq. (9),

$$\text{Strain (\%)} = \frac{a_{\text{substrate}} - a_{\text{GaAsPSb}}}{a_{\text{GaAsPSb}}} \times 100, \quad (9)$$

Fig. 4(a) shows the strain map when the respective GaAsPSb compositions are to be grown on a GaAs substrate.

We then predict the bandgaps using the SVM-RBF models described earlier [see Fig. 4(b)]. In regions with high Sb content, we find large compressive strains. The bandgap values in those regions are very small. On the contrary, in the high %P region, we find a large tensile strain. The bandgaps there are indirect in nature and, thus, are not appropriate for optoelectronic applications. The perfect lattice matching condition can be found in between, as shown by the dotted line in Fig. 4(a).

From the above discussions, it becomes clear that one can optimize the best material combinations for achieving specific optical applications using these diagrams. Similar diagrams for other substrates (GaP, GaSb, InP, and Si) can be found in the supplementary material, Fig. S11. We also provide interactive figures of the above GaAsPSb bandgap phase diagrams in the supplementary material.

Further, for the largest training dataset (the last point in Fig. 1), we predict the bandgap nature using the SVC-RBF model with the optimized hyperparameters from the SVR-RBF models. We obtain an accuracy score of 0.94 (± 0.01) in the out-of-sample performance. This is comparable to the performance of the hyperparameter-optimized SVC-RBF model (Table I). Similarly, we employ the SVR-RBF model with optimized hyperparameters from the SVC-RBF models to predict the bandgap magnitudes. For all the five SVR-RBF models here, we set the ϵ value to 0.02, which was the average value of previously hyperparameter-optimized SVR-RBF models. This results in an out-of-sample RMSE of 32 (± 1) meV for the predictions, again demonstrating accuracy similar to that of the optimized SVR-RBF models (Table I). This suggests that separate hyperparameter optimizations are not required for the SVR-RBF and SVC-RBF models independently. The optimized hyperparameters from the SVR-RBF model can be used for the prediction of SVC-RBF, and vice versa.

IV. SUMMARY

In this work, using machine learning models trained on first-principles calculations, we developed an efficient DFT-ML hybrid computational approach for mapping the bandgap magnitude and type (direct or indirect) over a wide range of composition and strain values in quaternary III-V semiconductors. The devised SVR-RBF and SVC-RBF-based ML models showed remarkable accuracy in predicting the bandgap properties of these materials despite using a very simple descriptor, i.e., composition and strain values. This strategy significantly accelerates the sampling efficiency over the large strain-composition space in multinary systems, which otherwise would be impossible to cover with first-principle calculations alone. Using the protocol, we constructed the composition-strain-bandgap mapping, or bandgap phase diagram, for GaAsPSb. This diagram can be used as a valuable tool for making judicious choices about the best materials for target applications. The study revealed that

within 5% strain, GaAsPSb compositions with high P concentrations are characterized by indirect bandgaps and are thus not suitable for optoelectronic devices. Notably, our computational protocol can be generalized to other multinary III-V semiconductors. Thus, the rapid estimation of bandgaps for a large number of composition and strain values using this approach will be extremely useful for screening multinary III-V materials. This provides a powerful approach for future material design, facilitating the development of novel strain-engineered semiconductor materials with tailored bandgap properties.

SUPPLEMENTARY MATERIAL

The supplementary material includes

- Supporting_Information.pdf: collection of supplementary supporting figures and tables.
- GaAsPSb_ML_database.zip: complete dataset for ML training and testing, contains “GaAsPSb_ML_database.xlsx.”
- GaAsPSb_bandgap_phase_diagram.mp4: bandgap phase diagram movie for GaAsPSb up to 5% tensile and compressive strain.
- Interactive_bandgap_phase_diagram.zip: interactive diagrams in HTML format. To view the diagrams, open the HTML files in a web browser.
 - Substrate_effect_strain_map.html: biaxial strain map of GaAsPSb when grown on different substrates [calculated using Eqs. (8) and (9)].
 - Substrate_effect_bandgap_phase_diagram.html: ML predicted the bandgap map of GaAsPSb when grown on different substrates.
 - Direct_indirect_transition_lines.html: ML predicted direct-indirect transition lines (without B-spline fitting) for GaAsPSb up to 5% tensile and compressive strain.
 - Bandgap_phase_diagram_GaAsPSb.html: bandgap phase diagram for GaAsPSb (within 5% tensile and compressive strain). The direct-indirect transition lines are without B-spline fitting.
- GaAsPSb_MachineLearning_scripts.zip: Python scripts for the ML codes used to generate the data in this manuscript. Additionally, a user guide titled “Helpers.txt” is included within the zip file to assist with executing the ML scripts.
- FinalBest5TrainedModels.zip: the final best five ML trained models used to create the bandgap phase diagram in this manuscript. The zip file includes a Python script that can be used to predict the bandgaps of the GaAsPSb system and a user guide titled “Helpers.txt” to assist with executing the script.
- FinalBest5TrainedModels_hyperparameters.zip: list of optimized hyperparameter values of the final best five SVR-RBF and SVC-RBF models, contains “FinalBest5TrainedModels_hyperparameters.xlsx.”

ACKNOWLEDGMENTS

We acknowledge the German Research Foundation (DFG) in the framework of the Research Training Group “Functionalization of Semiconductors” (Grant No. GRK 1782) for funding this project and HRZ Marburg, GOETHE-CSC Frankfurt, ZIH TU Dresden, and HLR Stuttgart for providing the computational resources. We thank Dr. Marcel Kröner and Professor Dr. Kerstin Volz from Philipps-Universität Marburg for discussions.

AUTHOR DECLARATIONS

Conflict of Interest

The authors have no conflicts to disclose.

Author Contributions

B.M. and R.T.-Z. contributed to the conception and design of the study, while B.M. was responsible for performing the calculations and analysis. J.W. and R.T.-Z. provided critical feedback throughout the project. B.M. drafted the manuscript, which was then reviewed and revised by J.W. and R.T.-Z. All authors reviewed and approved the manuscript prior to submission.

Badal Mondal: Conceptualization (equal); Data curation (equal); Formal analysis (equal); Investigation (equal); Methodology (equal); Resources (equal); Software (equal); Validation (equal); Visualization (equal); Writing – original draft (equal); Writing – review & editing (equal). **Julia Westermayr:** Formal analysis (equal); Investigation (equal); Methodology (equal); Resources (supporting); Supervision (supporting); Validation (equal); Visualization (supporting); Writing – review & editing (equal). **Ralf Tonner-Zech:** Conceptualization (equal); Formal analysis (equal); Funding acquisition (lead); Investigation (equal); Methodology (supporting); Project administration (lead); Resources (supporting); Supervision (lead); Validation (equal); Writing – review & editing (equal).

DATA AVAILABILITY

The density functional theory calculation data that support the findings of this study are openly available in NOMAD at <https://doi.org/10.17172/NOMAD/2022.08.20-2>, <https://doi.org/10.17172/NOMAD/2023.02.27-1>, and <https://doi.org/10.17172/NOMAD/2023.05.03-1>.^{134–136} In addition to the supplementary material, the interactive bandgap phase diagrams can also directly be viewed in GitHub at <https://bmondal94.github.io/Bandgap-Phase-Diagram/>.⁸⁸

REFERENCES

- ¹R. Soref, *Proc. IEEE* **81**, 1687 (1993).
- ²P. Y. Yu and M. Cardona, *Fundamentals of Semiconductors: Physics and Materials Properties*, 3rd ed. (Springer, Berlin, 2005).
- ³S. P. Philipps, F. Dimroth, and A. W. Bett, in *McEvoy's Handbook of Photovoltaics*, 3rd ed., edited by S. A. Kalogirou (Elsevier, 2018), pp. 439–472.
- ⁴J. F. Geisz and D. J. Friedman, *Semicond. Sci. Technol.* **17**, 769 (2002).
- ⁵S. Mokkapaty and C. Jagadish, *Mater. Today* **12**, 22 (2009).
- ⁶F. Dimroth, T. N. D. Tibbits, M. Niemeyer, F. Predan, P. Beutel, C. Karcher, E. Oliva, G. Siefert, D. Lackner, P. Fus-Kailuweit, A. W. Bett, R. Krause, C. Dräzek, E. Guiot, J. Wasselin, A. Tauzin, and T. Signamarcheix, *IEEE J. Photovoltaics* **6**, 343 (2016).
- ⁷T. Sato and M. Imai, *Jpn. J. Appl. Phys.* **41**, 5995 (2002).
- ⁸C. Fuchs, A. Brüggemann, M. J. Weseloh, C. Berger, C. Möller, S. Reinhard, J. Hader, J. V. Moloney, A. Bäumner, S. W. Koch, and W. Stolz, *Sci. Rep.* **8**, 1422 (2018).
- ⁹T. Hepp, J. Lehr, R. Günkel, O. Maßmeyer, J. Glowatzki, A. Ruiz Perez, S. Reinhard, W. Stolz, and K. Volz, *Electron. Lett.* **58**, 70 (2022).
- ¹⁰S. J. Sweeney, Z. Batool, K. Hild, S. R. Jin, and T. J. Hosea, in *2011 13th International Conference on Transparent Optical Networks (ICTON)* (IEEE, 2011), pp. 1–4.
- ¹¹S. Wang, Y. Song, K. Wang, Y. Gu, H. Zhao, X. Chen, H. Ye, H. Zhou, C. Kang, Y. Li, C. Cao, L. Zhang, J. Shao, Q. Gong, and Y. Zhang, “Novel dilute bismides for IR optoelectronics applications,” in *Asia Communications and Photonics Conference 2013* (OSA, Washington, DC, 2013), p. AF3B.5.
- ¹²A. Beyer, W. Stolz, and K. Volz, *Prog. Cryst. Growth Charact. Mater.* **61**, 46 (2015).
- ¹³I. Vurgaftman, J. R. Meyer, and L. R. Ram-Mohan, *J. Appl. Phys.* **89**, 5815 (2001).
- ¹⁴A. Beyer, N. Knaub, P. Rosenow, K. Jandieri, P. Ludewig, L. Bannow, S. W. Koch, R. Tonner, and K. Volz, *Appl. Mater. Today* **6**, 22 (2017).
- ¹⁵P. Ludewig, S. Reinhard, K. Jandieri, T. Wegele, A. Beyer, L. Tapfer, K. Volz, and W. Stolz, *J. Cryst. Growth* **438**, 63 (2016).
- ¹⁶S. Liebich, M. Zimprich, A. Beyer, C. Lange, D. J. Franzbach, S. Chatterjee, N. Hossain, S. J. Sweeney, K. Volz, B. Kunert, and W. Stolz, *Appl. Phys. Lett.* **99**, 071109 (2011).
- ¹⁷O. Supplie, O. Romanyuk, C. Koppka, M. Steidl, A. Nägelein, A. Paszuk, L. Winterfeld, A. Dobrich, P. Kleinschmidt, E. Runge, and T. Hannappel, *Prog. Cryst. Growth Charact. Mater.* **64**, 103 (2018).
- ¹⁸G. Stringfellow, “Fundamental aspects of MOVPE,” in *Metalorganic Vapor Phase Epitaxy (MOVPE)*, edited by P. C. Stuart Irvine (John Wiley and Sons, Ltd., 2019).
- ¹⁹K. Volz, J. Koch, F. Höhnsdorf, B. Kunert, and W. Stolz, *J. Cryst. Growth* **311**, 2418 (2009).
- ²⁰M. Feifel, J. Ohlmann, J. Benick, T. Rachow, S. Janz, M. Hermle, F. Dimroth, J. Belz, A. Beyer, K. Volz, and D. Lackner, *IEEE J. Photovoltaics* **7**, 502 (2017).
- ²¹B. Kunert, J. Koch, T. Torunski, K. Volz, and W. Stolz, *J. Cryst. Growth* **272**, 753 (2004).
- ²²K. Volz, T. Torunski, B. Kunert, O. Rubel, S. Nau, S. Reinhard, and W. Stolz, *J. Cryst. Growth* **272**, 739 (2004).
- ²³J. Veletas, T. Hepp, K. Volz, and S. Chatterjee, *J. Appl. Phys.* **126**, 135705 (2019).
- ²⁴T. Wegele, A. Beyer, P. Ludewig, P. Rosenow, L. Duschek, K. Jandieri, R. Tonner, W. Stolz, and K. Volz, *J. Phys. D: Appl. Phys.* **49**, 075108 (2016).
- ²⁵T. Hepp, L. Nattermann, and K. Volz, in *Bismuth-Containing Alloys and Nanostructures*, edited by S. Wang and P. Lu (Springer, Singapore, 2019), pp. 37–58.
- ²⁶P. E. Van Camp, V. E. Van Doren, and J. T. Devreese, *Phys. Rev. B* **41**, 1598 (1990).
- ²⁷R. F. Potter, *Phys. Rev.* **103**, 861 (1956).
- ²⁸P. A. Alekseev, V. A. Sharov, B. R. Borodin, M. S. Dunaevskiy, R. R. Reznik, and G. E. Cirilin, *Micromachines* **11**, 581 (2020).
- ²⁹A. K. Katiyar, K. Y. Thai, W. S. Yun, J. Lee, and J.-H. Ahn, *Sci. Adv.* **6**, eabb0576 (2020).
- ³⁰B. Lim, X. Y. Cui, and S. P. Ringer, *Phys. Chem. Chem. Phys.* **23**, 5407 (2021).
- ³¹G. Signorello, E. Lörtscher, P. Khomyakov, S. Karg, D. Dheeraj, B. Gotsmann, H. Weman, and H. Riel, *Nat. Commun.* **5**, 3655 (2014).
- ³²G. Signorello, S. Karg, M. T. Björk, B. Gotsmann, and H. Riel, *Nano Lett.* **13**, 917 (2013).
- ³³L. Balaghi, G. Bussone, R. Grifone, R. Hübner, J. Grenzer, M. Ghorbani-Asl, A. V. Krashennnikov, H. Schneider, M. Helm, and E. Dimakis, *Nat. Commun.* **10**, 2793 (2019).
- ³⁴J. Grönqvist, N. Søndergaard, F. Boxberg, T. Guhr, S. Åberg, and H. Q. Xu, *J. Appl. Phys.* **106**, 053508 (2009).
- ³⁵M. Hetzl, M. Kraut, J. Winnerl, L. Francaviglia, M. Döblinger, S. Matich, A. Fontcuberta i Morral, and M. Stutzmann, *Nano Lett.* **16**, 7098 (2016).

- ³⁶M. Montazeri, M. Fickenscher, L. M. Smith, H. E. Jackson, J. Yarrison-Rice, J. H. Kang, Q. Gao, H. Tan, C. Jagadish, Y. Guo, J. Zou, M. E. Pistol, and C. E. Pryor, *Nano Lett.* **10**, 880 (2010).
- ³⁷N. Sköld, L. S. Karlsson, M. W. Larsson, M. E. Pistol, W. Seifert, J. Trägårdh, and L. Samuelson, *Nano Lett.* **5**, 1943 (2005).
- ³⁸G. L. Bir and G. E. Pikus, *Symmetry and Strain-Induced Effects in Semiconductors* (John Wiley and Sons, NY, 1974).
- ³⁹Y. Sun, S. E. Thompson, and T. Nishida, *J. Appl. Phys.* **101**, 104503 (2007).
- ⁴⁰L. Tao, W. Ou, Y. Li, H. Liao, J. Zhang, F. Gan, and X. Ou, *Semicond. Sci. Technol.* **35**, 103002 (2020).
- ⁴¹G. Tsutsui, S. Mochizuki, N. Loubet, S. W. Bedell, and D. K. Sadana, *AIP Adv.* **9**, 030701 (2019).
- ⁴²H. Fang, M. Madsen, C. Carraro, K. Takei, H. S. Kim, E. Plis, S. Y. Chen, S. Krishna, Y. L. Chueh, R. Maboutian, and A. Javey, *Appl. Phys. Lett.* **98**, 012111 (2011).
- ⁴³M. Guden and J. Piprek, *Modell. Simul. Mater. Sci. Eng.* **4**, 349 (1996).
- ⁴⁴J. Westermayr, J. Gilkes, R. Barrett, and R. J. Maurer, *Nat. Comput. Sci.* **3**, 139 (2023).
- ⁴⁵B. Sanchez-Lengeling and A. Aspuru-Guzik, *Science* **361**, 360 (2018).
- ⁴⁶W. Kohn and L. J. Sham, *Phys. Rev.* **140**, A1133 (1965).
- ⁴⁷J. P. Perdew, K. Burke, and M. Ernzerhof, *Phys. Rev. Lett.* **77**, 3865 (1996).
- ⁴⁸P. Mori-Sánchez, A. J. Cohen, and W. Yang, *Phys. Rev. Lett.* **100**, 146401 (2008).
- ⁴⁹P. Rosenow, L. C. Bannow, E. W. Fischer, W. Stolz, K. Volz, S. W. Koch, and R. Tonner, *Phys. Rev. B* **97**, 075201 (2018).
- ⁵⁰D. Koller, F. Tran, and P. Blaha, *Phys. Rev. B* **83**, 195134 (2011).
- ⁵¹A. V. Krukau, O. A. Vydrov, A. F. Izmaylov, and G. E. Scuseria, *J. Chem. Phys.* **125**, 224106 (2006).
- ⁵²J. Heyd, G. E. Scuseria, and M. Ernzerhof, *J. Chem. Phys.* **118**, 8207 (2003).
- ⁵³M. S. Hybertsen and S. G. Louie, *Phys. Rev. B* **34**, 5390 (1986).
- ⁵⁴L. Hedin, *Phys. Rev.* **139**, A796 (1965).
- ⁵⁵F. Aryasetiawan and O. Gunnarsson, *Rep. Prog. Phys.* **61**, 237 (1998).
- ⁵⁶F. Tran and P. Blaha, *Phys. Rev. Lett.* **102**, 226401 (2009).
- ⁵⁷B. Mondal and R. Tonner-Zech, *Phys. Scr.* **98**, 065924 (2023).
- ⁵⁸B. Mondal, M. Kröner, T. Hepp, K. Volz, and R. Tonner-Zech, *Phys. Rev. B* **108**, 035202 (2023).
- ⁵⁹Within 0%–100% composition and –5% to +5% strain range, for a resolution of 0.1% in both composition and strain, the number of DFT calculations require for a quaternary compound of type $A_xB_yD_{100-x-y}$ = 50 651 601.
- ⁶⁰K. T. Butler, D. W. Davies, H. Cartwright, O. Isayev, and A. Walsh, *Nature* **559**, 547 (2018).
- ⁶¹C. C. Fischer, K. J. Tibbetts, D. Morgan, and G. Ceder, *Nat. Mater.* **5**, 641 (2006).
- ⁶²D. A. Carr, M. Lach-hab, S. Yang, I. I. Vaisman, and E. Blaisten-Barojas, *Microporous Mesoporous Mater.* **117**, 339 (2009).
- ⁶³G. Pilania, J. E. Gubernatis, and T. Lookman, *Phys. Rev. B* **91**, 214302 (2015).
- ⁶⁴T. Yamashita, N. Sato, H. Kino, T. Miyake, K. Tsuda, and T. Oguchi, *Phys. Rev. Mater.* **2**, 013803 (2018).
- ⁶⁵T. Gu, W. Lu, X. Bao, and N. Chen, *Solid State Sci.* **8**, 129 (2006).
- ⁶⁶A. C. Rajan, A. Mishra, S. Satsangi, R. Vaish, H. Mizuseki, K. R. Lee, and A. K. Singh, *Chem. Mater.* **30**, 4031 (2018).
- ⁶⁷A. Seko, T. Maekawa, K. Tsuda, and I. Tanaka, *Phys. Rev. B* **89**, 054303 (2014).
- ⁶⁸L. Ward, A. Agrawal, A. Choudhary, and C. Wolverton, *npj Comput. Mater.* **2**, 16028 (2016).
- ⁶⁹K. T. Schütt, H. Glawe, F. Brockherde, A. Sanna, K. R. Müller, and E. K. U. Gross, *Phys. Rev. B* **89**, 205118 (2014).
- ⁷⁰W. Li, Z. Wang, X. Xiao, Z. Zhang, A. Janotti, S. Rajasekaran, and B. Medasani, *Phys. Rev. B* **106**, 155156 (2022).
- ⁷¹T. Wang, X. Tan, Y. Wei, and H. Jin, *Nanoscale* **14**, 2511 (2022).
- ⁷²S. Prateek, R. Garg, K. Kumar Saxena, V. K. Srivastav, H. Vasudev, and N. Kumar, “Data-driven materials science: Application of ML for predicting band gap,” *Adv. Mater. Process. Technol.* (published online) (2023).
- ⁷³G. Pilania, A. Mannodi-Kanakithodi, B. P. Uberuaga, R. Ramprasad, J. E. Gubernatis, and T. Lookman, *Sci. Rep.* **6**, 19375 (2016).
- ⁷⁴K. L. Heng, S. J. Chua, and P. Wu, *Chem. Mater.* **12**, 1648 (2000).
- ⁷⁵V. Gladkikh, D. Y. Kim, A. Hajibabaei, A. Jana, C. W. Myung, and K. S. Kim, *J. Phys. Chem. C* **124**, 8905 (2020).
- ⁷⁶Y. Zhuo, A. Mansouri Tehrani, and J. Brgoch, *J. Phys. Chem. Lett.* **9**, 1668 (2018).
- ⁷⁷J. Lee, A. Seko, K. Shitara, K. Nakayama, and I. Tanaka, *Phys. Rev. B* **93**, 115104 (2016).
- ⁷⁸L. Wu, Y. Xiao, M. Ghosh, Q. Zhou, and Q. Hao, *ES Mater. Manuf.* **9**, 34 (2020).
- ⁷⁹T. Wang, X. Tan, Y. Wei, and H. Jin, *Mater. Today Commun.* **29**, 102932 (2021).
- ⁸⁰L. Weston and C. Stampfl, *Phys. Rev. Mater.* **2**, 085407 (2018).
- ⁸¹V. Venkatraman, *Comput. Mater. Sci.* **197**, 110637 (2021).
- ⁸²J. Westermayr and R. J. Maurer, *Chem. Sci.* **12**, 10755 (2021).
- ⁸³K. Ghosh, A. Stuke, M. Todorović, P. B. Jørgensen, M. N. Schmidt, A. Vehtari, and P. Rinke, *Adv. Sci.* **6**, 1801367 (2019).
- ⁸⁴W. Ye, C. Chen, Z. Wang, I.-H. Chu, and S. P. Ong, *Nat. Commun.* **9**, 3800 (2018).
- ⁸⁵J. Schmidt, J. Shi, P. Borlido, L. Chen, S. Botti, and M. A. L. Marques, *Chem. Mater.* **29**, 5090 (2017).
- ⁸⁶Y. Huang, C. Yu, W. Chen, Y. Liu, C. Li, C. Niu, F. Wang, and Y. Jia, *J. Mater. Chem. C* **7**, 3238 (2019).
- ⁸⁷Z. Zhu, B. Dong, H. Guo, T. Yang, and Z. Zhang, *Chin. Phys. B* **29**, 046101 (2020).
- ⁸⁸B. Mondal, “Bandgap phase diagram,” GitHub, <https://bmondal94.github.io/Bandgap-Phase-Diagram/>; accessed May 2023.
- ⁸⁹M. G. Craford, D. L. Keune, W. O. Groves, and A. H. Herzog, *J. Electron. Mater.* **2**, 137 (1973).
- ⁹⁰I. D. Henning and H. Thomas, *Phys. Status Solidi A* **79**, 567 (1983).
- ⁹¹Y. Tanaka and T. Toyama, *IEEE Trans. Electron Devices* **41**, 1475 (1994).
- ⁹²J. R. Lang, J. Faucher, S. Tomasulo, K. Nay Yaung, and M. Larry Lee, *Appl. Phys. Lett.* **103**, 092102 (2013).
- ⁹³K. Hayashi, T. Soga, H. Nishikawa, T. Jimbo, and M. Umeno, “MOCVD growth of GaAsP on Si for tandem solar cell application,” in *Proceedings of 1994 IEEE 1st World Conference on Photovoltaic Energy Conversion—WCPEC (A Joint Conference of PVSC, PVSEC and PSEC)*, 5–9 December 1994, Waikoloa, HI (IEEE, 1994), Vol. 2, pp. 1890–1893.
- ⁹⁴T. J. Grassman, D. J. Chmielewski, S. D. Carnevale, J. A. Carlin, and S. A. Ringel, *IEEE J. Photovoltaics* **6**, 326 (2016).
- ⁹⁵M. Weyers, M. S. Michio Sato, and H. A. Hiroaki Ando, *Jpn. J. Appl. Phys.* **31**, L853 (1992).
- ⁹⁶B. Kunert, K. Volz, J. Koch, and W. Stolz, *Appl. Phys. Lett.* **88**, 182108 (2006).
- ⁹⁷Y. Zhao, G. Chen, S. Wang, and S. F. Yoon, *Thin Solid Films* **450**, 352 (2004).
- ⁹⁸S. Loualiche, A. Le Corre, S. Salaun, J. Caulet, B. Lambert, M. Gauneau, D. Lecrosnier, and B. Deveaud, *Appl. Phys. Lett.* **59**, 423 (1991).
- ⁹⁹H. Shimomura, T. Anan, and S. Sugou, *J. Cryst. Growth* **162**, 121 (1996).
- ¹⁰⁰K. Nakajima, T. Ujihara, S. Miyashita, and G. Sazaki, *J. Cryst. Growth* **209**, 637 (2000).
- ¹⁰¹H. B. Russell, A. N. Andriotis, M. Menon, J. B. Jasinski, A. Martinez-Garcia, and M. K. Sunkara, *Sci. Rep.* **6**, 20822 (2016).
- ¹⁰²M. J. Jou, Y. T. Cherng, H. R. Jen, and G. B. Stringfellow, *Appl. Phys. Lett.* **52**, 549 (1988).
- ¹⁰³M. J. Cherng, R. M. Cohen, and G. B. Stringfellow, *J. Electron. Mater.* **13**, 799 (1984).
- ¹⁰⁴H. R. Jen, M. J. Cherng, and G. B. Stringfellow, *Appl. Phys. Lett.* **48**, 1603 (1986).
- ¹⁰⁵G. Kresse and D. Joubert, *Phys. Rev. B* **59**, 1758 (1999).
- ¹⁰⁶P. E. Blöchl, *Phys. Rev. B* **50**, 17953 (1994).
- ¹⁰⁷G. Kresse and J. Hafner, *Phys. Rev. B* **47**, 558 (1993).
- ¹⁰⁸G. Kresse and J. Hafner, *Phys. Rev. B* **49**, 14251 (1994).
- ¹⁰⁹G. Kresse and J. Furthmüller, *Phys. Rev. B* **54**, 11169 (1996).
- ¹¹⁰G. Kresse and J. Furthmüller, *Comput. Mater. Sci.* **6**, 15 (1996).
- ¹¹¹S. Grimme, J. Antony, S. Ehrlich, and H. Krieg, *J. Chem. Phys.* **132**, 154104 (2010).
- ¹¹²S. Grimme, S. Ehrlich, and L. Goerigk, *J. Comput. Chem.* **32**, 1456 (2011).
- ¹¹³A. Zunger, S. H. Wei, L. G. Ferreira, and J. E. Bernard, *Phys. Rev. Lett.* **65**, 353 (1990).

- ¹¹⁴A. van de Walle, M. Asta, and G. Ceder, *Calphad* **26**, 539 (2002).
- ¹¹⁵A. van de Walle, *Calphad* **33**, 266 (2009).
- ¹¹⁶A. van de Walle, P. Tiwary, M. de Jong, D. Olmsted, M. Asta, A. Dick, D. Shin, Y. Wang, L.-Q. Chen, and Z.-K. Liu, *Calphad* **42**, 13 (2013).
- ¹¹⁷O. Rubel, A. Bokhanchuk, S. J. Ahmed, and E. Assmann, *Phys. Rev. B* **90**, 115202 (2014).
- ¹¹⁸A. J. Smola and B. Schölkopf, *Stat. Comput.* **14**, 199 (2004).
- ¹¹⁹C. Cortes and V. Vapnik, *Mach. Learn.* **20**, 273 (1995).
- ¹²⁰C. J. Burges, *Data Min. Knowl. Discov.* **2**, 121 (1998).
- ¹²¹F. Pedregosa *et al.*, *J. Mach. Learn. Res.* **12**, 2825 (2011).
- ¹²²B. Schölkopf and A. J. Smola, *Learning with Kernels: Support Vector Machines, Regularization, Optimization, and Beyond, Adaptive Computation and Machine Learning Series* (MIT Press, 2018).
- ¹²³T. Hofmann, B. Schölkopf, and A. J. Smola, *Ann. Stat.* **36**, 1171 (2008).
- ¹²⁴S. Vempati, A. Vedaldi, A. Zisserman, and C. V. Jawahar, “Generalized RBF feature maps for efficient detection,” in *Proceedings of the British Machine Vision Conference {BMVC} 2010, Aberystwyth, UK, August 31-September 3, 2010*, edited by F. Labrosse, R. Zwiggleaar, Y. Liu, and B. Tiddeman (British Machine Vision Association, 2010), pp. 1–11.
- ¹²⁵L. Ward, R. Liu, A. Krishna, V. I. Hegde, A. Agrawal, A. Choudhary, and C. Wolverton, *Phys. Rev. B* **96**, 024104 (2017).
- ¹²⁶R. E. Goodall and A. A. Lee, *Nat. Commun.* **11**, 6280 (2020).
- ¹²⁷O. Isayev, C. Oses, C. Toher, E. Gossett, S. Curtarolo, and A. Tropsha, *Nat. Commun.* **8**, 15679 (2017).
- ¹²⁸O. A. von Lilienfeld, *Angew. Chem., Int. Ed.* **57**, 4164 (2018).
- ¹²⁹T. Viering and M. Loog, *IEEE Trans. Pattern Anal. Mach. Intell.* **45**, 7799 (2023).
- ¹³⁰M. Gastegger, J. Behler, and P. Marquetand, *Chem. Sci.* **8**, 6924 (2017).
- ¹³¹P. Dierckx, *Comput. Graphics Image Process.* **20**, 171 (1982).
- ¹³²L. Vegard, *Z. Phys.* **5**, 17 (1921).
- ¹³³A. R. Denton and N. W. Ashcroft, *Phys. Rev. A* **43**, 3161 (1991).
- ¹³⁴B. Mondal and R. Tonner-Zech (2022). “III–V binary semiconductors strain study,” NOMAD. <https://doi.org/10.17172/NOMAD/2022.08.20-2>
- ¹³⁵B. Mondal and R. Tonner-Zech (2023). “III–V ternary semiconductors strain study,” NOMAD. <https://doi.org/10.17172/NOMAD/2023.02.27-1>
- ¹³⁶B. Mondal, J. Westermayr, and R. Tonner-Zech (2023). “GaAsPsb bandgap phase diagram,” NOMAD. <https://doi.org/10.17172/NOMAD/2023.05.03-1>

Supporting Information

Machine learning for accelerated bandgap prediction in strain-engineered quaternary III-V semiconductors

Badal Mondal

*Wilhelm-Ostwald-Institut für Physikalische und Theoretische Chemie,
Universität Leipzig, 04103 Leipzig, Germany and
Fachbereich Physik, Philipps-Universität Marburg, 35032 Marburg, Germany*

Julia Westermayr

*Wilhelm-Ostwald-Institut für Physikalische und Theoretische Chemie,
Universität Leipzig, 04103 Leipzig, Germany and
Center for Scalable Data Analytics and Artificial Intelligence, Dresden/Leipzig, Germany*

Ralf Tonner-Zech*

Wilhelm-Ostwald-Institut für Physikalische und Theoretische Chemie, Universität Leipzig, 04103 Leipzig, Germany

(Dated: July 10, 2023)

ML : Machine learning
SVM-RBF model : Support Vector Machine with Radial Basis Function kernel machine learning model
SVR-RBF model : Support Vector Regression with Radial Basis Function kernel machine learning model
SVC-RBF model : Support Vector Classification with Radial Basis Function kernel machine learning model
RMSE : Root Mean Squared Error
MAE : Mean Absolute Error
Max error : Maximum error
 R^2 : Coefficient of determination

* ralf.tonner@uni-leipzig.de

S1. Hyperparameter optimization

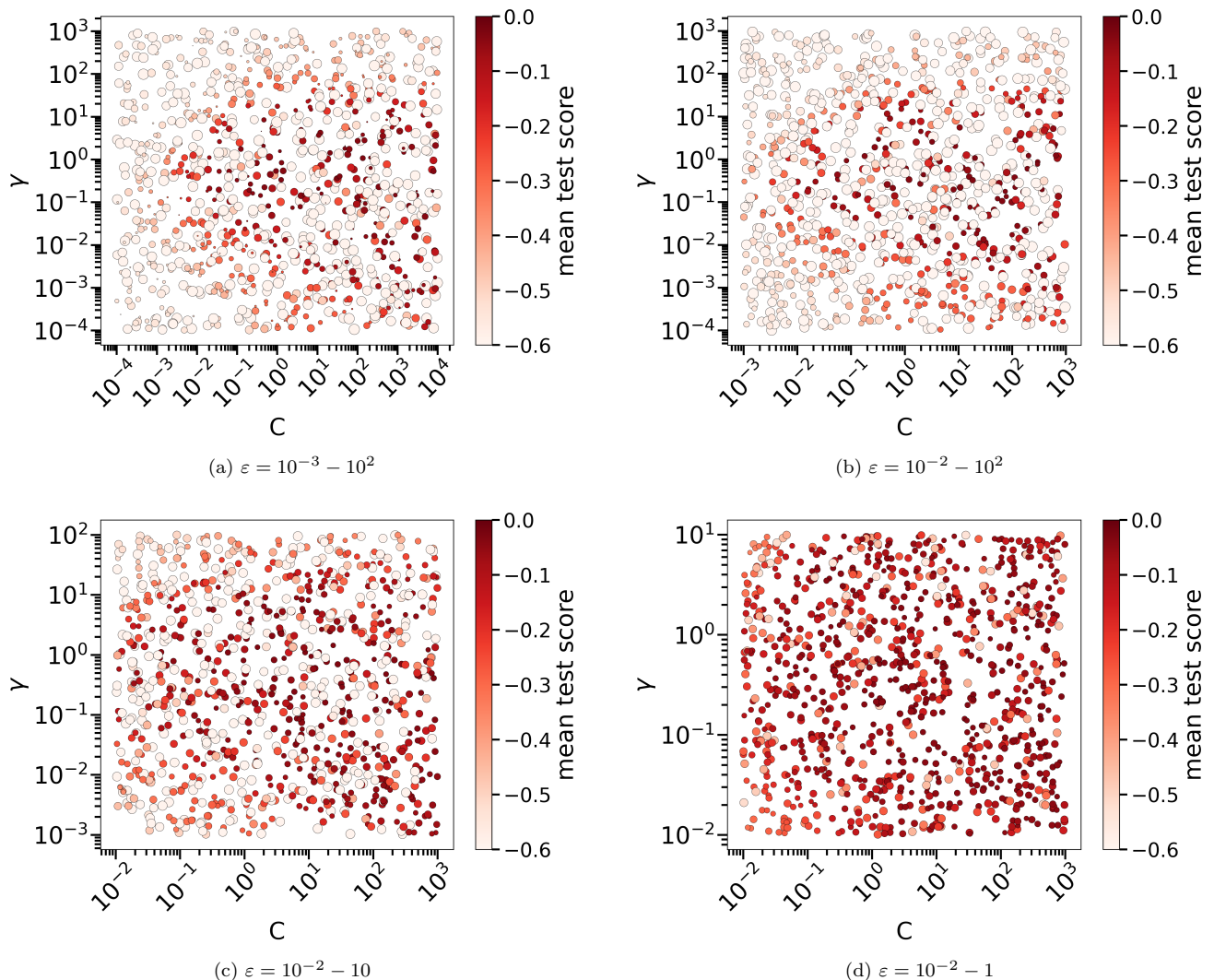


FIG. S1. Hyperparameter optimization with the largest dataset (3210 training data points) using random search cross-validation of the SVR-RBF model. The hyperparameter optimization scoring function is the negative RMSE, meaning that a small error or a high test-score (red) is beneficial. The random search is performed for each subfigure over 1000 random C , γ , and ε combinations from a logarithmic uniform distribution space. The sizes of the circles, depicted in log-scale, represent the ε values. Specifically, we plot $\log(10^3\varepsilon)$ values to ensure non-negative marker size. The ranges for C , γ , and ε are made tighter from (a) to (d).

In Fig. S1, we show the hyperparameter optimization with random search cross-validation of the SVR-RBF model. We tune the C , γ , and ε ranges and find Fig. S1d as the optimal choice, covering the regimes with the best hyperparameters set. The larger C value ($> 10^3$) would result in a hard margin in the SVR model and, thus, poor generalization on unknown data. Therefore, for C , no larger values are sampled here.

Note the mean test score values in Fig. S1 are displayed on a negative scale. As mentioned in the manuscript, we used the package `sklearn` for implementing the ML models in this article. The hyperparameter optimizations in this package are performed by evaluating the scoring function values over the cross-validation set. In `sklearn`, by convention, the convention is to maximize all scorer objects during optimization. However, in ML problems, the objective is to minimize the error for error functions. Thus metrics such as ‘mean squared error’ are available as ‘negative mean squared error’ in hyperparameter optimization scoring functions, which return the negated value of the metric.

S2. Negative direct bandgap

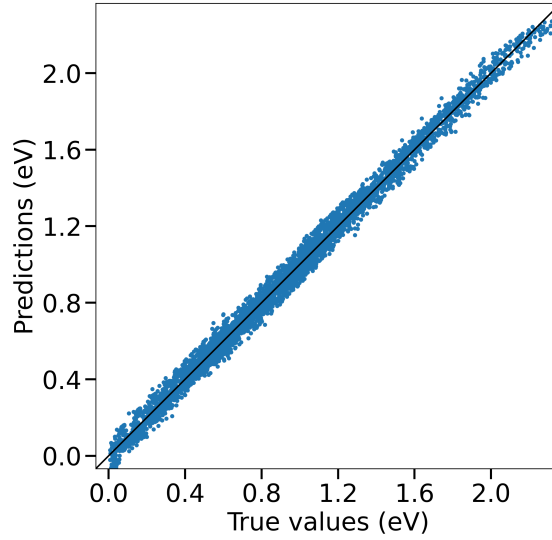


FIG. S2. The SVR-RBF model bandgap value predictions over all the samples. The true values are the DFT calculated bandgaps. The hyperparameters are optimized with RMSE metric.

In Fig. S2, the bandgap values were predicted using SVR-RBF model. The hyperparameters of the model were optimized using RMSE metric, Eq. S1. However, the corresponding SVR-RBF model predicted a few small negative direct bandgap values of up to -5 meV (see left-bottom corner in Fig. S2). In the manuscript, we thus converted all the predicted negative bandgap values (\hat{y}_i) to 0 ($\hat{y}_i=0$). The RMSE of the model predictions was calculated after the conversion. Accordingly, all the performance metrics evaluated did include this conversion.

$$\text{RMSE} = \sqrt{\frac{1}{n_{\text{samples}}} \sum_{i=1}^{n_{\text{samples}}} (y_i - \hat{y}_i)^2} \quad (\text{S1})$$

Where \hat{y}_i is the ML model predicted value of i -th sample and y_i is the corresponding true value. n_{samples} is the total number of samples.

S3. Machine learning dataset features and labels for GaAsPSb

The full data dataset can be found in the Supplementary Information attachment. In the table below, the ML features for 3 example data are given.

Sample 1: $\text{Ga}_{100}\text{P}_0\text{As}_{100}\text{Sb}_0$ (\equiv GaAs), unstrained

Sample 2: $\text{Ga}_{100}\text{P}_{25}\text{As}_{25}\text{Sb}_{50}$, 3.0% biaxial tensile strained

Sample 3: $\text{Ga}_{100}\text{P}_{50}\text{As}_{50}\text{Sb}_0$, 5.0% biaxial compressively strained

| Sample index | Features | | | | Labels | |
|--------------|----------------|-------------|--------------|------------|--------------------|-----------------------------|
| | Phosphorus (%) | Arsenic (%) | Antimony (%) | Strain (%) | Bandgap value (eV) | Bandgap nature ^a |
| 1 | 0 | 100 | 0 | 0.0 | 1.466 | direct |
| 2 | 25 | 25 | 50 | 3.0 | 0.629 | direct |
| 3 | 50 | 50 | 0 | -5.0 | 1.243 | indirect |

^a The direct and indirect bandgap natures are feature transformed to 1 and 0s before ML training.

S4. Dataset convergence

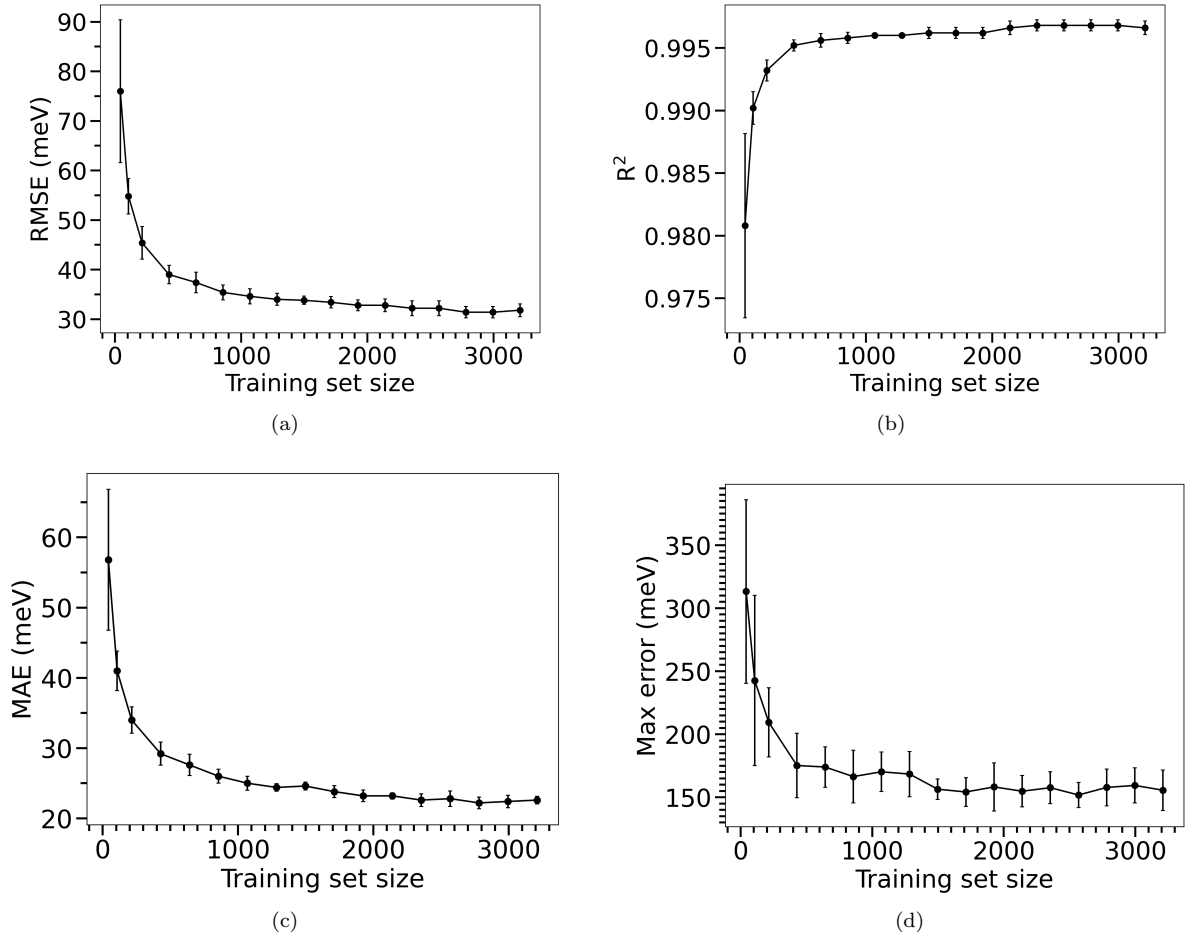


FIG. S3. Dependence of bandgap magnitude prediction (a) RMSE, (b) R^2 , (c) MAE, and (d) Max error from SVR-RBF model on the number of training data. Error bars show standard deviations for 5 trials. The hyperparameters are optimized with RMSE metric.

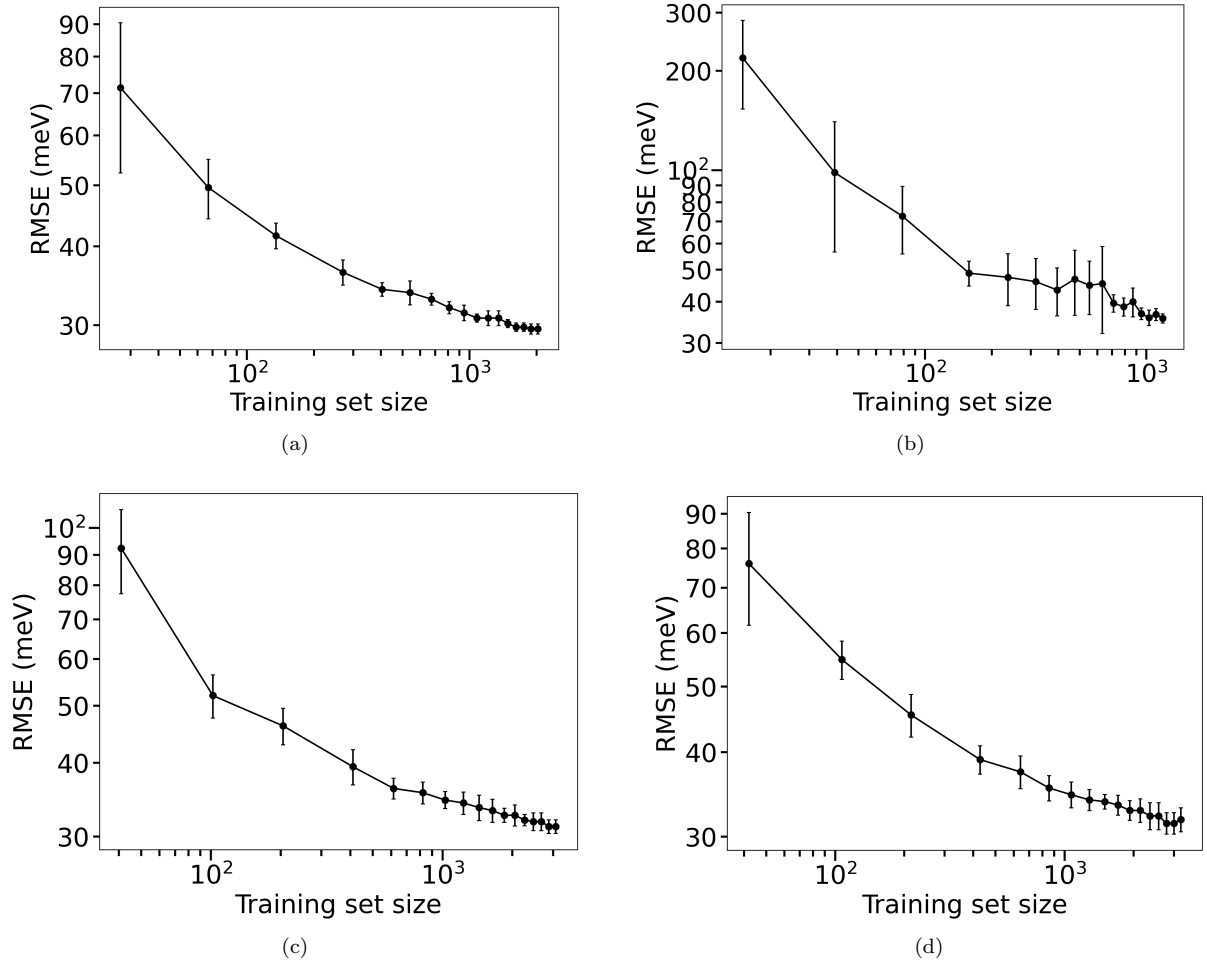


FIG. S4. Learning curve in log–log scale showing the performance of the SVR-RBF model for bandgap value predictions, with different dataset settings: (a) using the dataset that contains only direct bandgaps, (b) using the dataset that contains only indirect bandgaps, (c) using the dataset that contains both direct and indirect bandgaps while excluding the data points for which SVC-RBF model predicted an incorrect bandgap nature, and (d) using the original dataset. Figure (d) corresponds to Fig. 1a in the main manuscript. Error bars show standard deviations over 5 trials. The hyperparameters are optimized with RMSE metric.

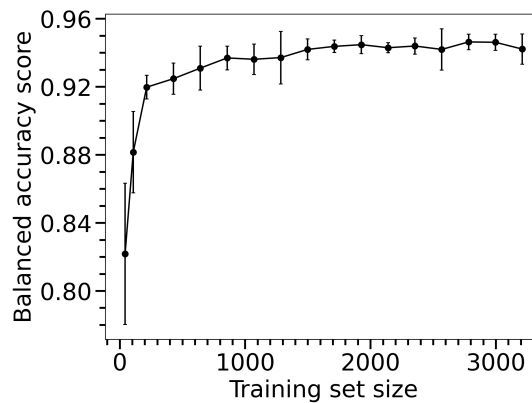


FIG. S5. Dependence of bandgap nature prediction balanced-accuracy-score from SVC-RBF model on the number of training data. Error bars show standard deviations for 5 trials. Hyperparameters are optimized with accuracy-score metric.

S5. Bandgap prediction validations

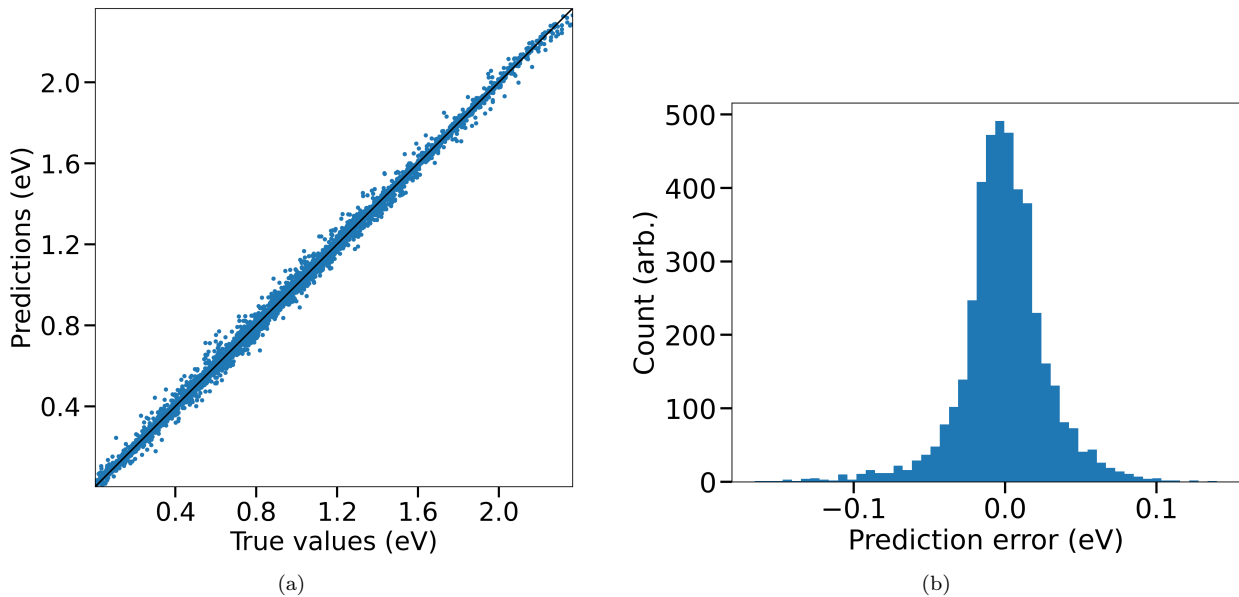


FIG. S6. The bandgap values prediction from the SVR-RBF models for all input data in the dataset. True values are the DFT calculated bandgap values. The predictions are the average bandgap values over the 5 model predictions from the trial set of the last point from Fig. 1a. (a) shows the comparison between true and predicted values, (b) is the prediction error (true value minus predicted value) distribution.

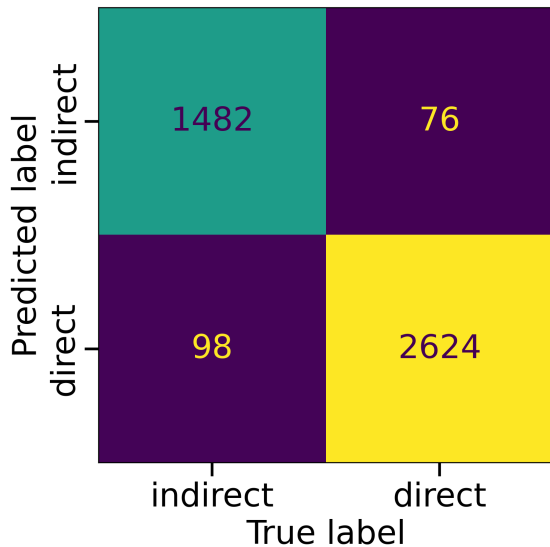


FIG. S7. The confusion matrix of the bandgap nature predictions, showing the number of correct and wrong predictions for each class (direct and indirect). True labels are the bandgap nature determined from DFT calculations for all input data in the dataset. The prediction labels are the most frequent outcomes over the 5 SVC-RBF model predictions (mode value) from the trial set of the last point from Fig. 1b.

S6. Standard deviation distribution of bandgap prediction

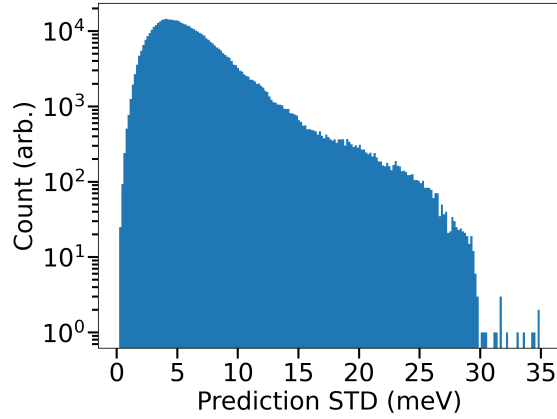


FIG. S8. The standard deviation (STD) distribution of bandgap value predictions using the 5 SVR-RBF models from the last point of Fig. 1a. The figure is plotted in semi-log scale.

S7. Smoothing direct-indirect transition line

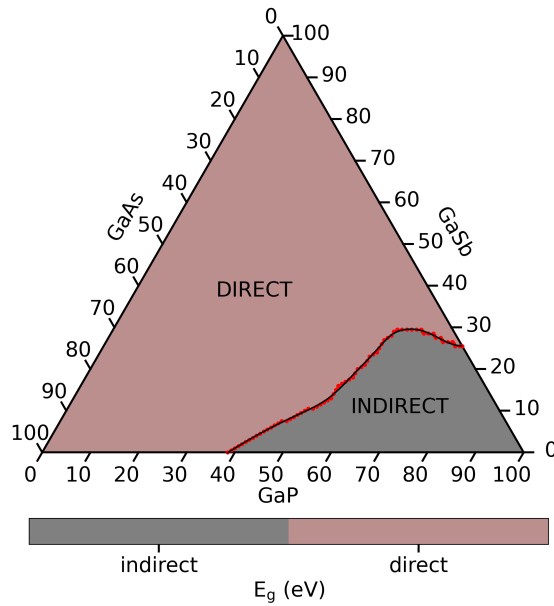


FIG. S9. The mapping of bandgap nature for unstrained GaAsPSb (0.0% strain). The labels ‘direct’ and ‘indirect’ describe the enclosed regions, with the nature of bandgap being direct and indirect, respectively. These areas are separated by the direct-indirect transition (DIT) points (red dots). The bandgap natures calculated are the most frequent outcomes over the 5 predictions (mode value) from the trial set of the last point from Fig. 1b. The calculated DIT points (red dots) are fitted (black line) with B-spline function with the smoothing factor, $s=5$.

We smoothen the calculated discrete direct-indirect transition (DIT) points with B-spline function [1] (smoothing factor, $s=5$) as is implemented in `scipy.interpolated` [2] routine.

```

from scipy.interpolate import splprep, splev
x = DIT_x #x-coordinate of the calculated DITs
y = DIT_y #y-coordinate of the calculated DITs
tck, u = splprep([x, y], s=5)
smoothen_DIT_x, smoothen_DIT_y = splev(u, tck)

```

S8. Bandgap values variation under strain for specific GaAsPSb

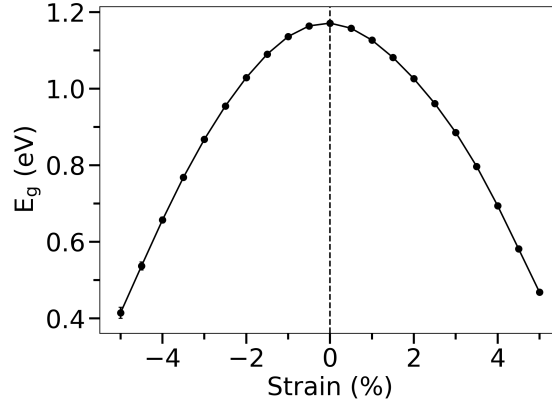


FIG. S10. The variation of bandgap values (E_g) under biaxial strain in $\text{GaAs}_{0.333}\text{P}_{0.333}\text{Sb}_{0.334}$. The positive and negative strain values indicate the tensile and compressive strains, respectively. The bandgap values are the average values over the 5 model predictions from the trial set of the last point from Fig. 1a and error bars show standard deviations.

S9. Substrate effect in GaAsPSb bandgap phase diagram

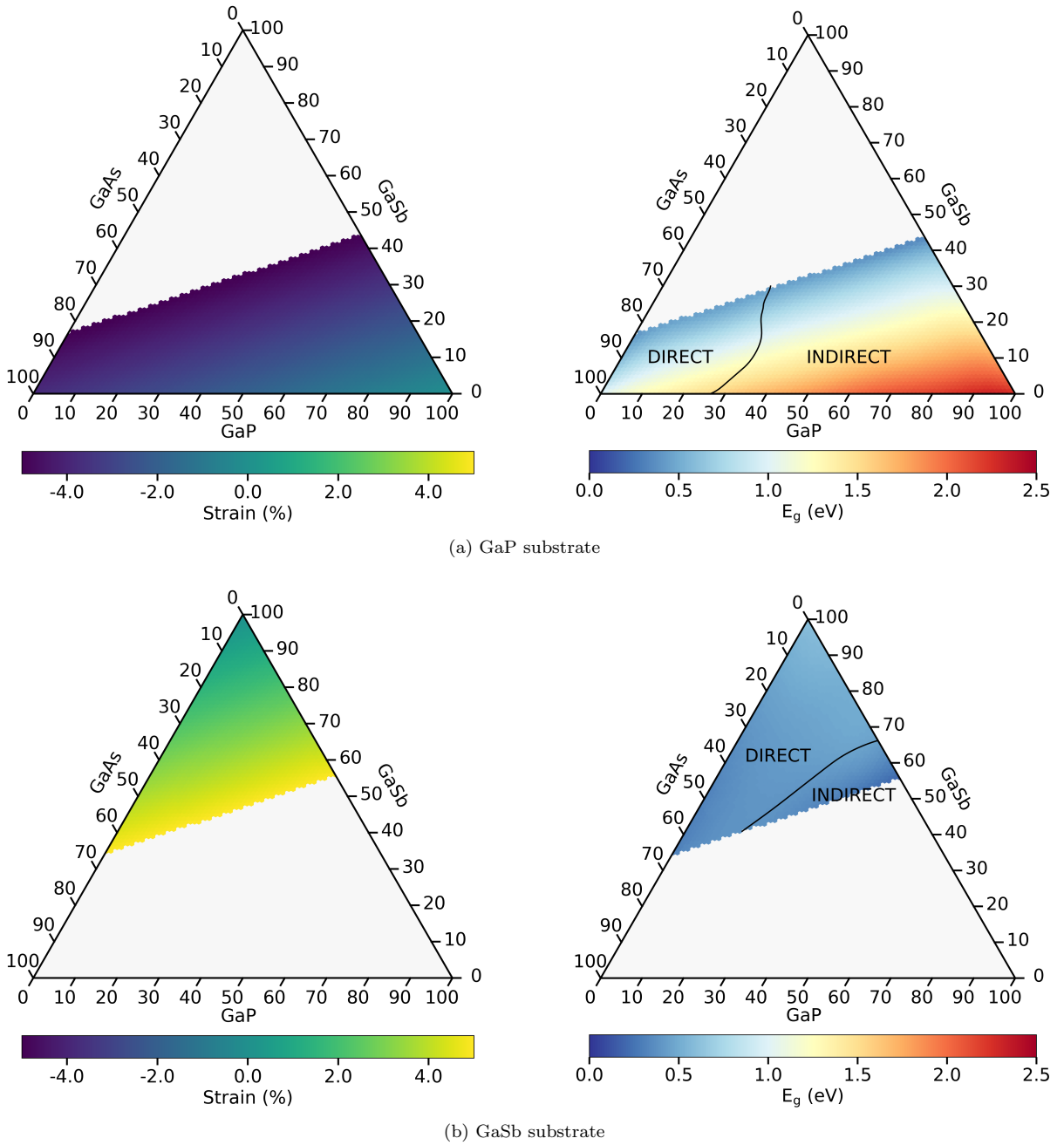
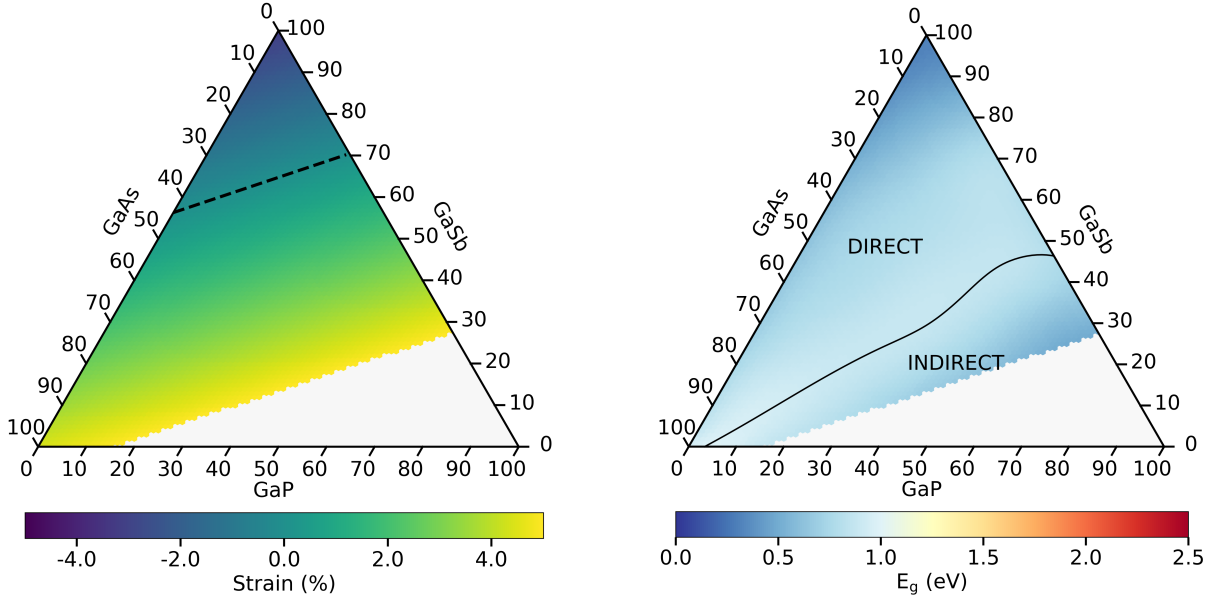
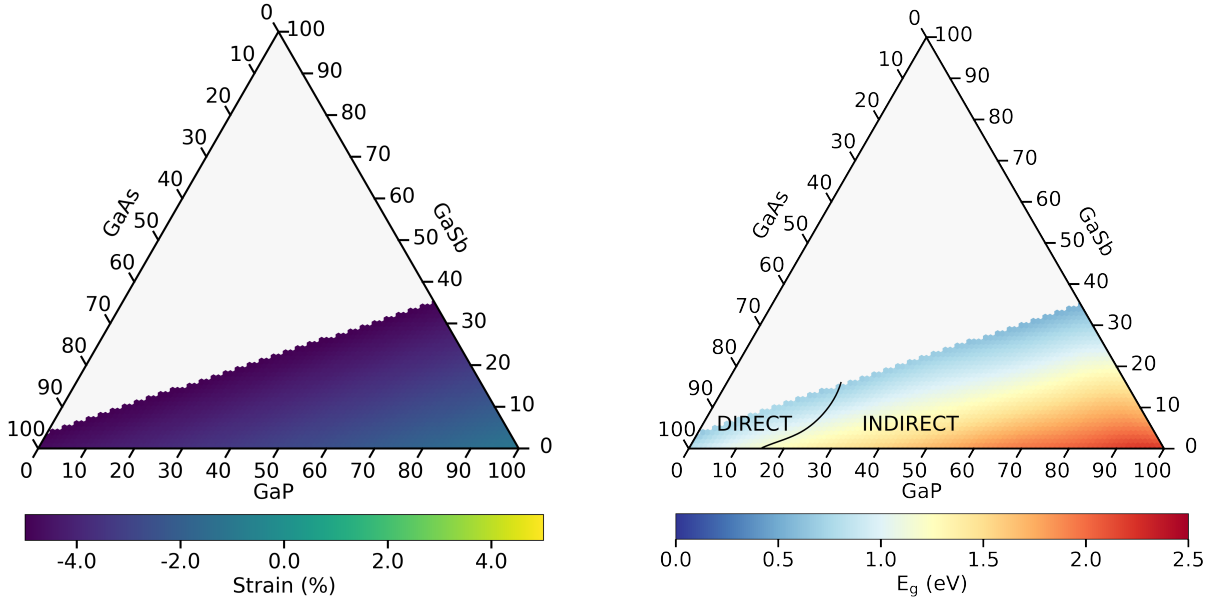


FIG. S11. The effect of substrate on GaAsPSb epi-layer under the ‘theoretical epitaxy’ model [3, 4] (up to 5% compressive and tensile strain). The left column shows the calculated biaxial strain values using Eqs. 8 and 9. The right column presents predicted bandgap values in color (E_g). The labels ‘direct’ and ‘indirect’ describe the enclosed regions, with the nature of bandgap being direct and indirect, respectively. The bandgap values are the average values over the 5 model predictions from the trial set of the last point from Fig. 1a. The nature of the bandgaps are the most frequent outcomes over the 5 predictions (mode value) from the trial set of the last point from Fig. 1b.



(c) InP substrate



(d) Si substrate

FIG. S11. (*continue*) The effect of substrate on GaAsPSb epi-layer under the ‘theoretical epitaxy’ model [3, 4] (up to 5% compressive and tensile strain). The left column shows the calculated biaxial strain values using Eqs. 8 and 9. The black dotted line in (c) indicates the perfect lattice matching (no strain) compositions. The right column presents predicted bandgap values in color (E_g). The labels ‘direct’ and ‘indirect’ describe the enclosed regions, with the nature of bandgap being direct and indirect, respectively. The bandgap values are the average values over the 5 model predictions from the trial set of the last point from Fig. 1a. The nature of the bandgaps are the most frequent outcomes over the 5 predictions (mode value) from the trial set of the last point from Fig. 1b.

-
- [1] P. Dierckx, Algorithms for smoothing data with periodic and parametric splines, *Comput. Graph. Image Process.* **20**, 171 (1982).
 - [2] P. Virtanen et al., SciPy 1.0: fundamental algorithms for scientific computing in Python, *Nat. Methods* **17**, 261 (2020).
 - [3] B. Mondal and R. Tonner-Zech, Systematic strain-induced bandgap tuning in binary III-V semiconductors from density functional theory, *Phys. Scr.* **98**, 065924 (2023).
 - [4] B. Mondal, M. Kröner, T. Hepp, K. Volz, and R. Tonner-Zech, Accurate first principles band gap predictions in strain engineered ternary III-V semiconductors, *Phys. Rev. B* **108**, 035202 (2023).

Abbreviations and Acronyms

| | |
|------------------|---|
| ATAT | Alloy Theoretical Automated Toolkit |
| BOA | Born-Oppenheimer Approximation |
| BSW | Bloch Spectral Weight |
| BZ | Brillouin Zone |
| CB | Conduction Band |
| CBM | Conduction Band Minimum |
| CMOS | Complementary Metal-Oxide Semiconductor |
| CPA | Coherent-Potential Approximation |
| DFT | Density Functional Theory |
| DIT | Direct-Indirect Transition |
| EBS | Effective Band Structure |
| LED | Light-Emitting Diodes |
| m-BJ | Modified Becke-Johnson |
| MAE | Mean Absolute Error |
| Max error | Maximum error |
| MBD | Many-Body Dispersion |
| ML | Machine Learning |
| MQW | Multiple Quantum Well |
| NM | Nanomembrane |
| PAW | Projector Augmented-Wave |
| PBC | Periodic Boundary Condition |
| QWH | Quantum-Well Heterostructure |

ABBREVIATIONS AND ACRONYMS

| | |
|----------------------|-------------------------------------|
| R² | Coefficient of determination |
| RBF | Radial Basis Function |
| RMSE | Root Mean Squared Error |
| SQS | Special Quasi-Random Structure |
| SV | Support Vector |
| SVC | Support Vector Classification |
| SVM | Support Vector Machines |
| SVR | Support Vector Regression |
| TS | Tkatchenko-Scheffler |
| VASP | Vienna Ab Initio Simulation Package |
| VB | Valence Band |
| VBM | Valence Band Maximum |
| VCA | Virtual-Crystal Approximation |